Study of the extragalactic background light imprint on gamma-ray spectra of 1ES 1011+496 and PKS 1424+240, and the low gamma-ray emission state of M87

Priyadarshini Bangale

München 2019

Study of the extragalactic background light imprint on gamma-ray spectra of 1ES 1011+496 and PKS 1424+240, and the low gamma-ray emission state of M87

Priyadarshini Bangale

Dissertation
an der Fakultät für Physik
der Ludwig–Maximilians–Universität
München

vorgelegt von
Priyadarshini Bangale
aus Nanded, India

München, den 21.01.2019

Erstgutachter: Prof. Dr. Christian Kiesling
Zweitgutachter: Prof. Dr. Masahiro Teshima
Tag der mündlichen Prüfung: 11.03.2019

Zusammenfassung

Diese Doktorarbeit befasst sich mit der Beobachtung von astrophysikalischen Objekten wie Aktiven Galaxienkernen (engl. AGN) im Spektralbereich sehr hochenergetischer (VHE, E>100GeV) γ-Strahlung mit den Major Atmospheric Gamma-ray Imaging Cherenkov (MAGIC) Teleskopen. Der erste Teil dieser Doktorarbeit widmet sich der Beobachtung der beiden Blazare 1ES 1011+496 und PKS 1424+240, und der bekannten Radiogalaxie M87. Ich nutze diese Daten um die dabei auftretenden extrem energiereichen nicht-thermischen Prozesse zu studieren. Typischerweise wird mit MAGIC in mondlosen Nächten beobachtet, hier jedoch wurde M87 auch in mondhellen Nächten beobachtet. Dadurch erhöht sich die von den Photomultipliern gemessene Hintergrundrate. Hierfür habe ich eine adaptive Mond-Analyse-Pipeline für MAGIC implementiert welche diese Effekte berücksichtigt. Der zweite Teil der Doktorarbeit beschäftigt sich mit der Messung des extra-galaktischen Hintergrundlichts (engl. EBL), dem Strahlungsfeld aller Licht emittierender Objekte wie Sterne und Galaxien seit dem Urknall welches das Universum durchdringt. Ich konnte in dieser Doktorarbeit die EBL-Dichte aufgrund der Energiespektren der Objekte 1ES 1011+496 und PKS 1424+240 einschränken.

Im Zeitraum Februar bis März 2014 hat MAGIC den Blazar 1ES 1011+496 ($z = 0.212$) während eines extremen VHE-Ausbruchs beobachtet. Ich habe die insgesamt 12.8 Stunden an angefallenen Daten mit der MAGIC-Standard-Analysesoftware ausgewertet. Die Quelle wurde auf einem sehr hohen Signifikanzniveau von $63\,\sigma$ detektiert [Ahnen et al. 2016]. Der während des Ausbruchs detektierte Fluss wurde im Bereich der Röntgenstrahlung über GeV bis hin zu TeV Gammastrahlen auf einem historischen Höchststand gemessen. Der gemessene Spitzen- und Durchschnittswert ($E > 200\,\mathrm{GeV}$) betrug $(2.28 \pm 0.13) \times 10^{-10}$ $\mathrm{cm}^{-2}\mathrm{s}^{-1}$ bzw. $(0.72 \pm 0.01) \times 10^{-10}$ $\mathrm{cm}^{-2}\mathrm{s}^{-1}$. Dies entspricht einem $\sim$14 bzw. $\sim$17 mal höheren integralen Spitzenfluss im Vergleich zu den Durchschnittswerten aus den Jahren 2007 und 2008, und $\sim$29 mal dem während der Multiwellenlängenkampagne von 2011 bis 2012 gemessenen durchschnittlichen integralen Fluss. Während des gesamten Ausbruchs blieb die Form des Spektrums konstant, während der Fluss von Nacht zu Nacht variierte. Dies war das erste Mal, dass von dieser Quelle ein solch außergewöhnlicher Ausbruch beobachtet wurde, dessen Spektrum sich von 48 GeV bis 3.6 TeV erstreckte. Damit war es möglich einen viel größeren Überlapp zwischen dem MAGIC- und *Fermi*-LAT-Spektrum zu erzielen. Die spektrale Energieverteilung von 1ES 1011+496 vom Röntgenbereich bis hin zu TeV-Energien lässt sich mit einem Ein-Zonen Synchrotron Self-Compton (SSC) Modell beschreiben, was widerum für einen leptonischen Ursprung der VHE γ-Strahlen-Emission spricht. Die hohe Rotverschiebung und das

gemessene Signal oberhalb von 1 TeV machten die 1ES 1011+496 Daten zu einem außerordentlich guten Studienobjekt um EBL-Absorption zu messen.

Im Zeitraum März bis Juni 2014 wurde der Blazar PKS 1424+240 ($z = 0.6$) regelmäßig von MAGIC beobachtet. Ich habe insgesamt 27.58 Stunden mit der MAGIC-Standard-Analysesoftware ausgewertet. Die Quelle wurde mit einer Signifikanz von $17.55\,\sigma$ detektiert. Im gesammten Zeitraum konnte keine Variabilität beobachtet werden, weder innerhalb einer noch von Nacht zu Nacht. Im Vergleich zu vorangegangenen Beobachtungen war 2014 der gemessene Fluss geringer als 2009, als MAGIC Mono-Beobachtungen durchführte, und im Rahmen der statistischen Fehler vergleichbar zu Daten aus den Jahren 2010 und 2011. Der differenzielle Fluss war im Rahmen der Messfehler mit allen vorangegangenen MAGIC-Beobachtungen vergleichbar, was auf eine konstante VHE γ-Strahlen-Emission hindeutet. Diesmal konnte das Spektrum zum ersten mal herunter bis zu 40 GeV gemessen werden, was eine größere spektrale Überschneidung zwischen MAGIC und *Fermi*-LAT bedeutet. Die spektrale Energieverteilung von PKS 1424+240 von Röntgen bis TeV kann nicht mit einem einfachen Ein-Zonen SSC-Modell gefittet werden, da das Spektrum im optischen und UV-Bereich nicht gleichzeitig mit den VHE-Daten reproduziert werden kann ohne einen viel höheren Doppler-Faktor anzunehmen. Jedoch beschreibt ein Zwei-Zonen SSC Modell die SED sehr gut. In dem Zwei-Zonen-Modell stammt ein Großteil der SSC-Emission (optisch bis GeV) von einer großen Emissionsregion (hier äußere Region genannt), und die Röntgen und VHE γ-Emission entstammt hauptsächlich einer kleineren Region (auch innere Region genannt) die von einer um eine Größenordnung höheren energetischen Population von Elektronen ausgefüllt ist. Diese befindet sich näher am zentralen Schwarzen Loch. Die hohe Rotverschiebung von 0.6 und das gemessene Signal oberhalb von 100 GeV machten die PKS 1424+240-Daten eben falls zu einem außerordentlich guten Studienobjekt ür dir EBL-Absorption.

M87 ist eine vom Radio-Bereich bis hin zu TeV bereits ausführlich untersuchte Radiogalaxie in einem Abstand von 16 Mpc. Mehrere Ausbrüche im TeV-Bereich wurden zwischen 2005 und 2010 dokumentiert. Von 2012 bis 2015 wurde M87 regelmäßig mit den MAGIC-Teleskopen während mondhellen Nächten beobachtet. Ich habe insgesamt ∼156 Stunden an Daten mit der an Mond angepassten Analysesoftware ausgewertet [Ahnen et al. 2019]. Die Quelle konnte für jedes einzelne Analysejahr signifikant detektiert werden, allerdings wurden keine Ausbrüche beobachtet. Aufgrund der gesteigerten Sensitivität von MAGIC nach Upgrades der Kamera und Ausleseelektronik [Aleksić et al. 2016a] stellen die M87-Beobachtungen von 2012 bis 2015 mit die genauesten Messungen dieser Quelle in einem Zustand geringer Emission dar. In den Jahren 2012, 2014 und 2015 wurde keine Variabilität beobachtet, weder auf einer Zeitskala von Tagen noch Monaten. Anzeichen für Variabilität auf einem Signifikanzniveau von $\sim 3\,\sigma$ wurden im 2013-Datensatz auf einer Zeitskala von Tagen gefunden. Diese Anzeichen für Variabilität bleiben auf einem ähnlichen Signifikanzniveau bestehen, auch wenn die systematischen Fehler mit in der Analyse berücksichtigt werden. Der VHE γ-Strahlen-Fluss oberhalb von 300 GeV

zwischen 2012 und 2015 ist der niedrigste seit 2005. Die kombinierte spektrale Energieverteilung aus MAGIC und *Fermi*-LAT zeigt zum ersten mal ein perfektes Potenzgesetz über 5 Dekaden in Energie von 200 MeV bis ∼10 TeV. Ich konnte zudem zeigen, dass anhand der gefitteten Position aus den Daten von 2012 bis 2015, zusammengenommen mit dem Hinweis auf Flussveränderungen auf einer Zeitskala von Tagen die äußeren Bereiche des Jets als Ursprungsort der VHE-Emission ausgeschlossen werden können. Nur noch Bereiche nahe des Zentrums oder in der Nähe des Hot Spots im Jet der als HST-1 bezeichnet wird kommen noch in Frage. Daraus lässt sich schlussfolgern, dass die TeV-Emission während der Ausbrüche von der selben oder einer ähnlichen Region kommt. Zwei Modelle kommen für die Beschreibung der Emission von Radio bis TeV in Frage: 1) Ein homogenes leptonisches (SSC) Modell oder 2) zum ersten mal ein hybrides photo-hadronisches l.

Im Zweiten Teil der Doktorarbeit habe ich Limits auf die EBL-Absorption anhand von γ-Strahlen Spektren des außergewöhnlichen Ausbruchs von 1ES 1011+496 (z=0.212) und aus Daten von PKS 1424+240 (z=0.6) berechnet. EBL ist ein diffuses Strahlungsfeld, welches sich von UV bis ins Infrarotlicht erstreckt und entsprechend der Epoche seiner Erzeugung rotverschoben ist. VHE γ-Strahlen werden Aufgrund ihrer Wechselwirkung mit EBL-Photonen via Paar-Erzeugung abgeschwächt, was sich auf die beobachtete spektrale Form der Spektren von AGNs auswirkt. Die Messung dieses charakteristischen Abdrucks lässt Rückschlüsse auf die EBL-Dichte zu. In dieser Studie habe ich einen modellabhängigen Ansatz für die Charakterisierung des EBL im Bereich des optischen bis infraroten Lichts anhand von MAGIC-Beobachtungen gewählt. Die Ergebnisse für die EBL-Dichte basierend auf 1ES 1011+496-Daten ergaben $\lambda F_\lambda = 12.61^{+2.40}_{-2.63}$ nW m^{-2} sr^{-1} bei 1.4 μm für ein EBL-Level $\alpha = 1.1^{+0.17}_{-0.28}$, für den Bereich 0.23 bis 2.96 μm, was den optischen Teil des kosmischen EBL-Spektrums abdeckt. Der Normierungsfaktor α, welcher auch ein Maß für das EBL-Level ist, ist ein Skalierungsfaktor für die optische Dichte. Die angegebenen Fehler von λF_λ und α enthalten statistische und systematische Unsicherheiten. Für die PKS 1424+240-Daten konnten keine signifikanten Limits berechnet werden, da das intrinsische Spektrum an sich zu hohen Energien weicher wird. Deshalb habe ich für diesen Datensatz Obergrenzen ausgerechnet. Die kombinierte Test-Statistik basierend auf beiden Quellen wird stark von 1ES 1011+496 dominiert und liefert folgende Ergebnisse für die EBL-Dichte: $\lambda F_\lambda = 12.61^{+2.41}_{-2.64}$ nW m^{-2} sr^{-1} bei 1.4 μm, im Wellenlängenbereich von 0.23 bis 2.96 μm für ein EBL Level $\alpha = 1.1^{+0.07}_{-0.23}$, was in etwa den selbe Werten wie für 1ES 1011+496 alleine entspricht. Die Fehler hierbei beinhalten nur statistische Unsicherheiten. Die gefundenen Grenzen für das EBL anhand dieser Daten sind kompatibel mit gängigen EBL-Modellen. Diese Ergebnisse stellen die ersten gut aufgelösten Ergebnisse basierend auf MAGIC-Beobachtungen dar [Ahnen et al. 2016].

Abstract

This thesis is focused on the study of distant sources such as active galactic nuclei (AGNs) in the very high energy (VHE, E>100GeV) γ-ray regime using the Major Atmospheric Gamma-ray Imaging Cherenkov (MAGIC) telescopes. The first part of the thesis is dedicated to a detailed analysis of the two blazars; 1ES 1011+496 and PKS 1424+240, and a very well known radio galaxy M87. I have used these data to investigate the non-thermal radiation and violent processes within the blazars and radio galaxy. Usually, MAGIC data is taken in dark conditions. However, most of the M87 data was taken in moon conditions. The presence of the Moon increases the night sky background (NSB) fluctuations, which increases the rate of photoelectrons continuously detected by every pixel of the camera. Therefore, I have developed the moon adapted MAGIC data analysis chain to analyze the M87 data taken in moon conditions properly. The second topic of the thesis focuses on the measurements of the extragalactic background light (EBL), which represents the integrated star and galaxy light emitted through the history of the Universe. In this thesis, I have derived constraints on the EBL density using the VHE γ-ray spectra from 1ES 1011+496 and PKS 1424+240 data.

During February-March 2014, the MAGIC telescopes observed the blazar 1ES 1011+496 ($z = 0.212$) in exceptionally high flaring state at VHE. I have analyzed a total of 12.8 hrs of data using standard MAGIC analysis chain, which resulted in a strong detection of the source with a significance of $63\,\sigma$ [Ahnen et al. 2016]. The flux observed during the flare was historically high from X-rays, GeV and TeV data. The peak and mean integral flux ($E > 200\,\mathrm{GeV}$) measured was $(2.28 \pm 0.13) \times 10^{-10}$ $\mathrm{cm^{-2}s^{-1}}$ and $(0.72 \pm 0.01) \times 10^{-10}$ $\mathrm{cm^{-2}s^{-1}}$, respectively. Compared to previous MAGIC observations, the peak flux was $\sim$14 and $\sim$17 times the mean integral flux from the observations performed in 2007 and 2008, respectively, and $\sim$29 times the mean integral flux from the observations performed during 2011-2012 MWL campaign. During the entire flare, no spectral variations were seen, but night-wise flux variability was detected. This was the first time such an extraordinary flare was observed from this source with the spectrum spanning from 48 GeV to 3.6 TeV, which allowed the better overlapping between MAGIC and *Fermi*-LAT spectrum. The multiwavelength spectral energy distribution (SED) of 1ES 1011+496 from optical to TeV can be fitted by a one-zone synchrotron self-Compton (SSC) model, which suggests a leptonic origin of the VHE γ-ray emission from this blazar. The relatively high redshift and the extraordinary flare, with significant excess above 1 TeV, made 1ES 1011+496 data excellent case to study the effect of EBL absorption on the AGN spectra.

During March-June 2014, the monitoring observations of blazar PKS 1424+240 ($z = 0.6$) were performed with MAGIC. I have analyzed a total of 27.58 hrs of data using standard MAGIC analysis chain, which resulted in a strong detection of the source with a significance of $17.55\,\sigma$. No significant night-wise and intra-night flux variability was observed during the entire monitoring performed in 2014. Compared to previous MAGIC observations, the mean integral flux from 2014 data is lower than 2009 MAGIC observation performed in mono mode, however, on a similar level within statistical uncertainties with 2010 and 2011 stereo observations. The differential flux was compatible with all previous MAGIC observations, which indicates a constant VHE γ-ray emission. This was the first time that the observed spectrum is found to be spanning from as low as 40 GeV, which allows better overlapping between MAGIC and *Fermi*-LAT spectrum. The multiwavelength SED of PKS 1424+240 from optical to TeV cannot be fitted by a simple one-zone SSC model, as fit to the SED failed to reproduce the optical-UV continuum together with the VHE data without applying a much higher Doppler factor. However, two-zone SSC model describes the SED of the source well. In the two-zone model, the majority of the low energy synchrotron radiation and SSC-emission (optical-UV and GeV components) originate from a larger emission region called the outer region, and the X-ray and VHE γ-ray emission originate mainly from a smaller emission region called an inner region containing one order higher energetic electrons, which is closer to the central black hole. The high redshift of 0.6 and signal excess past 100 GeV, made PKS 1424+240 data excellent case to study the effect of EBL absorption on the AGN spectra.

M87 is a well-studied radio galaxy from radio to TeV, located at a distance of 16 Mpc. There were several TeV flares detected between 2005 and 2010 from it. During 2012 to 2015 M87 has been monitored with MAGIC in moon conditions. I have analyzed a total ∼156 hrs of data using the moon adapted analysis chain [Ahnen et al. 2019]. The source was detected significantly in every yearly campaign, and no flare was detected. Due to increased sensitivity of MAGIC telescopes, after the camera and readout upgrade [Aleksić et al. 2016a], M87 2012-2015 observations described here are one of the most sensitive measurements done so far in the low emission state. No clear variability was observed in 2012, 2014 and 2015 data on daily and monthly time scales. A hint for variability on a $\sim 3\,\sigma$ level was found in 2013 data on a daily timescale. The hint of the variability remains at a similar significance level even when variable systematic uncertainties of the MAGIC measurements are taken into account. The VHE γ-ray flux level above 300 GeV between 2012 and 2015 is the lowest observed since 2005. The combined spectral energy distribution between MAGIC and the *Fermi*-LAT, for the first time shows an amazing match with a power law over 5 decades in energy from 200 MeV to ∼10 TeV. I further found that the fitted spatial location of the M87 access in TeV γ rays from 2012−2015 data and a hint of variability on a day timescale, the outer lobes are excluded as possible sites for the VHE emission. Only regions that are close to the core or a prominent hot spot in the jet called HST-1 are possible sites for this emission, which indicates the TeV

γ rays seem to come from the same or nearby site as during the flares. Two different models can fit the multiwavelength spectral energy distribution of M87 from radio to TeV: 1) a homogeneous leptonic (SSC) model and 2) for the first time a hybrid photo-hadronic model, which suggest the possibility of either of leptonic or for the first time hybrid lepto-hadronic origin of the VHE γ-ray emission from this blazar.

In the second part of the thesis, I have derived constraints on the EBL density using the VHE γ-ray spectra obtained with MAGIC from the extraordinary flare data of 1ES 1011+496 (z=0.212) [Ahnen et al. 2016] and monitoring data of PKS 1424+240 (z=0.6). The EBL is the diffuse radiation that extends from the ultraviolet to the far-infrared and is redshifted according to its emission epoch. VHE γ rays are attenuated due to their interaction with low energy EBL photons via pair production, which leaves a unique imprint on the observed spectra from distant sources, such as AGNs. Measurement of this unique imprint makes it possible to constrain the EBL density. In this study, I have used a model-dependent approach of constraining the EBL in the optical to far-infrared part of EBL for the first time for MAGIC observations. The best-fit EBL density resulted for 1ES 1011+496 at $\lambda F_\lambda = 12.61^{+2.40}_{-2.63}$ nW m^{-2} sr^{-1} at 1.4 μm for the EBL level $\alpha = 1.1^{+0.17}_{-0.28}$, in the wavelength range of 0.23 to 2.96 μm, which covers the cosmic optical background part of the EBL. Here, the normalization factor α, which represents the EBL level, is a scaling factor for the optical depth. The errors quoted on λF_λ and α include statistical as well as systematic uncertainties. For PKS 1424+240 data, no significant constraints were derived due to possible intrinsic spectrum softening. Therefore, I have derived upper limit from these data. The combined test statistics calculated from the two sources are highly dominated by 1ES 1011+496 test statistic value and therefore, results in EBL density of $\lambda F_\lambda = 12.61^{+2.41}_{-2.64}$ nW m^{-2} sr^{-1} at 1.4 μm, in the wavelength range of 0.23 to 2.96 μm for the EBL level $\alpha = 1.1^{+0.07}_{-0.23}$, which is very similar to 1ES 1011+496 case. Here, errors include only statistical uncertainty. The EBL level from these data is compatible with the EBL level predicted by the state of the art EBL models, and no significant excess has been found. The measurements of the EBL imprint presented here are the first ones so far to resolve the EBL significantly using MAGIC data [Ahnen et al. 2016].

Contents

List of Figures

List of Tables

List of Acronyms

1ES	First Einstein survey
2MASS	Two micron all sky survey
AGASA	Akeno giant air shower array
AGILE	Astro-Rivelatore Gamma a Immagini Leggero
AGN	Active galactic nucleus
AMC	Active mirror control
ASM	All-sky monitor (detector on board RXTE)
Az	Azimuth
BLR	Broad Line Region
CCD	Charged coupled device
CERN	Conseil Européen pour la Recherche Nucléaire
CGB	Cosmic Gamma-ray Background
CGRO	Compton gamma-ray observatory
CIB	Cosmic Infrared Background
CMB	Cosmic microwave background
COB	Cosmic Optical Background
COBE	Cosmic Background Explorer
CSFR	Cosmic Star Formation Rate
COMPTEL	Compton Telecope
CORSIKA	Cosmic ray simulations for KASCADE
CRB	Cosmic Radio Background
CR	Cosmic ray(s)
CTA	Cherenkov Telescope Array
CT	Cherenkov telescope
CUVOB	Cosmic Ultraviolet and Optical Background
CXB	Cosmic X-ray Background
DAQ	Data acquisition
DEC	Declination
DIRBE	Diffuse Infrared Background Experiment
DM	Dark Matter
DRS	Domino Ring Sampler
EAS	Extended air shower
EBL	Extragalactic background light
EGRET	Energetic gamma-ray experiment telescope
EM	Electromagnetic

FACT	First G-APD Cherenkov Telescope
FIR	Far-infrared
FoV	Field of view
FR	Full Range
FR I, II	Fanaroff-Riley type I and II
FSRQ	Flat spectrum radio quasar
FWHM	Full width at half maximum
G-APD	Geiger-mode Avalanche Photodiode
GBM	GLAST Burst Monitor
GC	Galactic Center
GRB	Gamma-ray burst
GZK	Greisen-Zatsepin-Kuzmin
HAWC	High Altitude Water Cherenkov Experiment
HBL	High-frequency peaked BL Lac
HEGRA	High energy gamma-ray astronomy
HE	High energy
H.E.S.S.	High energy stereoscopic system
HiRes	High Resolution
HST	Hubble space telescope
IACT	Imaging atmospheric Cherenkov telescope
IBL	Intermediate-frequency peaked BL Lac
IC	Inverse Compton
IR	Infrared
ISM	Interstellar medium
KASCADE	Karlsruhe shower core and array detector
KVA	Kungliga Vetenskapsakademien [telescope]
LAT	Large Area Telescope
LBL	Low-frequency peaked BL Lac
LE	Low Energy
LoNS	Light of the night sky
LST	Large Size Telescope
LUT	Lookup Table
M	Messier [catalogue]
MAGIC	Major atmospheric gamma-ray imaging Cherenkov
MARS	MAGIC analysis and reconstruction software
MC	Monte Carlo [simulations]
MIR	Mid Infrared
MJD	Modified Julian day
MMT	Multi Mirror Telescope
Mrk	Markarian

MST	Medium Size Telescope
MUX	Multiplex
NIR	Near Infrared
NLR	Narrow Line Region
NLRG	Narrow-Line Radio Galaxy
NSB	Night-sky background
OVRO	Owens Valley Radio Observatory
PAO	Pierre Auger Observatory
phe	photoelectrons
PKS	Parkes catalogue of radio sources
PMT	Photomultiplier tube
PSF	Point spread function
PWN	Pulsar wind nebula
QE	Quantum efficiency
RA	Right ascension
RF	Random forest
RMS	Root mean square
ROOT	An object-oriented data analysis framework
RXTE	Rossi X-ray timing explorer
SAM	Semi-Analytical Model
SED	Spectral energy distribution
SNR	Supernova remnant
SSC	Synchrotron-self Compton
SST	Small Size Telescope
Swift	The Neil Gehrels Swift Observatory
TS	Test Statistic
UHE	Ultra High Energy (E $>$ 100 TeV)
UV	Ultraviolet
VCSEL	Vertical cavity surface emitting laser
VERITAS	Very energetic radiation imaging telescope array system
VHE	Very high energy (E $>$ 100GeV)
VLBA	Very Long Baseline Arrays
WIMP	Weakly Interacting Massive Particle
WMAP	Wilkinson Microwave Anisotropy Probe
Zd	Zenith distance
ZL	Zodiacal Light

Introduction

Very high energy (VHE, $E < 100\,GeV$) γ-ray astronomy is a so-called final frontier of the electromagnetic spectrum and a promising field to extend the edge of our understanding of the emission from the sources in the depth of the Universe to the highest observable energies. The success of current generation Cherenkov telescopes such as MAGIC, H.E.S.S., and VERITAS along with *Fermi*-LAT satellite, leading to several exciting discoveries of γ-ray sources providing fascinating insights into the non-thermal Universe, confirmed the immense importance and potential of the γ-ray astronomy to uncover some of the fundamental questions in the modern astrophysics.

My Ph.D. thesis is focused on the scientific studies carried out in this exciting research field of VHE γ-ray astronomy of extragalactic sources such as active galactic nuclei (AGNs). AGNs harbor a supermassive black hole at the center and emit powerful collimated plasma jets, which extends to distances of many kpc to Mpc. They are one of the most energetic sources in the Universe and accelerate charged particles to the highest known energies. Therefore, they emit most of the non-thermal radiation in the Universe. Depending on the orientation of the relativistic jets, AGNs detected in γ-ray regime are divided into two categories; 1) blazars: when the jet is pointed towards the line of sight of the observer, 2) radio galaxy: when the jet is at an angle towards the observer. The study of well established two distant blazars 1ES 1011+496 and PKS 1424, and radio galaxy M87 and the high energy processes within their jets using new precision data taken with MAGIC are among the first major topics of this thesis. In February 2014, an exceptionally high flaring state activity was observed at TeV energies from 1ES 1011+496, which triggered observations with MAGIC. In contrast, PKS 1424+240 and M87 were found to be in low emission state in March-June 2014 and 2012-2015 MAGIC data, respectively. This was the first time for M87 to be studied in depth during the low emission state, as most of the spectral modeling was done to interpret high flaring states.

The second topic of this thesis is focused on measurements of extragalactic background light (EBL), which is the diffuse low energy radiation stacked up in the ultraviolet to far-infrared wavelengths, originating from star and galaxy formation through the history of the Universe. It is the second largest background radiation after the cosmic microwave radiation. Due to strong foregrounds from our solar system and the Galaxy, the direct measurements of the EBL are rather difficult. However, the observation of distant sources such as AGNs at VHE γ rays provides a unique opportunity to measure the EBL indirectly. When VHE γ rays from the AGNs interact with the low energy EBL photons via pair-production, it causes attenuation of the AGN observed energy spectra and leaves a unique imprint on it. This imprint

of the EBL on the AGN spectra can then be used to constrain the EBL density. In this thesis, the EBL measurements were carried out using the 1ES 1011+496 flaring data and PKS 1424+240 low emission state data.

Outline of the thesis:

I am starting this thesis with a brief introduction to cosmic rays, following an introduction to VHE γ-ray astrophysics including processes responsible for γ-ray production and sources of VHE γ-ray emitters in Chapter 1. In Chapter 2, basic introduction and classification to AGNs along with theoretical models of VHE γ-ray production is introduced. Chapter 3 is divided into three parts. In the first part, details on the imaging Cherenkov technique and the hardware details of MAGIC telescope are presented. In the second part, the standard and moon adapted analysis chains of the MAGIC data are described. In the third part, both the standard and moon adapted analyses are illustrated using a Crab Nebula data set. In Chapter 4, the analysis and results including one zone synchrotron self-Compton (SSC) modeling from the exceptionally flaring state data taken in February 2014 for 1ES 1011+496 are presented. In Chapter 5, the analysis and results including two zone SSC modeling from the low emission state data taken from March-June 2014 for PKS 1424+240 are presented. Chapter 6 deals with the analysis and results from the detailed low emission state monitoring data taken in years 2012-2015 for M87. The results include a location of the possible site for the VHE γ-ray emission, studying the source in the low emission state, and modeling the spectral energy distribution with SSC and photo-hadronic models. Chapter 7 focuses on EBL studies. In this chapter, first basic concepts of EBL are introduced, then a status of EBL measurements and EBL models, and EBL constraints are explained. The results include EBL measurements carried out with 1ES 1011+496 and PKS 1424+240 data sets. Finally, in Chapter 8, conclusions and a short outlook are presented.

1. Introduction to γ-Ray Astronomy

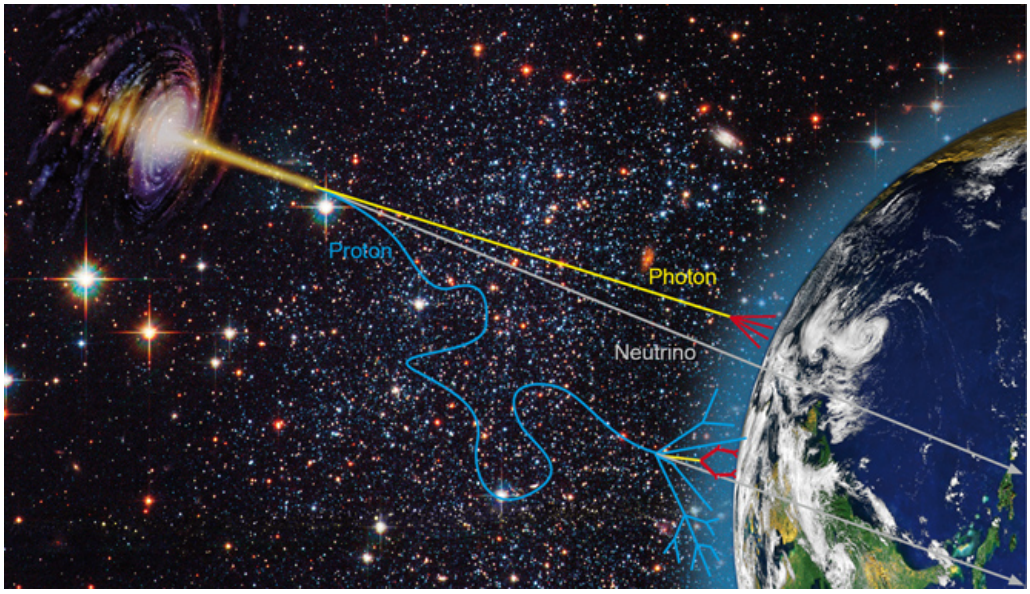

Figure 1.1: Artists illustration of astronomy with cosmic rays. Image credit `https://astro.desy.de/`

γ-ray astronomy is a study of astronomical objects using the most energetic form of electromagnetic radiation and claimed to be the last frontier of astrophysics. γ rays are not affected by intergalactic magnetic or electric fields. Therefore they are the ideal messengers of the violent, non-thermal processes in the Universe. They can serve as powerful probes of far regions of the cosmos as well as hidden regions of our Milky Way Galaxy. γ-ray astronomy presents unique opportunities to explore exotic objects such as pulsars, supernova remnants, and black holes, and the most energetic phenomena associated with them. By exploring the universe at γ-ray energies, it is possible to search and test for new theories in physics and also perform experiments which are impossible to carry out in the earth-based laboratories. Therefore the very high energy γ-ray astronomy plays a crucial role in exploring the Universe in the most extreme and violent form. The main motivations of this field are:

- The search for the origin of Cosmic rays
- Astrophysics of the intriguing sources such as supernova remnants, pulsars, and its nebula, binaries, and Gamma-ray bursts and also the relativistic outflows

from the jets of extremely energetic sources such as active galactic nuclei and microquasars

- Observation cosmology for γ rays.
- Searches for new phenomena and searches for the dark matter
- Search for gravitational waves

γ-ray astronomy with a particular emphasis on extra-galactic sources such as AGNs is the main focus of this thesis. As it is connected with the origin of cosmic rays (figure 1.1), in this chapter, first I will give a brief introduction to the cosmic rays and their characteristics, then an overview of γ rays along with their associated production and absorption mechanisms. This chapter will be concluded with a brief introduction to the astrophysical sources of very high energy γ rays.

Cosmic rays

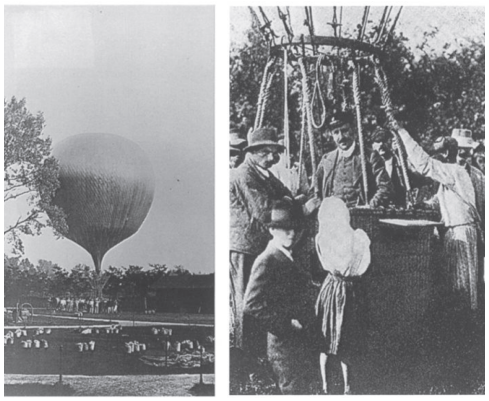

Figure 1.2: Victor Hess on a balloon flight. Left: Preparation for his flight in 1911-12. Right: Victor Hess after one of the successful balloon flights. Image credit [Longair 2011].

Cosmic rays (CRs) are the high energy charged particles which hit the Earth from all directions, originate in the outer space, and travel at nearly the speed of light. The big breakthrough came in 1912 when Victor Hess discovered CRs with the flying balloon experiment (figure 1.2). He found that, as he ascended in a balloon, an electroscope got discharged more quickly as the average ionization increased with altitude (1.5 km) compared to the sea-level. It was a definite confirmation that the radiation from the ionizing source must be located above the Earths atmosphere. Later in 1936, he won the Nobel prize for his findings. These high energy particles

were named as 'cosmic rays' by Robert Millikan, who was also first to propose their extragalactic nature.

In the balloon experiment, it was clear that the observed particles were not primary CRs, in fact, they were the secondary particles initiated due to the interaction between CRs and the atmospheric nuclei. Therefore, CRs are mostly composed of the nuclei of atoms but also of high energy photons, electrons, positrons, neutrinos. In the following sections, an overview of the characteristics of CRs is given including the CR composition and exceptional spectrum, acceleration mechanism and experiments carried out so far for the CR detection.

Energy spectrum

The spectrum of Cosmic rays is an exceptional power law extending to extremely high energies, from E $\sim 10^8$ eV to more than 10^{20} eV (see figure 1.3). The CR energy scale up to 10^{20}eV and the spectral nature of the power law indicate that CRs must have emitted from the sources which did not have time to emit thermalized emission. Therefore, CRs are messengers of non-thermal emission in the Universe.

So far, we still do not have a clear understanding of the production mechanism, the origin of CRs, composition observed over the energy range, and also how far CRs can propagate in the space. As shown in the figure 1.3, the CR spectrum spans over 13 decades, with fluxes dropping from 1 particle/(m^{2}s) at around 100 GeV to 1 particle/(km^2-century) for the highest energy observed. Below 10 GeV, the cosmic ray flux is not constant, as it rather depends on the solar activity. The CR spectrum has two unique features - the knee and the ankle. The differential flux of CR follows a power of form $dN/dE \approx E^{\alpha}$. At energies between 10^{15} and 10^{16} eV, the spectral index α of CR spectrum is -2.7; the region is known as the knee. Whereas, at energies above 10^{18} eV, α changes from -2.7 to about -3; this region is known as the ankle of the CR spectrum [Beringer et al. 2012]. Then from the ankle up to 30×10^{18} eV, spectrum gets harder again with α changes to -2.6. Due to the interaction between the charged particles and the cosmic microwave background (CMB) photons, a cut-off is expected for the highest energies with E$> 10^{20}$ eV in the CR spectrum. This cut-off is known as the Greisen-Zatsepin-Kuzmin (GZK) cut-off [Greisen 1966, Zel'dovich et al. 1964].

Composition

The chemical composition of CRs primarily include all the periodic table elements, similar to our solar system [Simpson 1983]. At a given energy, the hadronic component of the CR flux consists of 79% protons, 15% helium and remaining 1% of heavier nuclei such as carbon, oxygen, magnesium, silicon, and iron. Up to the knee, this chemical composition has been measured directly. In CR composition, electrons and positrons contribute to less than 1%. Their spectrum is steeper than the spectrum of protons and heavier nuclei. Therefore, only a small fraction of the CRs consti-

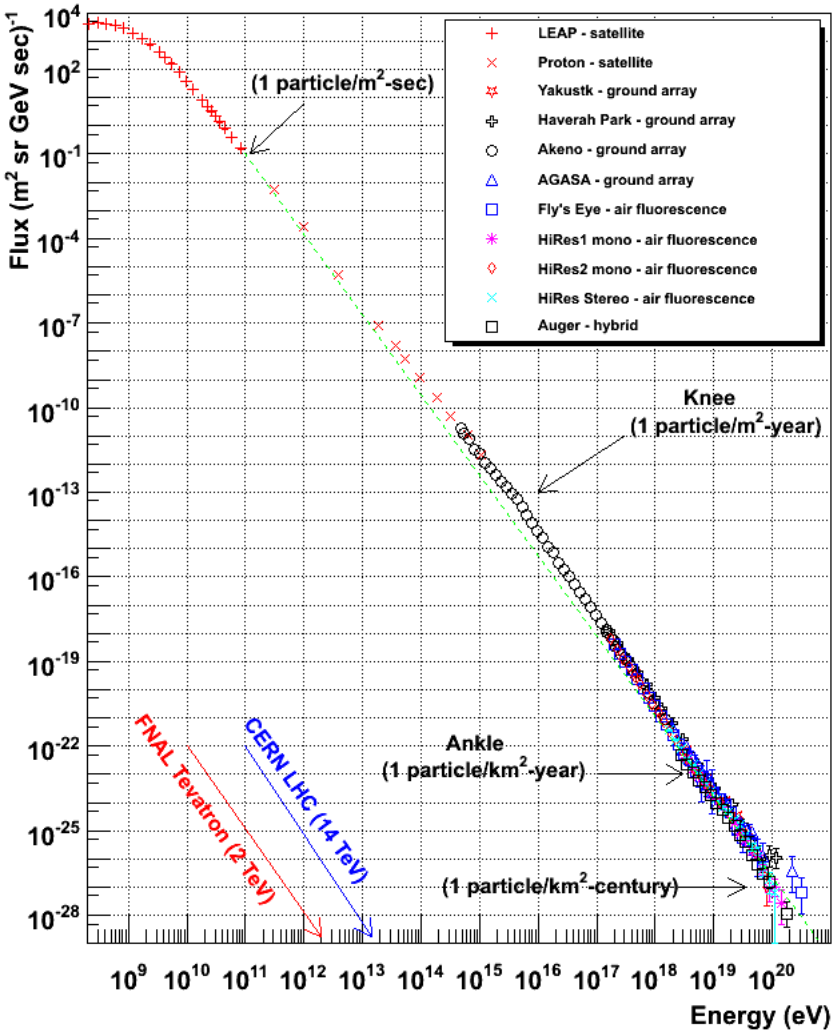

Figure 1.3: Cosmic ray spectrum with a single power law over ∼13 decades in energy, measured with various cosmic ray experiments. Image credit: `https://www.physics.utah.edu/~whanlon/spectrum.html`

tuted by neutral particles, such as γ rays and neutrinos. These neutral messengers are not deflected by the interstellar magnetic fields, and also give information about the origin of the radiation. The significant part of low energy (below 10 GeV) CRs originates from the Sun. It is assumed that below the knee, all particles are of galactic origin, whereas above the ankle, the extremely high energy CRs (EHECRs) are produced or accelerated outside of the Galactic disk in the regions such as - the halo of our Galaxy, or in the powerful extragalactic objects, e.g., active galactic nuclei, radio galaxies, and galaxy clusters [Aharonian 2004]. However, the region between the knee and the ankle is still under debate.

Acceleration mechanism

The classification for the origin of CRs (galactic or extra-galactic) depends on the acceleration mechanism responsible for generating CRs at highest energies. The CR spectrum has very few features, which indicates that same acceleration mechanism and the same source classes responsible for generating CRs. The principal mechanism responsible for the CR acceleration was first proposed by Enrico Fermi, known as 'Fermi acceleration' [Fermi 1949]. This process happens when a particle gains energy via upscattering in a moving ionized medium, i.e., plasma. Depending on the characteristics of the moving plasma, we can distinguish between 'first order (Fermi-I)' and 'second order (Fermi-II)' - Fermi acceleration [Longair 1994].

In the case of Fermi-II acceleration, a charged particle gain energy through the stochastic interaction with a moving plasma. Then the energy gain ΔE per interaction depends on the velocity of random scatter centers β as:

$$\frac{\Delta E}{E} \propto \beta^2 \tag{1.1}$$

In the case of Fermi-I acceleration, the scattering centers are not random due to the presence of shock. Therefore, the interaction of particles happens differently with plasma, compared to Fermi-II acceleration scenario. This process is also known as Diffuse Shock Acceleration (DSA). Here, particles gain energy while crossing the shock region back and forth several times, which also implies that the shock region radius should not be exceeded by the particle's giro radius. The energy gain in this case is:

$$\frac{\Delta E}{E} \propto \beta \tag{1.2}$$

To make the acceleration process effective, the following relation needs to be fulfilled:

$$L_{pc} > 2r_L \sim \frac{2E_{15}}{B_{\mu G} \times \beta c} \tag{1.3}$$

Where, L_{pc} is the size of the accelerating region in parsecs (pc), E_{15} is the energy in 10^{15} eV, $B_{\mu G}$ is the magnetic field in μG, and βc is the characteristic velocity of the scattering centers.

Sources of cosmic rays

Figure 1.4 represents the well-known Hillas diagram with candidate sites with highest energies in the Universe (E = 100 EeV[a] to 1 ZeV[b]) for the production of Cosmic rays. It proposed by Hillas in 1984, hence the name. It shows the relation between magnetic field strength and the size of the emitting region to the maximum acceleration energy, assuming the active DSA mechanism [Hillas 1984]. From the diagram,

[a] 1 EeV = 10^{18} eV
[b] 1 ZeV = 10^{21} eV

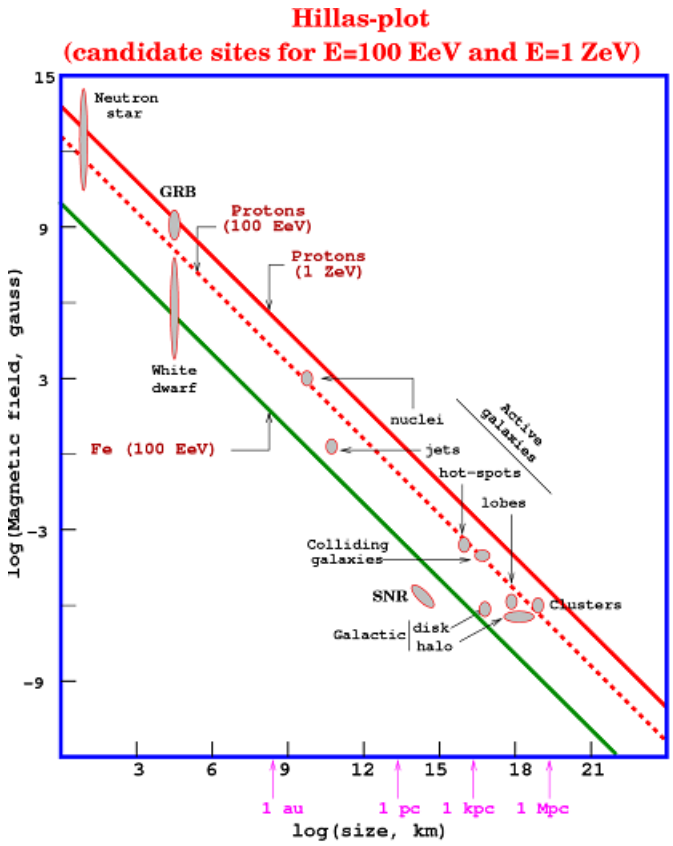

Figure 1.4: Hillas plot with candidate sites with highest energies in the Universe for the production of Cosmic rays [Fraschetti 2008].

we can see that extragalactic sources seem to maintain the physical conditions required for the particle acceleration up to 10^{20} eV. Table 1.1 summarizes the list of best known possible galactic and extragalactic cites for the origin of CRs. More details about these sources are given in section 1.4.

Galactic sources	Extragalactic sources
Supernova Remnants	Jets of Active Galactic Nuclei
Pulsars and associated nebulae	Gamma-Ray-Bursts
Binary systems and Microquasars	Starburst galaxies
star clusters	Galaxy clusters

Table 1.1: Summary of possile sites for the origin of CRs

VHE γ rays as the ideal messengers of the extreme Universe

As discussed in section 1.1.2, neutral CRs, i.e., neutrons, neutrinos, and γ rays do not interact with the intergalactic magnetic field, and therefore they are useful to probe the origin of CRs. However, neutrinos are rather difficult to detect, and due to the short lifetime of neutrons, almost all the particles reaching Earth are secondary particles such as protons and electrons. In contrast, γ rays do not decay, and they are more easily detectable. Therefore, γ rays are the ideal particles to be successfully observed from the Earth. Their study helps to determine CR acceleration sites, allowing an insight into the depth of the extreme Universe. They are messengers of violent, non-thermal processes occurring close to or at the source's location. Here the term γ rays is associated with the electromagnetic radiation of very short wavelength ($\lambda < 10^{-11}$ m) (see figure 1.5), In this thesis, I am dealing with γ rays in the so-called Very High Energy (VHE) band, i.e. with E>100 GeV and High Energy (HE) band, i.e. with E>100 MeV.

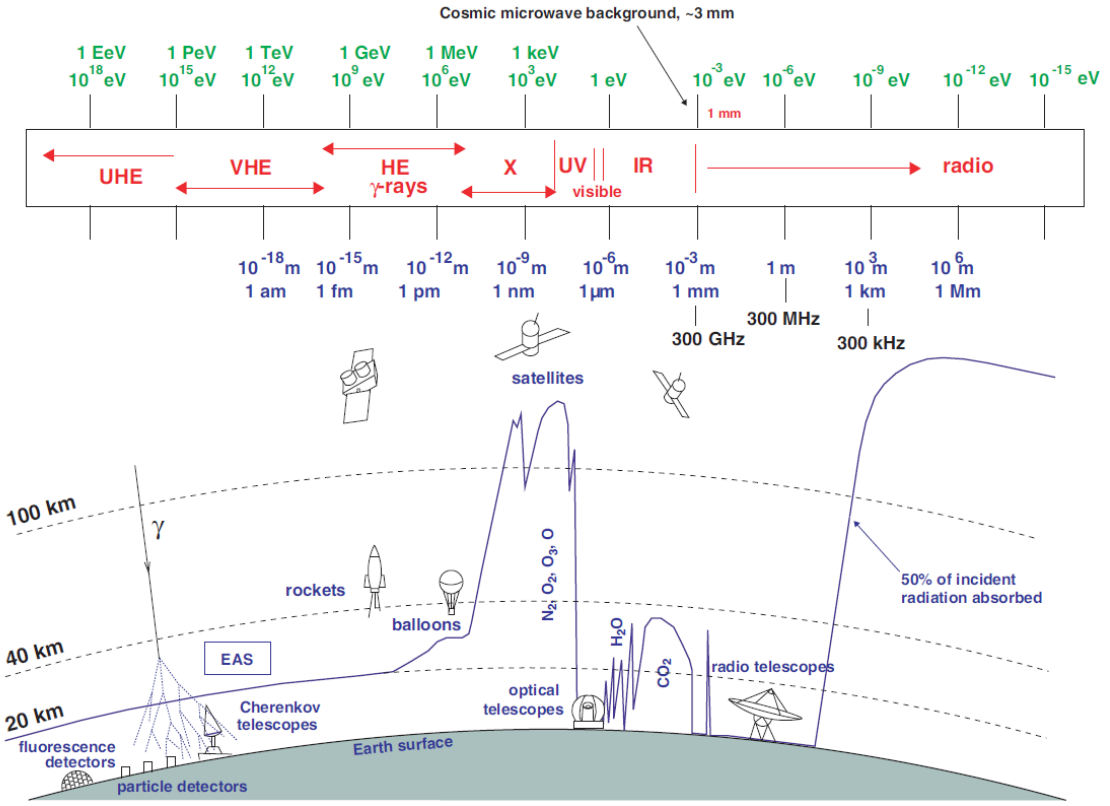

Figure 1.5: Atmospheric windows for the spectrum of electromagnetic radiation [Longair 1992].

For the detection of HE γs, only direct detection is possible via satellite detectors such as *Fermi*-LAT, as Earth's atmosphere is not transparent to these very energetic photons. However, for VHE γs, ground-based Cherenkov telescopes are needed, as earth's atmosphere plays an essential role (see chapter 3 for more details). The ultra-high energy (UHE, E>100 TeV) γs can be detected with ground-based experiments which consist of large arrays of particle detectors. However, no source above 100 TeV has ever been detected so far.

The VHE γ rays can bring us information about:

- The origin of astrophysical sources producing CRs
- The mechanism, the environment, basic cause for the particle acceleration in the universe, and also the cause of variability
- Contains information on the characteristics of the medium crossed during their propagation to the earth
- Test of laws of fundamental physics (e.g., Lorentz Invariance)
- Search for dark matter and in general for new physics beyond the standard model

Another advantage of VHE γ rays is they can be used for the indirect measurement of the extragalactic background light (EBL), which is also one of the main topics of this thesis. The EBL is the diffuse radiation field accumulated in the ultraviolet (UV) to far-infrared (FIR) wavelengths through the star and galaxy formation history of the Universe. Due to strong foreground emissions in the Solar system, the direct EBL measurements are very difficult.

When VHE γ rays from extra-galactic sources such as AGNs, travel from cosmological distances to reach earth, they interact with the EBL photons and get absorbed via electron-positron pair production as equation 1.4. Even with the extremely low density of matter and radiation in the Universe, the probability of interaction increases due to the cross section of pair production between the γ rays and the low energy photons, which belong to the evolving EBL. Therefore, VHE γ rays suffer absorption losses by interaction with the low energy photon fields. The attenuation of the original γ-ray flux depends on the distance of the source i.e. redshift of the source z, the energy (E_γ) of the primary VHE γ rays (γ_{VHE}) and also on the spectrum of the EBL which provides the low energy photons of EBL (γ_{EBL} at E_{EBL}). Therefore, EBL plays a crucial role to understand the VHE extragalactic sky and its luminosity. It is redshifted at the observer's point depending on the redshift of the emitting epoch. The corresponding pair-production of an electron-positron pair (provided $E_\gamma \cdot E_{EBL} > m_e^2 c^4$, where m_e is the mass of the electron) is given as:

$$\gamma_{VHE} + \gamma_{EBL} \rightarrow e^+ + e^- \tag{1.4}$$

This interaction attenuates the γ-ray flux from these extragalactic sources, which affects the observed energy spectra and leaves a unique imprint of EBL. This imprint can be used to study the EBL. The attenuation is strongly energy and redshift dependent. Only because of this strong dependency, VHE γ rays can be used to constrain the EBL density. Note that, the effect of EBL on the galactic sources is negligible up to energies of about 100 TeV. After this energy, the absorption on the photon field of the CMB starts to show effect. Study of EBL using spectra of VHE γ-ray sources is one of the main topics in this thesis. More details about it are given in the chapter 7. In the following sections, from the VHE astrophysics point of view, the most relevant non-thermal γ-ray emission processes and the classes of VHE γ-ray emitters are described.

Production mechanisms of γ rays

Astronomical objects emit energy in different types of processes. Most of the visible radiation from astronomical sources is emitted 'thermally' due to the atomic excitation, which has a black body spectra depending on the temperature of the emitting matter. Thermal radiation takes place from UV to infrared (IR), of which very small part is visible to human eyes. It dominates the emission spectra of stars, which are quite stable nuclear reactors for most of their lifetime. In contrast, γ rays are messengers of violent, and non-thermal processes, which dominate higher energies in the Universe. The term non-thermal refers to the continuum radiation of a distribution of particles by a non-Maxwellian energy spectrum. The most important non-thermal γ-ray production mechanisms are briefly described below. See [Aharonian 2004] and [Longair 1992] for more details.

- **Bremsstrahlung**
  Bremsstrahlung is a German term which means 'braking radiation' for electron losing energy, is one of the important mechanism in astrophysical processes. When an electron gets accelerated in the Coulomb field of ions or nuclei of atoms, it emits bremsstrahlung photons. It is also referred to as 'free-free emission', as interacted particles are not bound before and after the scattering process. In a non-relativistic regime, the energy spectrum of bremsstrahlung γ rays depends on the initial energy spectrum of electrons. In typical case of initial electron spectrum being a power law of form $Q(\varepsilon_e) \propto e^{-\Gamma}$, the corresponding spectrum for produced γ rays from a cooled steady-state will also be a power law of form $N(\varepsilon_e) \propto e^{-\Gamma}$. However, in the relativistic case, the bremsstrahlung γ-ray spectrum becomes flatter, i.e., $N(\varepsilon_e) \propto e^{-\Gamma+1}$, producing γ rays with power law index $\Gamma - 1$. At low energies, this process competes with the ionization losses. However, at a certain critical energy E_c (in hydrogen gas $E_c \sim 700 m_e c^2 \simeq 350\,\mathrm{MeV}$), the process becomes inefficient.

- **Synchrotron radiation**
  When a charged particle is accelerated in a magnetic field, it radiates energy. At relativistic velocities, it results in synchrotron radiation, whereas, non-relativistic velocities, it results in cyclotron radiation. Synchrotron radiation from accelerated electrons is one of the most important processes in astrophysics, especially in the non-thermal Universe. In magnetized astrophysical environments such as pulsar magnetospheres or magnetized accretion disks, production of γ rays from synchrotron radiation is possible. The probability of synchrotron radiation depends on a single parameter, i.e., $\chi_0 = \epsilon_0 B/B_{cr}$. Here, B is magnetic field component perpendicular to the particle speed vector, $B_{cr} = m^2c^3/e\hbar \approx 4.4 \times 10^{13}$ G is the critical value for the magnetic field relevant to quantum effects. At $\chi_0 \ll 1$, γ-ray spectra are very steep, however, at large values, $\chi_0 \geqslant 1$, γ rays are defined by a flat distribution. In the context of VHE γ rays, synchrotron radiation is one of the essential processes, as it is responsible for the generation of seed photons for Inverse Compton scattering (see below). However, the UHE cosmic rays can emit Synchrotron radiation directly in VHE regime.

- **Inverse Compton scattering**
  In Inverse Compton (IC) scattering process, ultrarelativistic electrons interact with the low energy photons transferring energy to them, which leads to the production of VHE γ rays. The process is called Inverse Compton as the electrons lose energy and photons gain the energy, unlike the standard Compton effect. It is one of the principal mechanism in astrophysics for γ-ray production and is widely used in many models to explain the high energy emission from exotic environments such as, in pulsars, active galactic nuclei or supernova remnants. Depending on the energy of the electrons (as the cross section for the production varies significantly) the IC can be defined in two regimes; the Thomson and the Klein-Nishina regime. For a population of accelerated electrons, a power law distribution can be defined as $dN_e/d\epsilon_e \propto \epsilon_e^{-\Gamma}$. Below the Thomson regime, the energy of the photon is smaller than $m_e c^2$, with m_e being electron mass, we can obtain γs with a power law index of $(\Gamma + 1)/2$. Here the energy loss rate is proportional to ϵ_e^2. In the case of Klein-Nishina (KN) regime, by taking into account the quantum effects, the photon energy is larger than $m_e c^2$. Therefore, the spectrum will be much steeper with a power law index of $\alpha = \Gamma + 1$. Here the energy loss rate is almost energy independent. This implies that, in the Thomson regime, electron spectrum becomes steeper, however, due to the Compton losses in the KN regime, the electron spectrum becomes harder. Thus, IC mechanism is especially efficient for the electrons, as from protons it is suppressed by a factor of $(m_e/m_p)^4$.

- **Pion decay**
  The π^0-decay process contributes unique information towards understanding the hadronic component of cosmic rays. In inelastic collisions with ambient

gas, relativistic protons and nuclei produce high energy γ rays, due to the production and decay of the secondaries such as pions, kaons, and hyperons. However, the main channel of conversion of the kinetic energy of protons to high energy γ rays are caused by the neutral π^0-mesons via $\pi^0 \rightarrow 2\gamma$. The kinetic energy threshold for the production of π^0-mesons is

$$E_{th} = 2m_\pi c^2 \left(1 + \frac{m_\pi}{4m_p}\right) \approx 280\, MeV \tag{1.5}$$

where $m_\pi = 134.97\,\mathrm{MeV}$ is the mass of the π^0-meson, which are the lightest mesons. Then the particle immediately decays to two γ rays. Compared to the lifetime of charged π-mesons, which is $\approx 2.6 \times 10^{-8}$ s, the mean lifetime of π^0-decay is significantly shorter, which is $\approx 8.4 \times 10^{-17}$ s. All three types of π-mesons, i.e., π^0 and $\pi^\pm$, are produced at high energies with comparable probabilities.

$$\pi^0 \rightarrow \gamma\gamma \quad (99\%) \tag{1.6}$$
$$\pi^0 \rightarrow e^+e^-\gamma \quad (1\%) \tag{1.7}$$

The γ-ray spectrum from the decaying π^0 is determined by the spectrum of the parent particle (protons) rather than by a large number of low-energy secondaries. However, as a result of the parent protons, these γ rays will have a distinct feature in their spectrum, i.e., a maximum will be at $E_\gamma = m_\pi c^2/2$, which is independent of the energy distribution of π^0-mesons. The decay of charged pions i.e. $\pi^\pm$ drives to ν_e and ν_μ neutrinos. Their spectra are pretty similar to the spectrum of the accompanying π^0-decay γ rays.

In VHE context, the hadronic processes of π^0 decay and IC scattering are the most important process. However, the exact origin of VHE γ-ray emission is still a highly debated issue. The π^0 decay favors hadronic models, whereas IC scattering favors leptonic models. These emission models are described in the next chapter.

Sources of VHE γ rays

In the following section, I will briefly summarize major classes of VHE γ-ray emitters, which are the science goals pursued by Cherenkov telescopes. Most of these classes are already detected in the VHE γ-ray regime, and few of them are still very good candidates. They emit VHE γ rays via the non-thermal processes discussed in the previous section. These sources are divided into classes according to their galactic or extragalactic origin. The current number of detected sources in the VHE regime as per listed in TeVcat[c] is about 240, and the number is still increasing (see figure 1.6).

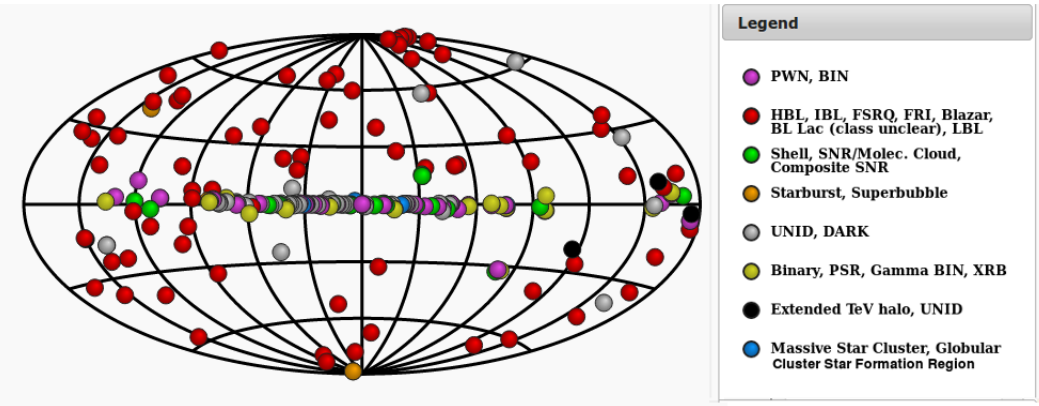

Figure 1.6: VHE γ-ray sources in galactic coordinates up to November 2018. Image credit: `http://tevcat2.uchicago.edu/`

Active galactic nuclei

Active galactic nuclei (AGN) are the most energetic sources in the universe, with the central region or nucleus of the galaxy is more luminous than the rest of the galaxy (figure 1.7). They numerously occupy extragalactic sky and show exceptional observational characteristics, which cover the entire electromagnetic spectrum. AGN emission is believed to be powered by the supermassive black hole accreting matter, which emits ultra-relativistic particles via two collimated jets. Non-thermal emission observed from the jets is found to be highly variable from radio to γ rays. Depending on the orientation of the jet, two types of AGNs can be observed in the VHE regime; blazars (jet along the line of sight of the observer) and radio galaxy (when the jet is not aligned towards observer's line of site).

[c] `http://tevcat2.uchicago.edu/`

The generation of VHE γ-ray emission is still in debate, as in many cases, both leptonic and hadronic models fit the observational data well. Studying blazars and radio galaxies with their γ-ray emission at VHE are the main topics of this thesis. Not only their emission can be used to probe relativistic jets and the non-thermal processes in the Universe but also to constrain the EBL by studying the attenuation of the VHE signal from very distant objects. A detailed description of AGN physics and VHE observations is given in chapter 2, and details about the how AGN emission in VHE γ-ray regime can be used to constrain the EBL are given in chapter 7.

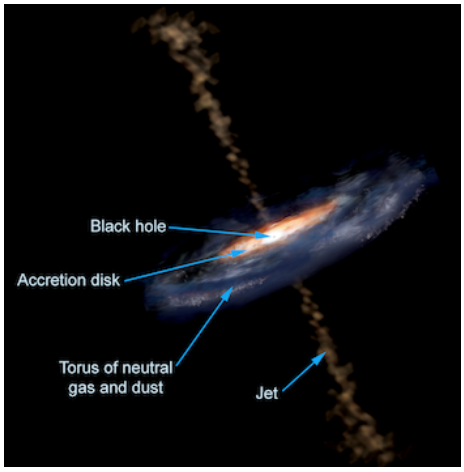

Figure 1.7: Illustration of the different features of an active galactic nucleus. Image credit: Aurore Simonnet, Sonoma State University (`imagine.gsfc.nasa.gov`)

Gamma-ray bursts

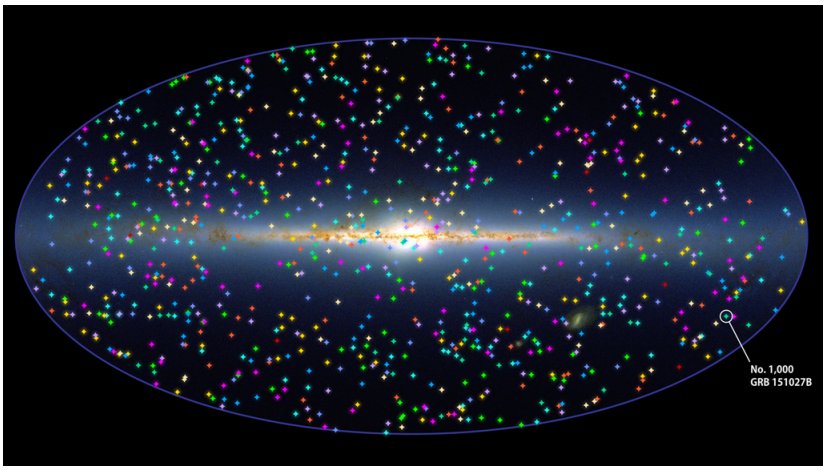

Figure 1.8: Locations of all 1,000 GRBs observed by Swift on the map of the whole sky, including the 1000^{th} GRB 151027B. Image credit: `https://svs.gsfc.nasa.gov/12055`

Gamma-ray bursts (GRBs) are highly energetic explosions, which last for a very short duration (seconds to minutes) with emission mostly at high and very high energies from keV to GeV. GRBs are isotropically distributed events with the ex-

tragalactic origin (figure 1.8) and observed at very large redshift such as z = 2.8, which makes them good investigators for studying cosmology or Lorentz invariance [Jakobsson et al. 2006]. The initial VHE γ-ray emission usually is characterized by the following afterglow emission in X-rays. Although the γ-ray emission mechanism is not well understood, depending on the burst duration, two classes of GRBs are defined which are likely to originate from different progenitor systems; 1) long duration bursts: associated to the core collapse supernova, and 2) short duration bursts: associated with the merger of binary neutron stars (e.g., [Woosley et al. 2006, Ackermann et al. 2010]).

GRB observations are challenging due to factors such as their short lifetime, large distances; due to which the EBL absorbs most of the VHE emission and small field of view of the Cherenkov telescopes. Therefore, MAGIC telescopes run a unique GRB alert and follow-up program, in which, telescopes can quickly (within some tens of seconds) be repositioned in the direction of the GRB alert given by satellite experiments such as *Fermi*-GBM or Swift. On 14^th January 2019, MAGIC finally achieved the historical detection of the GRB successfully for the first time among all the IACTs in VHE γ-ray regime [Mirzoyan 2019].

Supernova remnants

A supernova remnant (SNR) is the residue of a supernova, which is formed after the explosion of a super-massive star, results in the formation of a gas nebula with Neutron Star (NS) or a Black Hole (BH) at its core (figure 1.9) While they expand into lower density interstellar medium (ISM) due to the production of strong shocks, in few hundreds or several thousand years these objects become excellent backgrounds for cosmic ray acceleration.

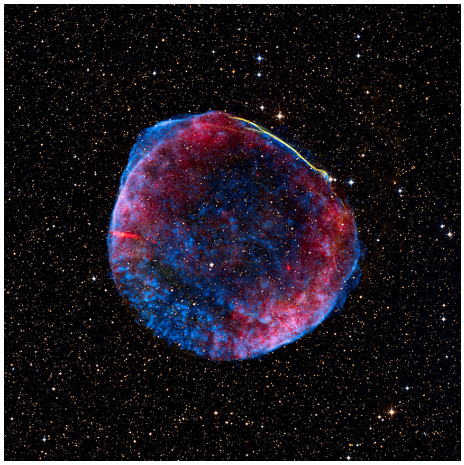

Figure 1.9: Supernova Remnant SN 1006. Image credit: `https://apod.nasa.gov/apod/ap140712.html`

Therefore, for first-order Fermi acceleration, SNRs are among the principal candidates. Here, the non-thermal processes drive the particles to accelerate up to TeV energies. To explain the emission from SNRs, both leptonic and hadronic origins have been proposed. However, due to γ-ray emission due to neutral pion decay hadronic models have been more favored. For example, in the case of SNR W51C observed by MAGIC, the VHE emission can be fitted well with hadronic model [Krause 2012].

Pulsars and PWNs

A pulsar is a very compact, highly magnetized, and fast rotating neutron star resulting from a core-collapse supernova. Therefore, the final object is formed of a neutron star surrounded by a nebula, known as pulsar wind nebula (PWN). The rotation and magnetic axes of the pulsar are misaligned. Therefore, the observer only sees an emission in a light-house manner when the beam crosses the line of sight. Pulsars are known to be one of the best clocks in the Universe, with their rotational periods ranging from seconds to milliseconds. The VHE γ-ray emission have been observed from the pulsar, and the PWN as well [Albert et al. 2008a, Aliu et al. 2008], and are one of the most abundant sources of VHE γ rays in the Galaxy. In some cases, near the pulsar region, the rotational energy of the neutron star is converted into a relativistic stream of particles, which power up the VHE γ-ray emission. The interaction between the supernova ejecta and the pulsar wind forms a shock, which results in the acceleration of electrons. Therefore, the VHE emission detected from PWNs is mostly having the leptonic origin. Here, the upscattering process is very efficient compared to the case of SNRs, which explains the abundance of PWNs detected at VHEs. The emission models for these sources predict a power law spectra with a different cutoff in the energy range of 10-100 GeV region. The best-studied example of such system at VHE is the Crab Nebula, which is at a distance of 2 kpc and is the remnant of the supernova explosion happened in the year 1054 A.D. (figure 1.10). Due to the brightness and steady emission in the VHE γ-ray regime, it is used as the standard candle for the Cherenkov telescopes. The pulsed component from Crab in the VHE range was firstly discovered by MAGIC telescopes [Aliu et al. 2008].

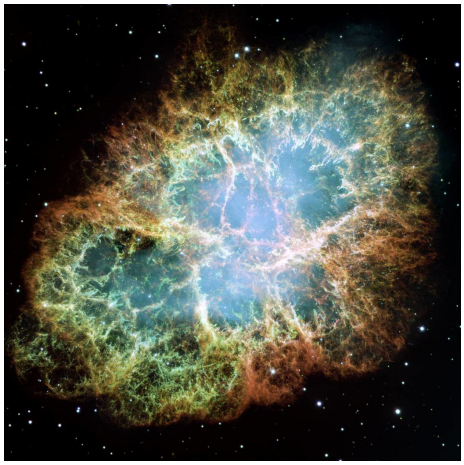

Figure 1.10: The Crab Nebula: a remnant of the supernova explosion happened in the year 1054 A.D. Image Credit: NASA, ESA, J. Hester, A. Loll (ASU)

Binary Systems and Microquasar

Binary systems are composed of a normal star (companion) and a compact object such as a neutron star or a stellar-mass black hole, which is still accreting matter from the companion star (figure 1.11). Depending on the mass of the companion star, there are two types of binaries: low mass X-ray binary (LMXB) with primary star mass of $< 1 M_{sun}$, and high mass X-ray binaries (HMXB) with primary star mass of

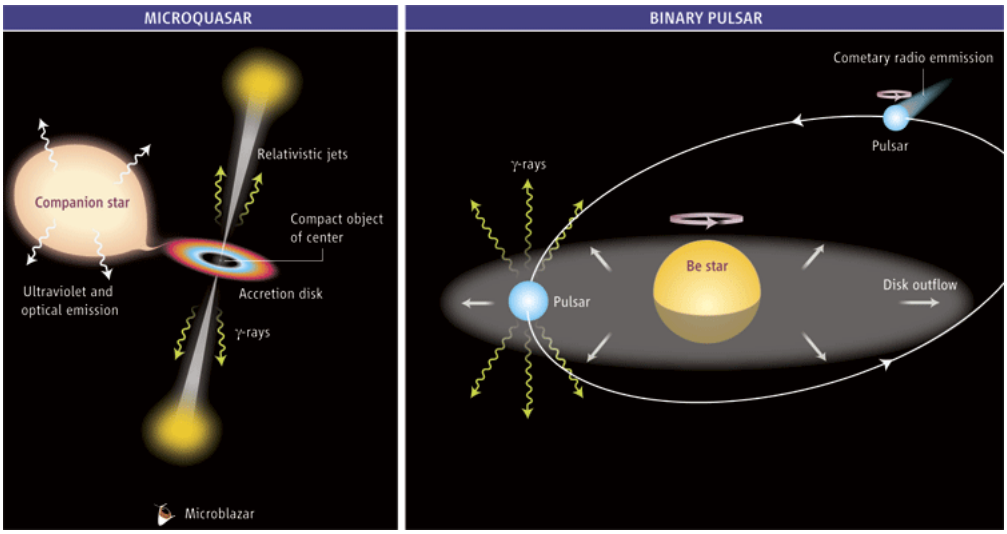

Figure 1.11: Two emission models of binary systems emitting γ rays. Left: microquasar accreting material from a massive companion star. Right: binary pulsar system with a Be star. Image credit: F. Mirabel `http://astromev.in2p3.fr/?q=aboutus/gamma-ray-binaries`

$> 1M_{sun}$, which mostly shows the VHE emission. If the compact object is considered as a mass accreting black hole, the binary system is considered as a microquasar, which shows VHE γ-ray emission mechanism similar to the AGNs. However, if the compact object is rotating neutron star that powers pulsar wind, the binary system is called as a binary pulsar. Here, the VHE γ-ray emission is produced due to the interaction between the companion star outflow and the shock from the pulsar wind. So far four binary systems have been detected by MAGIC in the VHE regime, i.e., Cygnus X-1 [Albert et al. 2007d], HESS J0632+057 [Aharonian et al. 2007a], LS I +61° 303 [Albert et al. 2009], and PSR J2032+4127 [Holder 2017].

As the name suggests, **microquasars** are stellar objects quite similar to quasars. They are a subset of X-ray binaries. The structure is often resolved as a pair of radio jets with strong and variable emission, and an accretion disk surrounding a black hole or neutron star. The black hole mass in this system is found to be from a few solar masses. Cygnus X-1 is the first microquasar detected in the VHE γ-ray regime [Albert et al. 2007d].

Galactic center and diffuse γ rays

The central region of our galaxy contains a large variety of astrophysical objects, mainly the supermassive black hole Sgr A* hosted by the galactic center itself, SNRs, pulsars and massive stellar clusters. Due to the densely populated objects which create source confusion and the absorptions along the line of sight due to other sources,

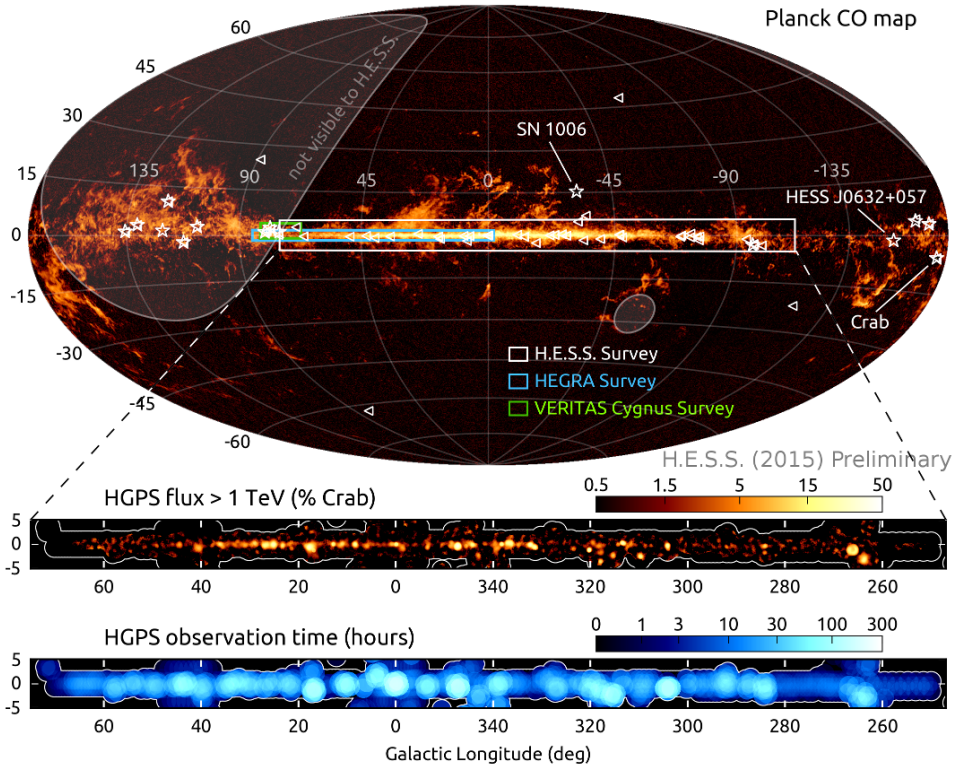

Figure 1.12: An overview of H.E.S.S. Galactic Plane Survey (HGPS) region (top), the measured TeV γ-ray flux (middle), and the observation time (bottom) [Donath et al. 2017].

observations, as well as interpretation of GC, are quite challenging. So far, most of the detected galactic sources in VHE γ rays are highly concentrated in the galactic plane region. In the recent systematic survey of the galactic plane H.E.S.S. (figure 1.12), a total of 78 VHE sources have been detected (3 binary systems, 8 SNRs, 12 PWNs, 7 composite systems and 47 with unidentified class) [Donath et al. 2017].

Also, the H.E.S.S. Collaboration reported the discovery of diffuse galactic emission, at energies above 100 GeV in a region of Galactic plane. The origin of VHE γ-ray emission is believed to be hadronic from a neutral pion decay due to the collisions between the charged CRs and dense molecular clouds and dust located in the galactic plane. A spatial correlation between the observed excess from the VHE γ-ray emission region and the distribution of the molecular clouds fits the evidence for this hypothesis.

Starburst Galaxies

Compared to most of the galaxies, starburst galaxy characterizes high star formation rate, especially in its central region. After a close encounter between two or more galaxies, these galaxies are often observed to have a burst of star formation, thus the name starburst.

Figure 1.13: The "cigar galaxy" also known as M82 is one of two starburst galaxies now know to radiate VHE γ rays. Image courtesy of NASA.

Due to the unusually high rate of supernova correlated with the high star formation, which provides strong shocks to accelerate the charged particles to the highest energies, these galaxies are a preferred site of accelerated charged CRs. The VHE γ-ray emission is assumed to originate from pion decay via the collision between CR protons and interstellar medium nucleons [Persic & Rephaeli 2011]. So far only two starburst galaxies have been detected in the VHE regime, i.e., M 82 and NGC 253.

Dark matter annihilation

The self-annihilation of the weakly interacting massive particles (WIMPs), which are a prime candidate for the cosmological dark matter (DM), can produce γ rays that extend up to the TeV range [Bringmann & Weniger 2012]. Such particles are predicted to be produced in the Big Bang. Some of them might have survived until current epoch, depending on their original features. So far, the most promising candidates for such emission are the dwarf galaxies, which are identified by an enhanced mass to luminosity ratio, and clusters of galaxies. In such sources, the concentration of baryonic matter is high. Thus they increase the possibility of having high DM concentrations. Also, many theories predict the conversion of DM to standard model particles via decay or interaction channel. Therefore, γ rays could also be produced in such a scenario. By observing sources with high matter concentration, Cherenkov telescopes can help to probe the parameter space of ΛCDM models [Aleksić et al. 2011a]. Despite a lot of efforts, so far no γ-ray emission has been detected with the sensitivity of MAGIC or other Cherenkov telescopes, only upper limits could be derived. Considering the improved sensitivity of the CTA, DM searches will be one the prime target of the key science projects of the CTA.

2. Active Galactic Nuclei

Motivation

Active galactic nuclei (AGN) are the most energetic sources in the Universe, populate the extragalactic sky numerously and pose unique observational signatures which cover the entire electromagnetic spectrum. Among AGNs, studying blazars and radio galaxies (subclasses of AGNs) with their γ-ray emission at VHE are the main topics of this thesis. Not only their emission can be used to probe relativistic jets and the non-thermal processes in the Universe but also to constrain the extragalactic background light (EBL). In the first part of the chapter, I will give an overview of AGNs along with their observational properties and classification; then the unification theory is explained. The chapter will be concluded with a discussion on the spectral characteristics and VHE γ-ray emission models of blazars. The details about how AGN emission can be used to constrain the EBL are given in chapter 7.

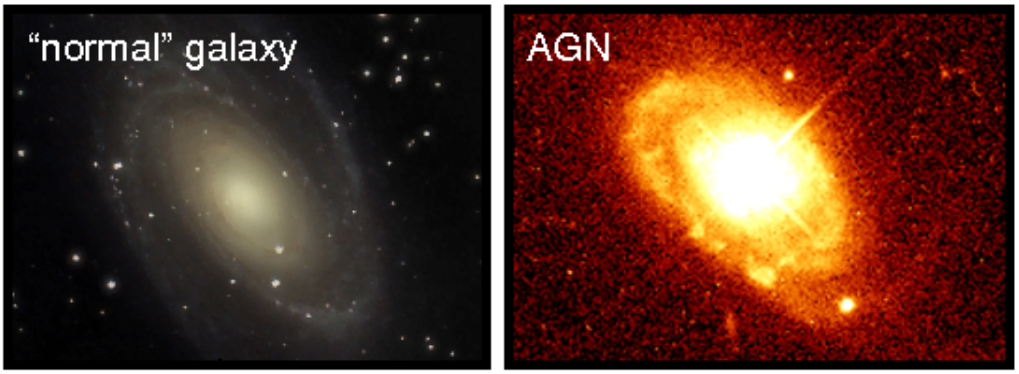

Figure 2.1: Illustration of comparison between the normal galaxy and the AGN. Image credit [Padovani et al. 2017]

Introduction

Active galactic nuclei (AGN) are the spectacular and most energetic sources in the universe. When the central region or nucleus of the galaxy is more luminous than the rest of the galaxy, the nucleus is called AGN (see figure 2.1). In the 1940s, Carl

Seyfert discovered that some galaxies were showing some excess component strongly at their center, and thus he discovered the first class of AGN, named after him as Seyfert galaxies [Seyfert 1943]. In his study, he obtained spectra from a sample of 6 galaxies, for which he found that for some galaxies, the central region showed broad line emission while others showed only narrow line emission. At that time, the nature of the strong central emission was still a mystery. It was not clear until around 1964, whether the center of AGN contains a hypermassive star or as per new idea that there lies a black hole [Salpeter 1964, Zel'dovich et al. 1964].

Later by the continuously growing scientific community, the most accepted model was based on the idea that the center of AGNs contains s supermassive black hole, which is from the collapse of a massive star, with its mass ranging from 10^5 to 10^{10} $M_\odot$. An example of this is the supermassive black hole found at the center of our galaxy [Salpeter 1964, Zel'dovich et al. 1964, Lyden-Bell & Rees 1971]. Also, variability in AGN luminosity on short timescales such as hours or days was observed quite commonly. Therefore, this model also explained the large energy excess via accretion phenomenon as well as the small size of the emission region and variability on short timescales. The short timescales in hours or days show that the size of the energy emitting source must be of order light hours or light days respectively. The luminosity in some cases appears to be as much as 10^4 times the luminosity of a typical galaxy, in a very compact region of volume probably as $\ll 1\,\mathrm{pc}^3$. Whereas, for example, the volume of the Milky Way is of orders of $10^{12}\,\mathrm{pc}^3$ [Krolik 1999].

The AGNs belong to a large family including nonstellar origin galaxies and shows strong emission in the entire electromagnetic spectrum, i.e., from radio, optical-UV, X-ray to γ rays. As radiation from AGNs is believed to be originated from accreting matter and ejection by the supermassive black hole, therefore much of the energy output is regarding non-thermal or non-stellar type emission. Since extreme physical processes are responsible for such radiation, thus the study of AGNs allows exploring the Universe on large scales to understand its formation and evolution [Urry & Padovani 1995]. As mentioned before, most accepted model to explain AGN suggests that AGNs are powered via the accretion process from the supermassive black hole. However, physics behind accretion mechanism, relativistic outflows and highly collimated jets (commonly observed in AGNs) is not fully understood till date, and thus the characteristics of AGNs that runs the emission processes are still a mystery to be solved [Beckmann & Shrader 2012].

Classification

As shown in figures 2.2 and 2.3, the AGN classification is based on their radio loudness and their optical spectra. Among all, 15%-20% AGNs are radio loud whereas remaining are classified as radio quiet. If the ratio between the radio flux at 5 GHz and the optical flux in B band, i.e., $F_5/F_B \geq 10$, then the AGN is considered as radio-loud [Kellermann et al. 1989]. For most of the radio loud and radio quiet AGNs (except

few exceptions), the spectra from optical to soft X-ray continuum are very similar, which suggests that the emission produced in the same way [Sanders et al. 1989]. Based on the optical and ultraviolet spectra characteristics, AGNs can be classified into three broad types, i.e., broad emission lines (Type 1), only narrow lines (Type 2), and weak or unusual line emission (Type 0). See [Urry & Padovani 1995] and references therein for more details. However, only the radio-loud AGNs shows the γ-ray emission, mainly blazars and radio galaxies, depending on the orientation of the jet (see figure 2.3). Since this thesis is mainly focused on radio galaxy and blazars, in the following sections, I will briefly discuss only these radio-loud AGNs.

Radio Loudness	**Optical Emission Line Properties**		
	Type 2 (Narrow Line)	**Type 1** (Broad Line)	**Type 0** (Unusual)
Radio-quiet:	Seyfert 2	Seyfert 1 QSO	
Radio-loud:	NLRG { FR I, FR II }	BLRG SSRQ FSRQ	Blazars { BL Lacs, (FSRQ) }
	decreasing angle to the line of sight $\longrightarrow$		

Figure 2.2: AGN classification scheme based on [Urry & Padovani 1995]. Image credit: [Padovani 1999]

- **Blazars:**
  In blazars, the jet is towards the line of sight of the observer. This scenario completely changes the spectral properties, and this makes blazars as the favored site for production of high energy photons in GeV-TeV range. In the radio-loud group, Type 0 AGNs include blazars ($\sim$5% among all AGNs). Blazars are broadly divided into two parts depending upon their optical spectra, i.e., FSRQs and BL Lacs. FSRQ spectrum shows evidence of both broad-line region (BLR) and narrow-line region (NLR), and its thermal spectra are associated with an accretion disk. In BL Lacs, the emission is characterized by rapid variability and strong optical polarization. When the flux exhibit fast variation in short time scale, then the AGN is considered in a flaring state. During the flaring state, luminosity can reach 40 times or even more just in few hours compared to normal value. A subset of Type 1 AGNs, i.e., quasars are also found at a small angle to the line of sight, and they also have a strong resemblance to BL Lac objects in continuum emission. These quasars include Optically Violently Variable (OVV), Core-Dominated Quasars (CDQ), Highly Polarized

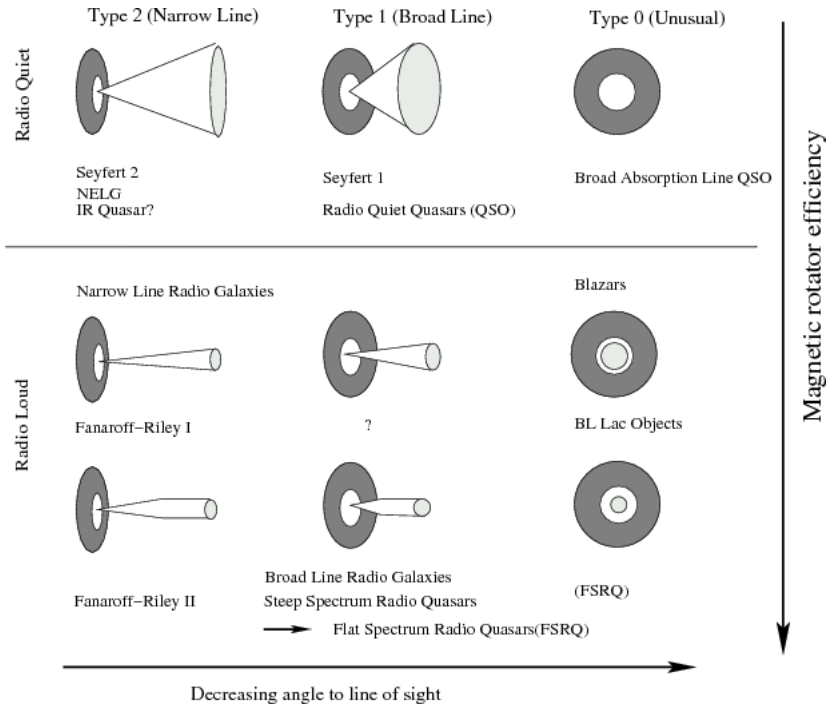

Figure 2.3: AGN classification based on the orientation of their jets w.r.t to the line of site. Image credit [Meliani et al. 2010].

Quasars (HPQ), or FSRQs. Although these objects have different empirical definitions, evidence suggests that these all are more or less the same thing. BL Lac objects and these quasars show similar characteristics such as high brightness temperatures, rapid variability, variable polarization and compact radio core with superluminal velocities.

The spectral energy distribution (SED) of blazars displays a two-bump structure, the first peaks in the infrared up to keV energy range and the second peaks at MeV up to GeV-TeV energies. BL Lacs are sub-divided into several types, defined by the location of the peak of the low-energy synchrotron SED component as low-, intermediate- and high-synchrotron peaked (i.e., LSP, ISP, and HSP) according to the position of the peak in the radio, optical and X-ray band. Table 2.1 summarizes details about these blazar types according to their Synchrotron peak position. In HBLs, VHE photon emission is commonly observed.

- **Radio Galaxies:**
  In radio galaxies, the jet is inclined at a large angle (>30 deg) w.r.t. the line of sight. The large torus covers the central region. Therefore, the reprocessed light is coming from the inner disk and the broad-line region. The radio emission

Blazar type	Synchrotron peak location	Synchrotron peak position [Hz]
LSP (FSRQ + LBLs)	Infra-red regime	$\nu_s \leq 10^{14}$
ISP (LBLs + IBLs)	Optical-near UV	$10^{14} < \nu_s \leq 10^{15}$
HSP (HBLs)	X-ray	$\nu_s > 10^{15}$

Table 2.1: Summary of blazar types according to their Synchrotron peak position.

observed is synchrotron radiation from the jets and the lobes. In the radio-loud group, Type 2 AGNs include narrow-line radio galaxies (NLRG). NLRG further divided into two subclasses; Fanaroff-Riley type I and II radio galaxies (FR I and FR II) [Fanaroff & Riley 1974]. FR I radio galaxies have low luminosities and often shows symmetric radio jets with their intensity falling away from the nucleus, whereas FR II radio galaxies have high luminosities and their jets are more highly collimated and lead to distinct lobes with prominent hot spots.

Unified scheme

AGNs contain a broad class which includes a large variety of subtypes. These subclasses collectively occupy a large parameter space. The AGN phenomenon was first defined based on observational characteristics. The idea of the unified scheme proposed by Urry and Padovani in 1995 [Urry & Padovani 1995] is that AGN emission is highly anisotropic in the inner parts as shown in figure 2.4a. The ultimate goal is to study in detail isotropic and intrinsic properties of the AGN and also to unify visually different but fundamentally identical classes of the AGN. The unified scheme illustrates a picture of the physical structure of an AGN which includes a central engine containing a supermassive black hole ($M \sim 10^6 - 10^9 M_{\odot}$). It is surrounded by accretion disk with fast-moving clouds. The massive gravitational potential energy from the central supermassive black hole is the ultimate source of AGN luminosity. Matter collapses into the black hole due to gravitational pull and loses its angular momentum via turbulent processes in the accretion disk, which in flattened configuration idealized as a toroidal shape.

In this whole scenario, the radiation process involved strongly depends on the mass of the supermassive black hole and the accretion rate. Therefore the gravitational potential energy (Eq. 2.1) and the luminosity (Eq. 2.2) of the source can be defined as:

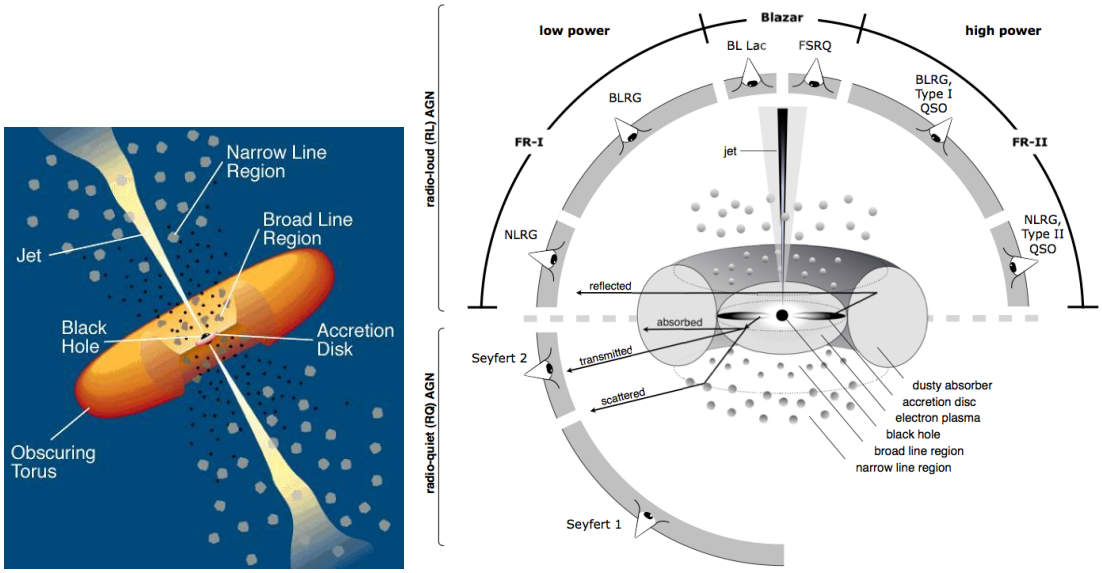

(a) (b)

Figure 2.4: (a): A schematic diagram of the current paradigm for radio-loud AGN. Image credit [Urry & Padovani 1995] (b): The type of object depends on the observer's viewing angle. Image credit [Beckmann & Shrader 2013].

$$\Delta E_{acc} = \frac{GMm}{R} \tag{2.1}$$

$$L_{acc} = \epsilon \dot{M} c^2 \tag{2.2}$$

Where, M is a mass of the source, G is the gravitational constant, R is the radius of the source, ϵ is the accretion efficiency and $\dot{M}$ is the mass accretion rate. From equation 2.1 it is clear that the accretion efficiency (energy release mechanism) is strongly dependent on accreting object's compactness, so for a larger ratio of M/R, greater efficiency we get [Frank et al. 1992]. Thus, accretion in terms of stellar mass $M_{\odot}$ for a black hole with radii $R \sim 2GM/c^2$ is $\sim 3(M/M_{\odot})$. From equation 2.2, it is clear that the luminosity of the source depends on the accretion disk mass rate. For example, in a case of BL Lacs, inefficient accretion $\epsilon \ll 0.01$ has been observed due to the optically thin disk, whereas, in contrast relatively high accretion $\epsilon \sim 0.1$ has been observed from an optically thick disk, however, FSRQ shows an efficient accretion. At high luminosities, acceleration rate is controlled by the outward momentum transferred to accretion material from the radiation by scattering and absorption [Frank et al. 1992]. Therefore, according to Eddington limit, when the inward gravitational force driver accretion is halted by exceeding outward force (considering a steady spherical symmetrical accretion), then the disk emission

results in the maximum luminosity also known as Eddington luminosity. For stars, this argument yields a maximum stable mass for a given relation between the mass and luminosity. Therefore, the equation for the Eddington luminosity is given as:

$$L_{Edd} = \frac{4\pi G M m_p c}{\sigma_T} = 1.3 \times 10^{38} \frac{M}{M_\odot} \text{ erg s}^{-1} \tag{2.3}$$

Here, m_p is the mass of the proton and σ_T is the Thomson cross-section.

During the accretion process, the falling matter from accretion disk to the supermassive black hole glows brightly at ultraviolet and soft X-ray wavelengths. However, hard X-ray emission is produced near the black hole possibly due to enveloping hot electrons above the disk. Here electromagnetic energy is extracted from the black hole itself provided that the black hole is spinning. An ultraviolet emission and strong optical lines are produced in the gas clouds, which is rapidly moving gas in the black hole potential (broad-line clouds). This optical and ultraviolet radiation is hidden by the torus along the line of sight and due to the dust outside of the accretion disk and broad-line region, as shown in figure 2.4a. The emission lines with narrower widths are produced beyond the torus by most distant and slower moving gas clouds. When the host galaxy is elliptical, collimated radio-emitting jets or giant radio sources are formed along the poles of torus due to the escaping outflows of energetic particles, however, when the host galaxy is gas-rich spiral, only very weak radio sources are formed. The plasma in the jets streams outward with a very high velocity, beaming radiation relativistically in the forward direction. At very high energy, when these relativistic jets are close to the line of sight of the observer, they can be detected as emitters of γ rays. Absorbing material obscures the luminous nucleus causes the first kind on anisotropy. Therefore the clouds emitting narrow lines, i.e., Type 2 AGN are seen along the transverse line of sight.

In radio-loud AGNs, as shown in figure 2.4b, relativistic jets are formed roughly perpendicular to the disk, which produces relativistic beaming, i.e., strong anisotropic and amplification of the continuum emission. Therefore, depending on the alignment of the relativistic jets with a line of sight, radio-loud AGN can be a blazar or radio galaxy. Second anisotropy comes from this relativistic effect (more details are given in section 2.5).

The ultimate goal of the unified scheme is to study the essential AGN characteristics such as black hole mass, accretion rate, and black hole spin and the process which governs the formation of jets, accretion of matter and the production of radiation in these spectacular objects. For example, Seyfert 2 galaxies have been unified with Seyfert 1 galaxies, whereas the FR I and FR II radio galaxies have been unified with radio quasars and BL Lacs [Antonucci 1993, Urry & Padovani 1995].

Relativistic jets in AGN

In radio-loud AGNs, as shown in figure 2.4a, two jets pointing in the opposite direction originate near the supermassive black hole. These jets are nearly perpendicular to the accretion disk and propagate from the proximity of the black hole to the large distances; parsec, kiloparsec and in some cases also megaparsec distances. The classical structure of jet consists of a hardly resolved 'core' from which a jet projects. It can appear as short or long, sharply curve or nearly straight, and nearly smooth or dominated by knots. Mostly, all knots move at apparent superluminal velocities; however, some of them move at subluminal speeds or stationary [Jorstad et al. 2001, Kellermann 2011]. Near the boundary of each radio lobes bright radio 'hot spots' are seen, which are results of the strong shocks formed near the end of the supersonic jet outflow. All these features are shown in the VLA radio image of the radio galaxy 3C405 known as Cygnus A (figure 2.5).

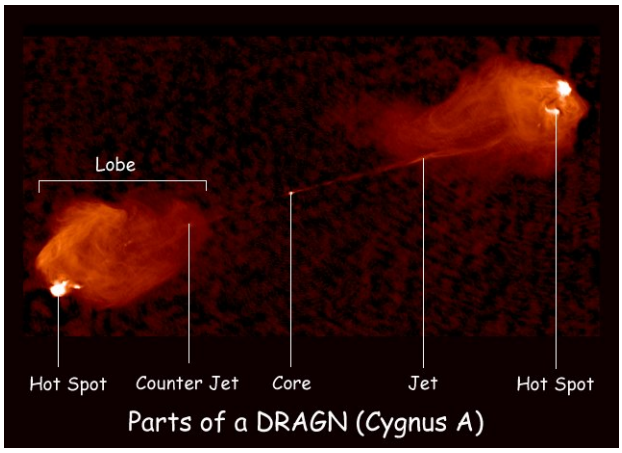

Figure 2.5: VLA radio image of the radio galaxy 3C405 (Cygnus A).
Image credit: `http://www.cv.nrao.edu/~abridle/dragnparts.htm`

According to accepted theories, the jet emission is a non-thermal component caused by electrically charged blobs, in which relativistic shock waves accelerate the material to the ultra-relativistic velocities and relativistically beams into the forward direction, which steers it to a Doppler-boosting into the line of sight (see [Blandford & Königl 1979] and [Marachi et al. 1992]). The non-thermal emission from jets is commonly associated with synchrotron radiation, which peaks at radio frequencies, emitted by ultra-relativistic electrons and their interaction with the randomly originated magnetic field inside the jet. The detection of such emission was the first evidence of particle emitting with ultra-relativistic nature. However, observations of jets also show the high energy component, which is probably associated with the inverse Compton scattering.

One of the ways to explain the jet emission in AGNs is by the Blandford-Znajek mechanism, in which the system of a black hole and the surrounding torus is submerged in a magnetic field, thus connecting the jet power generation nearly to the accretion rate and the disk luminosity [Blandford & Znajek 1977]. Here, the black hole's rotational energy is extracted via this magnetic field. This mechanism has recently been tested under various boundary conditions, and results showed its robustness over such restricted variations [Palenzuela et al. 2011]. The observations of the radio galaxy M87 with radio interferometers such as Very Large Array (VLA) radio telescopes have achieved to resolve the base and the jet structure spatially. These observations are indicating that jet is powered by the accretion disk spinning around the central black hole [Doeleman et al. 2012]. More details about M87 are given in chapter 6. Even though there is no solid explanation of jet formation, the commonly agreed theory still suggest that the jet emission spanning from radio to γ-ray frequencies are related to the blobs of electrically charged material which moves at relativistic speeds and its acceleration undergo in relativistic shocks.

Superluminal motion in the jets

In 1966, Rees discovered that in recently discovered radio galaxies, the bulk motion of relativistically moving plasma is the cause for efficient energy transfer from supermassive black hole region to the radio lobes. As discussed in [Ghisellini 2000], the superluminal motion is defined as the motion with apparent velocities close to the velocity of light (c) at a small viewing angle θ.

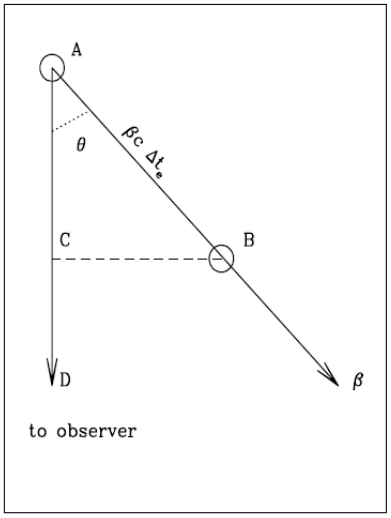

Figure 2.6: Explaination of the superluminal motion in the jets. Image credit [Ghisellini 2000].

As shown in figure 2.6, θ is the angle between observer's line of sight and the velocity vector. Suppose moving blob emits photon from position A directly towards the observer and then from position B with a small angle θ towards observer. The time between these two emissions measured is Δt_e as measured by an observer which sees the blob is moving. Then the distance AC = $\beta c \Delta t_e cos\theta$, AD=$c\Delta t_e$ and CB = $c\beta\Delta t_e sin\theta$. The arrival time difference from these two photons is $\Delta t_a = \Delta t_e(1 - \beta cos\theta$. Therefore the appaerent velocity is given as:

$$\beta_{app} = \frac{CB}{AD - AC} = \frac{\beta sin\theta}{1 - \beta cos\theta} \tag{2.4}$$

Here, we can see clearly that $\beta > 1$ for small viewing angle θ and $\beta \longrightarrow 1$. In this derivation, the Lorentz transformation factor was not required at all. Therefore, we can conclude as the superluminal motion effect occurs only from the Doppler reduction of the photon's arrival times.

Beaming effect

When the viewing angle between an observer and the jets is small, the radiation experiences beaming effect as the particles emitted from the jet move towards the observer and due to nature of the source the radiation gets amplified. As discussed in [Ghisellini 2000], due to relativistically moving source and strong anisotropic radiation, following effects occur:

- **Light aberration:**
  Due to relativistic velocities of the emitting particles from the jet, the photons are concentrated in a cone of semi-aperture angle $\theta = 1/\gamma$.

- **Arrival time of the photons:**
  As mentioned before, the time interval between emitting Δt_{em} and arriving i.e. observed Δt_{obs} photons is different.

$$\Delta t_{obs} = \Gamma(1 - \beta cos\theta)\Delta t_{em} = \frac{\Delta t_{em}}{\delta} \tag{2.5}$$

  Here, Γ is the Lorentz transformation factor, and δ is the Doppler factor. The Doppler factor is of orders of few tens in a case of blazars. From equation 2.5.2 it is clear that for small viewing angles, the observed time intervals are reduced. Therefore, if the jet emission is variable, then the observed variability timescale of it reduced due to this effect.

- **Blueshift/Redshift of frequencies:**
  As frequencies are the inverse of times, and as the source is moving relativistically, the frequency of photons is observed blueshifted or redshifted. For

example, in a case of blazars, the jets are along the line of sight of the observer, so the observed spectrum is shifted to higher energies as $\nu_{obs} = \delta\nu_{em}$. Therefore the luminosity of the observed emission L_{obs} is overestimated than that of luminosity of the emitted radiation L_{em}; as $L_{obs} = \delta^{\alpha} L_{em}$. Here parameter α has a value greater than one, and it depends on the characteristic of jet emission. As shown in figure 2.7, for $\theta \sim 0°$, $\delta \sim 2\gamma$, and $\alpha = 3$, the observed luminosity can be amplified by factors of thousands. Therefore, for jets pointing almost towards the line of sight of the observer leading to a Doppler-boosting, the emitted luminosity is overestimated typically by three orders of magnitude. Besides this amplification, beaming also causes strong collimation of the radiation, which is larger for higher γ, δ decreases by a factor $\sim$2 from its maximum value at $\theta \sim 1/\gamma$ and therefore, the inferred luminosity goes down by 2α.

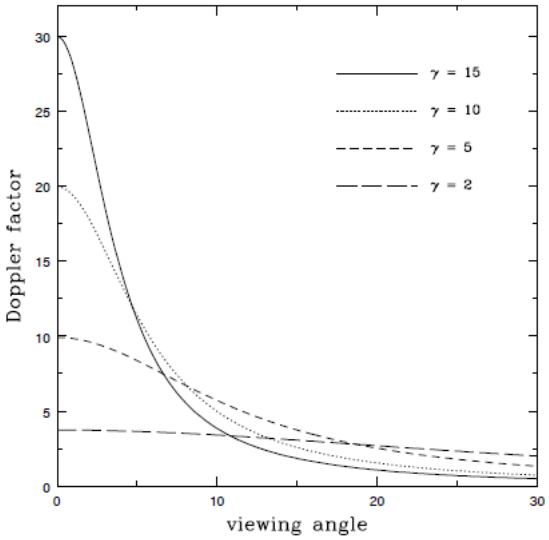

Figure 2.7: The dependence of the Doppler factor on the viewing angle to the line of sight for different Lorentz factors. Image credit [Padovani 1999].

Due to the beaming effect, relativistically moving objects can be visible up to large distances as they appear brighter if their beam is along the line of sight of the observer. Beaming is crucial to calculate the moving source's intrinsic physical parameters. The strong relativistic beaming explains the rapid variations, high polarization, and high luminosities characterized by blazars. This idea was supported by evidence from blazar observations at high energy. The model-independent argument of γ rays must be relativistically beamed came from the rapid variability in blazars. This argument does not depend on the physical mechanism responsible for

the γ-ray emission; rather it depends on the observed characteristics at high energies, such as luminosity, and variability timescales.

Emission models

Among the AGN community, compared to non-jetted AGNs, blazars and radio Galaxies are found to be orders of magnitude less abundant. However, despite their rareness, the extragalactic γ-ray sky is somewhat dominated by these sources. So far, in γ rays, non-jetted AGN has not been detected [Ackermann et al. 2012]. The output power of Blazars is dominated by non-thermal, blue shifted and Doppler boosted radiation from its jet pointing towards observer's direction [Urry & Padovani 1995]. For the VHE γ-ray emission, depending on the underlying mechanism of primary particle acceleration, i.e., whether lepton (electrons/positron) or hadrons (mostly protons), two different mechanisms are proposed to be associated with the blazar emission, i.e., leptonic and hadronic models. These models intend to reproduce the observational data as well as to constrain the jet parameters such as the geometry of the emission region, magnetic field strength and Lorentz boost factor of the jet. Before getting into these details, I will first briefly discuss the blazar SED and the blazar sequence.

Spectral energy density of blazars

The spectral energy density (SED) of blazars is described by a typical 'double humped' shape, and it covers the entire electromagnetic spectrum, from radio to γ rays. The low energy component of SED is from radio through UV or X-rays, and it peaks between the IR and the X-ray band (see figure 2.8). It is usually associated with synchrotron radiation produced by relativistic electrons moving in a magnetic field [Böttcher 2012]. The high energy component of SED is from X-rays to γ rays, and it peaks mostly in γ rays. The nature of this second SED component is still debated as two alternative explanations are being considered: **leptonic** (emission is due to inverse Compton scattering between the jet electrons and their own synchrotron emission, i.e., synchrotron self-Compton (SSC) or due to an external photon field, i.e., external inverse Compton) [Marachi et al. 1992] and **hadronic models** (emission is assumed to originate from high-energy protons either losing energy through synchrotron emission [Aharonian 2000] or via photo-meson interactions [Mannheim 1993]). These models are explained in section 2.6.3 and 2.6.4.

Blazars are associated with variability at all wavelengths. However, short timescales and largest amplitudes of variability have been observed at the high-frequency ends of the two SED components, i.e., X-ray and VHE regime (see figure 2.8). For example, rapid variability has been observed from Mrk 421 [Ahnen et al. 2016c] (see figure 2.9). The variability time scale is a critical parameter, and it can be used to assume constraints on the size and location of the emission region [Longair 1992].

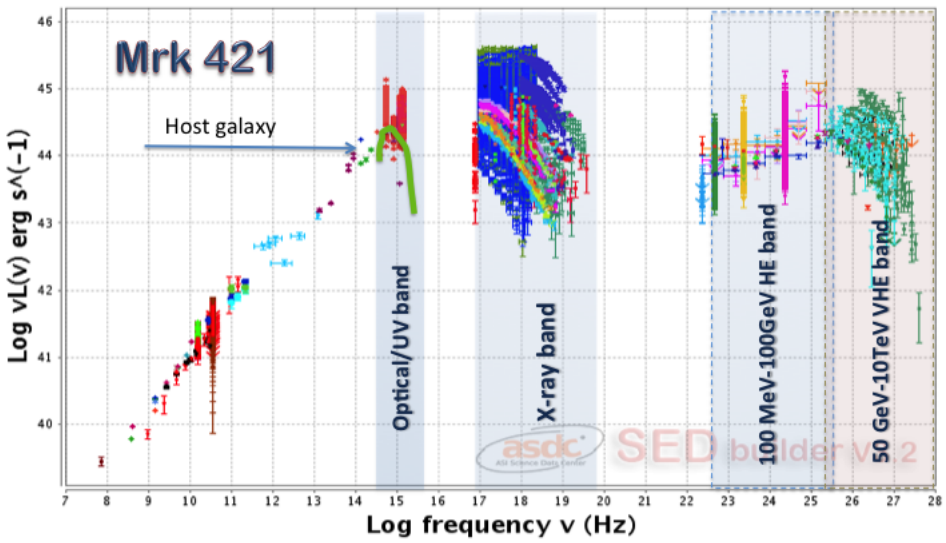

Figure 2.8: The SED of the BL Lac Mrk 421 using historical data from many years overlaid. It shows strong and variable emission from the radio to γ rays. Most prominent variability has been observed in the X-rays and γ rays, where the two SED components peak. The green line with an arrow represents the expected emission from a typical blazar host galaxy. Image credit [Padovani et al. 2017] and ASDC [`tools.asdc.asi.it/SED`.

Therefore, for instance, the size of the emitting region R from variability can be constrained as:

$$R \leq ct_{var}\frac{\delta}{1+z} \tag{2.6}$$

Here, z and δ correspond to the redshift and Doppler factor of the source, and t_{var} corresponds to the characteristic variability time scale.

Blazar sequence

[Fossati et al. 1998] identified a sequence associated with a trend of decreasing γ-ray dominance and overall decreasing bolometric luminosity along the sequence FSRQ $\rightarrow$ LBL $\rightarrow$ HBL, also knows as the 'blazar sequence'. In this sequence, a total of 126 blazars were considered, out of which only 33 were detected in γ rays by EGRET. According to this classification, the bolometric power output of FSRQs, especially during flaring states, is well dominated by γ rays, whereas, HBLs are assumed to be always synchrotron dominated. In order to build the average SED, these 126 objects were distributed into 5 GHz bins of radio luminosity, however, their luminosities were

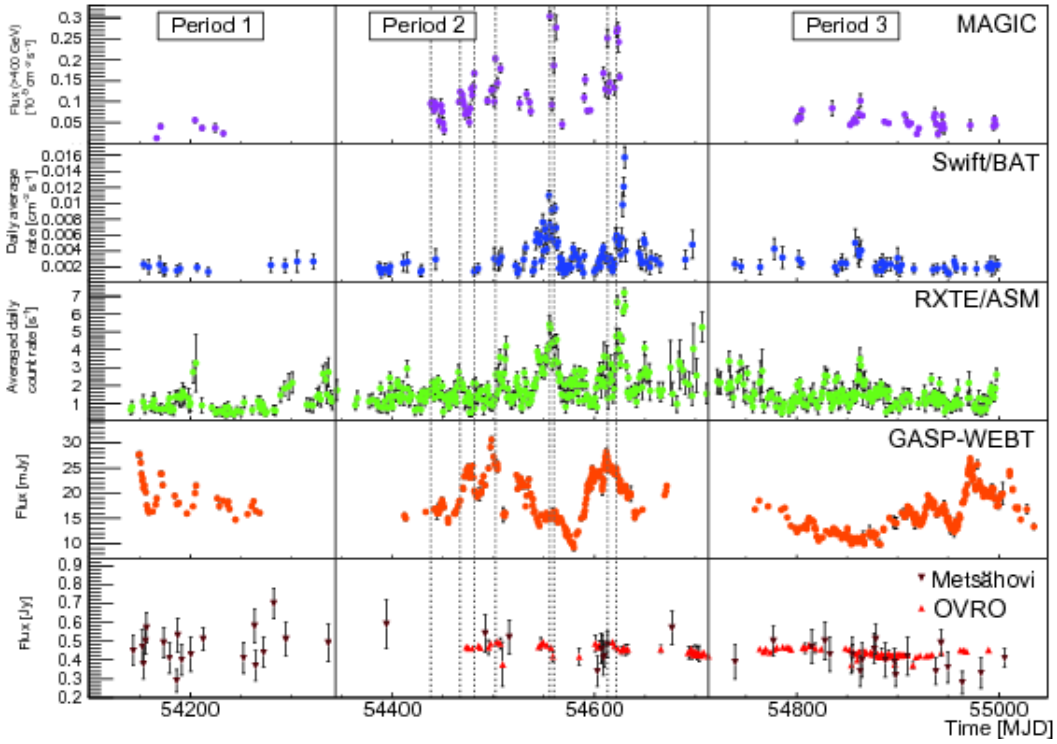

Figure 2.9: Multiwavelength light curves of Mrk 421 from February 2007 to July 2009 showing clear variability at all energy bands. Image credit [Ahnen et al. 2016c].

averaged at selected frequencies. The SED had a typical shape of two broad peaks, first at mm/soft X-rays frequencies, and second in the MeV-GeV band. As shown in figure 2.10, the blazar sequences shows the following trend:

- As bolometric luminosity increases, blazars become 'redder' (LBLs), which means the peak frequencies become smaller. At the same time, the high-energy peak becomes more prominent. So the Compton dominance (the ratio of the luminosity of the high energy hump over low energy hump) increases.
- As the bolometric luminosity decreases, blazars becomes 'blue' (HBLs) with the low and high energy humps peaking at approximately the same luminosity.
- With increasing bolometric luminosity, the X-ray slope becomes harder. However, the γ-ray slope becomes softer.

Due to the simplicity of the blazar sequence scheme, it became a popular idea. However, the validity of the blazar sequence was and still is a debated issue. The main criticism is that the sequence might be biased due to sample selection effects, not only when proposed, but even now despite the presence of more sensitive instruments [Ghisellini et al. 2017].

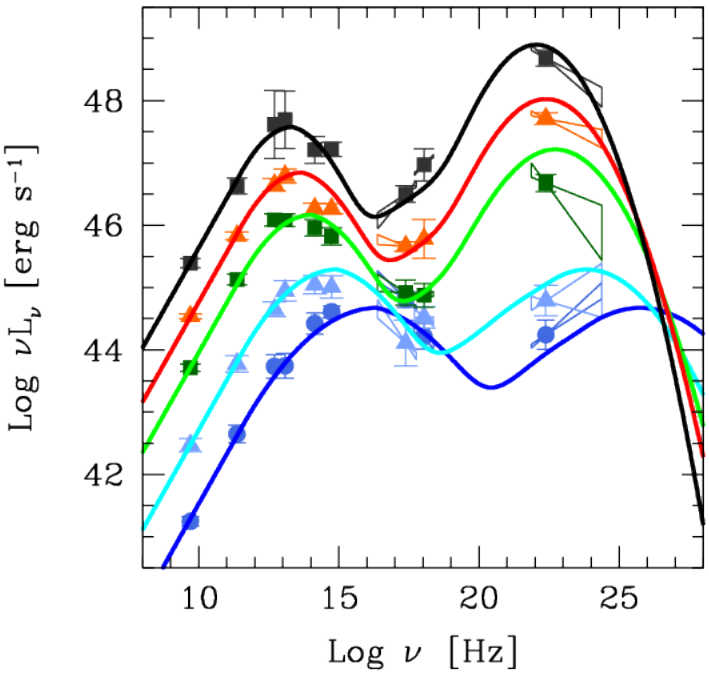

Figure 2.10: The original blazar sequence from [Fossati et al. 1998], with the 126 blazars with only 33 detected in γ rays by EGRET. Image credit [Ghisellini et al. 2017].

Blazar sequence was revisited by [Ghisellini et al. 2017]. Unlike original blazar sequence by Fossati, this new one considered a total blazar sample of 747 objects classified as BL Lacs (299) or FSRQs (448) from the third catalog of AGN detected by *Fermi*-LAT (3LAC) [Ackermann et al. 2015]. For easy comparison with original blazar sequence, these blazars were divided in 6 γ-ray bins and the average SED consisted of typical two hump structure was calculated using the spectral index listed in 3LAC catalog and the energy range of $0.1-100$ GeV (see figure 2.11).

Here are the main findings from Ghisellini 2017 for the new blazar sequence :

- The blazar sample from 3LAC do form a sequence. It still holds similar general properties as the original sequence.
- Unlike original sequence, the new one takes into account the mass of the black hole along with luminosity function, and also consist of a much bigger and complete sample of blazars regarding γ-ray luminosity.
- If FSRQ and BL Lac samples were considered separately, then FSRQ form a

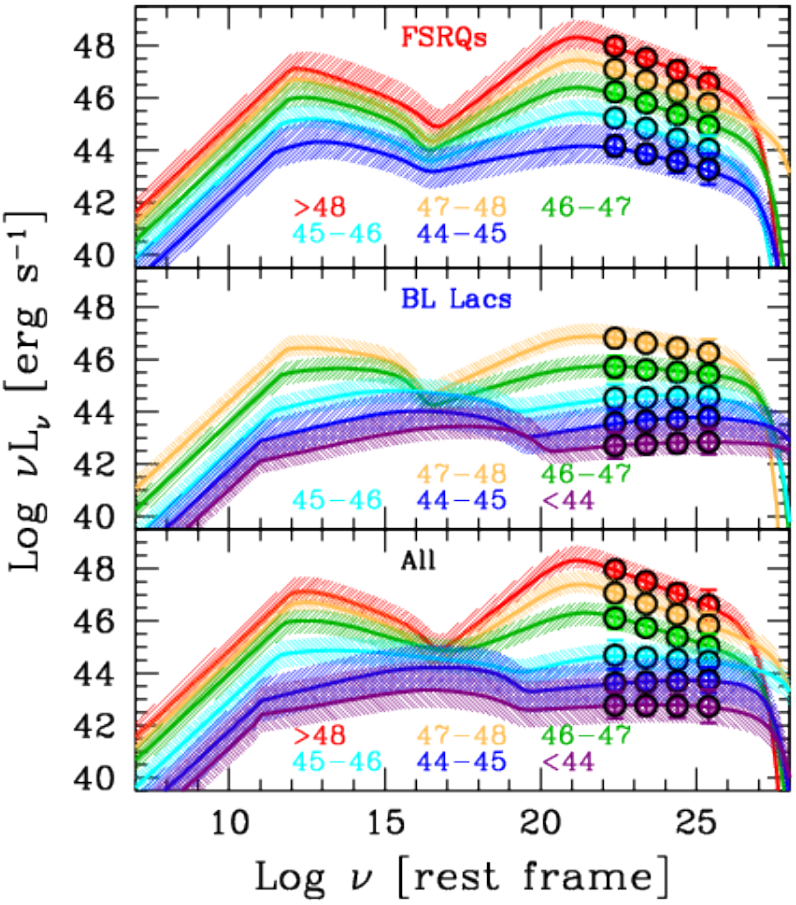

Figure 2.11: The new blazar sequence with 747 blazars detected in 3LAC [Ackermann et al. 2015] *Fermi*-LAT data . Image credit [Ghisellini et al. 2017].

sequence only in Compton dominance and in X-ray slope. They do not become redder when more luminous; however, BL Lacs do.

- The accretion disc becomes visible in FSRQs at high redshift and luminosities.

Leptonic emission models

As mentioned in section 2.6.1, in leptonic models of TeV blazars, the high-energy emission is produced due to Compton upscattering of soft photons due to the accelerated ultrarelativistic electrons. These electrons are responsible for producing the

synchrotron emission. There are two types of scenarios which can serve as target photons; the synchrotron photons which are produced within the jet itself, i.e., Synchrotron Self-Compton (SSC) [Bloom & Marscher 1996, Marachi et al. 1992], and [Marscher & Gear 1985], and the external photons, i.e., External Compton process. Possible sources for the external seed photons involve the accretion disk radiation [Dermer et al. 1992, Dermer & Schlickeiser 1993], reprocessed optical-UV emission from circumnuclear material e.g., the BLR; [Blandford & Levinson 1995, Dermer et al. 1997], and [Ghisellini & Madau 1996], infrared emission from warm dust [Błażejowski et al. 2000], or synchrotron emission from faster or slower regions of the jet itself [Georganopoulos & Kazanas 2003, Ghisellini & Tavecchio 2008]. SSC model is the simplest to explain the leptonic emission compared to all other models proposed (having ranging complexity depending on the nature of the radiation field involved).

As discussed in [Tavecchio et al. 1998], the homogeneous SSC model assumes that the radiation is produced in a single zone of the jet like a spherical emission region with radius R, which is filled with an isotropic electron population, moving at relativistic velocities at small angle θ to observer's line of sight. Therefore, the observed radiation will be heavily influenced by the relativistic effects. The key parameters for the model are: 1) radius of emission region R, which can be constrained using the observed variability timescale t_{var} information (equation 2.6, 2) Doppler factor of the bulk motion $\delta = [\Gamma(1 - \beta cos\theta)]^{-1}$, where $\beta = \nu/c$, and 3) magnetic field B.

The usually observed SED shape needs that relativistic electron spectrum steepens with increasing energy. It can be approximated with a broken power law, with spectral indices n1 < 3 and n2 > 3, and the break energy of $\gamma_b m_e c^2$. The break energy is assumed to have resulted from a balance between cooling and escape of electrons and that the soft photon lags measured in some sources derive from the radiative cooling of high energy particles [Tavecchio et al. 1998]. Therefore, the electron spectrum is given as:

$$N(\gamma) = \begin{cases} K\gamma^{-n1} & \text{if } \gamma < \gamma_b \\ K\gamma_b^{n_2-n_1}\gamma^{-n_2} & \text{if } \gamma > \gamma_b \end{cases} \tag{2.7}$$

With these approximations, the model can be completely specified using seven parameters: B, R, δ, the slopes $n1$ and $n2$, the Lorentz factor of the electrons at the break γ_b, and the electron density parameter K. The peak synchrotron power E_b emitted by electrons with the break energy is given as:

$$E_b = \gamma_b m_e c^2 \tag{2.8}$$

The maximum energy γ_{max} attained by electrons and a possible lower limit γ_{min} are unimportant here provided that $\gamma_{max} \gg \gamma_b$ and $\gamma_{min} \leq 100$. It is possible to derive following 6+1 observable quantities as input parameters while testing this model on the available SED data (see figure 2.12).

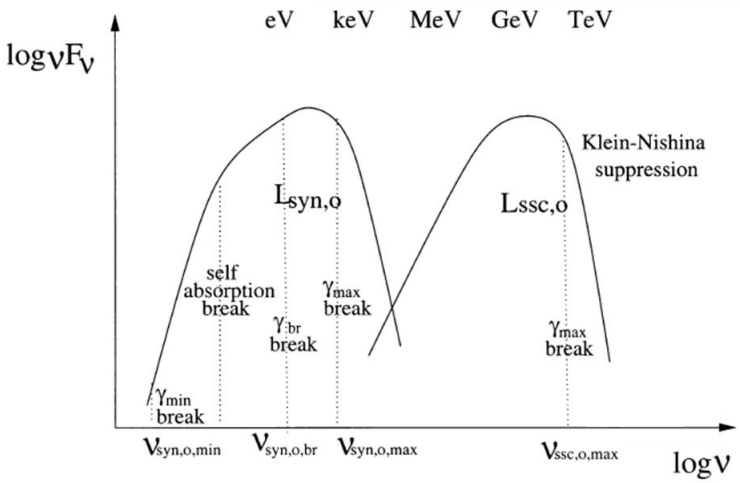

Figure 2.12: Schematic of the typical TeV blazar SED at multifrequency. The break in the electron spectrum here leads to a feature in the observed synchrotron spectrum. The observed bolometric luminosities are of synchrotron ($L_{syn,o}$) and SSC ($L_{ssc,o}$) components. The Klein-Nishina effect suppresses the observed flux around the TeV energy region, compared to the Thomson regime. Image credit [Kino et al. 2002].

$\alpha 1$	the spectral index of the rising part of the SED bumps
$\alpha 2$	the spectral index of the falling part of the SED bumps
νs	the frequency of the synchrotron peak
νc	the frequency of the inverse Compton peak
Ls	the luminosity of the synchrotron peak
Lc	the luminosity of the inverse Compton peak
t_{var}	the minimum variability timescale

As t_{var} is directly connected to the size of emission region R (see equation 2.6), it is feasible to determine the overall dimensions of the system. Furthermore, one can obtain the lower limit on the value of the Doppler factor, if the transparency of the source to γ rays is taken into account (as via pair production high energy photons may interact with low energy photons). From observations of TeV sources, a limit can be set on the optical depth of the source and the density of the soft radiation. This limit further can be used to obtain a lower limit on the Doppler factor.

In general, leptonic models have been very successful in modeling the observed spectra (and in some cases spectral variability also) quite well for many blazars. In the observers frame, for typical magnetic field B of $\sim$1 G, the radiative cooling timescales of synchrotron-emitting electrons are of the order of several hours to nearly a day at optical frequencies and $<\sim$1 hr in X-rays [Böttcher 2012]. Therefore, the model is compatible with these observed intra-day variabilities. However, for recent observations with hard energy spectrum for several decades or rapid VHE γ-ray

variability with timescale down to a few minutes, simple one zone leptonic models faces severe problems in fitting the spectra. Even with large bulk Lorentz factors of ∼50, the requirement for a size of the emitting region will be smaller than the Schwarzschild radius of the central black hole of the AGN [Begelman et al. 2008]. Therefore, more complicated models have been proposed for the observed emission, similar to SSC models but with multiple emission zones with a small spine of ultrarelativistic plasma within a larger, slower-moving jet (e.g., [Graff et al. 2008, Tavecchio & Ghisellini 2008]). The magnetic reconnection in a Poynting-flux dominated jet will be the plausible power source for such fast-moving small-scale jets [Giannios et al. 2009].

Hadronic emission models

According to hadronic models, the emission is produced via the hadronic interactions. Therefore, in the jets of AGN, along with electrons, protons get accelerated as well to relativistic energies [Mannheim 1993]. Among various hadronic scenarios, some of them propose the triggering mechanism behind VHE γ-ray emission is synchrotron pair cascades (e.g., [Mannheim 1993]). In a strongly magnetized environment, if a significant fraction of jet power is converted into accelerating relativistic protons and also reaches to the threshold for $p\gamma$ pion production, then it will result in developing cascades of the synchrotron-supported pair. The cascade will be initiated by the primary π^0 decay photons and synchrotron emission at ultra-high γ-ray energies from secondary particles such as pions, muons, and electrons/positrons, where the emission region is highly opaque to $\gamma - \gamma$ absorption [Mannheim & Biermann 1992, Mannheim 1993]. High energy radiation can also happen due to protons via direct synchrotron radiation, but this process is identified as quite inefficient. For proton energies larger than 10^8-10^{10} GeV, via inelastic proton-photon collisions generate hard photons with energies from keV to TeV. In this scenario, the photo-meson production, via $p\gamma$ or pp interaction drives the generation of electrically and neutrally charged pions like mesons.

$$p + \gamma \rightarrow p + k\pi \tag{2.9}$$

$$p + p \rightarrow \pi + X \tag{2.10}$$

Where X are for hadrons. In proton-induced cascade model, these are the processes used to explain γ-ray production in blazars [Mannheim 1993].

The neutral pions decay into photons ($\pi^0 \rightarrow 2\gamma$), while charged pions generate charged muons ($\pi^+ \rightarrow e^+ + \nu$ and $\pi^- \rightarrow e^- + \nu$). Finally, this decay results in the production of electron-positron pairs, further powering the leptonic production of high energy photons. In case if these will not escape from the jet, the photons can produce new electron-positron pairs, which afterward radiate a new generation of photons. Apart from this mechanism, synchrotron radiation of primary ultra-high

energy (UHE) protons [Aharonian 2000, Mücke & Protheroe 2000], and secondary muons [Mücke et al. 2003, Rachen & Mészáros 1998] can also initiate the high energy radiation. This emission via cascades initiated by proton can dominate the SSC emission and bremsstrahlung (also at X-ray frequencies), which produces a flatter inverse Compton peak compared to leptonic models.

To compare leptonic and hadronic modeling, in 2013, [Böttcher et al. 2013] conducted a study on a sample of SEDs of 12 *Fermi*-LAT detected blazars with good multiwavelength coverage, in which they performed leptonic and hadronic modeling on all 12 of the blazar. In their findings, they concluded that:

- All types of blazars among those 12 can be well fitted with leptonic models. The parameters used were close to the equipartition between the magnetic field and relativistic electrons in the emission region.

- The leptonic model used in this study was unable to provide a good fit to the hard *Fermi*-LAT spectrum of AO 0135+164. The problem was the mismatch between the very steep synchrotron in IR-optical to UV regime, compared to the very hard γ-ray spectrum along with Klein-Nishina effects observed at the highest γ-ray energies.

- The hadronic model used in the study provides appropriate fits for all blazars in the sample of 12 blazars, except for SED of 2 FSRQs, where the model had difficulties describing the GeV-break. However, the fits required very large powers in relativistic protons, in order of 10^{47}-10^{49} erg s^{-1}, which in most cases dominating the total power in the jet.

Hybrid emission models

According to hybrid or photo-hadronic models, the emission is produced within a confined region via Fermi-I and Fermi-II processes, where the low energetic electrons and protons are co-accelerated to high energies [Weidinger & Spanier 2015]. Here, the contributions from non-thermal proton distribution from the proton collisions at average densities within the jet are neglected, since no thermal background protons are considered as an additional parameter [Eichmann et al. 2012]. In this scenario, electrons lose energy due to the usual synchrotron and inverse Compton processes; however, protons radiate synchrotron photons which further lead to photo-meson and $\gamma - \gamma$ production as given below:

$$P^+ + \gamma \rightarrow n_0\pi^0 + n_+\pi^+ + n_-\pi^- + neutrons \quad (2.11)$$
$$\pi^+ \rightarrow \mu^+ + \nu_\mu \quad (2.12)$$
$$\pi^- \rightarrow \mu^- + \bar{\nu}_\mu \quad (2.13)$$
$$\pi^0 \rightarrow \gamma + \gamma \quad (2.14)$$
$$\mu^+ \rightarrow e^+ + \nu_e + \nu_\mu \quad (2.15)$$
$$\mu^- \rightarrow e^- + \bar{\nu}_e + \nu_\mu \quad (2.16)$$

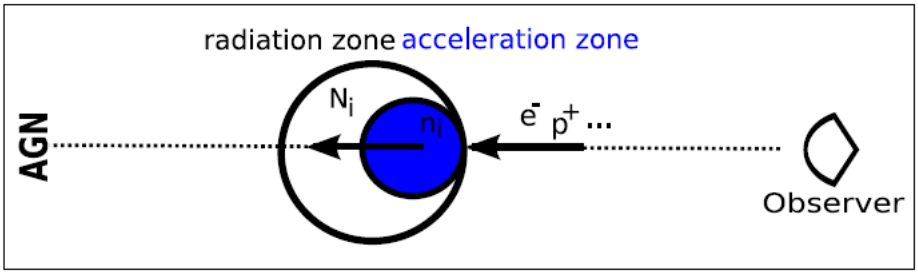

Figure 2.13: Basic model geometry for photo-hadronic model. All escaping particles from the acceleration zone serve as injection for the radiation zone. Image credit [Weidinger & Spanier 2015].

As discussed in [Weidinger & Spanier 2015], the time-dependent photo-hadronic model assumes that the emission is produced in a spherical region with an acceleration zone nested inside a radiation zone (see figure 2.13). Therefore, all the escaping particles from the acceleration zone work as an injection for the radiation zone. Due to the time-dependent numerical approach, it is possible to use exact cross sections including all nonlinear interactions and also to access variability even in the lepto-hadronic case. Therefore, it is possible to investigate the structure of the VHE peak involving various timescales of variability in the hybrid scenario including leptonic and hadronic emission with this model. When the emitting region or a blob moves along the jet axis towards the observer with a bulk Lorentz factor Γ, electrons, and protons are picked up, which forms the highly turbulent acceleration zone at the edge of the blob. At this point, a blob is filled with an isotropic electron population, which moves at relativistic velocities with small angle θ to the line of sight of the observer. Here, the acceleration and radiation zones are assumed to be homogeneous, and both contain a randomly orientated magnetic field B and isotropic particle distributions as well. Note that, when only electrons are accumulated into the acceleration zone, the model reduces to the SSC case (see [Weidinger & Spanier 2010a] and [Kirk et al. 1998] for more details). In this thesis, for M87 multi-wavelength SED modeling, a leptonic, as well as photo-hadronic modeling, has been performed. Details of it are given in section 6.5.2.

3. Imaging Atmospheric Cherenkov Technique and the MAGIC telescopes

How to detect γ rays?

The techniques to detect γ rays can be divided into two main categories; direct or indirect detections. The identification for these detection methods depends on the type of the primary particle. Earth's atmosphere is not transparent to very energetic photons with energy ranges from X-rays to UHE; therefore, direct detection is possible only via space-borne experiments, i.e., using detectors on the board of satellites. The main advantages of having a detector on board of satellite include an excellent background rejection, spatial resolution, and energy reconstruction. However, these space-based detectors face some technical difficulties, such as the size of the detector due to the limitation on weight and size of the payloads to be sent to space.

Therefore, another method is used to detect the γ rays via indirect measurements using ground-based experiments (see section 3.3 and 3.4). In this approach, the earth's atmosphere plays an essential role, as this is the medium where the primary cosmic particle interacts with air molecules and produces secondary particles shower, which provides information about the primary. Therefore, the earth's atmosphere can be considered as part of the detectors. Due to the ultra-relativistic speed, the secondary particles produce visible light through the Cherenkov effect, which propagates through the atmosphere and can be detected via ground-based detectors equipped with photosensors. This detection technique of using the Cherenkov light produced by the secondary particles is currently used in ground-based experiments like the Major Atmospheric Gamma Imaging Cherenkov (MAGIC), the High Energy Stereoscopic System (H.E.S.S.), and the Very Energetic Radiation Imaging Telescope Array System (VERITAS) telescopes.

In the following sections, first space-based detectors will be discussed briefly, then the physics related to atmospheric air showers along with Cherenkov emission will be discussed. The following part of the chapter is addressed to the introduction of the imaging technique. Last two parts of the chapter are dedicated to the descriptions of the MAGIC telescopes hardware components and the data analysis threads.

Space-borne γ-ray detectors

As mentioned in the previous section, the electromagnetic radiation coming from space cannot penetrate through Earths atmosphere due to its high opacity and reach to the surface, except for radio frequencies and a narrow window centered on the optical band. Therefore, space-based γ-ray detectors onboard satellites opened a new window of observations in the field of astrophysics [Longair 1992]. Currently, these space-based missions include the AGILE[a] and the *Fermi*[b] satellites covering the energy range of 30 MeV to 30 GeV and 20 MeV to >300 GeV respectively. Unlike hard X-rays, γ rays cannot be detected through lenses or mirrors. Therefore, depending on the energy range of the primary γ, there are three competing processes developed to retrieve information about the primary γ ray; photoelectric absorption, Compton scattering, and pair production.

- **photoelectric absorption:** at low energies between 0.1 to 0.3 MeV, photoelectric effect is the dominant process. Here, the detectors have characteristics similar to the X-ray telescopes, which use scintillator counters and solid state detectors.

- **Compton scattering:** This process becomes dominant in the transition region between the energy range of 0.5 to 10 MeV. In this region, pair production cannot be excluded even though the Compton scattering is the dominant process. Typical Compton instruments consist of two separated detector layers, a converter and other is an absorber. The incoming direction of the primary γ that Compton scatter with an electron of the converter lies in a cone of fixed angle w. r. t. the converter plane. An example of this type of detector was the COMPTEL instrument on board the CGRO.

- **pair production:** In the high energy range of 0.03 to 300 GeV, the $e^+ - e^-$ pair production becomes the dominant interaction, in which the primary γ-ray is first converted to the $e^+ - e^-$ pair. Then these two leptons are then detected by formal means in the following layers of the detector. In this high energy range, the main three elements of a detector are:

  1. a converter region where the primary gamma interacts,
  2. a tracker competent to implement the direction of the $e^+ - e^-$ tracks in addition to the dE/dx loss estimation,
  3. a calorimeter region, which brings the electrons and positrons to rest in order to measure their remaining energy.

[a] http://agile.rm.iasf.cnr.it/
[b] https://fermi.gsfc.nasa.gov/

Examples of such an instrument were on-board the OSO-III, SAS-II and COS-B satellites and EGRET on-board CGRO and more recently AGILE and *Fermi* satellites.

As non-γ particles largely dominate the CR flux, therefore, the ratio γ-particles/non-γ-particles is very small even with a small field of view (FoV) instrument. Therefore, a basic requirement for all γ-ray satellite detectors is to have a good anti-coincidence system, which is capable of suppressing the cosmic ray background of non-gamma particles which hit the detector isotropically. In the case of the Large Area Telescope (LAT) onboard of *Fermi*, the effective area at 100 GeV is 1.3 m^2 [Bastieri et al. 2005] resulting in maximum detectable energy of $\sim$300 GeV. Therefore, the detection of VHE γ rays with satellites is very challenging because of low γ fluxes and small detection areas that would require months or even years to detect just a few γ rays from the strongest VHE sources at energies around 1 TeV. Fortunately, there was a technique discovered that Earth's atmosphere could be used as a part of the detector to observe VHE γ rays.

Extensive Air showers

When a primary cosmic ray such as a photon, proton, an electron, a positron or a nucleus enters in the atmosphere, it creates extensive air showers (EAS) via cascade effect. After primary particles interact with the air molecules and atoms, depending on the primary particle type, it triggers a cascade of secondary particles. The primary particle plays the main role, and it influences the development of further EAS due to the interaction mechanism. A strong difference can be found between air showers produced due to protons (also due to heavier nuclei such as He, C, etc.) known as 'hadronic showers' and the air showers produced by electrons or γ rays known as 'electromagnetic (EM) showers'.

Electromagnetic Showers

When a high-energy γ rays interact with Earth's atmosphere, it creates the electron-positron pair (e^-e^+) in the electric field of air molecules and atoms. Each e^-e^+ pair generates the high energy photons via Bremsstrahlung, which leads to the production of EM processes cascade. As shown in figure 3.1a, the process further continues for the secondary photons to produce e^-e^+ pair and for the Bremsstrahlung, until the photon energy is not sufficient for further pair creation. During the cascade development of air shower, the average energy of the particles decreases at each interaction level. Once the energy of the particles falls below the characteristic energy (E_c) i.e. $\sim$85 MeV [Ulrich et al. 2011], e^- and e^+ lose their energy through ionization of air molecules. Therefore, shower particles do not have enough energy to create new particles and no new e^-e^+ or γ rays are produced. The remaining particles lose their energy in ionization, and the shower dies quickly.

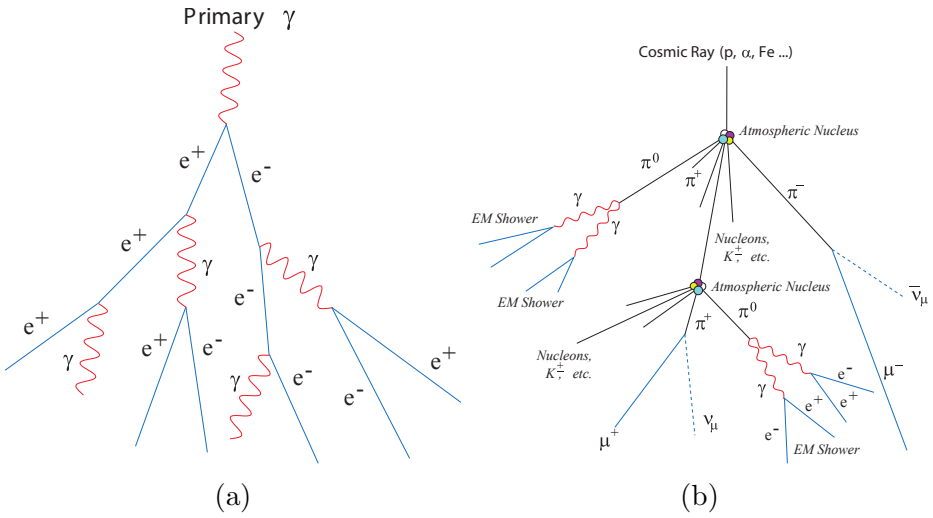

Figure 3.1: Illustration of extended air showers. (a): Electromagnetic shower. (b): Hadronic shower. (Image credit from [Wagner 2006]

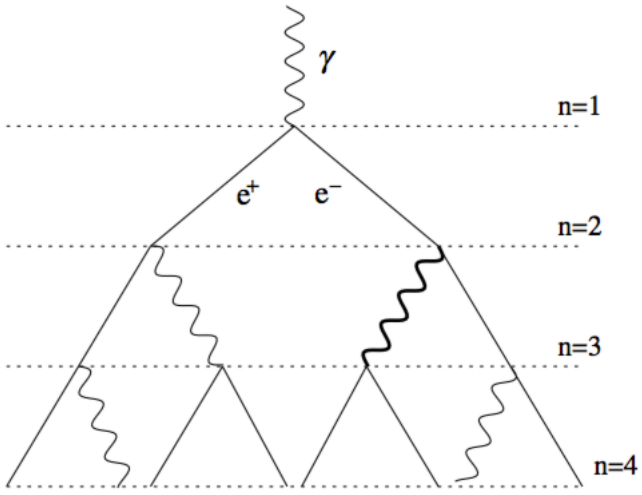

Figure 3.2: Electromagnetic shower as explained in the Heitler model. (Image credit [Ulrich et al. 2011])

As discussed in the Heitler model (see figure 3.2) for essential properties of air shower [Heitler 1954], in longitudinal development of electromagnetic cascade, the interaction of the primary particle with energy E after one splitting length is $\lambda_e = 2X_0$. Here, after one radiation length $X_0 \sim 37$ g/cm^2, the electromagnetic radiation produces two secondaries with an energy of E/2. This simple model gives that the maximum number of generated particles N_{max} is directly proportional and the highest depth of shower X_{max} is logarithmically proportional to the primary particle energy E_0.

$$N_{max} = \frac{E_0}{E_c} \sim E_0 \tag{3.1}$$

$$X_{max} = \lambda_e \frac{ln(E_0/E_c)}{(\ln 2)} \sim \lambda_e \ln E_0 \tag{3.2}$$

Therefore, the higher the energy of the primary particle, the deeper is the cascade of the shower until it reaches the critical energy. For the energies of primary *gamma*-rays between 50 GeV to 10 TeV, the maximum shower length is 13 to 7 km above sea level.

Hadronic Showers

When a hadron (proton or atom nucleus) as primary particle interacts with the nucleus in the atmosphere, it initiates hadronic shower (see figure 3.1b) with the production of a great variety of secondary particles such as pions, kaons, and nuclei. Here, all the hadronic cosmic-ray particle kinetic energy is sooner or later transferred to pions. Therefore, in this cascade, mostly pions π^+, π^-, π^0 are created with a proportion of 1 : 1 : 1, which carry relatively high transverse energy via strong interaction of their 3-particle productions. The total energy also gets almost equally distributed in these pions. The lifetimes in the rest frames are 8.4×10^{-17} s and 2.6×10^{-8} s for π^0 and charged pions respectively. However, in the hadronic cascade, along with pions kaons and further nucleons are also created, but their number is less than that of pions.

Further collision of hadrons and pions initializes next level of cascade (see equation 3.4 to 3.7). Once the pion production from the secondary particles have reached the critical energy, their decay is dominant feeding the muonic shower component. Neutral pion decays to photons, whereas, charged pions (π^+, π^-) decays to muons $(\mu^\pm)$ and neutrinos. Then the muonic shower further decays to electrons, positrons, and neutrinos. As long as energy per nucleon is below the 1 GeV threshold of pion production, this hadronic shower continue to grow. The track lengths for large Lorentz factor Γ of 1000 for charged pions are of $\sim$10 m, however, negligible for neutral pions. The main processes involved in the production of hadronic shower are:

$$\pi^0 \rightarrow 2\gamma \tag{3.3}$$
$$\pi^+ \rightarrow \mu^+ + \nu_\mu \tag{3.4}$$
$$\pi^- \rightarrow \mu^- + \bar{\nu}_\mu \tag{3.5}$$
$$\mu^+ \rightarrow e^+ + \nu_e + \nu_\mu \tag{3.6}$$
$$\mu^- \rightarrow e^- + \bar{\nu}_e + \nu_\mu \tag{3.7}$$

Therefore, as described in section 3.3.1, the decay of neutral pions resulting in γ rays follow the EAS process of the EM showers. Figure 3.3 shows the Monte-Carlo simulations of the air showers induced by primary particles of 100 GeV with CORSIKA [Schmidt 2014], which clearly shows that the structure of hadronic EAS is much more irregular and broader than that the one of electromagnetic EAS. This structural difference helps to separate the hadronic EAS from those which are created by γ-ray induced EAS.

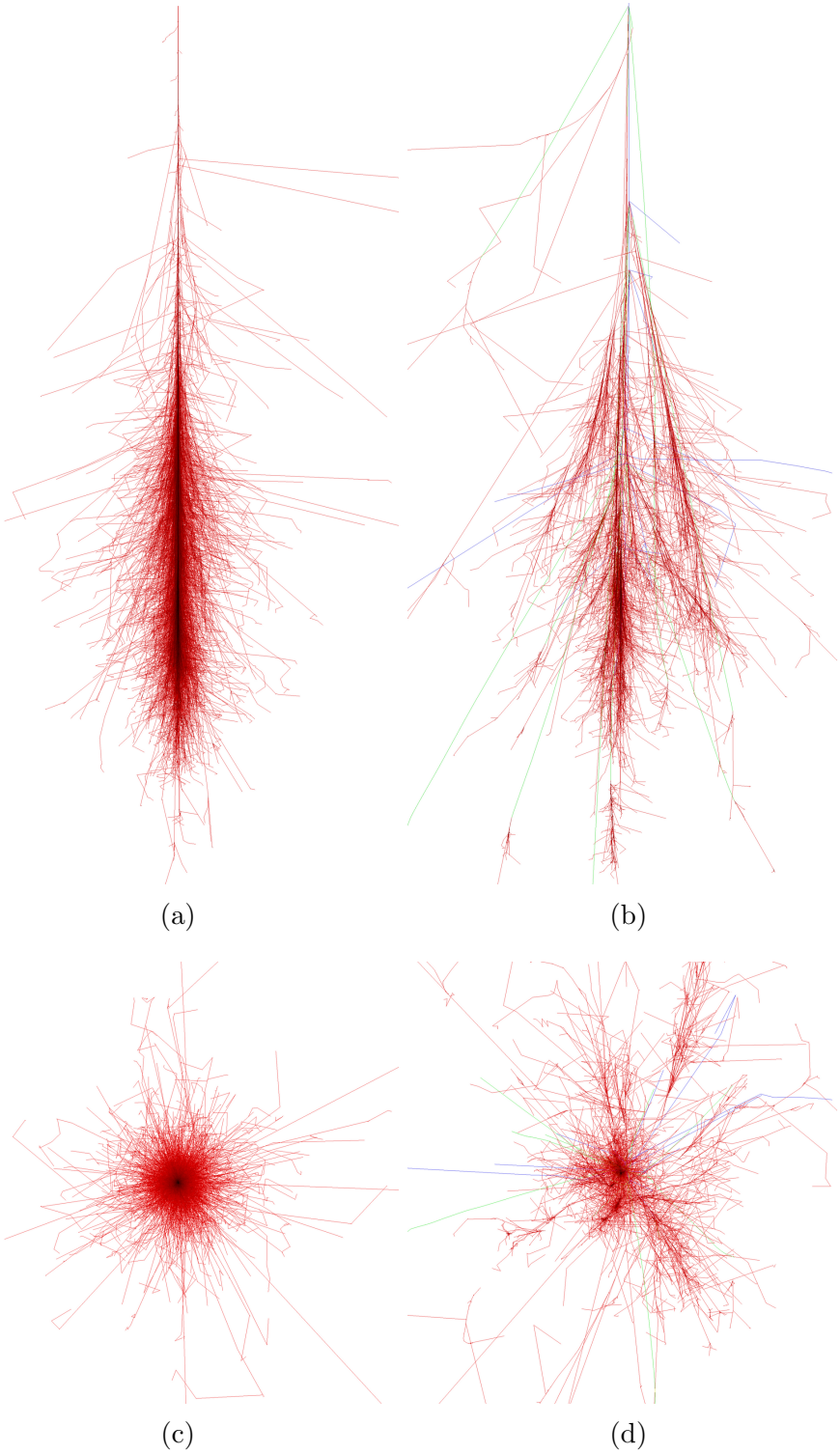

Figure 3.3: (a,c): Side and bottom view of particle tracks in the electromagnetic shower. (b,d): side and bottom view of particle tracks in hadronic showers. The air-showers were simulated with CORSIKA, which were induced by primary particles with the energy of 100 GeV. (Image credit: [Schmidt 2014])

Emission of Cherenkov light

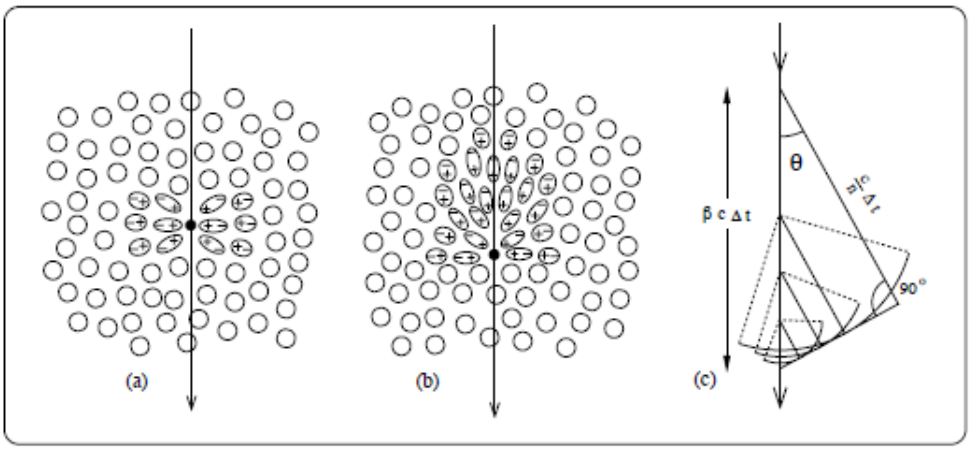

Figure 3.4: Illustration of Cherenkov light effect. Polarization produced in a dielectric medium by a moving charged particle with (a) small velocity, and (b) high velocity. (c): Huygens's construction of the Cherenkov light wavefront with Cherenkov angle θ. Image credit: [Tescaro 2010]

In 1934, Cherenkov radiation was first observed by P. A. Cherenkov and later in 1937, Frank and Tamm theoretically explained it. When charged particles travel in a transparent dielectric medium of refractive index n and velocity $v = \beta \cdot c$, where v is greater than the speed of light in the medium and $\beta > 1/n$, Cherenkov light effect occurs. The radiation takes place when previously polarized electric dipoles, generated by the moving charge, re-orient. Therefore, a charged particle traveling through a medium polarizes the nearby atoms and creates electromagnetic fields in its vicinity. Then if the speed is very high, the dipole radiation does not destructively interfere, and Cherenkov radiation is produced. As the charge moves away, these dipoles dissipate away releasing the electromagnetic potential energy in the form of photons. However, unless the speed of the moving charge is faster than the speed of light in the medium, the photons can not constructively interfere, and hence there is no net radiation (figure 3.4a). In case the polarizing charge is moving faster than the emitted photons (figure 3.4b), the wavefronts emitted at different locations of the particle's trajectory can sum coherently (according to Huygens's construction, figure 3.4c). The angle of Cherenkov light θ w.r.t. the velocity vector $\vec{v}$ from the direction of propagation of the particle can be derived with a simple geometrical argument as:

$$\cos\theta = \frac{1}{\beta n} \tag{3.8}$$

The surface delimited by the angle θ is called Cherenkov cone. If the charged

particles cross the atmospheric medium, in that case, this equation can be rewritten to obtain the Cherenkov angle as a function of the altitude z:

$$\theta_c(z) = \cos^{-1}\Big(\frac{1}{\beta n(z)}\Big) \tag{3.9}$$

The energy threshold for a particle with mass m_0 and threshold velocity to produce Cherenkov light $\beta_{\min} = 1/\mathrm{n}$ is:

$$\mathrm{E}_{th} = \frac{m_0 c^2}{\sqrt{1-\beta^2_{\min}}} = \frac{m_0 c^2}{\sqrt{1-n^{-2}}} \tag{3.10}$$

When very high energy (VHE) γ rays enter the atmosphere, Cherenkov radiation proves quite useful to detect them. As mentioned in the section 3.3.1, VHE γ-ray initiates an EM shower, the created $\mathrm{e^+e^-}$ pair gain velocities greater than the speed of light in air. Ground-based light detectors can then detect the optical Cherenkov radiation radiated by these electrons and positrons.

The number of Cherenkov photons by a particle with charge Ze emitted per unit of photon wavelength (λ) per unit of path length is given by [Yao et al. 2006]:

$$\frac{\mathrm{d}^2 N}{\mathrm{dx}\ \mathrm{d}\lambda} = \frac{2\pi\alpha Z^2}{\lambda^2}\Big(1 - \frac{1}{\beta^2 n^2}\Big) \tag{3.11}$$

where $\alpha = 1/137$

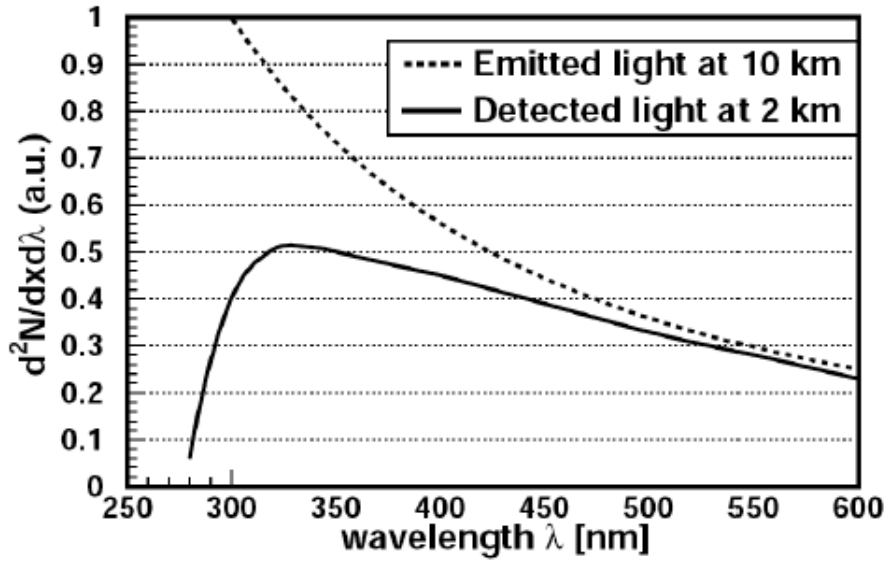

Figure 3.5: Cherenkov light spectrum at the shower maximum (dashed curve) and after traveling down to altitude of 2 km. (Image credit: [Tescaro 2010])

Depending on the energy and type of the primary particle, the density of the Cherenkov photons changes at the ground, which is known as 'light pool'. In most of the cases, Cherenkov radiation is produced by electrons (due to the low energy threshold) with their travel across the atmosphere. As altitude changes, the emitted Cherenkov photons have different propagation angles w.r.t. the shower axis, which divides the emission into three parts; tail, core, and head (as shown in figure 3.6).

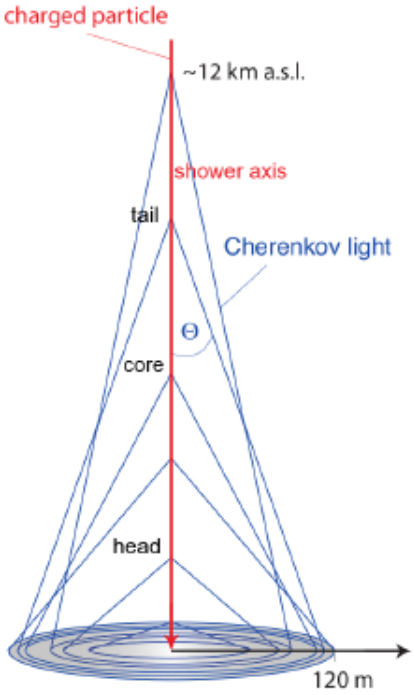

Figure 3.6: Illustration of the Cherenkov angle variation with altitude. As altitude changes, the emitted Cherenkov photons have different propagation angles w.r.t. the shower axis, which divides the emission into three parts; tail, core, and head. (Image credit: [Schultz 2013]

This angle is mainly defined by two factors: 1) the multiple Coulomb scattering of the particles ($\sim 5°$) and 2) the Cherenkov emitting angle ($\sim 0.7°$). Due to change of the refraction index of the air, it decreases[c] during the shower development. Another minor factor which affects the Cherenkov angle is the scattering of the photons due to the atmospheric dust. Cherenkov photons suffer three attenuation processes in the atmosphere; Rayleigh scattering, Mie scattering, and ozone absorption.

- **Rayleigh scattering:** It results from the scattering of photons by polarizable molecules such as air molecules. Here the size of these molecules is much

[c]for example, the Cherenkov angle of 0.74° at 8 km decreases to 0.66° at 10 km [Aharonian et al. 2008]

smaller than the wavelength of light. The cross-section of Rayleigh scattering is proportional to λ^4. As described above, the Cherenkov light has a spectrum as shown in figure 3.5, and due to the Rayleigh scattering, most of the shorter wavelengths (mainly the UV part of the Cherenkov spectrum) are absorbed.

- **Mie scattering:** It results from the interaction of Cherenkov photons with small air suspended dust particles, i.e., aerosols, whose size is comparable to or same as the wavelength of the light. Aerosols are mostly limited to the boundary layer of typically 1-2.5 km thickness above the surrounding terrain. When fog, clouds, or dust pollutes the atmosphere, this effect especially becomes critical. The spectral dependence of the Mie cross section is proportional to λ^a with $1.0 \leq a \leq 1.5$

- **Ozone absorption:** In the upper part of the atmosphere with h $\geq$ 10 km, the absorption in the ozone layer takes place. It mainly affects all the photons with wavelengths shorter than 340 nm with a maximal absorption around the 250 nm. The absorption happens through the $O_3 + \gamma \longrightarrow O_2 + O$ process. This process is the dominant one for ultraviolet light absorption (see figure 3.5).

As shown in figure 3.7, in the case of verticle γ-ray induced showers, the light density is approximately constant up to around 120 m away from the shower axis, then an abrupt drop occurs, and the number of photons starts to fade away. The typical area on the ground which gets illuminated is quite extended ($\sim$ 40,000 m^2).

Another factor affecting the Cherenkov photon density is related to the zenith angle of observation. Therefore, the distance between the shower maximum position and the telescope increases. As the crossing path for the Cherenkov light in the atmosphere increases, the absorption or interaction of Cherenkov radiation is more severe. When charged particles cross the atmosphere, along with ionization of atoms, they also excite atoms. Some of this relaxation of the excited states appears in the form of 'fluorescence' from nitrogen molecules (78% in the atmosphere). The fluorescence radiation peaks at UV wavelengths (300 - 450 nm), with typically 5000 photons per km of track length [Perkins 2009]. Fluorescent light emits isotropically. It is also used to detect the air showers, in experiments such as the Pierre Auger Observatory (PAO), the Akeno Giant Air Shower Array (AGASA) and the High-Resolution Flys Eye (HiRes) [Bauleo & Martino 2009, Abraham et al. 2010].

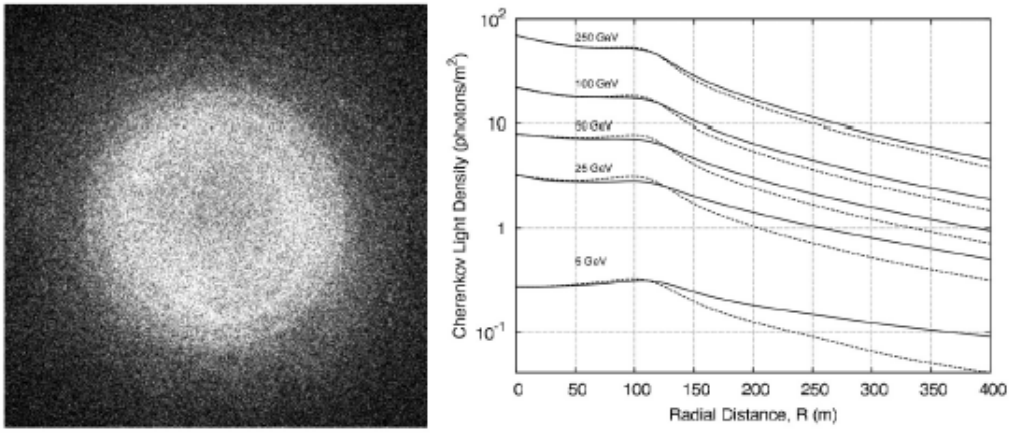

Figure 3.7: An air shower originated by γ-ray generates a circular Cherenkov light pool at ground level. Left: The light pool produced by a 300 GeV γ-ray showing uniform density, which is observed on the ground. Right: Simulation of the light pool density profile. Starting from the core center, the light density is approximately consistent up to around 120 m away from the shower axis, then an abrupt drop occurs, and the number of photons starts to fade away. The solid and dashed lines show the development of shower along the Earths magnetic field and perpendicular to it. (Image credit: [Aharonian et al. 2008])

Imaging atmospheric Cherenkov telescope technique

Up to date, the most effective way to detect γ rays above ~ 50 GeV is with Cherenkov telescopes. In 1963, it was suggested by Jelley and Porter that, it is possible to provide the detailed information on the true direction of the shower and the type of the primary particle by the high resolution of the image [Jelley & Porter 1963]. However, due to technical difficulties and low sensitivity of the early instruments, it was not until 1989, that with Whipple telescope a γ-ray signal from the Crab nebula was detected [Weekes et al. 1989]. This detection became the prime motivation for continuing operation of the existing and building better instruments, and finally lead to many of today's great discoveries using the Imaging Atmospheric Cherenkov Telescopes (IACTs). An IACT has two basic components: 1) mirrors, where the Cherenkov photons are collected, and 2) camera, equipped with a sensitive light detector and positioned in the telescope focal plane of the reflector, where parallel light rays are focussed to the same point (see figure 3.8). As the flash of Cherenkov light lasts just for a few nanoseconds, the camera needs to have very fast detectors in order to integrate the signal without adding too much noise from the unwanted background light. This is usually accomplished using a matrix array of Photomultiplier Tubes (PMTs), where the Cherenkov photons are measured, and a pixelated image of the shower can be extracted from it.

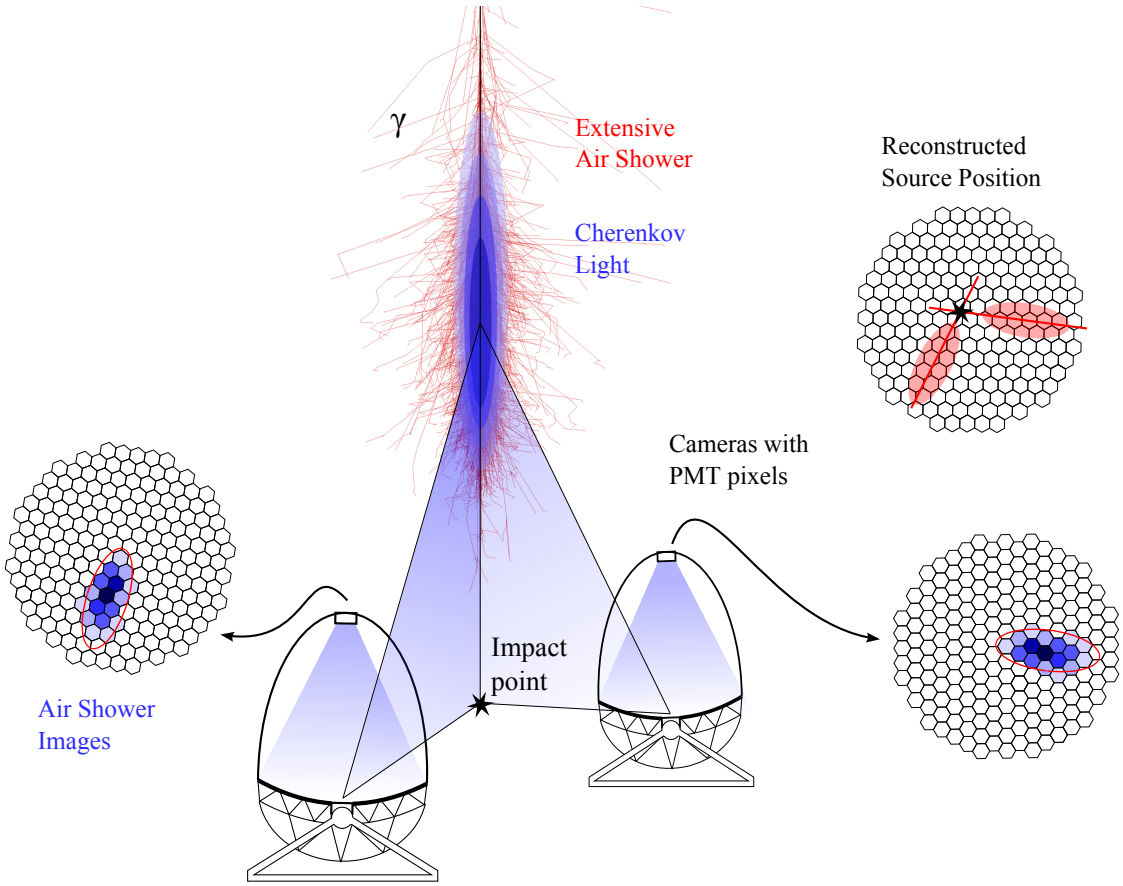

Figure 3.8: Illustration of the basic principle of the imaging atmospheric shower Cherenkov technique in stereoscopic mode. The telescopes are located inside the Cherenkov light pool of an EAS (light blue cone). Once the light is collected by the big mirror dishes, it gets mapped on the fast and sensitive imaging cameras with PMT pixels. The elliptical shape, width, length, and orientation of the resulting images can be used to reconstruct the type, energy and the direction of origin of the primary particle. (Image credit [Fruck 2015])

Principle of shower reconstruction

The Cherenkov photons are projected on different regions of the camera depending on the angle between the telescope axis and the incoming photon direction, due to differences in the origin of the emission by the particle shower. In general, the amount of Cherenkov photons detected provides information about the density of the shower particles at different altitudes of the atmosphere. In addition, the shower image properties contain information about the incoming directional nature of the primary particle, as the arrival direction of hadronic showers is isotropically distributed in the sky, whereas, an EAS originating from γ rays usually a point source with a well-

defined position in the sky. This means, having high precision in a reconstruction of the arrival direction of the measured showers helps in achieving better background discrimination.

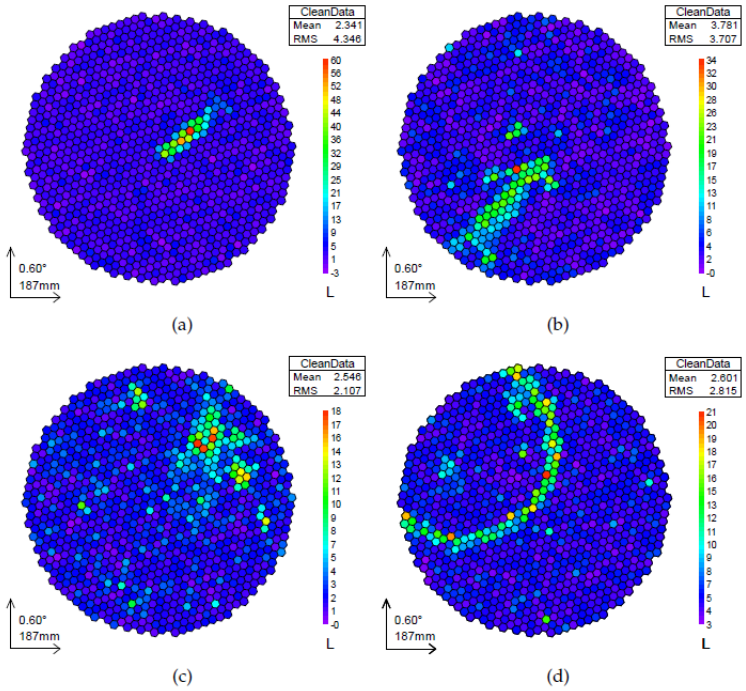

Figure 3.9: Three types of air-shower images observed with MAGIC: (a)γ-like, (b,c) hadron-, and (d) muon- induced recorded events/images with MAGIC (Image credit: [Fruck 2015])

In general, the Cherenkov radiation image of a γ-ray induced particle cascade has a compact elliptical shape. Its edges represent the head and tail of the particle shower, and the central part corresponds to the core of the shower. The major axis of the ellipse presents the projection of the shower axis onto the image plane. In contrast, compared to γ induced shower images, hadronic induced particle cascades exhibit a more complex structure. Three types of such hadron-, muon- and γ-induced recorded events/images with MAGIC are shown in 3.9. These visible differences in the image shape between electromagnetic and hadronic showers are used to select the γ-ray induced images from hadronic ones.

Therefore, pixelization of the camera holds significant importance, as camera pixels with a small field of view improve reconstruction of the shower arrival direction. Also, after the shower images are either marked as γ like events or background, which is referred to as γ/hadron separation (see section 3.6.1.7 for more details), night sky background rejection and γ/hadron separation can be improved with finer camera pixels. For example, the orientation of the shower ellipse with respect to the camera

center is one of the selection criteria. In case of a γ-ray source, it is expected that shower images with the orientation of main axis points towards the direction of the source in the camera, whereas hadronic induced shower images show a random orientation.

Stereoscopic configuration

Observations are carried out by more than one IACTs, i.e., in 'stereoscopic' configuration, where the same shower event is seen from different angles (see figure 3.8). It achieves an improved background rejection at the trigger level by the selection of coincident events, which results in lowering the energy threshold. In addition, a stereoscopic system provides a better angular resolution, accurate reconstruction of the arrival direction of the primary particle and also an improvement in energy estimation. Another important factor to be considered in the stereoscopic configuration is the distance between several IACTs has to be optimized in a such a way that at least two IACTs provide observations of the same Cherenkov light pool, and also assuring at the same time different viewing angles of the same shower. The distance between several IACTs in a stereoscopic configuration has to be optimized such that at least two IACTs provide observations of the same Cherenkov light pool and guaranteeing at the same time different viewing angles of the same shower. In general, the larger the distance of the telescopes within the Cherenkov light the better the stereoscopic view of the event. With increasing distance between the IACTS reduces the effective area. However, the effective area increases with the close spacing of the telescopes, but at the cost of a less accurate reconstruction of the shower core. Therefore, it is a compromise between the telescope spacing and effective area.

IACTs in the world

The Whipple 10 m γ rays telescopes and the High Energy Gamma-Ray Astronomy (HEGRA) telescope are the pioneer Cherenkov telescopes. Current generations of IACTs include stereoscopic configurations of MAGIC, H.E.S.S., VERITAS (shown in figure 3.10) , which are situated in La Palma (Canary Islands), Namibia (Africa), and Arizona (USA) respectively.

All these telescopes around the globe possess different design and configurations of different properties. The MAGIC telescopes are composed of two 17 m diameter Cherenkov telescopes with an energy threshold of 50 GeV and a camera FoV of 3.5° [Colin et al. 2009, Cortina et al. 2010]. However, H.E.S.S. and VERITAS are both arrays of four 12 m diameter telescopes (both arrays show different configurations), each with an energy threshold of 100 GeV and a camera FoV of 5° and 3.5° respectively [Vasileiadia et al. 2005, Holder 2007]. In 2012, the H.E.S.S. experiment inaugurated the new 28 m diameter H.E.S.S. II telescope in the center between the 4 existing telescopes. It has modified design with the aim of having energy threshold as low as 20 GeV. MAGIC and VERITAS are located in the northern hemisphere,

Figure 3.10: Location of the current generation IACTs: MAGIC, H.E.S.S., and VERITAS (Image credit: Prandini, E. `http://slideplayer.com/slide/8568821/`)

whereas the H.E.S.S. is situated in the southern hemisphere. H.E.S.S. telescope is well fitted for galactic plane observations due to its location and large FoV.

All these telescopes have conventional photomultiplier tube (PMT) based cameras. The First G-APD Cherenkov Telescope (FACT), is the first Cherenkov telescope that having the camera with novel photosensors such as Geiger-mode Avalanche Photodiodes (G-APDs). It consists of a single telescope with a mirror of 9.5 m^2 area and is situated next to the MAGIC telescopes. FACT is intended at monitoring bright AGNs in the TeV range. Due to new sensors, FACT has an additional benefit over other IACTs, i.e., it can operate under bright illumination giving the plausibility to extend the IACTs operation under strong moon conditions. However, FACT is less sensitive instrument compared to HESS, MAGIC, and VERITAS.

Recently, MAGIC, H.E.S.S, and VERITAS collaborations joined their efforts to build a new generation instrument and had started to work on a collaborative project for the next generation of IACT's development, known as Cherenkov Telescope Array (CTA). The current plan of CTA involves a giant array of ~ 120 Cherenkov telescopes of different sizes at two locations, one in the northern and one in the southern

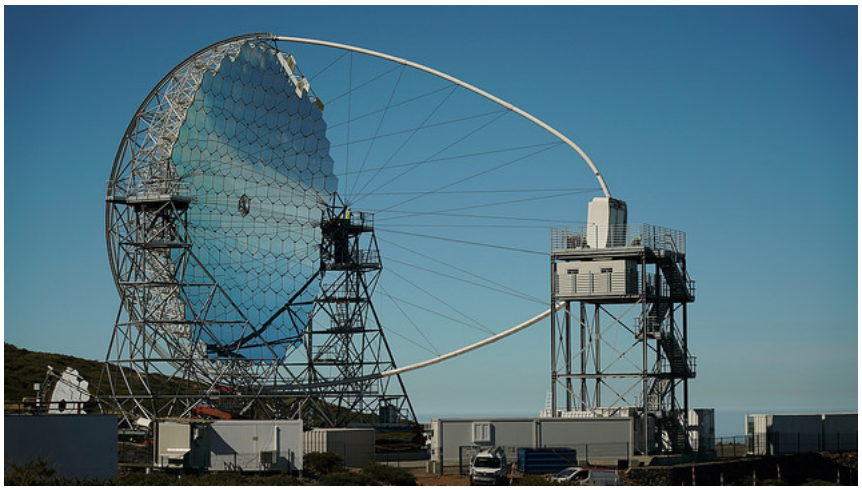

(a)

(b)

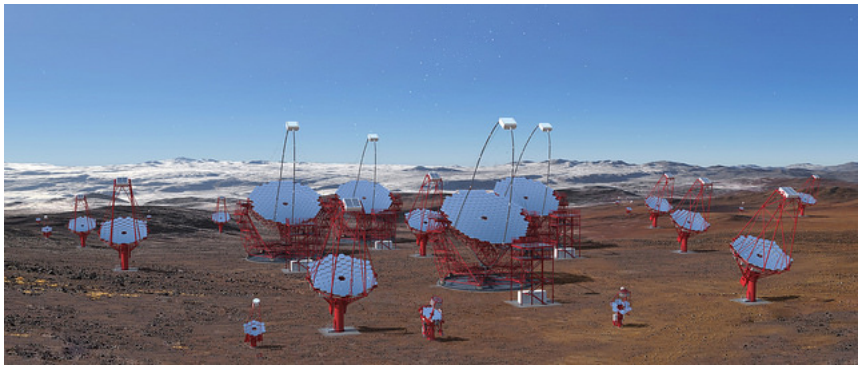

(c)

Figure 3.11: (a) LST Prototype, the LST-1 (Image Credit: Iván Jiménez. (b), (c) This is an artistic rendering of CTA's northern and southern hemisphere sites. These images also illustrate all three classes, i.e. LST, MST and SST. (Image credit: `https://www.cta-observatory.org/outreach-education/multimedia/images/`)

hemisphere (see figure 3.11). The proposed site for the southern location is at the Paranal Observatory (Chile), whereas, Roque de los Muchachos Observatory (Spain) has already been chosen for the northern site. The prototype for the Large-Sized Telescope has been already inaugurated on 10^{th} October 2018 (see figure 3.11a).

The summary of the individual CTA telescope types based on the principle design, and intensive MC simulations [Hassan et al. 2017], which balances costs as well as performance aiming to, is given below [CTA Consortium, 2018].

- CTA Northern Site: 4 Large-Sized Telescopes (LSTs) and 15 Medium-Sized Telescopes (MSTs) (area covered by the array of telescopes: ~ 0.6 km^2)
- CTA Southern Site: 4 LSTs, 25 MSTs and 70 small-Sized Telescopes (SSTs) (area covered by the array of telescopes: ~ 4 km^2)
- Individual CTA telescopes will have Cherenkov cameras with a wide field of view: $> 4.5°$ for the LSTs, $> 7°$ for MSTs and $> 8°$ for SSTs.
- The expected energy coverage for photons is from 20 GeV to at least 300 TeV, to give CTA reach to high-redshifts and extreme accelerators.

The principal purposes of CTA include the achievement of a low energy threshold of ~ 20 GeV and high sensitivity, which will be one order of magnitude better than the current generation of IACTs (see figure 3.12). With the improvement in performance and sensitivity, CTA will be dedicated to exploring the extent of our Universe in VHE γ rays, to investigate cosmic processes leading to relativistic particles. The key science projects of CTA will focus on the following topics:

- Understanding the origin and role of high energy particle accelerators in the Universe and their role in the star and galaxy formation.
- Probing extreme environments such as black holes and jets, neutron stars and relativistic outflows, and Cosmic voids to study the evolution of the extragalactic background light over time.
- Exploring frontiers in physics such as the nature of the dark matter, the possibility of a quantum gravitational effect on the photon propagation, the existence of the axion-like particle, the physics beyond the Standard Model.

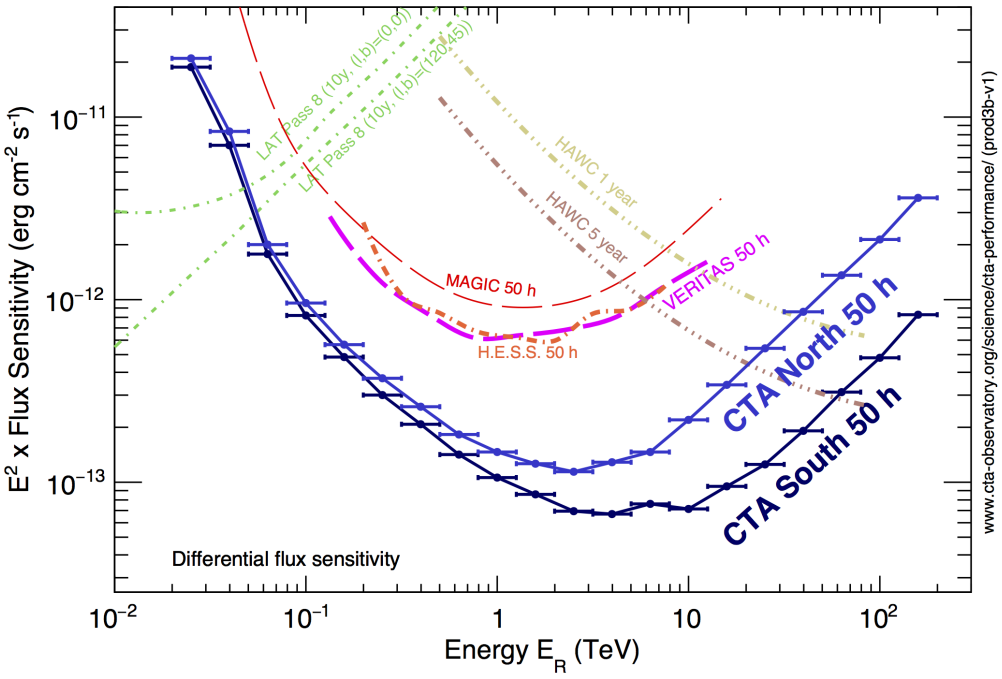

Figure 3.12: Comparison of the differentail sensitivities of CTA (south and north) to existing γ-ray instruments. Image Credit: `https://www.cta-observatory.org/science/cta-performance/#1472563157332-1ef9e83d-426c`

The MAGIC telescopes

The MAGIC telescopes or Florian Goebel MAGIC telescopes is a stereoscopic system of two 17-m diameter IACTs. They are hosted by the Observatorio Astrofisico del Roque de Los Muchachos (ORM) situated at the Roque de Los Muchachos, on the Canary island of La Palma (28.75°N, 17.86°W) at the height of 2200 m above sea level. MAGIC-I started operation in 2003, and MAGIC-II started operation in 2009, thus since the fall of 2009, MAGIC is a fully operative stereoscopic system of the largest Cherenkov telescopes in the world. A group of more than 150 people, among astronomers, physicists, and engineers, constitutes the MAGIC Collaboration. These people are working for the operation and maintenance of the telescope as well as the data analysis. In 2011, the readout electronics of both telescopes and in 2012, the camera of MAGIC-I were upgraded. The upgrade made both telescopes more similar to each other, the MAGIC-I camera better, and also the readouts/triggers for both telescopes better. One of the main key advantages of the upgrade was achieved low energy threshold of 50 GeV [Aleksić et al. 2012], which makes it possible to have better overlap to HE data with space telescopes like *Fermi*. Another achieved performance value with the new system is the integral sensitivity above 220 GeV

Figure 3.13: Picture of the two 17 m diameter MAGIC telescopes, with MAGIC-I on the left, MAGIC-II on the right, and counting house in the middle. (Image courtesy: R. Wagner)

in 50 hours achieved is of (0.66 ± 0.03)% of the Crab Nebula flux at low zenith angles [Aleksić et al. 2016a]. In the following sections, details about the MAGIC subsystems, the performance of the system, data taking and data analysis are given.

MAGIC subsystems

Structure and drive system

The MAGIC telescopes are composed of two 17 m diameter parabolic dishes, which are separated by a distance of 80 m, and with Alt-Az mount of single facet mirrors. The telescope dish and structure consist of light weight ($\sim$ 5 tons) carbon tubes and steel tubes respectively, which are joined by aluminum knots (see figure 3.14).

In addition to strength, the main advantage of light weight material is enabling fast repositioning of the telescope in any direction of the sky for quick response to the GRB observations within 20 - 30 seconds [Lorenz 2004]. Other advantages include resistance to hard atmospheric conditions at the site, such as temperature variations during summer and winter, high wind, rain, and snow. Telescopes are moved by 11 kW electric motors; two on the azimuthal axis and one on elevation

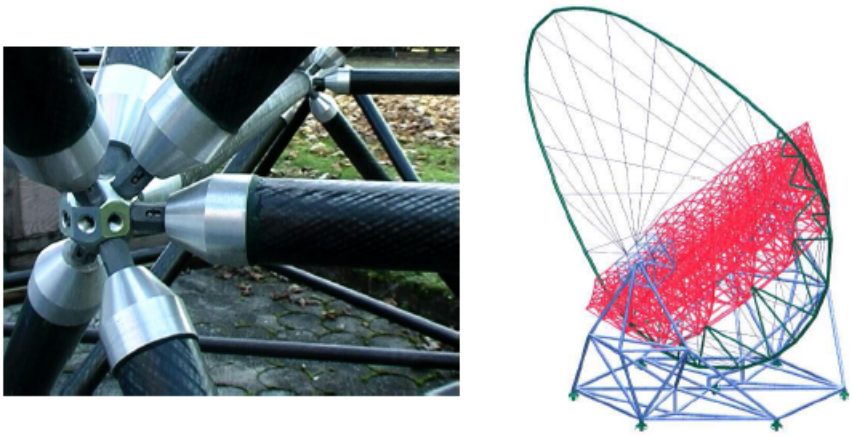

Figure 3.14: (left): Aluminum knot junction between carbon tubes used in the MAGIC telescope frame, and (right): a general scheme of the MAGIC frame. (Image credit: [Tescaro 2010])

axis [Lorenz 2004] (see figure 3.15). The camera is mounted on a vertical Aluminum arch, which is stabilized by ten pairs of steel cables fastened to the main frame. This arch supports the camera against the horizontal oscillation caused by steel cables, and its circular shape continues over the back of the dish becoming support for the counter weights and rail for the altitude drive. It allows the telescope to move from 0 to 90% in the zenith angle. The whole structure is connected to a circular rail by six bogeys, which enable the azimuth movement in −90% to +318%. Two absolute shaft encoder continuously monitors the position of the two telescope axes, which makes tracking of the source with a precision of 0.02% during the regular observations. The positioning of the telescope is continuously monitored with a CCD camera (called as the star-guider camera) mounted on the center of the mirror dish performs the calibration between shaft encoder values and real pointing coordinates. The highest repositioning time of the telescope is about 100 s, however, in the case of GRB alert, the repositioning time is set to 30 s.

Mirrors and reflectors

A three-layer frame octagonal shaped mirrors $f_{(focal\ length)}/D_{(diameter)} = 1$ are mounted on the support structure of carbon tubes. The overall parabolic shape including the spherical mirror facets of different radii of curvature measures as 964 $0.5 \times 0.5\,\mathrm{m}^2$ for MAGIC-I and 247 $1 \times 1\,\mathrm{m}^2$ for MAGIC-II [Kellermann 2011]. Due to the isochronous surface of the parabolic reflector, on the camera plane, relative arrival times of the photons are conserved. Therefore, the parabolic shape of the mirrors provides better imaging quality for timing resolution, which is an important quality required for IACT observations and is preferred over optical resolution. To keep the constant

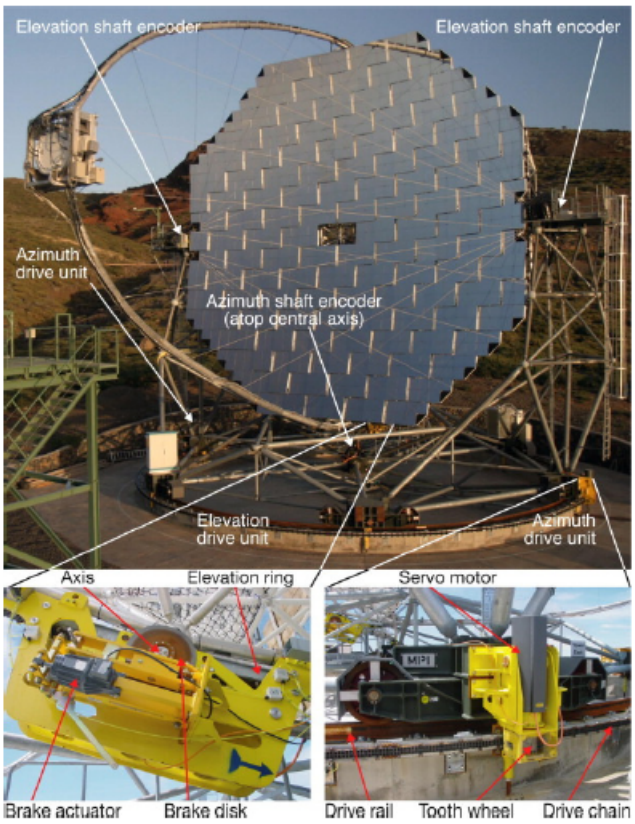

Figure 3.15: Elements of the MAGIC drive system. Top: The major elements of the drive system installed at the MAGIC-I telescope are shown. Bottom: The elevation drive (left) and the azimuth bogeys (right) (Image credit: [Schultz 2013])

minimum point spread function (PSF) of the reflector, single mirrors of MAGIC-II and 2×2 facets of MAGIC-I are individually adjustable. Depending on the orientation of the telescope, their mirrors are adjusted by an Active Mirror Control (AMC) system. During observations, this information about the adjustment of mirrors is provided by the Look-up tables [Biland et al. 2008]. The position of panels is corrected online, to position the light emitted by lasers situated in the center of each panel correctly on the camera plane.

Camera

The camera in MAGIC telescopes is one of the most important and critical system as well as a major factor in gamma sensitivity, energy threshold and γ-hadron separation, as these factors, greatly depend on the quality of shower images (see figure 3.17). In summer of 2012, MAGIC-I camera upgraded to a more finely pixelized one. Since the upgrade, MAGIC-I and MAGIC-II cameras are equipped with clusters of 1039 photomultiplier tubes (PMTs) each [Sitarek et al. 2013a].

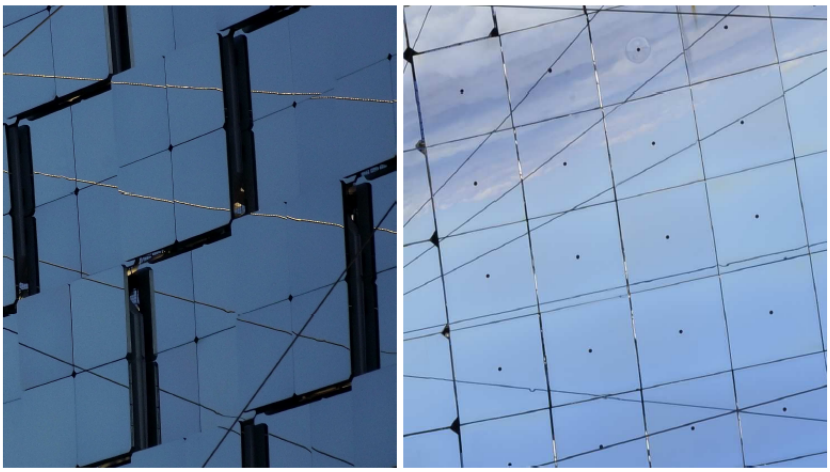

Figure 3.16: (left): MAGIC-I with each mirror of size $0.5 \times 0.5\,\mathrm{m}^2$, (right): MAGIC-II with each mirror of size $1 \times 1\,\mathrm{m}^2$ (Image credit: [González 2015])

Figure 3.17: Picture of MAGIC-II camera; (left): front view, (right): rear view. After the upgrade, MAGIC-I camera has the same design as MAGIC-II. (Image credit: [González 2015])

These PMTs convert the air shower Cherenkov photons into electrical signals. The distinctiveness of MAGIC is that after the light signal is converted to the electrical ones, the signals are preamplified and then converted back to light (through VCSELs) and sent to the counting-house in an analog way (novel technique) through $\sim$165m optical cables. The readout electronics inside the counting-house converts light signals back to electrical ones by means of pin-diodes in the receiver boards and split into two branches: trigger branch (see section 3.5.1.4) and the readout branch (see section 3.5.1.5). Depending on wavelength, these PMTs in both cameras have a quantum efficiency (QE) of 20-30%. Due to the upgrade of MAGIC-I camera, the area of trigger region increased by a factor of 1.7. It covers innermost 2.5° diameter

region, which is 70% larger than the pre-upgrade trigger region [Sitarek et al. 2013a]. In both telescope's camera configuration, Winston cones are used as light concentrators for PMTs operations, which are hexagonal and optimized for collecting light only from the solid angle occupied by the mirror [Aleksić et al. 2016a]. The field of view of the cameras is 3.5°. The angular diameter mapped onto a pixel is about 0.1° [Tridon et al. 2010].

Trigger

The standard trigger system of MAGIC telescopes is a multilevel decisional system. The trigger logic is based on the digital coincidence of N next-neighbor (NN) pixels, in which, each needs to pass a certain trigger threshold simultaneously to acquire an event in time coincidence with an EAS as well as to reject the storage of background events. Most of the time, PMTs are hit by photons of NSB, however, in rare events, those belong to Cherenkov radiation by EAS. This light from Cherenkov radiation is typically much more intense than NSB events and illuminates several pixels at the same time and produces a compact shower image for a short duration in the Camera. Thus, based on the topological and temporal structure of the shower image, a simple trigger logic has been developed to recognize the adjacent triggered or NN pixels to detect the signal originating from Cherenkov light and determine its acquisition. The trigger region in the upgraded MAGIC-I camera and MAGIC-II camera covers the 547 inner pixels [Aleksić et al. 2016a]. Although the trigger region is restricted to inner camera region, the entire FoV could be utilized, as shower images covering the edge of the camera along with the inner part can also trigger the events. To study the extended sources as well as the performance of the sky, this enlargement provides higher potential.

To operate trigger in the stereo mode, a coincidence of events from both telescopes is required. Currently, there are three basic types of trigger systems used in MAGIC telescopes; L0, L1, and L3.

- **L0:** First layer of the threshold is based on the discriminator threshold (DT), which is adjusted for each pixel automatically within the trigger region by the Individual Pixel Rate Control (IPRC). If the pixel's signal reaches the threshold, receiver board generates a ~ 4 ns duration effective width digital trigger for each channel and then it is sent to the next trigger level. L0 trigger is useful for avoiding accidental triggers in case of a bright star gets inside the FoV.

- **L1:** The next stage trigger is based on the next-neighbor trigger logic. In this, the next neighbors are the closely packed groups of N number of pixels, such as 2NN, 3NN, 4NN, and 5NN, which passes the L0 trigger. Once the cluster of the pixels is determined, it passes the signal to the next level trigger. However, at the beginning of every observation, it is possible to select only one pattern logic at a time [Aleksić et al. 2016a].

- **L3:** Last step in this process is the stereo L3 trigger. In this, to adjust the coincidence pattern on pixels and the time difference between incident light flashes on both telescopes, it is important to take into account the geometric orientation of the telescopes. The trigger gate is about 180ns in which coincident signals are accepted. One can make it smaller by another factor of 2 which would reduce the accidental triggers by the same factor. However, reducing the coincidence window increases the possibility of mis-adjustment and therefore missing gamma events. In this mode, all the events triggered by only one of the telescope are rejected. An event is finally recorded when all three trigger conditions are fulfilled.

Recently, more advanced additional analog trigger system known as 'sum-trigger' has been installed in MAGIC. The main advantage of sum-trigger is having lower energy threshold ($\sim 30\,\mathrm{GeV}$) and higher sensitivity for lower energies ($\mathrm{E} < 200\,\mathrm{GeV}$) [García et al. 2014] with its associated scientific outcome for MAGIC, as it allows even fainter events to trigger. The working principle of this trigger is, the actual signal from cosmic event distributes over several pixels and propagates linearly. However, the random noise propagates with the square-root of the analogically summed up the number of channels. In this trigger, always patches of 19 pixels are summed up and checked with the discriminator threshold. As this mechanism is very similar to the L1 trigger, sum trigger could replace it completely [Haefner 2011, Haefner et al. 2012].

Readout

In the first upgrade stage in 2011, the core element of MAGIC readout system has been upgraded to a digitizer system based on Domino Ring Sampler version 4 (DRS-4) chip instead of DRS-2 [Sitarek et al. 2013]. The DRS-4 chip consist of a switched capacitor array which can store 1024 samples of the waveform and the sampling speed of its operation is 0.7 to 5GHz. However, for MAGIC, the sampling speed of 1.64 G-Samples/s with a buffer length of 624 ns is being used, which is needed for the L3 buffer to make a coincidence between the two telescopes at every Zd and Az combination. Once a trigger occurs, an ADC of 14 bit precision and speed of 32 MHz charges the capacitors and sampling get stopped at this moment. Then the event is stored from a 30 ns long particular region of interest where an actual signal is expected. The real readout process happens at lower frequencies. Also, for each event, it generates deadtime of 30 ns. However, due to the upgrade, the dead time is significantly reduced to less than 1% [Tescaro et al. 2012].

Calibration system

The calibration box of the MAGIC telescopes is installed at approximately the center of the mirror dish, i.e., $\sim$17m away from the camera plane. The calibration is performed via the uniform illumination of the PMT camera with well-characterized light

pulses of different intensity produced by the calibration box. After the upgrade, both MAGIC-I and II calibration boxes are based on a system with a passively Q-switched Nd:YAG laser (third harmonics, with a wavelength of 355 nm) that produces pulses of 0.4 ns FWHM. The adjustment of light intensity is made possible through the selection of a calibrated optical filter. Here the uniformity is achieved by means of an Ulbricht sphere[d] that diffuses the light right before the exit window. After the Ulbricht sphere, the laser pulse has an FWHM of ~ 1 ns, which is comparable to the time spread of the photons in the Cherenkov shower [Aliu et al. 2009]. Before performing observation for any new source, a calibration runs consisting of 2000 events at a fixed light intensity is taken [Aleksić et al. 2016a].

In the second step, absolute calibration is performed using the F-Factor method, which relies on the knowledge of the added noise of the PMT [Mirzoyan 1997]. The F-Factor is a numerical value which accounts for the noise introduced by the readout and amplification chain and assumes that those are independent of the signal intensity. The calibration system is used to achieve the conversion factors between the input (number of phe produced in the photocathode and collected by the first dynode of the PMTs) and output measured by the number of ADC counts from the digitized signal via the F-factor method. [Aleksić et al. 2016a].

As presently both telescopes are using a readout based on DRS4, the calibration light pulses are also used to cross-calibrate the analog arrival times in the DRS4 channels, which are different channel by channel (due to variations in propagation time between the DRS4 chip and the focal plane) and it depends on the position of trigger signal in the DRS4 ring buffer [Sitarek et al. 2013]. In addition, during data taking the calibration laser performs the interleaved calibration events constantly at 25 Hz, which helps to monitor the gain of the readout chain of the individual channels. The calibration system is also useful for the fine tuning of the trigger signal delays.

Observation modes

Observations with MAGIC are performed only during the night due to great backgrounds like the Sun. However, during the night also dominating background such as the Moon exists. The ideal observation or data taking condition include the dark or moonless night. However, due to recent advancement in the MAGIC electronics and usage of different UV-filters enabled the data taking also during twilight as well as the presence of moderate to strong moonlight conditions. Data taking during the full moon or very strong moonlight conditions is still not possible. Other challenges in data taking which decreases the data quality include bad weather, high wind, calima[e], high humidity, and a presence of clouds. Since the upgrade, to improve the image resolution and to increase the FoV, a stereo mode is used as the standard

[d] An Ulbricht sphere also knowns as the integrating sphere, is an optical device, which is used for measuring the transmissivity or reflectivity of the optical components such as laser diode.

[e] A dust wind originating from the Sahara

mode of data taking, in which observations are performed with both telescopes simultaneously. However, MAGIC telescopes can work separately in mono mode also. The observations can be carried out in one of these two different modes of operation; the On/Off mode or the wobble mode [Fomin et al. 1994]. Choosing the right observation mode is important, as it affects the estimation of the background signal.

- **On/Off mode:** It is usually called the tracking mode. In this mode, On and OFF data are separately taken. During On mode, both telescopes point directly towards the source. So, the camera center of each telescope contains the nominal position of the source. To estimate the background, data is taken in OFF mode, in which telescopes are pointed towards some other region of the sky where no known γ-ray source is in the FoV. It is also important to maintain similar observation conditions as ON mode such as zenith distance, NSB level, and weather conditions. The main disadvantage of such observation mode is a significant reduction of actual source observations time, as extra dedicated time is required to perform the OFF mode observations.

- **Wobble mode:** To efficiently use the available time, most of the observations with MAGIC are performed in wobble mode [Fomin et al. 1994]. In this mode, two or four positions in the sky separated by an offset of 0.4° from the source position are alternatively tracked by the telescopes. The Off data in this mode is taken from the counter source position. Therefore, the background estimation is done using the same field of observations, which saves a significant amount of actual source observations time, as no need of taking OFF data extra. If a γ-ray source is positioned far from the camera center (more than 0.4°), it is still possible to define the OFF regions in the same FoV not affected by the source. In a case of only two alternating positions are used for wobbling, the off region will be the counter source position situated with a rotation angle of 180°. During data taking, wobbling of directions happens for every $\sim$20 minutes, in order to avoid the possible camera inhomogeneities and also to provide a more reliable calculation of Off at lower energies. Despite the efficient source observation time saving, the disadvantage of wobble mode is a reduced trigger efficiency (10-20% of γ rays are outside of trigger region due to a displacement of the source position).

Performance of MAGIC telescopes

In the field of IACTs, determining the energy threshold of the analysis is not a straightforward work. One usually needs to rely on the Monte Carlo simulations provided that they represent the data correctly. The energy threshold can be defined as the peak in the distribution of events detected which are binned in energy. To get this value, an energy spectrum of a hypothetical source (similar to a real potential source) is used in MC simulations to determine the position of the peak of the Gaussian distribution after applying the cuts.

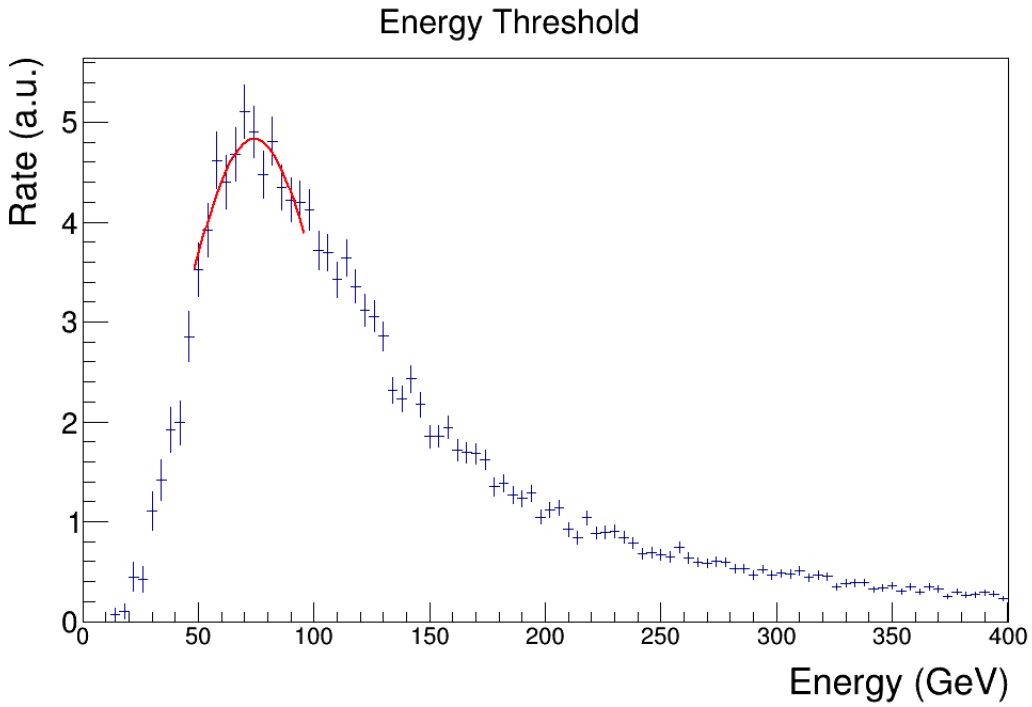

Figure 3.18: The rate of MC γ-ray events (in arbitrary units) that are surviving the image cleaning, for a source with a spectral index of -2.6 and with at least 50 phe. The red line shows the peak of the narrow region of the 2D Gaussian distribution.

Usually, for γ-ray sources, a spectrum can be fitted with a power law with spectral indices between -2 and -4, this peak defines the low energy threshold for the γ-ray detectability. Figure 3.18 shows a histogram to detect the energy threshold for MAGIC. Here, a spectrum similar to Crab is used with a spectral index of -2.6 in the zenith angle of 5° to 50°. The energy threshold obtained from this example is ~ 74 GeV for zenith angle $< 50°$. This threshold value is determined by fitting a Gaussian distribution around the narrow region around the peak as shown in red. The energy threshold of the analysis can be approximated by an empirical formula $74 \times cos(zenith\_angle)^{-2.3}$ GeV. It is stable for low zenith angle observations; however, it increases for higher zenith angles due to absorption of Cherenkov light in the atmosphere. The trigger threshold is computed from all the events that triggered both telescopes, which is ~ 50 GeV at low zenith angles, naturally, the lowest one [Aleksić et al. 2016b].

Two methods can calculate the angular resolution or point spread function (PSF) for MAGIC telescopes. In the first method, the angular resolution is defined as the standard deviation of the 2D Gaussian fit for the distribution of reconstructed events in the direction of γ-ray excess [Aleksić et al. 2016b] (shown in figure 3.19a). This method is useful when looking for a small extension in VHE γ-ray sources. In the second method, angular distance is calculated which encircles 68% of the excess

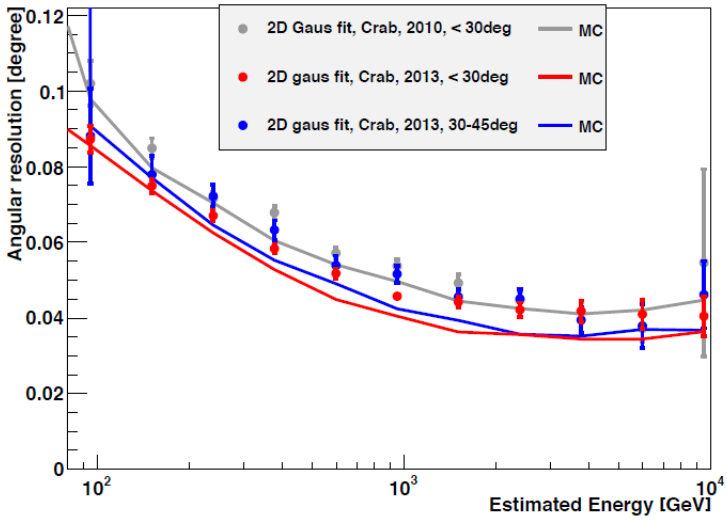

(a)

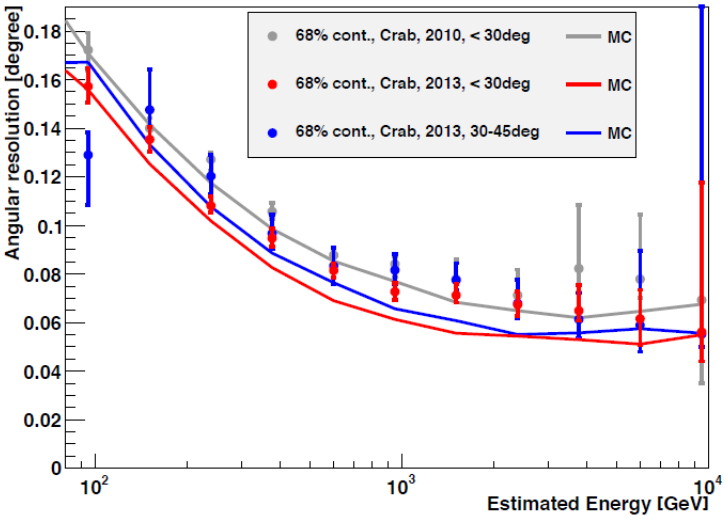

(b)

Figure 3.19: Angular resolution of the MAGIC telescope system after the upgrade, which depends on the estimated energy. The PSF has been defined from Crab nebula observations (datapoints) and MC (lines) by fitting; (a): a 2D Gaussian fit, (b): 68% containment radius. (Image credit: [Aleksić et al. 2016b])

events around the source (shown in figure 3.19b).

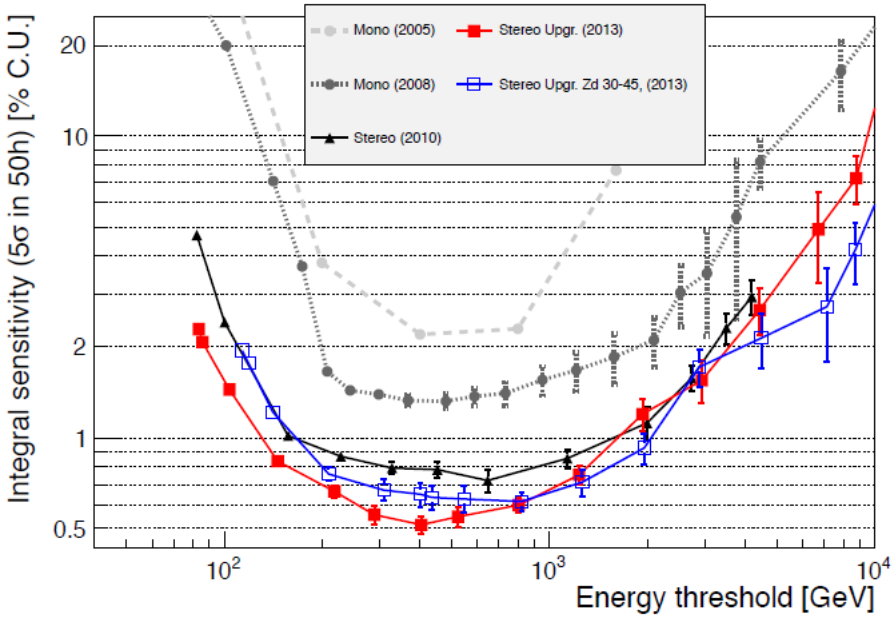

Figure 3.20: Evolution of integral sensitivity of the MAGIC telescopes, red and blue shows after the upgrade in 2012, and black and gray are shown for earlier development stages. The Sensitivity is given in terms of an integral flux in units of the Crab Nebula flux. It needs to reach a $5\,\sigma$ detection within 50 hours. (Image credit: [Aleksić et al. 2016b])

During MAGIC performance study, the PSF of MAGIC was studied using MC simulations and verified on a Crab data sample. From a 2D Gaussian fit at 250 GeV, the angular resolution is 0.07° with the systematic uncertainty of 0.02° on the reconstructed source position [Aleksić et al. 2016b]. However, it improves with energy and reaches to 0.04° for energies above few TeVs. The energy resolution is defined as the RMS value obtained from a Gaussian fit of the relation $(E_{est} - E_{true})/E_{true}$. The bias of this method is estimated in terms of the mean value of the distribution. The energy resolution of MAGIC telescopes ranges between 15% and 20% on a relative scale, and it depends on the observed energy.

In ground-based γ-ray astronomy, the sensitivity S is computed as the source flux exceeding the 5σ detection after the effective observation time of 50 hours. In the equation below, N_{ex} are the number excess events, and N_{off} are the estimated background events in the signal region, T is the effective observation time.

$$S(50hr) = \frac{N_{ex}}{\sqrt{N_{off}}} 50\sqrt{T} \tag{3.12}$$

The integral sensitivity for IACTs is usually stated in the units of Crab Nebula flux, which is a minimum fraction of Crab nebula flux needed to detect the source in 50 hours with 5σ level significance. The integral sensitivity curves from 2005 to recent upgrade of MAGIC are shown in figure 3.20 [Aleksić et al. 2016b]. As discussed in [Aleksić et al. 2016b], in 50 hours of observations the integral sensitivity reaches to 0.55% of C.U. around a few hundred GeV. Since the upgrade of the MAGIC-I camera and readout of both the MAGIC telescopes have to lead to a notable improvement in sensitivity in the whole range, however, the performance improvement is significantly visible at lowest energy. Especially, in the energy bin of 60 - 100 GeV, the differential sensitivity has dropped from 10.5% C.U. to 6.7% C.U. It reduces the observation time needed to detect the source by a factor of 2.5. Therefore, the value of energy threshold, angular and energy resolution, and integral sensitivity clearly makes the MAGIC telescopes an excellent instrument for γ-ray observations.

Systematic Uncertainties

IACT is a complex system. There are many factors which cannot only be estimated in their precision and thus contributing to the systematic uncertainty of the measurement. Among all, the most important factor is the systematic errors of the γ-ray collection efficiency. It is the error on the absolute flux level, absolute light scale, and the reconstructed spectral slope [Aleksić et al. 2012]. The important elements contributing to the systematic errors affect the various subsystems of an IACT, as well as imperfections of MC simulations concerning the atmospheric conditions, which eventually affects the precision of the energy reconstruction due to inconsistencies between real data and simulated γ-ray events. Therefore, an estimation is then performed on these leading sources of uncertainties affecting the energy scale, the flux normalization, and the spectral slope. For MAGIC, a combined systematic error has been summed up in quadrature from the systematic uncertainties from each subsystem. As discussed in [Albert et al. 2008a], at low and medium energies, MAGIC determines the energy scale with a precision of 17% to 15% respectively. The systematic error on the spectral slope measurement is ± 0.15. At lower and medium energies, the flux normalization is affected by a systematic error of 19% and 11% respectively.

MAGIC data analysis

Once the observations have been performed, and the data are stored, the key role of the MAGIC data analysis begins to separate the γ rays from hadron-like events and also to determine the direction and energy of the primary γ rays. The software used by MAGIC collaboration to perform the data analysis is called as 'MARS'. It is written in C++ inserted in the framework of ROOT libraries from the CERN data analysis framework and its C++ interpreter CINT [Brun & Rademakers 1997].

MARS is composed of several sets of executives and macros, which will be described in the following sections (see figure 3.21). In this work, there are two types of MAGIC analyses performed; standard analysis on the dark or twilight time data and non-standard moon adapted analysis on the data with the presence of moderate to strong moonlight (discussed in section 3.6.2).

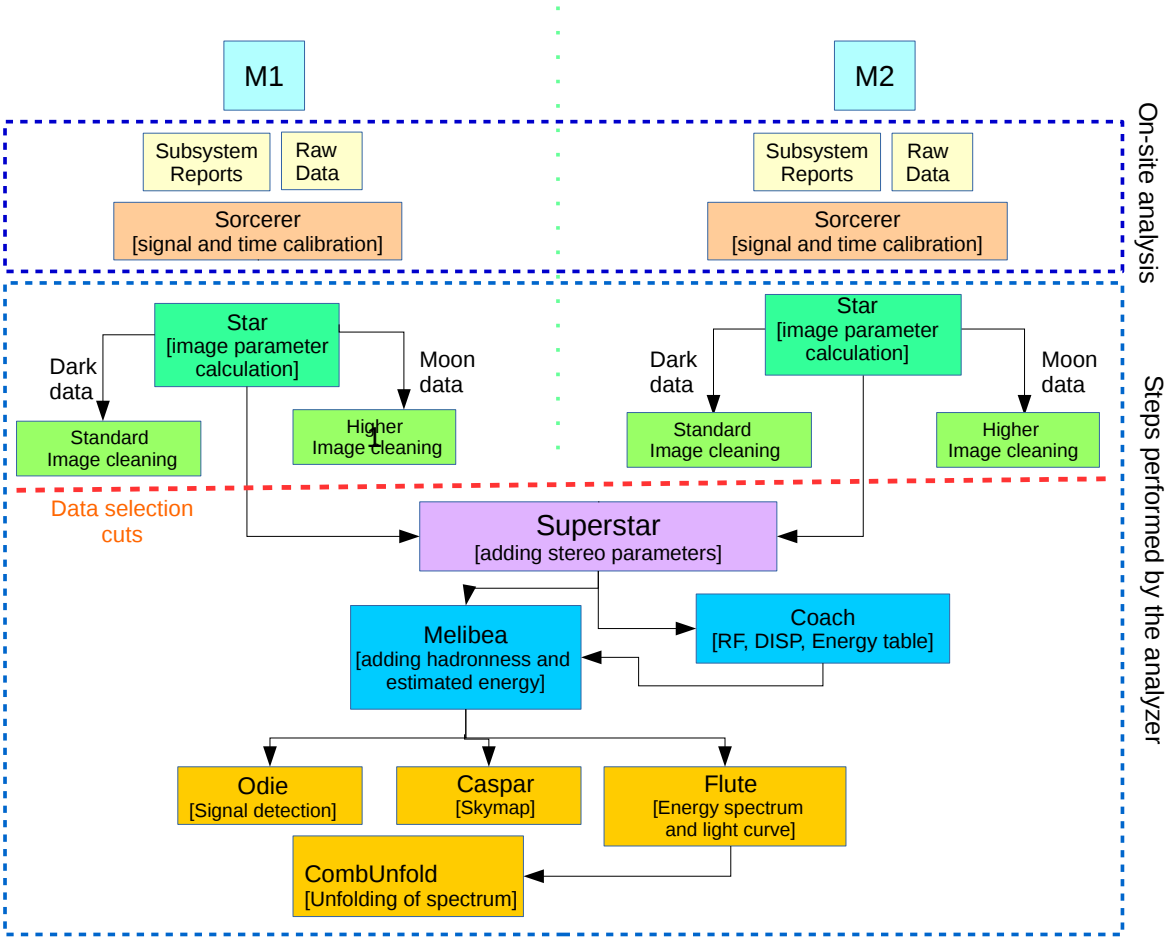

Figure 3.21: Schematic for the MARS stereo analysis chain for the data taken with MAGIC telescopes based on [Zanin et al. 2013].

Standard analysis

Most of the data with MAGIC is taken during dark night conditions, in order to have less NSB fluctuations, to achieve lowest possible energy threshold and also to save the life of sensitive PMTs from excessive light illumination from the moon. These data takings do not include observations during moonlight condition. In the following sections, the standard MAGIC data analysis procedure and tools with

MARS [Zanin et al. 2013] are explained step by step.

Calibration

In the beginning, the raw data files are converted to ROOT compatible format using MARS. In this process, information regarding subsystem performance and observation conditions are added to these files. As the first step in the analysis, Calibration is usually done automatically either on-site or at a data center by using MARS routine "Sorcerer". The MAGIC telescopes record each event triggered by the atmospheric shower, which consists of the waveform span of 30 ns observed in each of the pixels. The purpose of the calibration of the data is to obtain two pieces of information for each pixel in each of these events: charge measured in photoelectrons (phe) and time at which this signal arrived. Then the output of this conversion will be stored in the ROOT file format. The signal extraction is performed from the recorded data after merging. Presently both telescopes are using a readout based on the DRS4 chip [Sitarek et al. 2013]. The data acquisition system (DAQ) stores information in DRS4. On average, one phe produces a signal of the order of ~ 100 integrated readout counts, and the signal of each pixel is recorded into a 30 ns waveform.

The conversion of phe from integrated readout counts is done using the F-Factor (excess noise factor) method [Mirzoyan 1997], which is based on the fact that a PMT adds only a little extra noise to the intrinsic fluctuations of the phe flux. The F-factor method works as follows: the charge of a triggered event which is collected by each PMT is calibrated, and then it is converted to the number of phe [Mirzoyan 1997]. These calibration events follow Poisson-like distribution (e.g., a pulsed laser), i.e., the distribution of the phe has a mean value of N phe, and a root mean square (RMS) of $\sqrt{N}$. The pedestal subtracted signal charge is parametrized by its mean charge $\langle$Q$\rangle$ and RMS of σ. As the measured charge distribution is usually wider than the pure Poisson distribution, the difference in the widths is compensated by implementing the F-Factor method as:

$$F \cdot \frac{1}{\sqrt{N}} = \frac{\sigma}{\langle Q \rangle} \tag{3.13}$$

Here, $\langle Q \rangle$ is the mean value, σ is the RMS of the output charge of the PMT, and F is the F-factor. The conversion factor C depends on F^2 as:

$$C = \frac{N}{\langle Q \rangle} = F^2 \frac{\langle Q \rangle}{\sigma^2} \tag{3.14}$$

Image cleaning

Next important step in the analysis is image cleaning. The purpose of image cleaning is to remove the pixels containing noise and then calculate the image parameters

using the survived pixels. In standard analysis, image cleaning is usually done automatically either on-site or at a data center by using MARS routine 'Star'. It is performed on the calibrated data, which contains signal information regarding the arrival time of each camera pixel and a number of phe to reject the diffuse background in each shower image. This task needs to be done carefully due to fading away Cherenkov light on the shower image edge, which depends on signal intensity as well as image cropping (due to the removal of pixels), which results in drastic reduction of dimensions of the data files. This helps in saving data storage space and further analyzing time. To perform image cleaning combination of the two essential signal information is required, i.e., the timing information and the signal intensity (see figure 3.22).

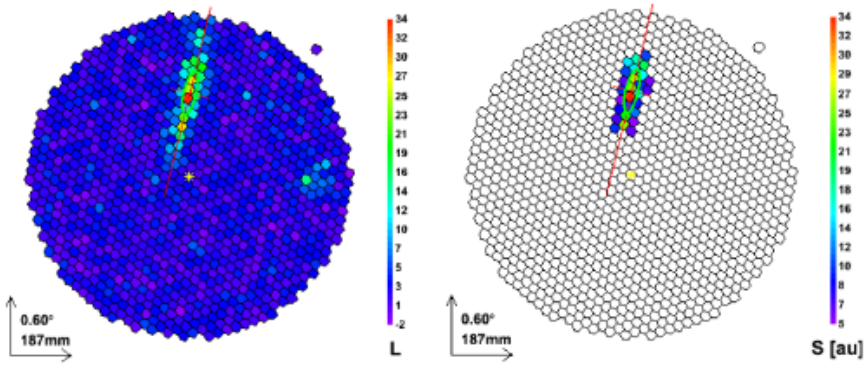

Figure 3.22: Example of image cleaning with actual shower image of MAGIC-II camera: (a) reconstructed charges, and (b) cleaned image using 6-3.5 standard cleaning. The shower image is superimposed with the Hillas ellipse parameterization. (Image credit: [González 2015])

For image cleaning, the 'absolute' cleaning is most commonly used. The cleaning algorithm is based on two different threshold levels concerning phe to determine core and boundary pixels. The higher threshold is set for the core pixels with minimum criteria of two neighboring pixels exceeding this threshold. When the charge of the pixel exceeds this minimum threshold criterion and also one of its neighboring pixels are considered to be part of the core, then the pixel is allocated as boundary pixel. These threshold settings are depending on the absolute number of phe recorded by each pixel, where the lower one is typically half of the higher one. Therefore, for all image pixels those exceeds the higher threshold, all its neighboring pixels have to fulfill lower threshold only, and remaining pixels are discarded.

As mentioned before, along with signal intensity, timing information will be al-

located to each extracted event as a number of time slices to further constraint the core and boundary pixels [Aliu et al. 2009]. As a contrast to absolute cleaning, in 'sum' cleaning, all possible near neighbor combinations, i.e., 2NN, 3NN, and 4NN are summed up and also the amplitudes of the signal are clipped. When this sum is above charge threshold, then only pixels belonging to the summed group are assigned as core pixels (within a given time window). The clipping is applied to make sure that the summed signal will not get overshadowed by PMT afterpulses or NSB fluctuations.

After the camera upgrade of MAGIC-I, the cleaning levels, i.e., level of the core to the boundary pixels have been fixed. The selection is based on a real compromise that produced comparatively reasonable results without worsening the shower image quality. As with more relaxed cuts, even though the analysis threshold gets lowered, the risk of adding noise regarding NSB to the shower image increases. Since the upgrade of MAGIC telescopes, an absolute cleaning level of 6 phe for the core pixels and 3.5 phe for the boundary pixels were applied for MAGIC-I and II. These cleaning levels are a compromise between performance and robustness optimized for any FoV, for extra-galactic or galactic sources, as well as under dark to dim moonlight conditions.

Image parametrization

The following final step performed by 'star' is the image parametrization with the Hillas parameters [Hillas 1985], which is implemented on the cleaned shower images. It is based on the information extracted from the shower images recorded by Cherenkov telescope cameras. In 1985, Hillas suggested fitting an ellipse to the shower image after removing the background from the light of night sky (LoNS) and draw the ellipse parameters such as size, width, two misaligned major axes, and the distance of the center of the ellipse to the source. From these parameters, it is possible to recover the information of primary particles regarding its direction, and energy as well as its nature, i.e., whether it is a γ-ray signal or hadronic background. A brief description of the Hillas parameters is given below, and a graphical description of this parametrization in mono mode is shown in the figure 3.23. For the further analysis, these parameters are entirely sufficient; therefore, to reduce the data size significantly, information which is not relevant for higher analysis is dismissed, for example, data from single pixels signal.

- **SIZE:** This parameter represents the total number of collected photoelectrons of an air shower measured with the PMTs. It depends on the energy of the primary γ-ray and the impact parameter, which is the possible distance of the primary γ-particle from the shower axis to the telescope axis.

- **WIDTH:** It is the half width of the minor axis of the ellipse of the shower image. It provides information on the lateral development of the shower. As

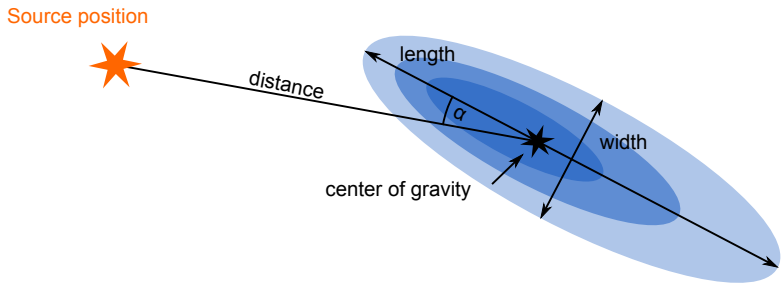

Figure 3.23: Illustration to explain the image parametrization scheme based on [Hillas 1985]. An ellipse is fitted to the shower image. To distinguish signal from background, parameters such as length, width, and the distance of the shower core from the source position or the angular miss-alignment of the major axis can be used. Image credit: [Fruck 2015]

compared to γ-ray shower, hadronic showers shows larger lateral momentum, therefore, this parameter plays a major role in background suppression.

- **LENGTH:** It is the half-length of the major axis of the ellipse of the shower image. It provides information on the longitudinal development of the shower.
- **DIST:** The distance from the camera center to the shower image center of gravity, which is associated with the impact parameter of the shower image and also provides information about the distance to the shower maximum. Therefore, it is a critical factor in calculating the energy reconstruction of the primary particle.
- **LEAKAGE:** This parameter is the fraction of the total signal contained in the outer pixels of the camera. It is one of the critical parameters as it allows to estimates the fraction of signal loss due to excessively large impact parameter, which allows the rejection of incorrectly parameterized images.
- **Time Gradient:** This parameter estimates the response of the arrival time changes along the major image axis.
- **Time RMS:** This parameter gives the value of the root mean square of the arrival times of all pixels belonging to the image after cleaning.

Stereo parametrization

Next step in the analysis is to combine the same events based on the L3 Trigger numbering from both telescopes that contain two different views of same shower image that survive image cleaning and data quality selection. The surviving events are paired to produce one file containing all necessary information and stereo parameters are calculated for a basic stereo reconstruction of the shower image using the MARS

routine 'Superstar'. This step is not applicable if data is taken in mono mode with only one telescope. In shower reconstructions, the image parameters are renamed including telescope number in the standard Hillas parameters and also the stereo parameters such as primary incoming direction, ground impact point w.r.t. two telescopes and the height of the shower maximum are calculated [Kohnle et al. 1996]. One of the advantages of stereoscopic reconstruction is the estimation of maximum shower height, which corresponds to the maximum of the shower from which a substantial amount of Cherenkov light is coming.

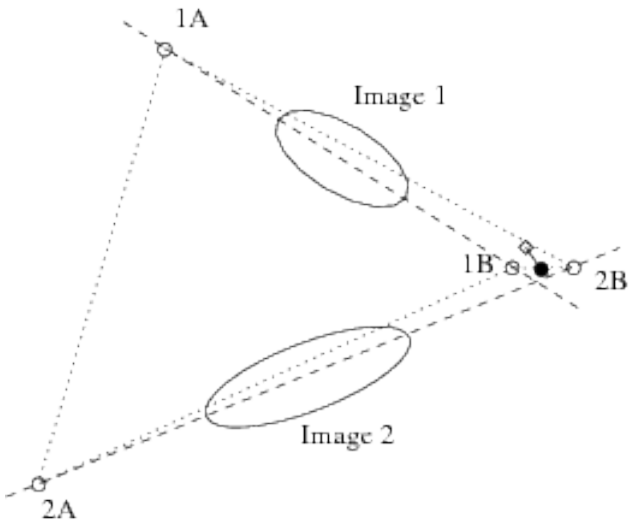

Figure 3.24: Principle of the Stereo DISP RF method. The main axes of the shower images are plotted with dashed lines. The two DISP RF reconstructed positions for each telescope (1A, 1B, 2A, 2B) are shown in empty circles. The 4 angular distances (1A-2A, 1B-2B, 1A-2B, and 1B-2A) are shown in dotted lines. The final reconstructed position is a weighted average of the two closest '1' and '2' points (the filled circle). The final true source position is marked with a diamond. Image credit: [Aleksić et al. 2016b]

For MAGIC analysis, the event-wise directional reconstruction of the incoming γ-ray is performed using the DISP RF method, where, for each telescope, the estimated distance is called as DISP, which is the distance between the image centroid and the reconstructed source position. As shown in figure 3.24, as the source position is considered to be on the line carrying the main axis of the Hillas ellipse, there are two possible solutions on either side of the image centroid. This method takes into account the timing information and image shape, especially, the time gradient measured along the main axis of the image [Aleksić et al. 2010].

In this method, we compute the 4 distances between the 2 reconstructed positions from each of the telescopes as shown by the dotted lines in figure 3.24. Then the pair is selected for which the reconstructed positions gives the smallest distance,

which in the given example is 1B-2B. As the estimation of the DISP parameter often gives inconsistent results for hadronic background events as it is trained with simulated γ rays. This provides an additional γ/hadron separation criterion. If for both telescopes, none of the four pairs give a similar arrival direction, the event is discarded. The DISP RF method explained above improves the reconstruction of the arrival direction as well as the estimation of other shower parameters.

Data selection

In standard analysis, analyzer performs analysis from this level onwards. Data selection is usually carried out over 'Star' files. The data at this level is arranged in sub-runs with 2 to 3 minutes of observations for each telescope. Sub-runs (> 10) form a data run for ~ 20 minutes of data. The advantage of doing the data selection at star level is that if a certain quantity in a sub-run does not pass quality criteria, the sub-run can be discarded without losing a whole run. However, this process is time-consuming as data selection needs to be performed separately for each telescope. In contrast to this, the data selection can also be performed at 'Superstar' level, where the data is already merged from both telescopes into files which correspond to one run (see section 3.6.1.4). This process is less time consuming as data selection can be performed on the stereo files. However, the whole run will be discarded in case if it does not passes the quality criteria. Therefore, in the analysis presented in this thesis, the data selection was preferred to perform at the Star level. Data quality selection is based on the following factors:

- **Weather:** Impact of bad weather is significant and unavoidable as it reduces the transparency of the atmosphere. In general, the factors considered under the bad weather are cloudiness (clouds in the sky and transparency of the atmosphere), high wind, and Calima (dust from the desert). The transparency of the atmosphere is based on sky clearness, so if more clouds or Calima are present, then it affects the data greatly. The effect can be seen in terms of dropping trigger rates, a number of stars detected in Starguider and cloudiness factor in the data files. High cloudiness makes the atmosphere less transparent leading to partial absorption of the Cherenkov light. Therefore energy correction from such data would be difficult in reconstructing the shower image. For the sources where low energy threshold is required, a total absence of clouds is necessary. However, for sources like AGNs, low cloudiness is bearable. A special device called 'pyrometer' is installed at the MAGIC site to measure the cloudiness and transparency of the atmosphere continuously. Cloudiness information is included in the data stream and is used as a quality cut during the data selection phase. Another technique to correct MAGIC data recorded during adverse weather conditions is using the information from the light detection and ranging (LIDAR) system. It is also installed at the MAGIC site and is operated alongside with the MAGIC telescopes.

- **Moonlight:** the Second factor which affects the data is a presence of moonlight, as it increases the background fluctuations. This effect can be seen regarding increased direct currents (DC) in the data. To correct the effect of moonlight, higher image cleaning is necessary to get rid of the spurious islands generated due to background fluctuations in the shower image. More details are given in section 3.6.2.1.

- **Hardware problems:** the third factor which affects data quality is potential hardware problems that might occur in the subsystems of telescopes. For example, camera reflector and especially reflectivity of the mirrors, which could distort the point spread function.

Monte Carlo production

Monte Carlo (MC) simulations play an essential role in MAGIC analysis, as MC γ-ray simulations determine the properties of the γ rays in our data. However, to describe the background we do not use MCs, we use the data itself. In these simulations, a large number of γ-induced air showers are simulated with CORSIKA program [Heck et al. 1998]. The detector simulation is split into two stages: Reflector and Camera, which include all the detection process with MAGIC and therefore play an essential role in the analysis. These detection processes include the simulations for air shower, the tracking of Cherenkov photons from the shower to the reflector and into the camera, the formation of shower images in the pixels of camera, the data acquisition, and the trigger. The tracking of Cherenkov photons and its conversion to signal waveform in each pixel is performed using the γ-ray tracking code 'Reflector' and camera simulation code 'Camera' respectively. After this process, events follow the further usual analysis chain of real data such as calibration, image cleaning, and parametrization. It is essential to update the MC simulations whenever there is a change in the hardware of the telescopes, as it could affect the detection process.

γ-hadron separation and energy estimation

Most of the events recorded by the MAGIC telescopes are cosmic γ rays showers, which mainly consist of hadronic origin. In the MAGIC analysis, from the reconstructed direction of the shower and image shape information, the rejection of the hadronic background is performed. The γ-hadron separation is performed using a machine learning algorithm called Random Forest (RF) [Breiman 2001, Albert et al. 2008]. It enables combining in a direct way, the image shape parameters, the stereo parameters and the timing of the shower into a single classification parameter called 'hadronness'.

Once the stereo-parametrization of data is performed, the MC simulations are divided into statistically independent samples: the training and the test sample, from the same hardware period and in the same zenith, azimuth and NSB conditions matching with the data. The training sample is used in the production of RF

algorithm, which uses training samples to find a set of classification trees in the space of image parameters. The test sample is used for the evaluation of the instrument response functions such as effective area, energy resolution, angular resolution, etc. RF is performed with simulated γ-shower events to represent γ rays and OFF data from real observations to represent background using the MARS routine 'Coach', as this algorithm needs input as events from electromagnetic and hadronic showers.

The training sample representing the background is created by selecting events randomly from the experimental data. Then the mean classification from all the trees is expressed as a number in terms 'hadronness', related to the probability that the events are either hadron-like (hadronness = 1) or γ-like (hadronness = 0). Then, the simulated γ-like events from MCs are used concurrently with real data in case of hadronness. In the testing phase, both simulated and real events using the test sample MCs are used during the training phase are assigned with their reconstructed energy and hadronness. All this information then is handled by the MARS routine "Melibea" which performs the energy estimation and stores a classifier to sort out hadron induced air-showers. Melibea uses a random forest made by Coach to assign an energy and hadronness estimator to each event. Melibea converts Hillas Parameter files produced by Star or the stereo parameter files produced by SuperStar to fully analyzed Event files. The energy threshold of the analysis is estimated from the peak of the reconstructed energy distribution of γ-like events from the MC data. This threshold is also dependent on other factors such as the status of telescope hardware and zenith angle during the observations.

Source detection and skymap

Next step in the analysis is to calculate the excess and its significance in the sky from the direction of the source. This task is performed using the MARS routine 'Odie'. To evaluate the significance, this program uses the two histograms in θ^2; one for the source position (ON) and other for the background positions (OFF). The OFF distribution includes events located at a specific offset w.r.t. the observed source position in the Cherenkov camera. θ^2 is the squared angular distance w.r.t. sky coordinates of nominal source position. The data supplied into these histograms have usually been preprocessed by applying γ-hadron separation cuts, in order to actively suppress the background. As hadronic events follow isotropic arrival direction, their θ^2 will be flat (see figure 3.25).

Thus, the signal can be extracted by plotting the θ^2 distribution of the ON and OFF data after the application of selection cuts such as energy threshold, size of events passing the image cleaning and stereoscopic reconstruction in photo-electrons for each telescope, and appropriate cut in hadronness. The histogram of θ^2 peaks around zero from given source position from ON region, while the OFF sample shows a flat distribution. Therefore, θ^2 distribution allows us to check the consistency of background around the source with the background computed from OFF region. The significance of the source can be calculated according to Li & Ma equation (see

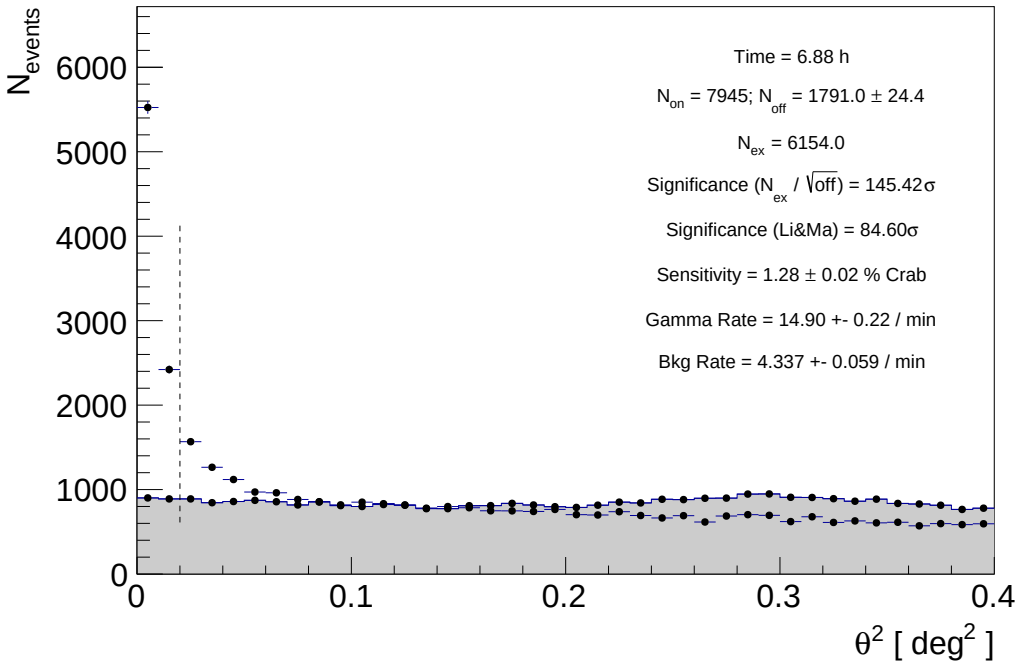

Figure 3.25: Example of a θ^2 distribution for the Crab Nebula data with E < 100 GeV using the standard analysis. The blue points represent the γ-ray excess events, whereas, the background estimation is shown by the shaded histogram. The signal region is defined between $\theta^2 = 0$ and the vertical dashed line.

[Li & Ma 1983] for details) as given below:

$$S = \sqrt{2}\left\{N_{on}\ ln\left[\frac{1+\alpha}{\alpha}\left(\frac{N_{on}}{N_{on}+N_{off}}\right)\right] + N_{off}\ ln\left[(1+\alpha)\left(\frac{N_{off}}{N_{on}+N_{off}}\right)\right]\right\}^{N_{off}} \tag{3.15}$$

where S is the significance, t_{on} is the time of observation towards the source and N_{on} is the photon count, t_{off} is the time interval for background measurements and N_{off} is the corresponding photon count, α is ratio of on-source time to the off-source time, and N_{ex} is number of excess events.

$$N_{ex} = N_{on} - (\alpha N_{off}) \tag{3.16}$$

Skymap or exposure map for γ-ray sources is created by choosing the pre-selected events into a 2D sky coordinates (RA, Dec) histogram by using the MARS routine 'Caspar'. It contains γ-ray as well as hadronic events, which are γ-like background events, which pass the γ-hadron cuts and separation as well. Here the background model for observations is required to separate the γ-ray excess from hadrons. There are two methods available in Caspar to perform this task: blind map and the wobble

map. For the wobble map, it is assumed that the signal from the source is fully contained in one camera half, whereas the opposite half has background events only. The blind map option has to be used when the observed source extends beyond the central 0.4° circle or the extension is unknown. Further, the significance of excess is again calculated using the LiMa equation given in equation 3.16.

Energy spectrum

Once the source is detected with a minimum significance of 5σ, next step in the analysis is to calculate the VHE γ-ray emission via measurement of the differential and integral flux emitted by the source. This task is performed by the MARS routine 'flute'. The differential spectrum can be calculated as:

$$\frac{dN}{dE}(E) = \frac{N_\gamma}{dE \cdot dA_{\text{eff}} \cdot dt_{\text{eff}}} \tag{3.17}$$

The the spectral energy distribution (SED) is a measure for the power emitted per logarithmic bandwidth. Therefore, the SED is always comparing fluxes in the intervals with the same $\delta E_\gamma / E_\gamma$, and it can be calculated as:

$$E^2 \frac{dN}{dE} = E^2 \frac{dN_\gamma}{dE \cdot dA_{\text{eff}} \cdot dt_{\text{eff}}} \tag{3.18}$$

Where, E is the energy, N_γ are the excess events, i.e., a number of detected γ rays in the finite energy bin dE. The analyzer decides the energy bin. A_{eff} is the effective collection area and t_{eff} the corresponding effective observation time. Measuring effective observation time is relatively straight forward and needs to take into account the dead time of 26×10^{-6} s introduced by the readout system per event. On the other hand, calculating collection area is complicated. It is strongly energy dependent, especially close to the threshold (see figure 3.26) A_{eff} includes area folded by the detection efficiency in which the telescope can likely observe air showers after application of all the analysis cuts such as θ^2 and hadronness.

These cuts are accordingly determined using MC simulations to get a target survival probability in a dedicated way for each data set in order to match that probability for each energy bin. The detection efficiency can be determined from the ratio of the number of simulated γ-ray showers which survives all the cuts to the total number of γ-ray showers. For $\text{E} < 300\,\text{GeV}$, effective area rapidly decreases with decreasing energy, however, above this threshold after applying all cuts it is rather constant around mean value of orders of $10^5\,\text{m}^2$. Therefore, after taking into account all these details, the differential flux and the SED can be characterized.

Light Curve

Apart from calculating differential spectrum, 'flute' can also be used to determine the integral flux to get the light curves for γ-ray emission above certain energy as

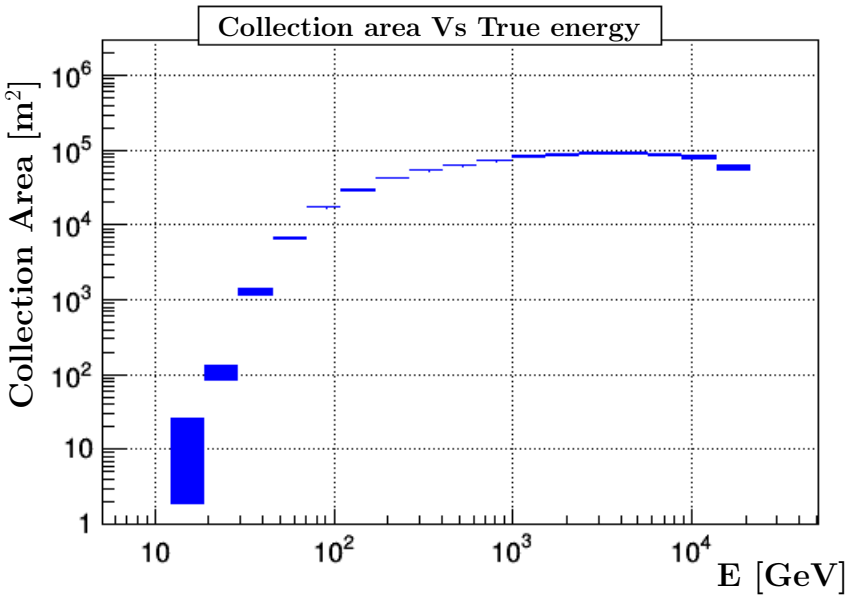

Figure 3.26: Example of collection area vs true energy from a real observation.

a function of time. Thus, an integration of the differential energy flux above an arbitrary energy E_0:

$$F_{E>E_0}(t) = \int_{E_0}^{\infty} \frac{dN_\gamma}{dE\ dA_{\text{eff}}(t)\ dt_{\text{eff}}(t)} \tag{3.19}$$

The parameters are the same as in Equation 3.18. Light curves are obtained by making time bins and measuring the number of excess events in each time bin separately for a given range in estimated energy. For each time bin, the effective collection area is calculated separately by using the MC γ-event sample with the zenith angle distribution of the data events in a given time bin. Therefore, the collection area and effective on-time are necessary to be calculated separately for each time bin to determine the integral flux in each of that energy bin.

Unfolding

In order to correct the known biases for the energy reconstruction, an unfolding method is applied to the raw differential energy spectra computed using the estimated energy of the γ rays using 'flute'. Figure 3.27 shows an example of the migration matrix from the true energy to the estimated energy for the MC data set with an energy spectrum similar to the Crab Nebula. The correction to be applied to the energy spectrum cannot be done through the simple inversion of the migration due to two basic facts, i.e., 1) the strong correlation within the adjacent energy bins, and 2) not always the matrix is invertible. Therefore, pre-assumptions regarding the true energy spectrum have to be done, for example, a parametrization of the differential

energy spectrum in many cases is a power law for many astrophysical γ-ray sources. The distortion due to energy estimation biases and finite resolution can be written in the form:

$$Y(y) = \int M(x, y)\ S(x)\ dx \tag{3.20}$$

where M is the migration matrix, S is the true and Y is the measured distributions, x is the true energy, and y is the estimated energy. The MARS routine 'CombUnfold.C performs the unfolding. This program performs unfolding of spectra using the algorithms of [Bertero 1989], [Schmelling 1994], and [Tikhonov & Arsenin 1977], as well as the forward folding method. In order to minimize the difference between the folded spectrum and the observed spectrum, the parameters are varied, and the energy migration matrix is applied to the spectral assumption. Use of more than one algorithm to perform the unfolding provides the cross check to ensures that no wrong spectral reconstruction has been done.

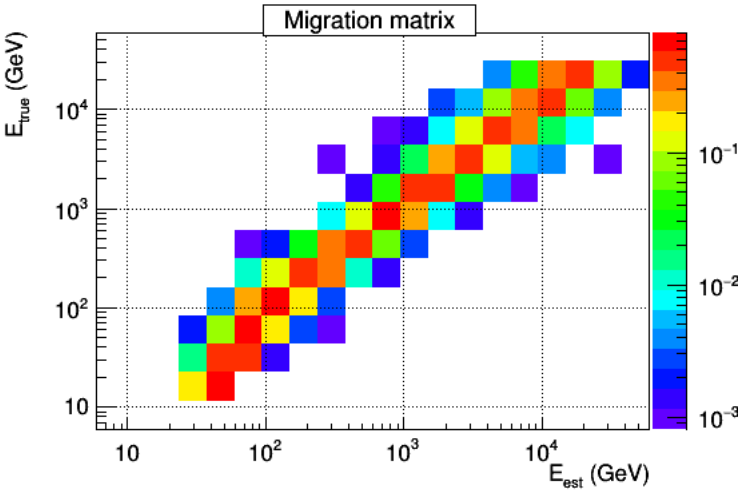

Figure 3.27: Example of Migration matrix from a real observation.

Moon adapted analysis

IACT telescopes use sensitive PMTs to detect Cherenkov flashes in nanoseconds produced by extended air showers. To have the less NSB fluctuations in the data, and as PMTs can draw too much anode current that the high voltage (HV) cannot be properly applied and they can also age quickly in the bright environment, IACT telescope arrays are typically optimized to take data during dark nights. The brightness of the whole sky greatly depends on the Moon phase and its zenith angle, and the effect of scattered clouds. For example, if Moon is present at zenith angle of 10° to the telescope, it will not be directly shining into the camera, whereas, if Moon is present at zenith angle of 170° to the telescope, then observations will not be possible, as Moon will be shining directly into the camera. If scattered clouds are present, the moonlight gets scattered from the cloud and makes the addition to the background. Due to these restrictions, around the full moon, for several nights in a row, observations are stopped completely. So when IACT instruments work only in moonless nights, their overall duty cycle is limited to 18%, i.e., $\sim$1500 hours/year. Then there is time loss due to bad weather or hardware problems as well. Running IACT telescopes during moonlight and twilight would increase the observations duty cycle up to $\sim$40% [Ahnen et al. 2017]. The enhanced duty cycle has many scientific benefits; more observing time, obtain a large amount of data, and no full moon time breaks which could be critical in observing transient events during moon time such as AGN flares, GRB, and neutrino alerts or gravitational wave detection follow-ups. Therefore, observations during moonlight make IACTs more responsive towards unpredictable and variable γ-ray sky.

To make the observations possible and to increase the duty cycle during moonlight, different hardware approaches have been developed in MAGIC since the upgrade. Few of them to note here are; usage of UV-pass filters, usage of reduced high voltages (HV) to PMTs to reduce the gain (see [Ahnen et al. 2017] for more details). Another approach is to use novel photosensors such as silicon photomultipliers (SiPM) instead of conventional PMTs. These are robust devices and can be exposed to high illumination levels of moonlight without carrying any damages. They are successfully operating in the First G-APD Cherenkov Telescope (FACT) camera and can operate even during full moon being inside the FoV of the camera by switching off those SiPMs that get moonlight directly [Knoetig et al. 2013].

In my thesis, none of the methods described above were used. We simply take data with standard hardware settings until the moon becomes too bright. However, even the hardware setup is standard; the analysis is not. During the observations performed in moonlight [Ahnen et al. 2017] condition, the presence of Moon increases the NSB fluctuations, which increase the rate of photoelectrons continuously detected by every pixel. In this work, during the observations, we do not measure the NSB spectrum directly, but just monitor the DC in every camera pixel. We infer the NSB level by comparing the measured median DC in the cameras with a reference average median DC that is obtained in a well-defined set of observation conditions.

We use the Crab Nebula data taken in the dark conditions with no Moon in the sky or near the horizon and good weather and refer to it as NSB_{Dark}, which corresponds to the median DC1 $\sim 1.1 \mu A$ for MAGIC-I (see figure 3.29a).

For the data taken using nominal HV settings, for the given median DC level and using the reference NSB_{Dark}, NSB_{level} can be calculated as [Ahnen et al. 2017]:

(3.21)

In our analysis, we define two median DC ranges as:

- moderate moonlight (low DC): DC < 3.5 μA (M1) and DC< 1.75 μA (M2)
- strong moonlight (high DC): $3.5 <$ DC < 6 μA (M1) and $1.75 <$ DC < 3 μA (M2)

Due to the difference in PMT gain in MAGIC-I and MAGIC-II, the corresponding difference can be seen in the median DC levels. For moderate to strong moonlight conditions, the median DC level in the data also increases [f]. In figure 3.29a and 3.29b, to highlight the effect of moonlight on DC levels, a comparison is shown between data taken in moderate moon condition (blue points) with dark data (red points). It is possible to have more fine groupings for the median DC to define the state of moonlight, but it makes the analysis more time-consuming.

To analyze the MAGIC data during moonlight conditions, all the steps from the standard analysis, i.e., calibration to flux estimation (see section 3.6.1) are performed along with some extra considerations regarding increased NSB levels due to the moonlight, which makes the analysis more complex and time intensive. In the following sections, only those analysis steps which are different from the standard analysis are explained.

Image Cleaning

As mentioned in the previous section 3.6.1.2, in standard analysis, an absolute cleaning level of 6 phe for the core pixels and 3.5 phe for the boundary pixels are used in MAGIC-I and II. These cleaning levels are a compromise between low energy threshold and robustness optimized for any FoV, for extra-galactic or galactic sources, as well as under dark to dim moonlight conditions.

During the observations performed in moonlight condition, the presence of Moon increases the NSB fluctuations. Now, to overcome the problem of excess NSB fluctuation due to moonlight and to properly analyze the data, there is a two-step solution possible. The first step is to apply a similar cleaning algorithm as discussed in section 3.6.1.2, but with higher cleaning levels. Increased DC level also works as an indicator to apply higher cleaning level. However, with the increased cleaning levels,

[f] NSB level changes from $\sim$1-6 NSB_{DARK} according to equation 3.21 for our median DC range of 1.1 to 6 μA

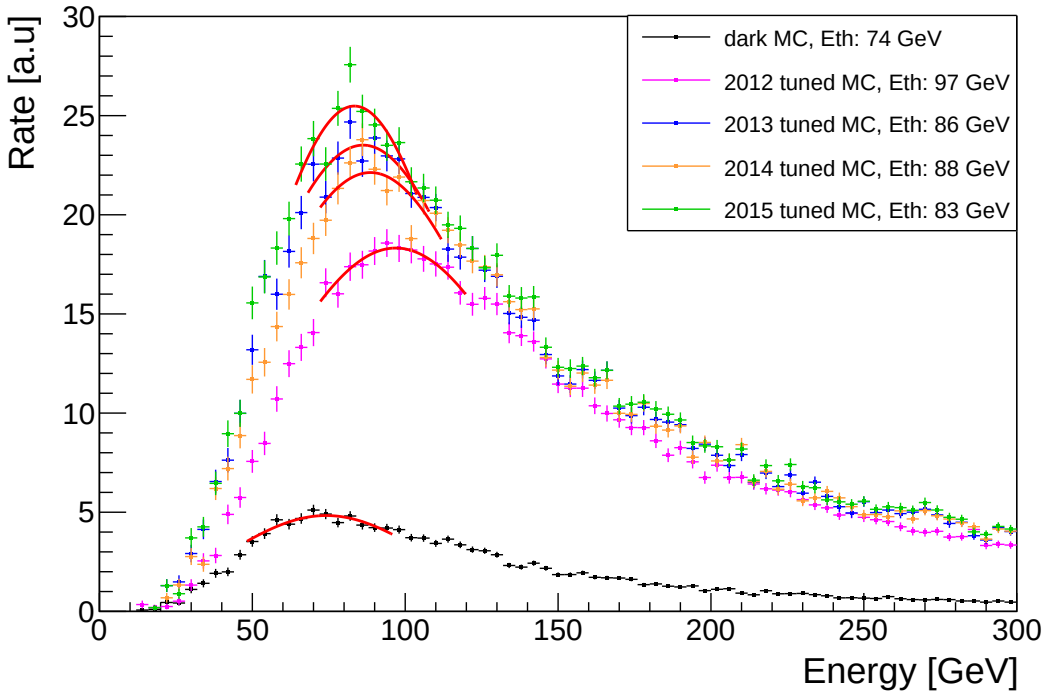

Figure 3.28: The rate of MC γ-ray events (in arbitrary units) that surviving the standard and higher image cleaning, for a source with a spectral index of -2.4 and with at least 50 phe. Eth is the energy threshold value obtained from the peak of the narrow region from each of the 2D Gaussian distribution (shown in red line).

the analysis energy threshold shifts towards higher energies (see figure 3.28). Due to moonlight, the degradation in the effective area impacts more at the lowest energies, as the Cherenkov images are small and dim. Thus the increased energy threshold is the expected price to pay for the moonlight observations. The second step is to include the noise in MCs to mimic the effect of the increases NSB due to moonlight to match it better with the data taken in the moonlight. Details about the second step are discussed in the next section.

There are two ways of adjusting the cleaning levels: check the fraction of pedestal events that survive the image cleaning and check the number of islands in Cherenkov images from the data. The purpose of adjusting these cleaning levels is to have a similar noise fraction after the image cleaning as in the dark data. These two factors were tested on the Crab Nebula data, which is our standard candle (see table 3.1).

1. **Fraction of pedestal:**
   A careful approach is necessary to modify the image cleaning levels to ensure that the fraction of pedestal events (fpe) which survives the image cleaning is less than 10%. This number can be obtained from the output of 'Star'. If fpe is above $\sim$10%, it could affect the analysis significantly as it would create

fake islands (isolated groups of pixels containing pedestal) in the real events. Therefore, a comparison was made for the distribution of fpe with cleaning levels of 8-4, 7-3.8 and 6-3.5 for moonlight data and with cleaning level of 6-3.5 for the dark data (figure 3.30a and 3.30b). From these figures, it is clear that the distribution of fpe from dark data is comparable for the moonlight data with cleaning level of 8-4 and 7-3.8.

2. **Number of spurious islands events:**
   These are the number of isolated groups of pixels also known as islands that survive the image cleaning of real data. In most of the cases, γ-ray showers are expected to produce single island image, whereas, hadronic showers are supposed to produce several islands. However, moderate to strong moonlight can also generate several islands from background light fluctuations. Therefore, to get rid of these spurious islands it is important to increase the image cleaning level. From the comparison as shown in figure 3.31a and 3.31b, it is clear that standard cleaning levels are not good enough in moderate moonlight conditions, as the distribution of spurious islands from dark data is comparable to that of cleaning level 8-4 and 7-3.8. The distribution of median DC for strong moonlight condition for Crab M1 data is shown in figure 3.32 and comparison of different cleaning levels for same DC with dark data is shown in figure 3.33. From the comparison, it is clear that all moderate moonlight cleaning levels are not good enough in strong moonlight conditions, as the distribution of spurious islands from dark data is only comparable to that of with cleaning level of 8-4.

From the study of the effect of moonlight on median DC, the number of spurious islands and the fraction of pedestal, I derived for the low DC data with cleaning levels of 8-4 and 7-3.8, results are similar to the dark data. However, for the high DC data, I found that only with a higher image cleaning of 8-4 phe I obtain results similar to those of the dark data. During moonlight observations, the noise level continuously changes, so it is not practically possible to fine tune our MC for every observation. Also, it is necessary to use the same image cleaning on calibrated MC files as well. As we have both low and high DC data, to save computational time, we have applied cleaning level of 8-4 to both low and high DC data.

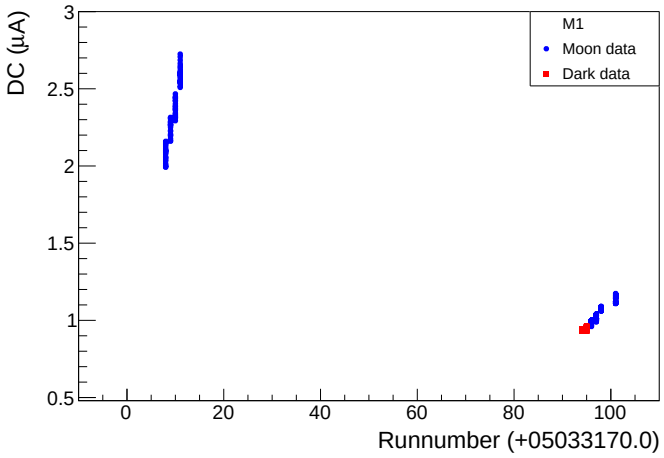

(a)

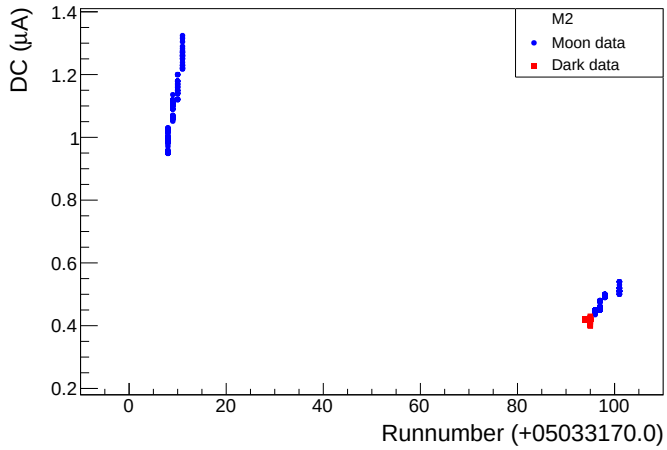

(b)

Figure 3.29: Comparison of median DC for Crab data with M1 and M2 in the moon and dark condition

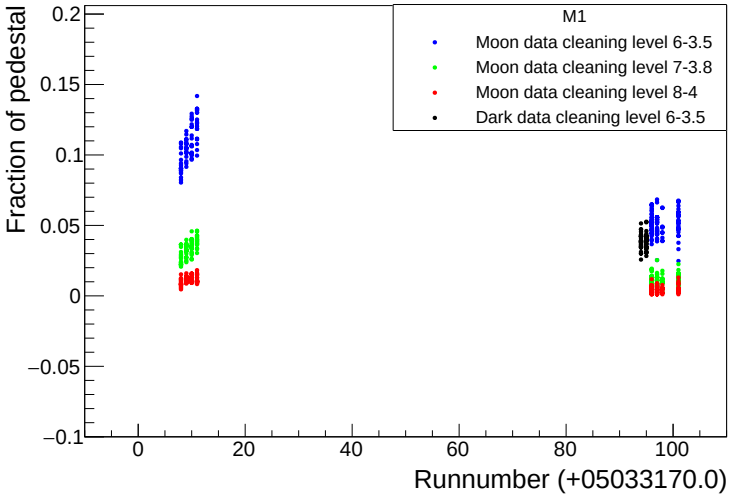

(a)

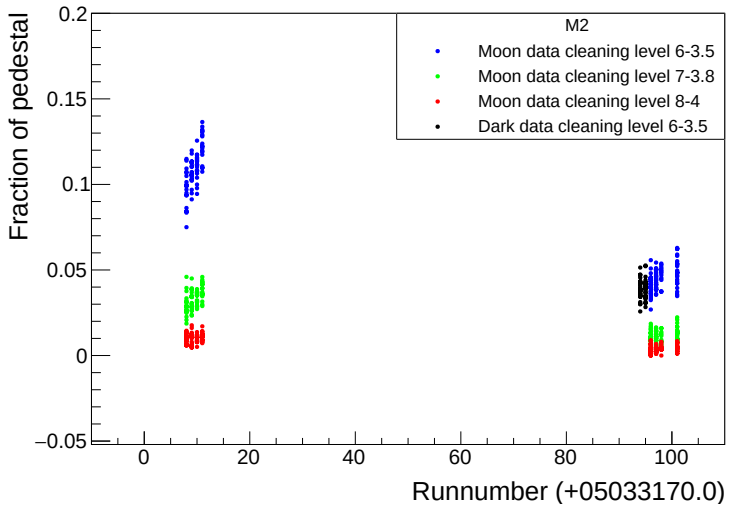

(b)

Figure 3.30: Comparison of the fraction of pedestal at different cleaning levels for Crab data with M1 and M2 in the moon and dark condition

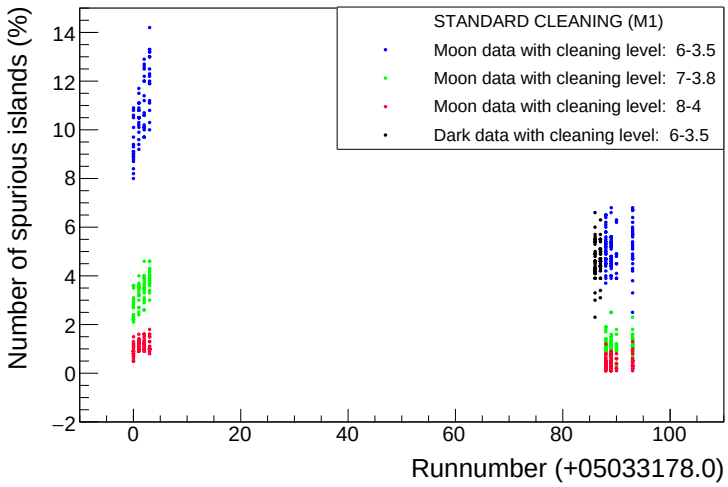

(a)

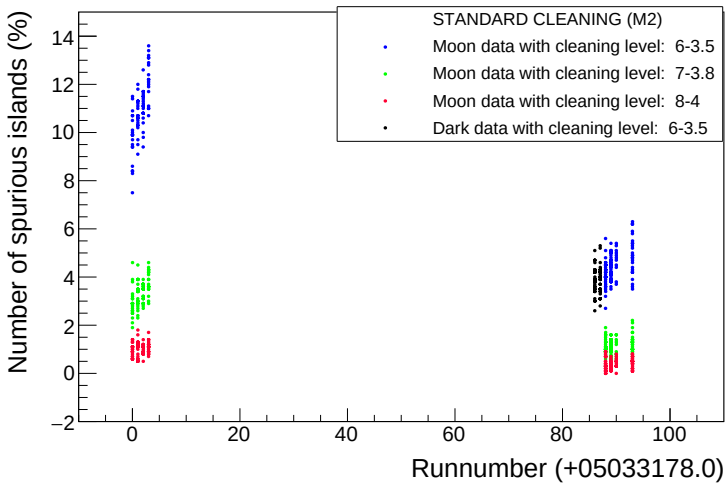

(b)

Figure 3.31: Comparison of the number of spurious islands at different cleaning levels for Crab data with M1 and M2 in the moderate moon and dark condition

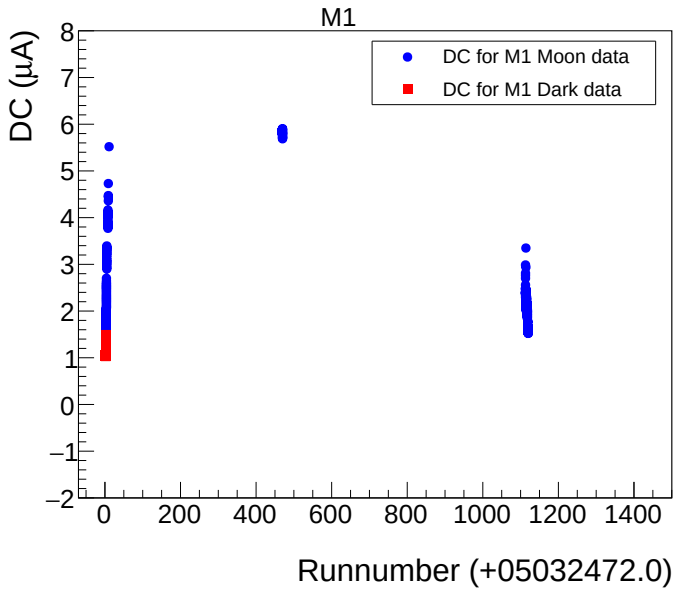

Figure 3.32: Distribution of median DC for Crab data with M1 in strong moon condition

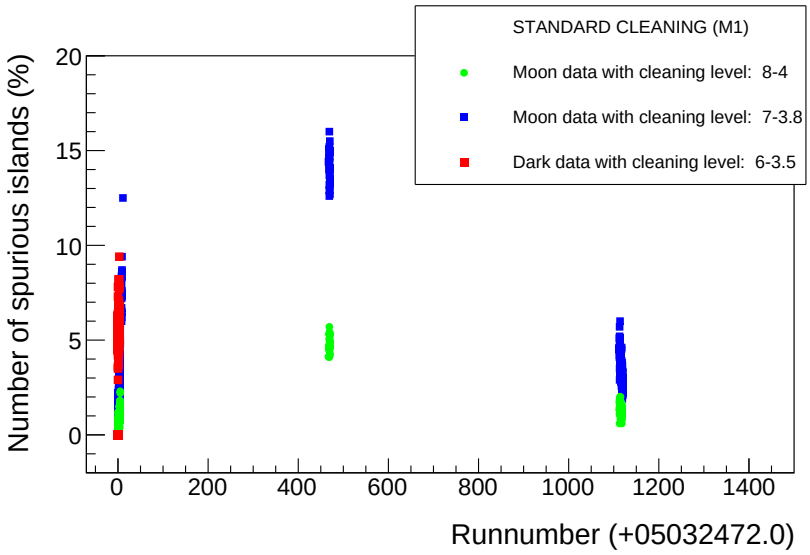

Figure 3.33: Comparison of number of spurious islands at different cleaning levels for Crab data with M1 in strong moon and dark condition

Moon adapted MC simulations and RF training

As discussed in previous section 3.6.1.6, standard MCs are provided by the collaboration. However, when analyzing data in moon condition, analyzers have to produce MCs from 'star' level on their own. This is time intensive task due to the huge number of MC calibrated files to process. To produce the moon adapted MC files, extra noise is added to mimic the effect of the increased NSB level. Note that these tuned MCs are only for moderate to strong moon data and can not be used for dark data, as due to the extra noise added the matching between MCs and dark data would be improper (see section 3.7.2.3 for details). This whole procedure of MC data needs to be performed separately for each telescope, and then files are combined using 'Superstar' for further high-level analysis. Then the MCs are divided into two subsets of training and testing, and it follows the similar steps as discussed in section 3.6.1.6 and 3.6.1.7.

Differential and integral flux estimation

A very similar approach to the standard analysis (as discussed in section 3.6.1.9) is followed to get the flux estimation in moon adapted conditions. To correct the effect of moonlight on the differential spectrum and SED, I run 'flute' separately on the moderate and strong moonlight condition data by using corresponding sets of MCs as discussed in the previous section. Then the two different spectra were combined using unfolding methods (discussed in 3.6.1.9). The same approach was used to calculate integral fluxes to get two separate light curves for moderate and strong moonlight conditions and later were combined manually to obtain the final light curve for the entire dataset.

Cross-check with Crab Nebula Analysis

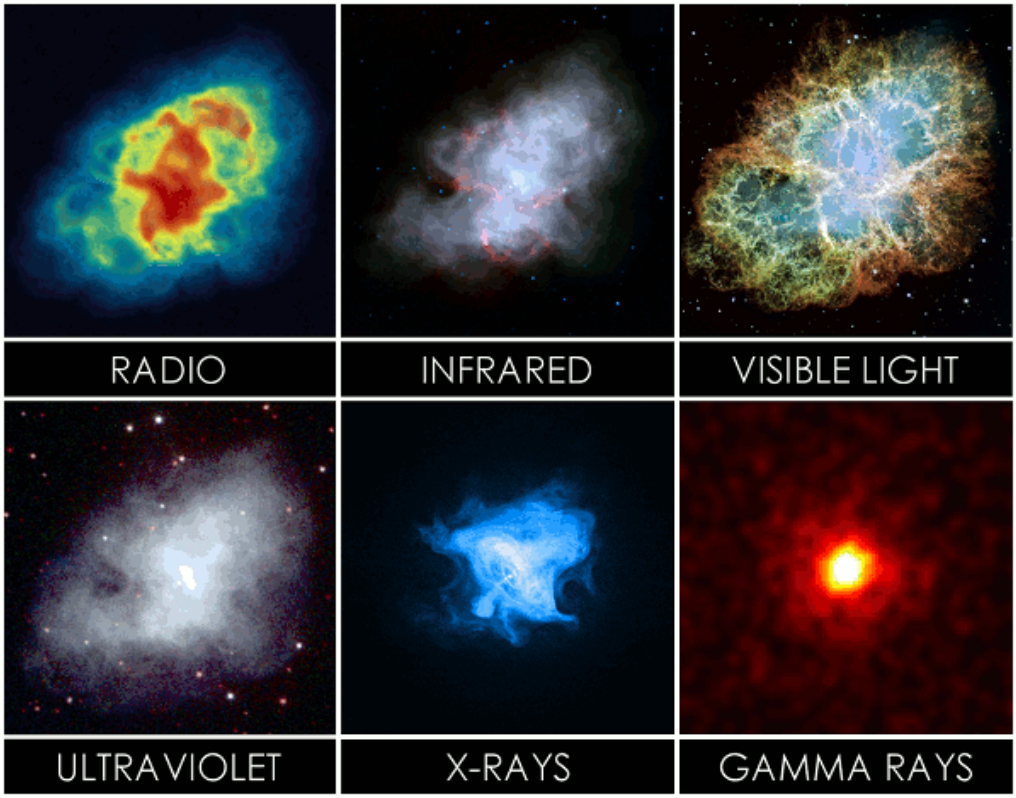

Figure 3.34: The Crab Nebula in various wavelengths. [Image credit: `http://qdl.scs-inc.us/2ndParty/Pages/16754.html`]

The Crab Nebula is a pulsar wind nebula, and the first source detected in VHE γ rays [Weekes et al. 1989], which is located at a distance of $\sim$1.9 kpc [Trimble 1973]. Figure 3.34 shows the Crab Nebula in various wavelengths, from radio to γ rays. It is commonly referred to as 'standard candle' of VHE γ-ray astronomy, as the Crab Nebula is the brightest steady source. So far no confirmed significant variability in the VHE range at short or long term time scale is found. These properties allow us to compare Crab Nebula observations taken in the given period and different light conditions (dark, moderate moon, strong moon) with historical data from MAGIC [Albert et al. 2008a], [Aleksić et al. 2015] and HESS [Aharonian et al. 2006a]. The general procedure for performing the cross-check is to take a data sample of Crab Nebula in a similar period to the source to be analyzed. The vicinity in observation period is required to reduce the possibility that the observations performed for the source and Crab Nebula were with different hardware conditions of the telescope, which could weaken the effectiveness of the crosscheck. Also to ensure the quality of

cross-checking, the Crab Nebula sample needs to be taken in similar observational conditions of the main source to be analyzed, such as zenith angles, observation modes, i.e., wobble with same camera offset, light, and atmospheric conditions. As the Crab Nebula is a bright point-like source, therefore to perform a reasonable cross-check analysis, only a few hours of data is enough. For the cross-check, the four most important things to check are the sensitivity, skymap, spectrum, and light curve. In the following sections, cross-check results from Crab Nebula data are discussed for standard, and the moon adapted analysis.

Standard analysis

For this cross-check, a test sample of three days of Crab Nebula observations performed in dark night conditions on 01-11-2013, 13-11-2013 and 23-12-2013 in the zenith range of 5° to 50° was used. The total effective observation time was 5.91 hours. The period, zenith range and atmospheric conditions of the Crab Nebula sample taken in dark night conditions were very close concerning the two sources data taking, i.e., 1ES 1011+496 (see chapter 4) and PKS 1424+240 (see chapter 5) for which the standard analysis was applied. In the following sections, results of the crosscheck are described.

Sensitivity

The first step in the cross-check analysis is to check the achieved sensitivity. To estimate the sensitivity, 'standard' cuts were used for low energy and full energy range. For low energy (LE) range (E<100 GeV), cuts were applied with size of events passing the image cleaning and stereoscopic reconstruction of >60 photo-electrons for each telescope, and the hadronness cut of <0.28, whereas, for full energy (FR) range (E > 250 GeV), cuts were applied with size of events passing the image cleaning and stereoscopic reconstruction of > 300 photo-electrons for each telescope, and the hadronness cut of < 0.16. These cuts were optimized from the independent training samples of the Crab Nebula data. To provide fast references and comparisons with other experiments , the significance of a signal can be calculated with the simplified formula $N_{excess}/\sqrt{N_{off}}$ [Aleksić et al. 2016b]. Here, N_{excess} is the excess of events over well-defined background events of N_{off}. Then, the sensitivity can be defined as the flux of a source giving $N_{excess}/\sqrt{N_{off}} = 5$ after 50 hours of effective observation time. The sensitivity can also be calculated using the Li & Ma equation (see equation 3.15) [Li & Ma 1983], however, it will depend on the number of OFF positions used for the background estimations. The sensitivity is usually given in a percentage of Crab nebula Units (C.U.). Sensitivity in absolute units can be defined from the equation below:

$$\frac{dN}{dE} = f_0 \left(\frac{E}{1TeV} \right)^{a+blog_{10}(E/1TeV)} \tag{3.22}$$

where, parameters from the fit derived using the forward unfolding are, $f_0 = (3.39 \pm 0.09_{stat}) \times 10^{-11}$ cm^{-2} s^{-1}, $a = -2.51 \pm 0.02_{stat}$ and $b = -0.21 \pm 0.03_{stat}$ for the energy range of 65 GeV to 13.5 TeV [Aleksić et al. 2016b].

The θ^2 distribution for Crab Nebula data for LE and FR is shown in figure 3.35. For the standard LE cuts, the sensitivity is expected to be around 1.3 % C.U. [Aleksić et al. 2016b], which is in good agreement with the obtained sensitivity of 1.27 ± 0.02 % C.U. from the cross-check analysis (see figure 3.35a). For the Crab Nebula, the best integral sensitivity is achieved at higher energies since background suppression improves fast with energy. For the standard FR cuts, the sensitivity is expected to be around 0.7 % C.U. [Aleksić et al. 2016b], which is in good agreement with the obtained sensitivity of 0.72 ± 0.04 % C.U. from the cross-check analysis (see figure 3.35b).

Skymap

Figure 3.36a shows the spatial distribution of the source significance above 100 GeV in the sky coordinates RA and DEC. To check the consistency of the reconstructed source position with the catalog position, a 2D Gaussian function was used to fit the excess of the skymap. The resolution or PSF is defined as the σ of this 2D Gaussian fit. The position obtained from this 2D Gaussian fit with RA: $05^h\ 34^m\ 29.2(2)^s$ and DEC: $+22^\circ\ 00^m\ 32(2)^s 5(3)^s$ is consistent with a point-like source located at the catalog position of Crab Nebula with a slight deviation observed in RA: $0.0069(8)^\circ$ and DEC: $0.0053(7)^\circ$. The grey star in figure 3.36a indicates the reconstructed source position. The color scale on the right indicates the relative flux values (the ratio between the exposure map and the background map, i.e., $N_{ex}/N_{bg(<0.1deg)}$) of the source. Figure 3.36b shows the test statistics (TS) distribution of the source significance above 100 GeV, resulted in maximum TS value of > 100. The color scale indicates the test statistic value defined as the significance from Li & Ma equation (see equation 3.15) [Li & Ma 1983].

Energy spectrum and light curve

Next step in the cross-check is to compare the obtained Crab Nebula energy spectrum and light curve with the literature results. The observed SED of the Crab Nebula was fitted with a single log-parabola function as,

$$E^2 \frac{d\phi}{dE} = E^2 f_0 \Big(\frac{E}{300GeV} \Big)^{\alpha + \beta log(\frac{E}{300GeV})} \tag{3.23}$$

Here, E is the energy, f_0 is the flux normalization factor at normalization energy of 300 GeV, α is the spectral index, and β is the curvature index. Figure 3.37a and 3.37b show the SED and light curve for Crab Nebula data taken between November-December 2013 with 5.91 hours of exposure and the historical spectrum. The agreement between the observed spectrum with the historical Crab Nebula spectrum from MAGIC [Albert et al. 2008a], [Aleksić et al. 2015] and HESS

[Aharonian et al. 2006a] confirms the validity of the produced RF and the MC sample used for the test. Similarly, in the light curve, the good agreement between the mean integral flux (solid blue line) from the Crab Nebula observed data, and historical one (dotted red line) further confirms the sanity and quality of the crosscheck. The high value of χ^2 is due to the difference in the integral fluxes caused by the individual night conditions and relative run-to-run systematic uncertainty.

In conclusion, from these results, I am confident in the dark data analysis, as my analysis chain reproduced expected results of sensitivity, sky position, and energy spectrum from the Crab nebula.

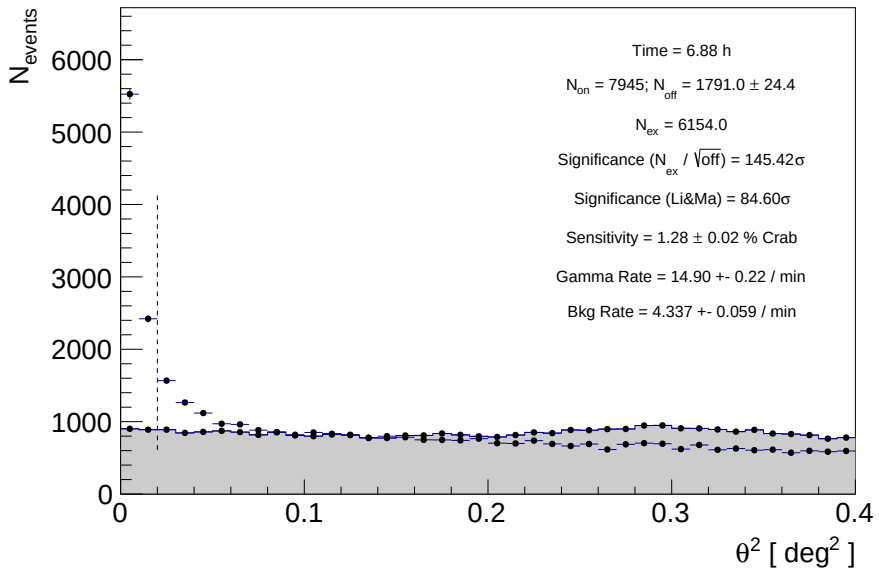

(a)

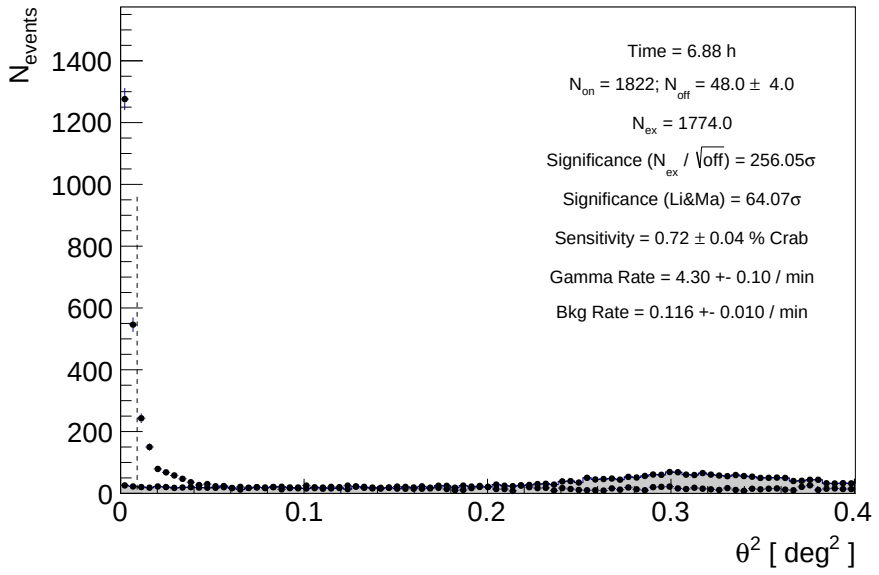

(b)

Figure 3.35: The θ^2 distribution for Crab Nebula data for standard analysis in two energy ranges: (a) $E < 100\,GeV$ and (b) $E > 250\,GeV$. The blue points represent the γ-ray excess events, whereas, the shaded histogram shows the background estimation. The signal region is defined between $\theta^2 = 0$ and the vertical dashed line.

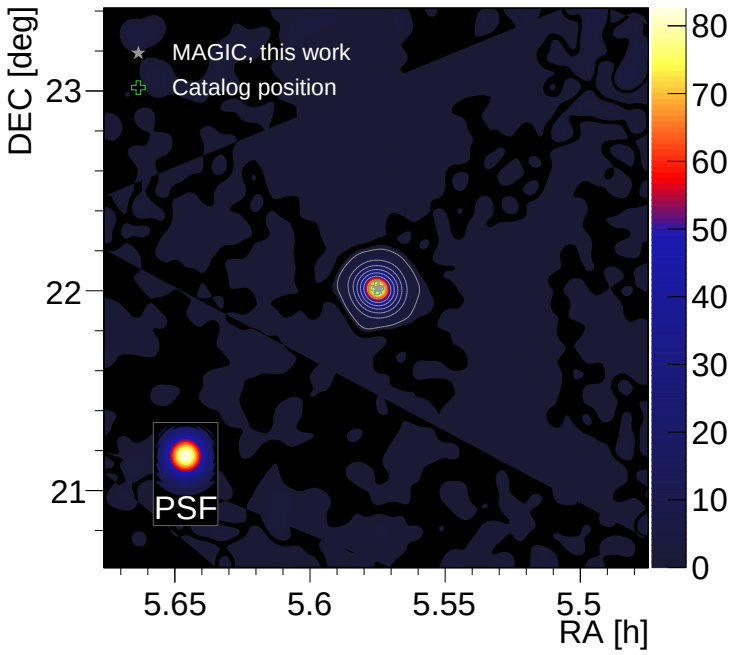

(a)

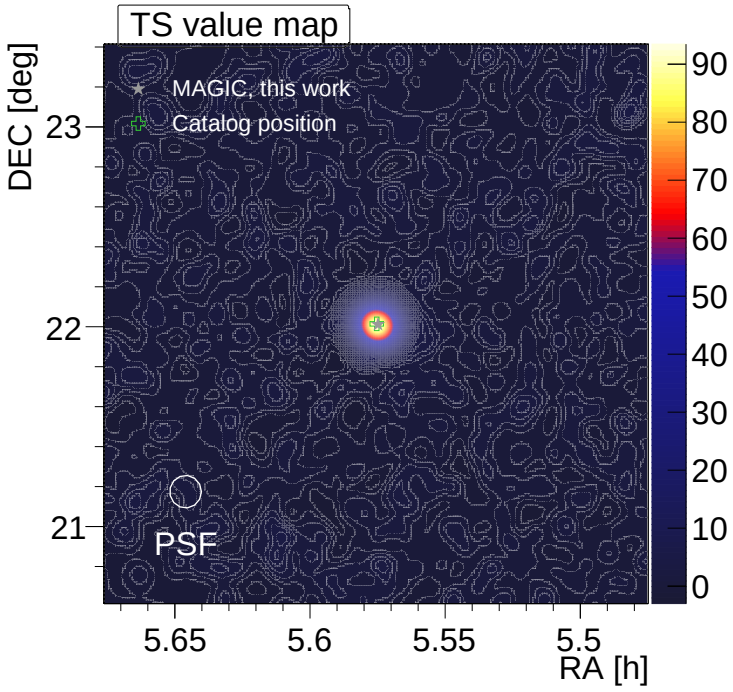

(b)

Figure 3.36: (a): Flux map of Crab Nebula sky region above 100 GeV taken in dark condition. The grey star indicates the reconstructed source position. The color scale represents the relative flux values in $N_{ex}/N_{bg(<0.1deg)}$. In the lower left is the point-spread function of 0.071° used for this analysis. (b): Significance map of Crab Nebula data taken in dark condition. The color scale represents the test statistics value distribution. In the lower left is the point-spread function of 0.071° used for this analysis.

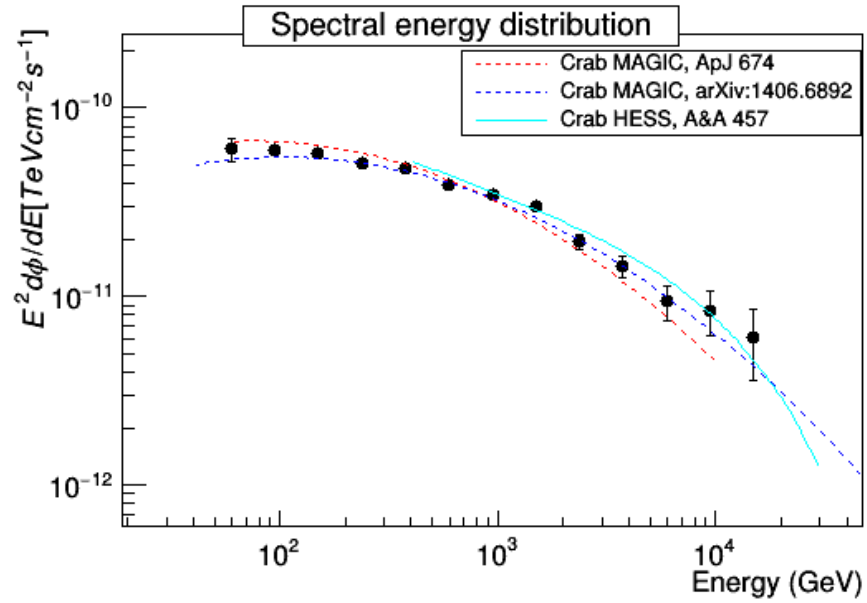

(a)

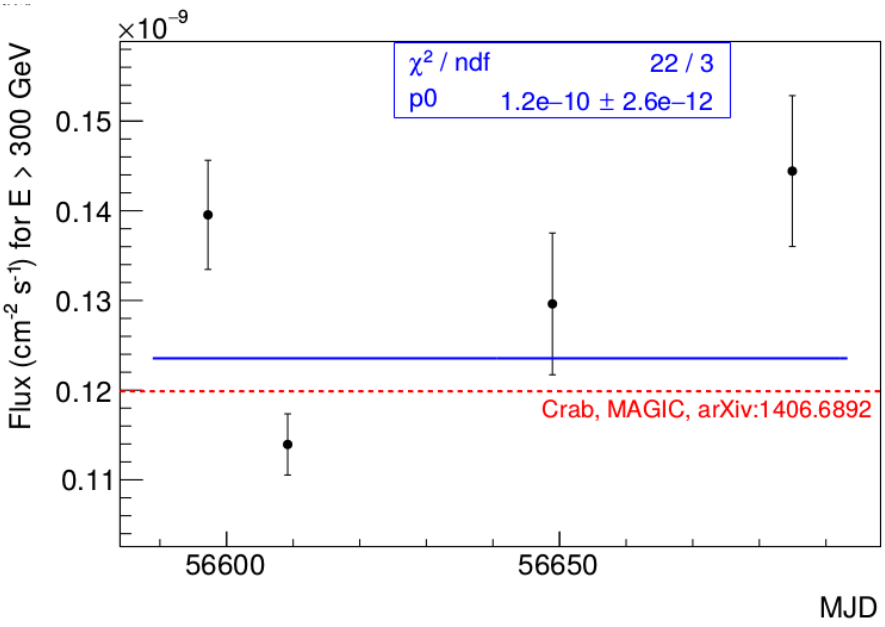

(b)

Figure 3.37: (a): Spectral energy distribution of Crab nebula data selected for this crosscheck. For the comparison, Crab Nebula spectrums from already published data for MAGIC in dotted red and blue lines from [Albert et al. 2008a] and [Aleksić et al. 2015] respectively and for HESS in solid blue line from [Aharonian et al. 2006a] are also shown. (b): The night-wise light curve for Crab Nebula data. The integral fluxes with the threshold of $E > 300\,\mathrm{GeV}$ are shown in black dots and the mean integral flux is shown in solid blue line. For comparison, the mean integral flux from published data for MAGIC [Aleksić et al. 2015] is also shown.

Moon adapted analysis

For the cross-check analysis procedure for the data taken in moon conditions, four test samples of Crab Nebula observations performed during 2012 to 2015 in the zenith range of 15° to 50° were used. The summary of these observations is given in the table 3.1. The period, zenith range and atmospheric conditions of the Crab Nebula sample were very close compared to the M87 observations, for which the moon adapted analysis was applied. Due to a presence of the moonlight, moon adapted analysis was performed on the Crab Nebula data (see section 3.6.2). As discussed in the section 3.6.2.1, higher image cleaning for the core to boundary level of 8-4 was applied. The Crab Nebula data was divided into high and low DC level for 2013 and 2014 data (see figure 3.38). Due to unavailability of Crab nebula data for high DC, for 2012 and 2015, SED and light curve plots are shown only for low DC.

For the cross-check analysis procedure for the data taken in moon conditions, four test samples of Crab Nebula observations performed during 2012 to 2015 in the zenith range of 15° to 50° were used. The summary of these observations is given in the table 3.1. The period, zenith range and atmospheric conditions of the Crab Nebula sample were very close compared to the M87 observations, for which the moon adapted analysis was applied. Due to a presence of the moonlight, moon adapted analysis was performed on the Crab Nebula data (see section 3.6.2). As discussed in the section 3.6.2.1, higher image cleaning for the core to boundary level of 8-4 was applied. The Crab Nebula data was divided into high and low DC level for 2013 and 2014 data (see figure 3.38). Due to unavailability of Crab nebula data for high DC, for 2012 and 2015, SED and light curve plots are shown only for low DC.

- moderate moonlight (low DC): DC $< 3.5\,\mu$A (M1) and D $< 1.75\,\mu$A (M2)
- strong moonlight (high DC): $3.5 <$ DC $< 6\,\mu$A (M1) and $1.75 <$ DC $< 3\,\mu$A (M2)

Then two different MC test samples and corresponding energy spectra for each year were produced according to the high and low DC level.

In the following sections, results of the crosscheck for the moon adapted analysis are described.

Sensitivity

As mentioned before, the first step in the cross-check analysis is to check the achieved sensitivity. To estimate the sensitivity, 'standard' cuts were used for full energy range (FR, E>250 GeV), with size cut >300 photo-electrons for each telescope, and the hadronness cut of <0.16. Due to the shift in analysis threshold towards higher energies in moon adapted analysis (see section 3.6.2.1, FR cuts were applied instead of low energy range (LE, E>100 GeV) cuts. Then the significance and sensitivity were

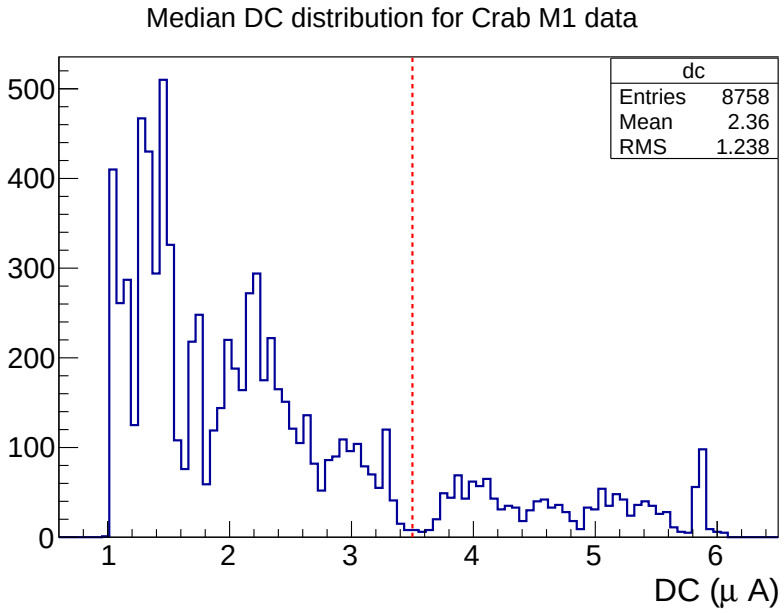

(a)

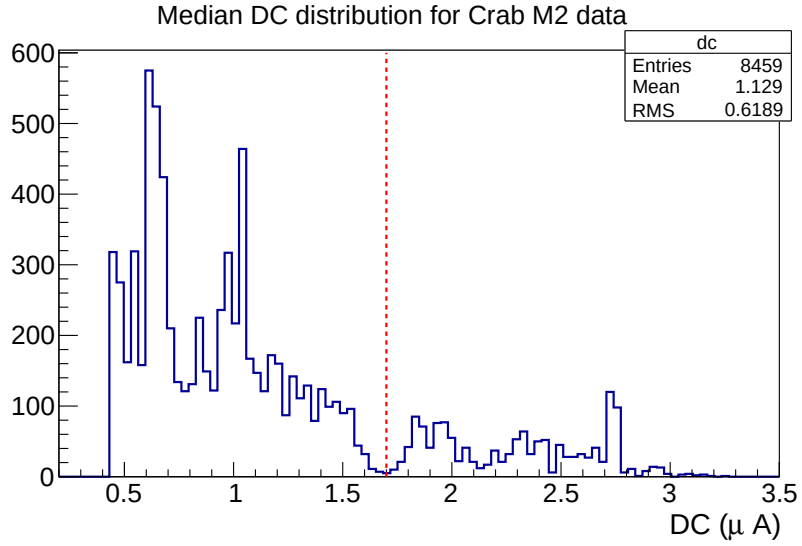

(b)

Figure 3.38: The median DC distribution for Crab Nebula data taken in moderate and strong moonlight condition. The red dotted line indicates the median DC cut applied to separate the data according to the moonlight level.

calculated as described in section 3.7.1.1. For the standard FR cuts, the sensitivity is expected to be around 0.7 % C.U., which is in good agreement with the obtained

Test sample	Obs_dates	T_{eff} (hours)
2012	2012-03-15	2.21
2013	2013-01-19, 2013-01-20, 2013-02-02, 2013-02-16	6.42
2014	2013-11-29, 2014-01-22	3.57
2015	2014-12-15	2.00

Table 3.1: Summary of Crab Nebula observations in moon condition between 2012 to 2015

sensitivity of 0.74 ± 0.07 % C.U. for 2012, 0.66 ± 0.03 % C.U. for 2013, 0.64 ± 0.05 % C.U. for 2014, and 0.66 ± 0.06 % C.U. for 2015 from the cross check analysis (see figure 3.39 and 3.40).

Skymap

Figure 3.41a shows the spatial distribution of the source significance above 100 GeV in the sky coordinates. To check the consistency of the reconstructed source position with the catalog position, a 2D Gaussian function was used to fit the excess of the skymap. The resolution or PSF is defined as the σ of this 2D Gaussian fit. The position obtained from this 2D Gaussian fit with RA: $05^h\ 34^m\ 29.4(1)^s$ and DEC: $+22^\circ\ 00^m\ 29(1)^s$ is consistent with a point-like source located at the catalog position of Crab Nebula with a slight deviation observed in RA: $0.0064(5)^\circ$ and DEC: $0.0063(5)^\circ$. The grey star in figure 3.41a indicates the reconstructed source position. The color scale on the right indicates the relative flux values (the ratio between the exposure map and the background map, i.e., $N_{ex}/N_{bg(<0.1deg)}$) of the source. Figure 3.41b shows the test statistics (TS) distribution of the source significance above 100 GeV, resulted in maximum TS value of > 100. The color scale indicates the test statistic value defined as the significance from Li & Ma equation (see equation 3.15) [Li & Ma 1983].

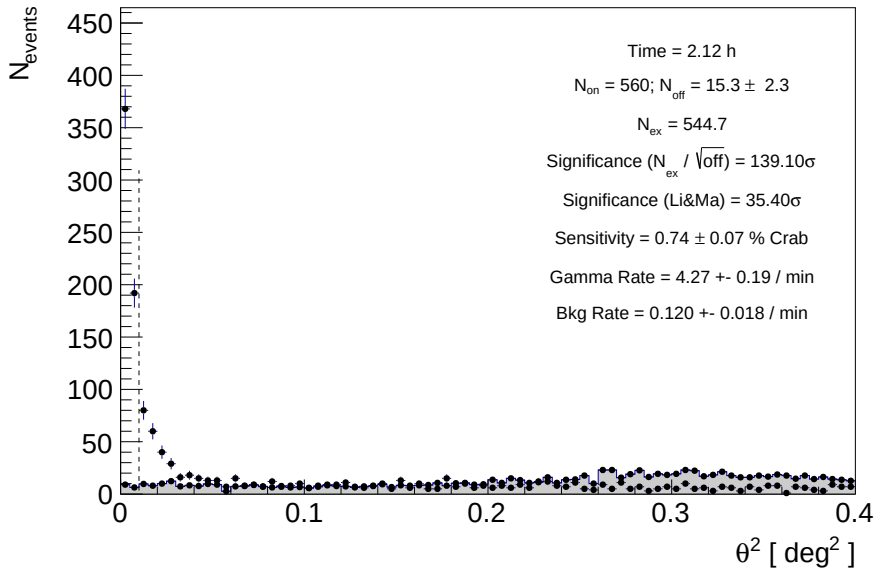

(a) 2012

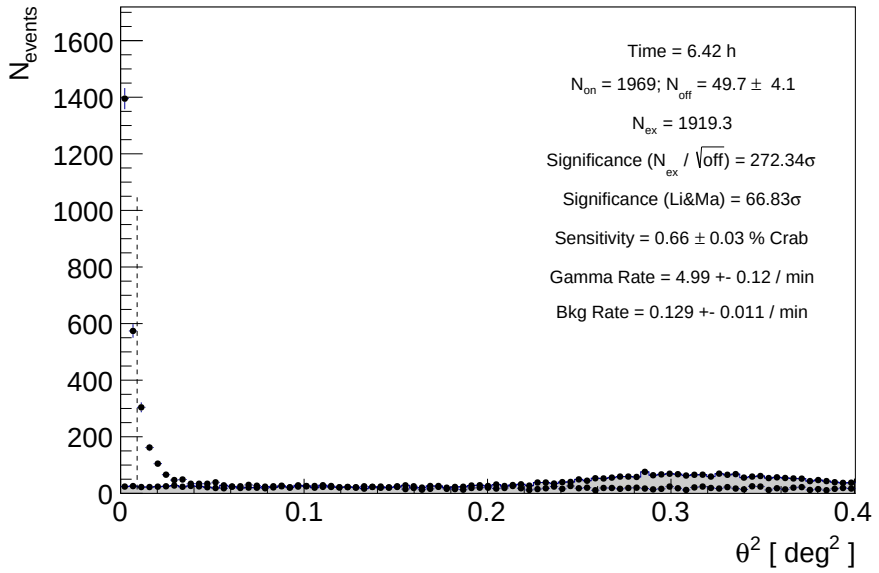

(b) 2013

Figure 3.39: The θ^2 distribution for Crab Nebula data taken during 2012 and 2013 for the moon adapted analysis with FR cuts ($E > 250\,GeV$). The blue points represent the γ-ray excess events, whereas, the shaded histogram shows the background estimation. The signal region is defined between $\theta^2 = 0$ and the vertical dashed line.

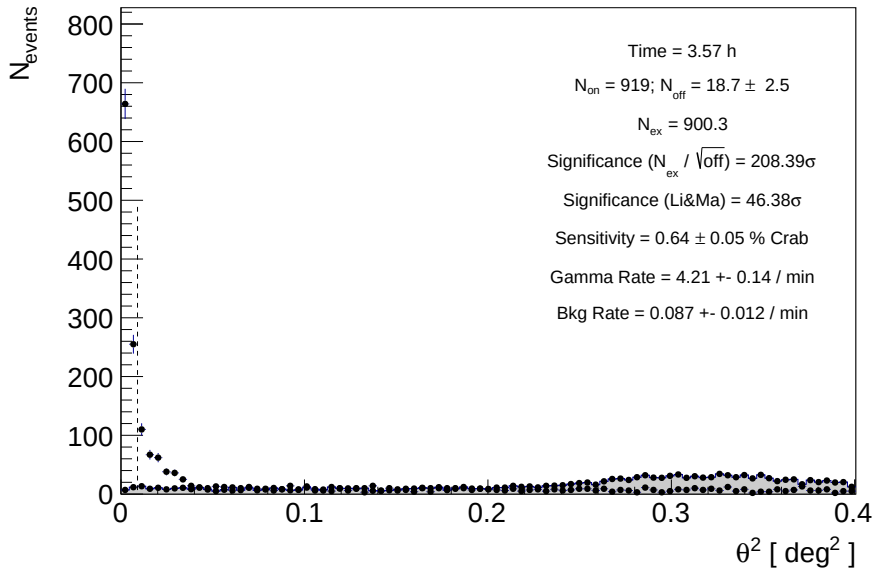

(a) 2014

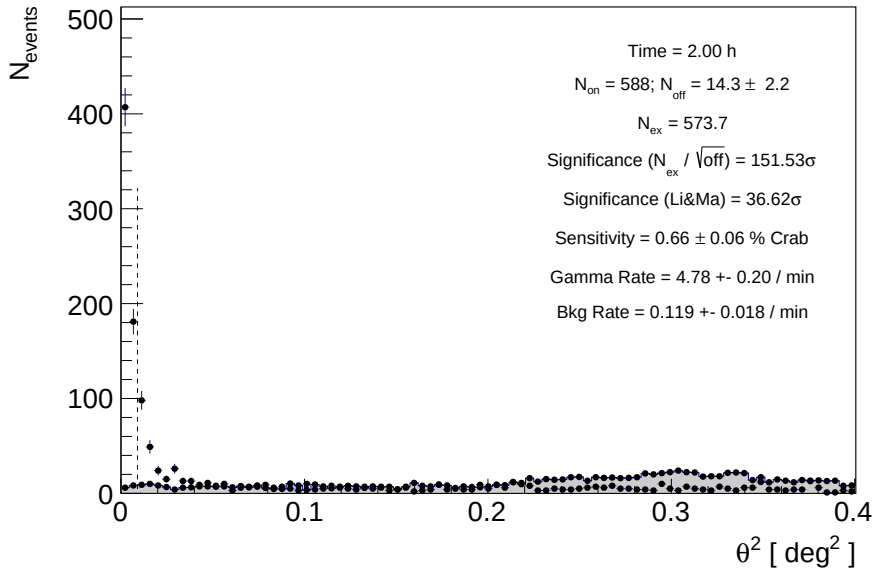

(b) 2015

Figure 3.40: The θ^2 distribution for Crab Nebula data taken during 2014 and 2015 for the moon adapted analysis with FR cuts ($E > 250\,GeV$). The blue points represent the γ-ray excess events, whereas, the shaded histogram shows the background estimation. The signal region is defined between $\theta^2 = 0$ and the vertical dashed line.

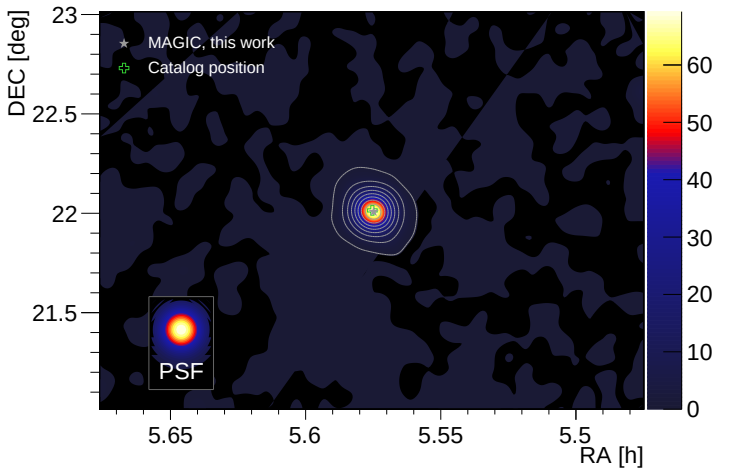

(a)

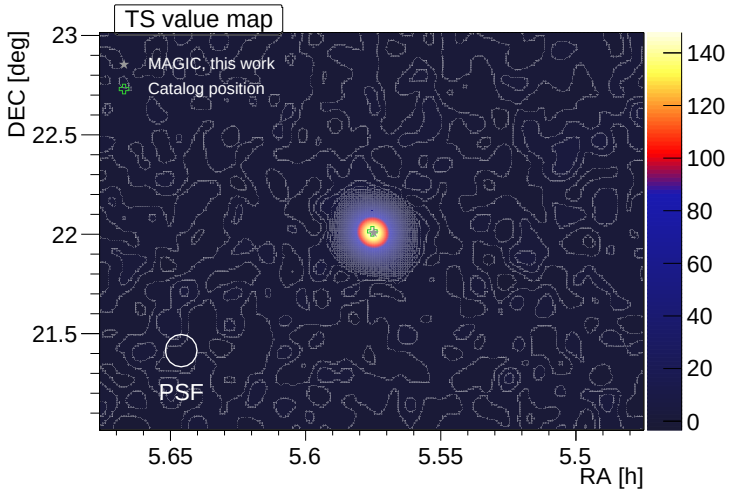

(b)

Figure 3.41: (a): Flux map of 2012-2015 Crab Nebula sky region above 100 GeV taken in moonlight condition. The grey star indicates the reconstructed source position. The color scale represents the relative flux values in $N_{ex}/N_{bg(<0.1deg)}$. In the lower left is the point-spread function of 0.071° used for this analysis. (b): Significance map of Crab Nebula 2012-2015 data taken in moonlight condition The color scale represents the test statistics value distribution. In the lower left is the point-spread function of 0.071° used for this analysis.

Energy Spectrum and light curve

The next step to compare in the cross check is the obtained Crab Nebula energy spectrum and the light curve with the literature results. To test the importance of applying the moon adapted analysis, standard dark data analysis has been performed. To get the SED and the light curve, data taken in November 2013 and January 2014 with 6.42 hours of exposure in the moon conditions were used (see table 3.1, and figure 3.42a and 3.42b). From these results, it is clear that the flux level (below 1 TeV) from the observed spectrum is lower than the historical Crab Nebula spectrum from MAGIC [Albert et al. 2008a], [Aleksić et al. 2015] and HESS [Aharonian et al. 2006a]. The effect can be seen more clearly in the light curve, where observed mean integral flux (solid blue line) is at a lower level than the historical one (red dotted line). This confirms that without applying the higher cleaning level and correcting the moonlight effect in the MC and RF, the SED and light curve show a reduction in the flux as the effective area is overestimated and energies are not mis-reconstructed. This confirms that the dark data analysis does not work with data taken in moonlight conditions.

Then moon adapted analysis was performed on the same data set. To get the energy spectrum, two different samples of MCs according to the DC levels were used. For low and high DC, two different spectra were calculated. The SED of the Crab Nebula was fitted with a single log-parabola function as shown in equation 3.23.

Figure 3.43a and 3.43a show a SED and light curve for Crab Nebula data taken in moderate (low DC) and strong (high DC) moon conditions from 2012 to 2015 as used before for the the study of moon adapted analysis (see table 3.1) and the literature data for comparison. The agreement between the observed spectrum with the historical Crab Nebula spectrum from MAGIC [Aleksić et al. 2015] confirms the validity of the moon data analysis chain. Similarly, in the light curve, the good agreement between the mean integral fluxes from the Crab Nebula observed data, and historical one (dotted red line) further confirms the sanity and quality of the crosscheck. These plots show that the moon adapted analysis is needed for the data taken in the moon conditions.

In conclusion, from these results, I am confident that the moon adapted analysis chain is robust, as it reproduced expected results of sensitivity, sky position, and energy spectrum from the Crab nebula.

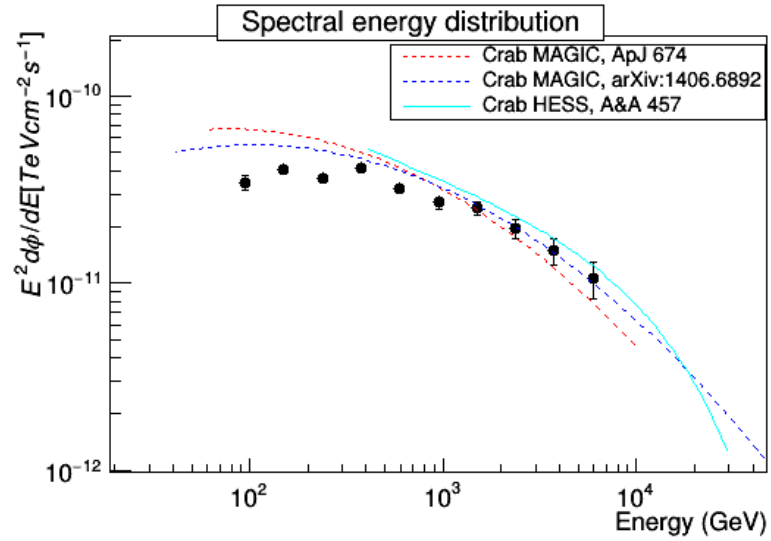

(a)

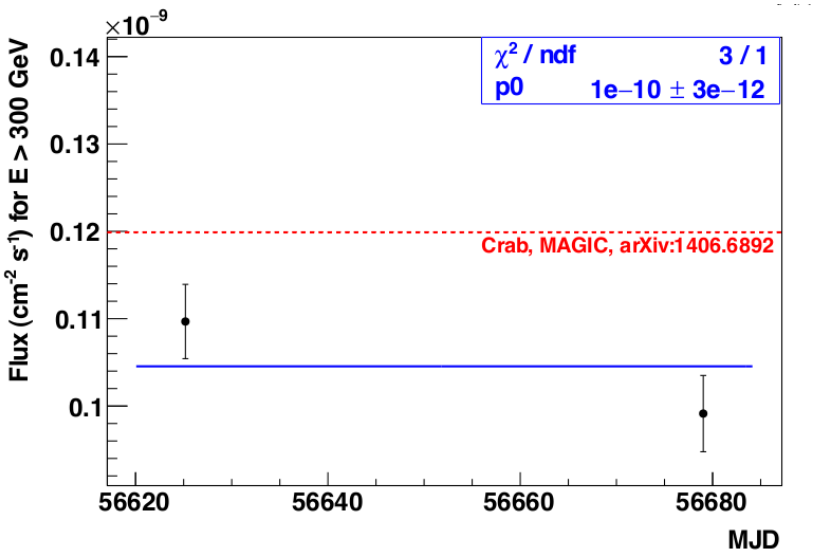

(b)

Figure 3.42: (a): Spectral energy distribution with standard analysis of Crab nebula data taken in moon conditions. For the comparison, Crab Nebula energy spectrums from already published data for MAGIC in dotted red and blue lines from [Albert et al. 2008a] and [Aleksić et al. 2015] respectively and for HESS in solid blue line from [Aharonian et al. 2006a] are also shown. (b): The night-wise light curve with standard analysis for Crab Nebula data taken in moonlight condition. The integral fluxes with the threshold of $E > 300\,GeV$ are shown in black dots, and the mean integral flux is shown in solid blue line. For comparison, the mean integral flux from published data for MAGIC [Aleksić et al. 2015] is also shown. The lower level of flux from the observed Crab Nebula data to the published one indicates that the dark data analysis underestimates the real fluxes for the data taken in moonlight conditions.

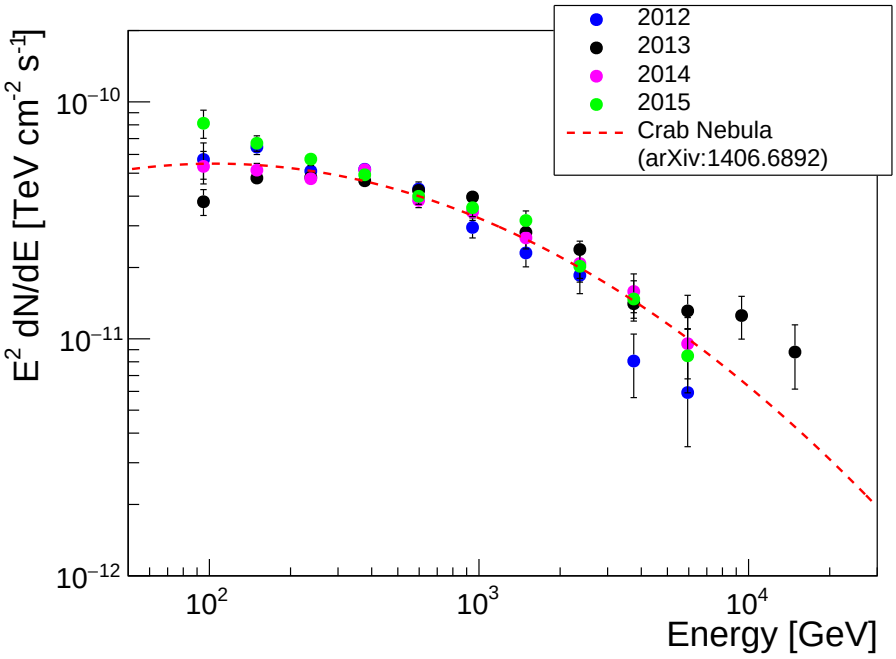

(a)

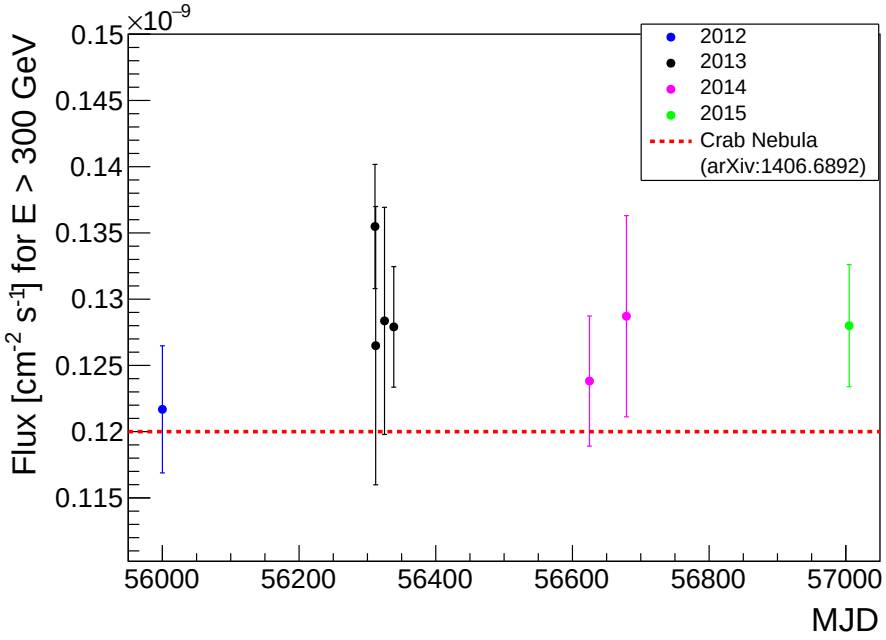

(b)

Figure 3.43: (a): Spectral energy distribution of Crab nebula data with low DC selected for this crosscheck. For the comparison, Crab Nebula spectrums from already published data for MAGIC [Aleksić et al. 2015] is shown in dotted red line. (b): The night-wise light curve for Crab Nebula low DC data. For comparison, the mean integral flux from published data for MAGIC [Aleksić et al. 2015] is also shown.

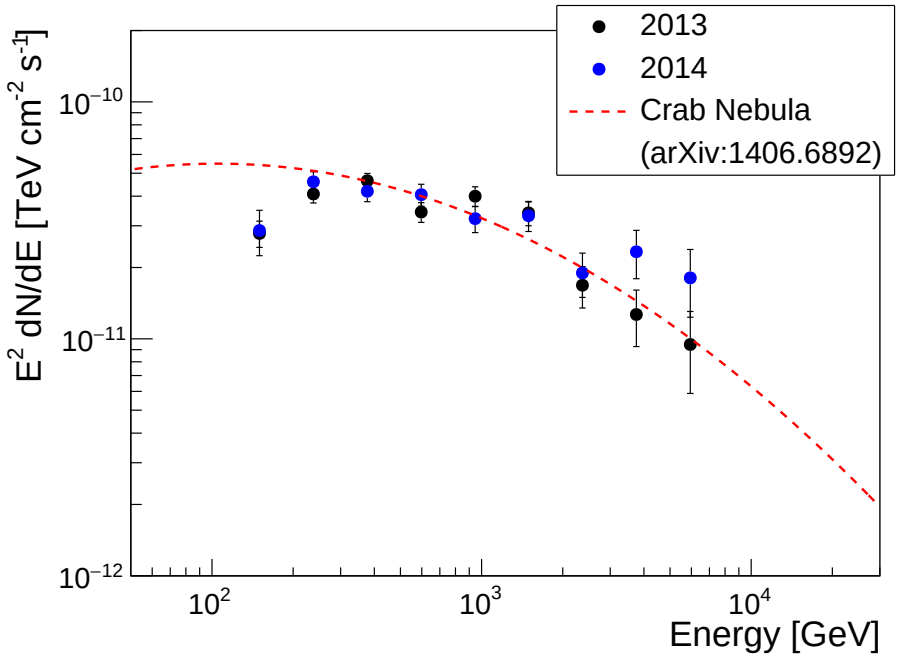

(a)

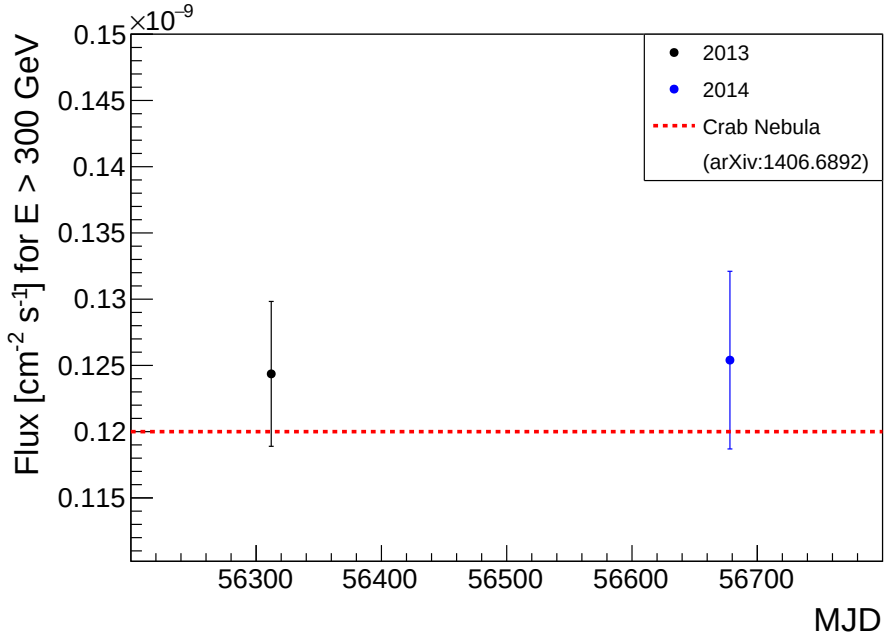

(b)

Figure 3.44: (a): Spectral energy distribution of Crab nebula data with high DC selected for this crosscheck. The first energy point from both the data sets is not compatible here. For the comparison, Crab Nebula spectrums from already published data for MAGIC [Aleksić et al. 2015] is shown in dotted red line. (b): The night-wise light curve for Crab Nebula high DC data. For comparison, the mean integral flux from published data for MAGIC [Aleksić et al. 2015] is also shown.

4. Observations of the exceptionally high flare of HBL 1ES 1011+496

Motivation

1ES 1011+496 is a high-peaked BL Lac with the redshift of 0.212. It has been monitored with MAGIC since 2007. In February 2014, an exceptionally high state (flare) activity was observed at TeV energies from the source, which triggered observations with MAGIC. The flux detected during this flare was historically high for observation spanning from X-rays to TeV observations [Mirzoyan 2014]. This chapter aims to present the analysis and results from MAGIC observations during the flare in February 2014. In the following sections, first I will discuss the status of the previous observations, then details about the observations and analysis with MAGIC (section 4.3). In the results section, first I will discuss the details of the signal detection plots (section 4.4.1), then light curve (section 4.4.2), energy spectrum (section 4.4.3 and 4.4.4), and multiwavelength spectral modeling (section 4.4.5). These results have already been published in Astronomy & Astrophysics journal [Ahnen et al. 2016], of which I am one of the corresponding authors. The relatively high redshift and the extraordinary flare, with significant excess above 1 TeV, make 1ES 1011+496 data excellent case to study the effect of extragalactic background light (EBL) on the AGN spectra. The EBL related results will be discussed later in chapter 7.

Status of the previous observations

1ES 1011+496 is an AGN classified as high-frequency peaked BL Lac (HBL) (see section 2.3), with RA: $10^{h}\,15^{m}\,04.1^{s}$ and DEC: $+49^{\circ}\,26^{m}\,01^{s}$ located at redshift of z=0.212 [Albert et al. 2007a]. The redshift was determined using the optical spectrum obtained using the Blue Channel Spectrograph with the Multi Mirror Telescope (MMT) (Figure 4.1) [Albert et al. 2007a]. It was first observed in radio as a flat radio spectrum core dominated source with the Very Large Array (VLA) radio telescope [Machalski & Condon 1983]. Later it was also detected as an X-ray source [Elvis et al. 1992]. In the past observations, 1ES 1011+496 has been classified differently than HBL. During 2005-2010, multi-band monitoring was performed using the McGraw-Hill Telescope. These data showed a peak in the op-

tical regime (∼2-3 eV), indicating an intermediate-frequency BL Lac (IBL) nature [Böttcher et al. 2010]. However, it has historically been classified as an HBL [Donato et al. 2001, Nieppola et al. 2006, Abdo et al. 2010a]. For 1ES 1011+496, various models have been proposed for the high-frequency peak; the most popular one invokes inverse Compton scattering [Albert et al. 2007a].

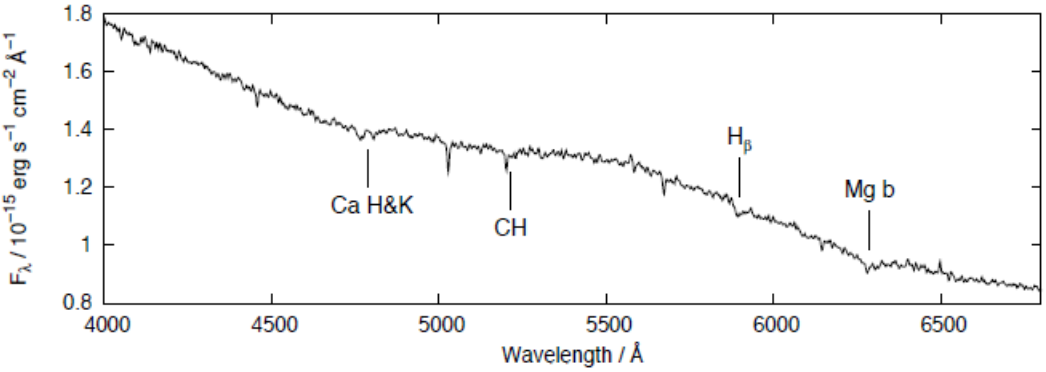

Figure 4.1: Optical spectrum of 1ES 1011+496 obtained using Blue Channel Spectrograph of the MMT. From the clearly visible absorption lines, the redshift of z = 0.212±0.002 was determined [Albert et al. 2007a].

In the past, at high energy γ rays (HE, E>100 MeV) γ rays, 1ES 1011+496 was not detected in EGRET observations (see [Fichtel et al. 1994, Lin et al. 1996], [Mattox et al. 2001], and [Sowards-Emmerd et al. 2005] for more details), but significant detection was achieved by *Fermi*-LAT observations. It was also included in the *Fermi*-LAT bright source list of the first year LAT catalog (1FGL) [Abdo et al. 2010]. In the first 5.5 months of *Fermi*-LAT data, no sign of variability was observed [Abdo et al. 2009]. The source was observed first time at VHE with HEGRA and Whipple Observatory 10m γ-ray telescope. But it resulted only in upper limits of integral flux (see [Aharonian et al. 2004] and [Fegan et al. 2005]). After that, it was also observed with MAGIC-I (mono observations) in 2004-2006, resulting again in upper limits [Albert et al. 2008c]. Thanks to the Turola Blazar Monitoring Program, 1ES 1011+496 has been continuously monitored in optical at R band since 2003 till present day. The optical long term light curve of the source is shown in the figure 4.2.

In 2007, finally, 1ES 1011+496 was discovered at VHE by MAGIC I telescope (mono observations) after following a high optical state reported by the Tuorla Blazar Monitoring Program. At the time of the discovery, it was the most distant source known to emit VHE γ rays [Albert et al. 2007a]. The observed spectrum was well fitted using the power law with normalization factor $f_0 = (2.0\pm0.1)\times10^{-10}$ TeV^{-1} cm^{-2} s^{-1}, spectral index $\Gamma = 4.0\pm0.5_{stat}\pm0.2_{sys}$ and normalization energy of 200 GeV. The systematic uncertainty for the absolute flux was estimated to be around 75% and for

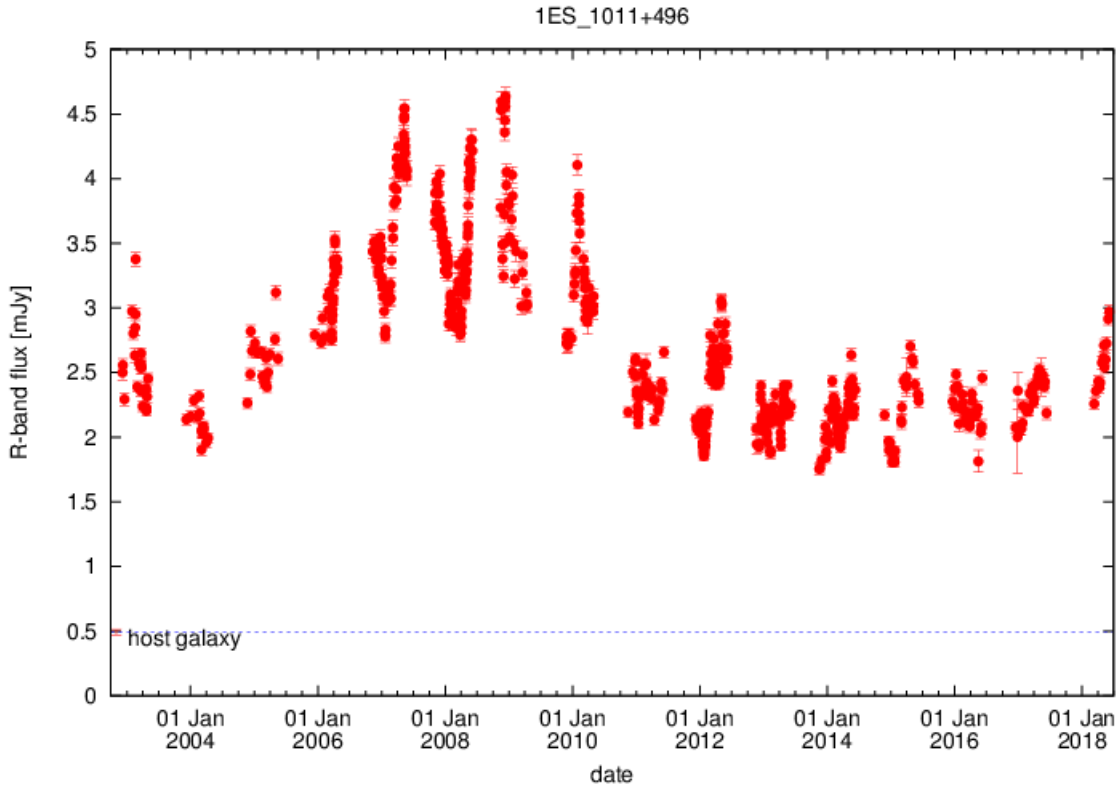

Figure 4.2: Long term optical light curve of 1ES 1011+496 measured in R-band from the Tuorla Observatory Blazar Monitoring Program from 2003 to August 2018. [Credit: `http://users.utu.fi/kani/1m/1ES_1011+496_jy.html`].

the spectral index to be 0.2. The integral flux for E>200 GeV was observed to be $(1.58\pm0.32)\times10^{-11}$ photons cm^{-2} s^{-1} without any sign of flux variability. The estimated intrinsic spectrum assuming the [Kneiske et al. 2002] EBL absorption model, was a power law with photon index $\Gamma_{int} = 3.3 \pm 0.7_{stat}$ [Albert et al. 2007a].

In spring 2008, following the discovery, a multi-wavelength (MWL) campaign was organized by MAGIC [Ahnen et al. 2016b]. The integral flux of $(1.8\pm0.5)\times10^{-10}$ photons cm^{-2}s^{-1} for E>200 GeV measured during 2008 observations is found to be in good agreement with flux level of 2007 discovery. The spectrum was fitted with power law with normalization factor of $f_0 = (1.3 \pm 0.3) \times 10^{-10}$ TeV^{-1} cm^{-2} s^{-1}, spectral index $\Gamma = 3.3 \pm 0.4_{stat}$ and normalization energy of 200 GeV. The estimated intrinsic spectrum was a power law with photon index $\Gamma_{int} = 2.2 \pm 0.4$ [Ahnen et al. 2016b], assuming the Domínguez 2011 model [Domínguez et al. 2011] for the EBL absorption. In this MWL campaign, MAGIC observations were centered around common observation windows of the AGILE satellite [Tavani et al. 2009]. In the MWL observations, optical observations were performed using the KVA and Bell telescopes, radio observations were performed using the Metsähovi radio telescope and X-ray observations were performed using Swift satellite.

During March to April 2011 and January to May 2012, a second MWL campaign was organised by MAGIC [Ahnen et al. 2016a] along with Metsähovi and Owens Valley Radio Observatory (OVRO) radio telescopes, KVA optical telescope, Swift X-ray satellite and *Fermi*-LAT high energy γ-ray telescope. The integral flux of $(0.75\pm0.12)\times10^{-11}$ photons cm^{-2}s^{-1} for E>200 GeV measured during 2011-2012 observations is found to be at lower level than that of 2008 and no sign of variability is observed. The spectrum was fitted with power law with normalization factor of $f_0 = (1.33 \pm 0.06) \times 10^{-10}$ TeV^{-1} cm^{-2} s^{-1}, spectral index $\Gamma = 3.66 \pm 0.22_{stat}$ and normalization energy of 200 GeV. The estimated intrinsic spectrum assuming the Domínguez 2011 model [Domínguez et al. 2011] for the EBL absorption, was a power law with photon index $\Gamma_{int} = 3.0 \pm 0.3$ [Ahnen et al. 2016b]. Figure 4.3 and Table 4.1 summarize the spectral properties for these data taken in 2007, 2008 and 2011-2012.

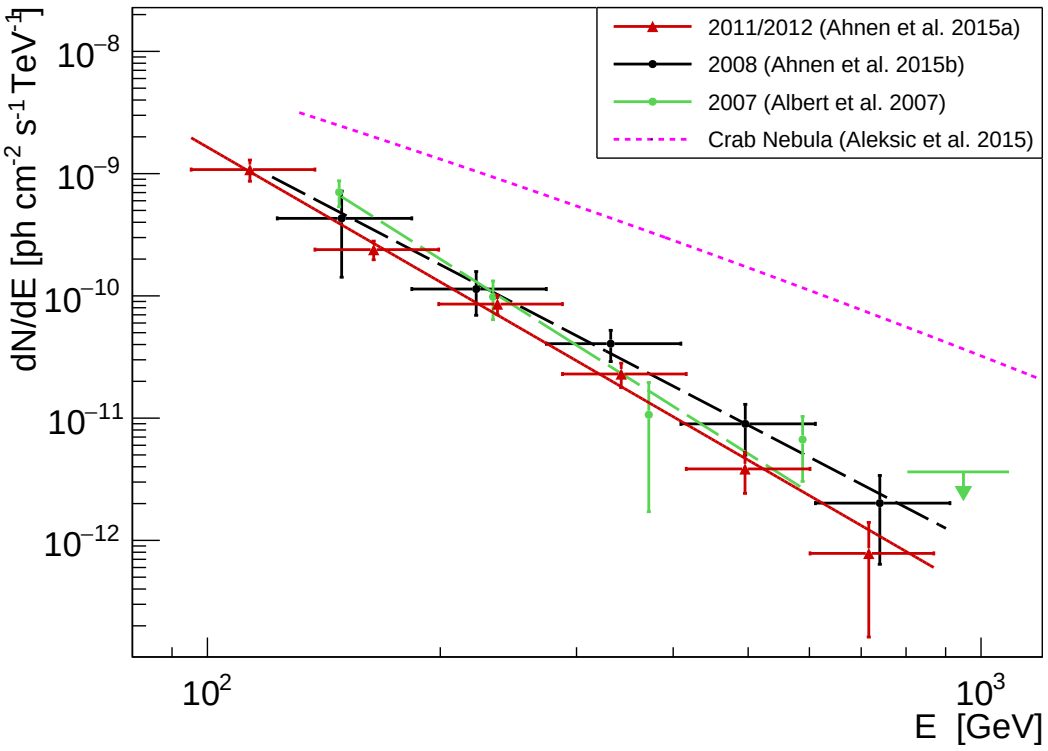

Figure 4.3: Historically observed differential spectra taken with MAGIC prior to 2014 flare [Ahnen et al. 2016a]. The Crab nebula spectrum is also shown for reference in pink dashed line [Aleksić et al. 2015].

Year	f_{obs} (10^{-10} cm^{-2} s$^{-1}TeV^{-1}$)	Γ_{obs}	Γ_{int} (10^{-11} ph cm^{-2} s^{-1})	$F_{>300\,\mathrm{GeV}}$
2007	2.0±0.1	4.0±0.5	3.3±0.7	1.58±0.32
2008	1.8±0.5	3.3±0.4	2.2±0.4	1.3±0.3
2011-2012	1.33±0.06	3.66±0.22	3.0±0.3	0.75±0.12

Table 4.1: Summary of VHE γ-ray spectra of 1ES 1011+496 for the MAGIC observations performed in 2007 [Albert et al. 2007a], 2008 [Ahnen et al. 2016b], and between 2011 and 2012 [Ahnen et al. 2016a]

Observations & Analysis

After the 1ES 1011+496 high flaring state alert issued by VERITAS on February 5^{th}, 2014, MAGIC triggered the ToO (Target of Opportunity) observations [Mirzoyan 2014]. These observations were performed during February-March 2014 for 17 nights in the zenith range of $20°-56°$. As discussed in section 3.6.2.1, due to strong moonlight, NSB fluctuations in the data increases, which results in higher energy threshold for the detection. Therefore, during strong moonlight between 13^{th} to 21^{st} February no observations were performed. The data were taken in the wobble-mode, where the pointing direction alternates between four sky positions at 0.4° away from the source (see section 3.5.2). To decrease the systematic uncertainties in the background estimation, four wobble positions were used. Except for the 7th March night observations (due to the presence of moonlight and clouds), data taken on all other nights were under good weather and dark conditions. After applying the quality cuts, total 12.80 hrs of good data, in the zenith range of $20°-50°$, were used for the further analysis. As discussed in section 3.6.1, data were analyzed with the standard MAGIC analysis using the routines in the MAGIC software package for stereoscopic analysis, MARS [Aleksić et al. 2016b].

Results

θ^2 plot and Skymaps

On applying low energy (LE) cuts (E<100 GeV, Hadronness < 0.28, size of events passing the image cleaning and stereoscopic reconstruction of >60 photo-electrons for each telescope) and the zenith angle range of 20-50° on total selected data of 12.80 hrs resulted in 5569.3 excess events above the background events.

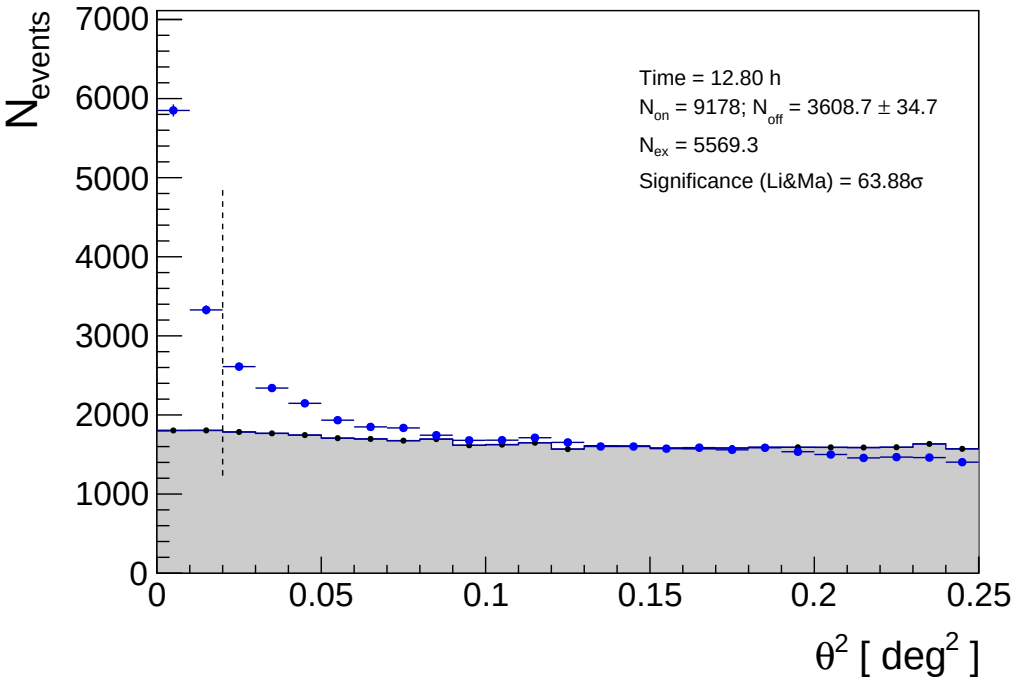

Figure 4.4: θ^2 distributions of the 1ES 1011+496 signal and background estimation from 12.80 hrs of MAGIC stereo observations taken from 6^{th} February to 7^{th} March 2014. The signal region is defined between zero and the vertical dashed line at 0.026 degrees^2.

Figure 4.4 shows the distribution of the squared angular distance θ^2 between the reconstructed event direction and the nominal position of 1ES 1011+496. The residual background events were estimated using three simultaneous OFF regions (OFF data is taken from the counter source position) with the same γ-ray acceptance as the ON-source region. The source was detected with a very strong detection with significance of 63.88σ (Figure 4.4). This was the first time that 1ES 1011+496 was detected with such a high sigma value since the discovery with MAGIC. The summary of the observation dates, effective observation time and the individual significances is given in the table 4.2. The significance was calculated according to Li & Ma equation 3.15 [Li & Ma 1983] (see section 3.6.1.8 for details).

Figure 4.5 shows the spatial distribution of the source significance above 100 GeV in the sky coordinates. To check the consistency of the reconstructed source position with the catalog position, a 2D Gaussian function was used to fit the excess of the skymap. The position obtained from this 2D Gaussian fit with RA: 10^h 15^m 0.7(4)^s and DEC: +49° 26^m 5(3)^s is consistent with a point-like source located at the catalog position of 1ES 1011+496 with a slight deviation observed in RA: 0.008(1)° and DEC: 0.0011(9)°. The grey star in figure 4.5 indicates the reconstructed source position. The color scale on the right indicates the relative flux values (the ratio between the exposure map and the background map, i.e., $N_{ex}/N_{bg(<0.1deg)}$) of the source. Figure 4.6 shows the test statistics (TS) distribution of the source significance above 100 GeV, resulted in maximum TS value of >80. The color scale indicates the test statistic value defined as the significance from Li & Ma equation (see equation 3.15) [Li & Ma 1983].

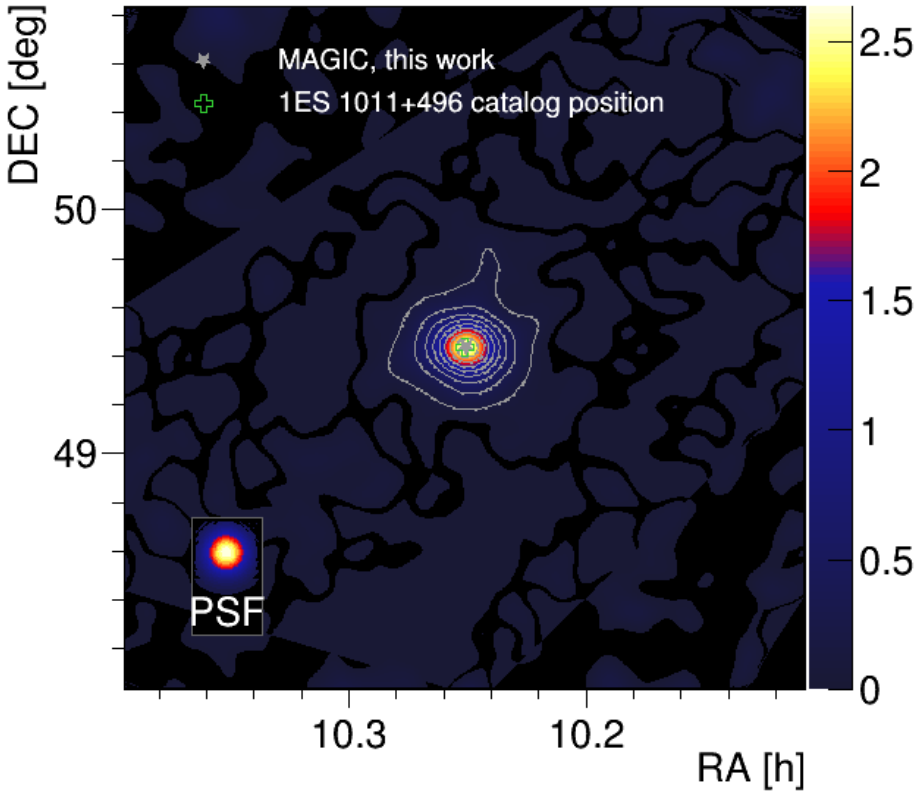

Figure 4.5: Flux map of 1ES 1011+496 sky region above 100 GeV from 12.80 hrs of MAGIC stereo observations (6^{th} February to 7^{th} March 2014). The grey star indicates the reconstructed source position. The color scale represents the relative flux values in $N_{ex}/N_{bg(<0.1deg)}$. In the lower left is the point-spread function of 0.071° used for this analysis.

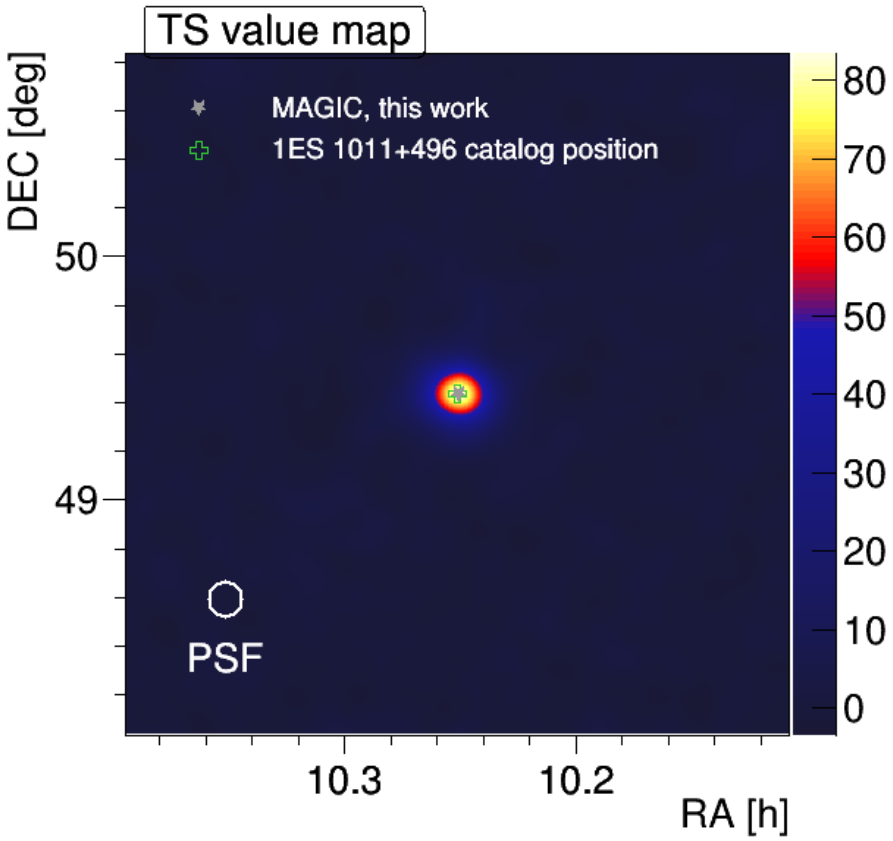

Figure 4.6: Significance map of 1ES 1011+496 sky region above 100 GeV from 12.80 hrs of MAGIC stereo observations (6^{th} February to 7^{th} March 2014). The color scale represents the test statistics value distribution. In the lower left is the point-spread function of 0.071° used for this analysis.

Light Curve

The integral fluxes (E > 200 GeV) for the observed period of 6^{th} February to 7^{th} March 2014 are shown in the night-wise γ-ray light curve in Figure 4.7. Summary of the observation dates, effective observation time and integral fluxes with threshold of E>200 GeV for 1ES 1011+496 2014 data is given in Table 4.2. The peak and mean integral flux measured was $(2.28 \pm 0.13) \times 10^{-10}$ cm^{-2}s^{-1} and $(0.72 \pm 0.01) \times 10^{-10}$ cm^{-2}s^{-1} respectively.

For the comparison, mean integral fluxes from the previous observations are given in Table 4.3 and are also shown in Figure 4.7. During this exceptionally high flare, the peak integral flux was even higher than the Crab Nebula flux. It was 14 and 17 times the mean integral flux from the observations performed in 2007 and 2008 respectively [Albert et al. 2007a, Reinthal et al. 2012] (blue dashed line and solid green line) and ∼29 times the mean integral flux from the observations performed during 2011-2012 MWL campaign [Aleksić et al. 2015a] (magenta dot and dashed

Date	MJD	Effective time [hrs]	Significance [σ]	$F_{(E>200\,GeV)}$ [10^{-10} cm^{-2} s^{-1}]
2014-02-06	56694	0.65	17.31	1.18 ± 0.11
2014-02-07	56695	2.31	24.86	0.76 ± 0.04
2014-02-08	56696	1.95	41.60	1.70 ± 0.00
2014-02-09	56697	1.30	21.76	1.13 ± 0.00
2014-02-10	56698	0.65	24.85	2.28 ± 0.13
2014-02-11	56699	0.49	16.52	1.43 ± 0.12
2014-02-22	56709	0.60	9.72	0.45 ± 0.07
2014-02-23	56710	0.64	8.63	0.48 ± 0.07
2014-02-25	56713	0.49	9.61	0.69 ± 0.10
2014-02-26	56714	0.65	8.11	0.49 ± 0.07
2014-02-27	56715	0.48	10.11	1.02 ± 0.12
2014-03-01	56717	0.49	8.60	0.32 ± 0.08
2014-03-02	56718	0.49	4.93	0.20 ± 0.07
2014-03-03	56719	0.49	3.94	0.34 ± 0.08
2014-03-05	56721	0.65	6.61	0.30 ± 0.06
2014-03-07	56723	0.48	5.96	0.38 ± 0.08
All		12.80	68.88	

Table 4.2: Summary of the observation dates, effective observation time, significances and integral fluxes with threshold of E>200 GeV for 1ES 1011+496 2014 data.

line).

During the whole flare observations, a high night-wise flux variability was observed; however, no significant intra-night variability was observed. Due to strong moonlight, no observations were performed during 13^{th} to 21^{st} February, hence showing the gap in the light curve.

Spectral energy distribution

The average observed spectral energy distribution (SED) is shown in Figure 4.8. As the observed spectrum is clearly curved, several functions were tried for fitting the spectrum, such as a power law (PWL), log parabola (LP), a smoothly-broken power law (SBPL) and a power law with an exponential cut-off (EPL).

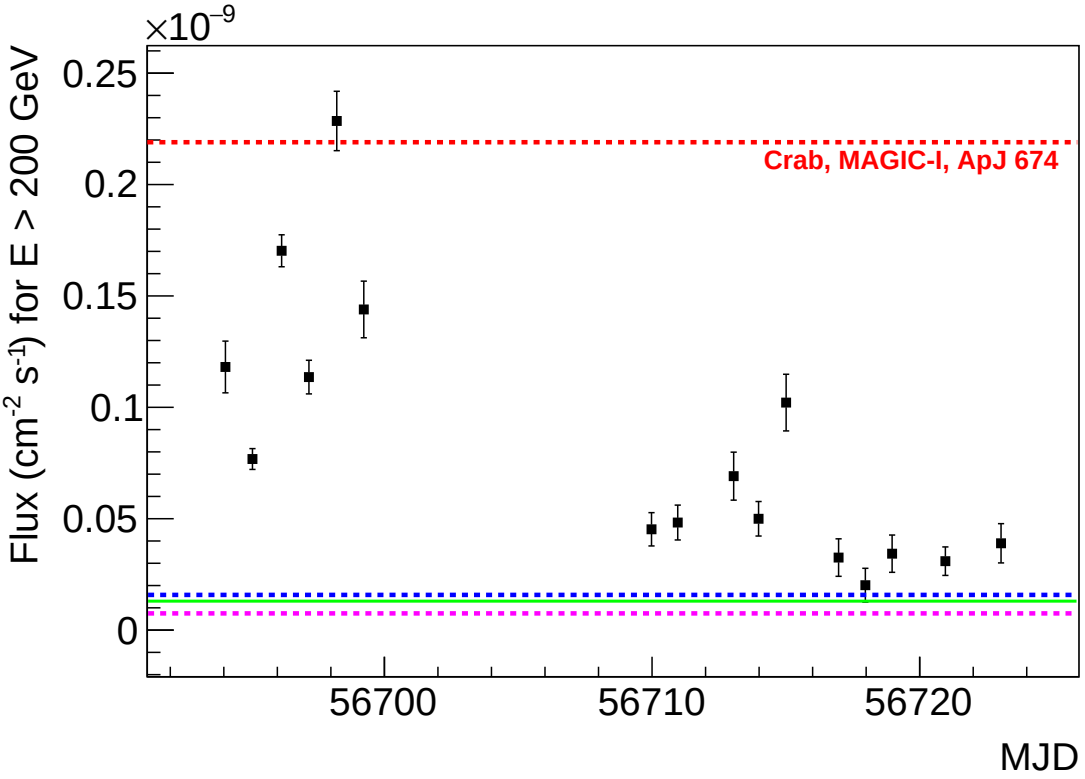

Figure 4.7: The night-wise light curve for 1ES 1011+496. The integral fluxes with the threshold of E > 200 GeV are shown for the observed period of 6^{th} February to 7^{th} March 2014. For comparison, the mean integral fluxes from 2007 discovery observations (blue dashed line) [Albert et al. 2007a], from 2008 observations (solid green line) [Ahnen et al. 2016b] and from the 2011-2012 MWL campaign (magenta dotted line) [Aleksić et al. 2015a] are also shown. The red dashed line shows the Crab nebula flux from MAGIC performance study [Albert et al. 2008a].

Here are the functions used for the modeling of the intrinsic spectrum:

power law:

$$\frac{dN}{dE} = f_0 \left(\frac{E}{E_0}\right)^{-\Gamma} \tag{4.1}$$

Log Parabola:

$$\frac{dF}{dE} = f_0 \left(\frac{E}{E_0}\right)^{-\Gamma-\beta\log(E/E_0)} \tag{4.2}$$

power law with Exponential Cutoff:

Year	$F_{>200\,\mathrm{GeV}}$ (10^{-11} ph cm^{-2} s^{-1})
2007	1.58±0.32
2008	1.3±0.3
2011-2012	0.75±0.12
2014	7.2±0.2

Table 4.3: Comparison of the integral fluxes above 200 GeV for 1ES 1011+496 observed in 2007 [Albert et al. 2007a], 2008 [Ahnen et al. 2016b], between 2011 and 2012 [Ahnen et al. 2016a] and in 2014 with MAGIC. The integral fluxes have been extrapolated from the log parabola fit to the observed spectrum of 2014 data and simple power law fits to the observed spectra of 2007, 2008, and 2011-2012 data.

$$\frac{dN}{dE} = f_0 \left(\frac{E}{E_0}\right)^{-\Gamma} \exp\left(-\frac{E}{E_{cut}}\right) \tag{4.3}$$

Smoothed Broken power law:

$$\frac{dN}{dE} = f_0 \left(\frac{E}{E_0}\right)^{-\Gamma_1} \left[1 + \left(\frac{E}{E_b}\right)^{g}\right]^{\frac{\Gamma_1-\Gamma_2}{g}} \tag{4.4}$$

In Figure 4.8, the observed SED is fitted with LP (red line) and with SBPL (blue line). Among all these, only SBPL achieves acceptable fit with probability of 95% and χ^2/NDF = 2.67/8, normalization factor $f_0 = (4.6 \pm 0.8) \times 10^{-11}$ cm^{-2}s^{-1}TeV^{-1}, normalization energy E_0 = 200 GeV, first spectral index $\Gamma_1 = 2.10 \pm 0.28$, the second spectral index $\Gamma_2 = 3.7 \pm 0.1$, the energy break $E_b = 241 \pm 34$ GeV, and the parameter $g = 4.9 \pm 3.0$. The next-best fit is provided by the LP with probability of 12% and χ^2/NDF = 15.08/10, normalization factor $f_0 = (3.9 \pm 0.1) \times 10^{-11}$ cm^{-2}s^{-1}TeV^{-1}, normalization energy E_0 = 200 GeV, the spectral index $\Gamma = 2.72 \pm 0.05$, and curvature index $\beta = 0.95 \pm 0.11$.

The unfolded observed (blue filled squares) and de-absorbed (magenta filled squares) differential energy spectra of the entire data of 12.8 hrs from 6^{th} February to 7^{th} March 2014 are shown in Figure 4.9. Unfolding is the reshuffling of events to estimate the true energy of the cosmic ray particle from the estimated energy from the number of Cherenkov photons [Albert et al. 2007e]. It was performed using the Schmellings algorithm [Schmelling 1994]. The observed spectrum is fitted with log parabola (blue line). The de-absorbed spectrum was achieved after correcting the effect of EBL using Franceschini 2008 model [Franceschini et al. 2008] (see chapter 7 for more details), and it was fitted with a simple power law function (magenta line). For comparison, we also show the observed differential spectra from MAGIC stereo observation in 2011/2012 [Ahnen et al. 2016a] (red filled circles) and MAGIC mono

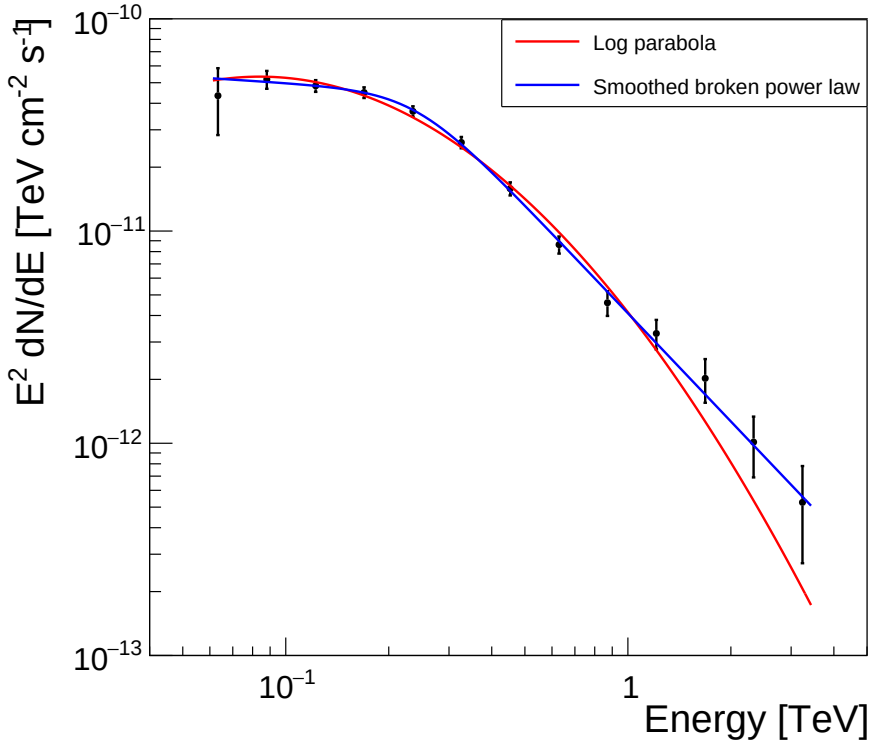

Figure 4.8: Spectral energy distribution of 1ES 1011+496 MAGIC observations during the high flaring state from 6^{th} February to 7^{th} March 2014. The spectrum is fitted with log parabola (red line) and also with a smoothed broken power law (blue line).

observations (black and green filled circles) in 2008 [Ahnen et al. 2016b] and 2007 [Albert et al. 2007a]. The comparison of spectral parameters is given in table 4.4. The spectral index of the 2014 flare data is harder than the all previous MAGIC observations. Since the discovery, for the first time such an extraordinary flare has been observed and with the spectrum spanning from 48 GeV to 3.6 TeV. However, even if statistically the spectral point is present at 48 GeV, it will not be used for further analysis in the following section, as the effect of the telescope systematics is not well known below the current MAGIC energy threshold of 50 GeV. Also, this was for the first time that the observed spectral shape was curved and hence fitted with log parabola, as opposed to simple power law function which was used to fit all other archival spectra. Interestingly, the complicated curved function such as log parabola is also not a good fit to the observed curved spectrum. However, the intrinsic (de-absorbed) spectrum can be well fitted with a power law, which shows that we observed the EBL imprint in the 1ES 1011+496 spectrum. During the entire flare, only flux variations were seen, but no significant spectral variability was observed.

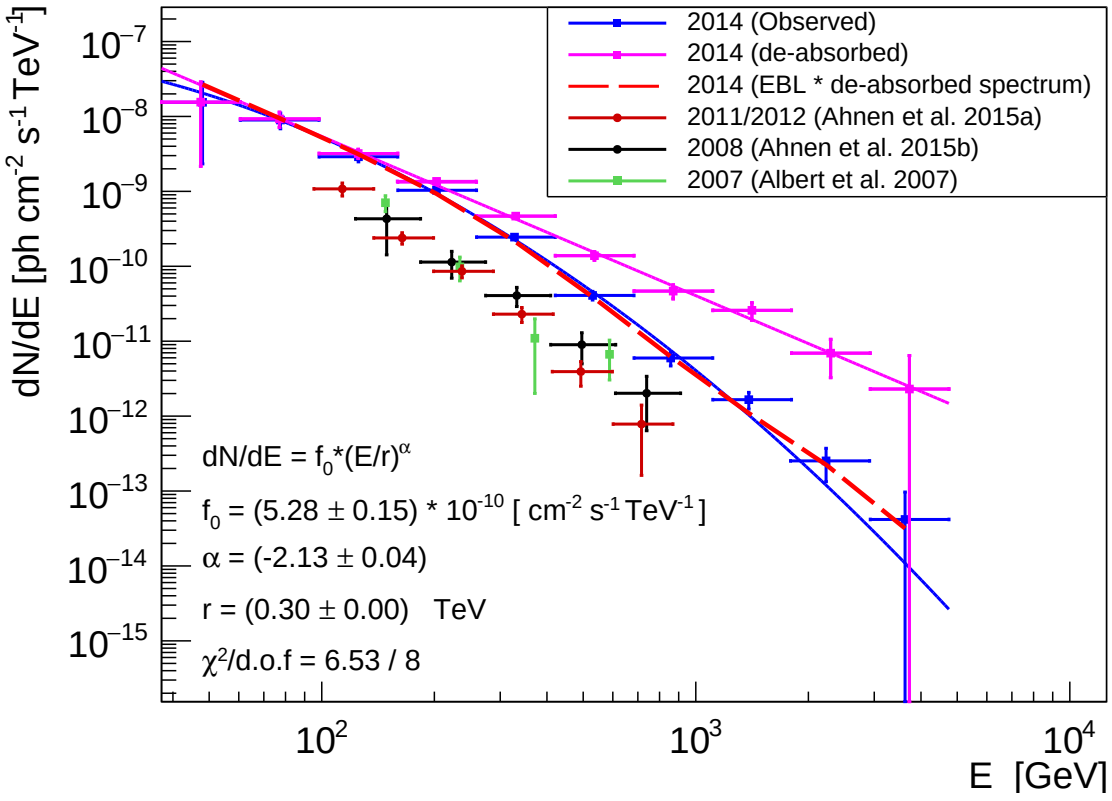

Figure 4.9: Unfolded observed differential spectrum (blue filled squares) of 1ES 1011+496 MAGIC observations during the high flaring state from 6^{th} February to 7^{th} March 2014. The observed differential spectrum is fitted with a log parabola (blue line). The de-absorbed spectrum was achieved by correcting the EBL using Franceschini 2008 model [Franceschini et al. 2008] (magenta filled squares) and fitted with a simple power law (magenta line). The dashed red line shows the effect of EBL absorption on the observed spectrum. The parameters from the de-absorbed spectrum are given in the left corner. For comparison, we also show differential spectra from MAGIC observation prior to 2014 flare [Ahnen et al. 2016a, Ahnen et al. 2016b, Albert et al. 2007a].

Year	$f_{(E=200\,\mathrm{GeV})}$ (10^{-10} cm^{-2} s$^{-1}TeV^{-1}$)	Γ_{obs}	Γ_{int}
2007	2.0±0.1	4.0±0.5	3.3±0.7
2008	1.8±0.5	3.3±0.4	2.2±0.4
2011-2012	1.33±0.06	3.66±0.22	3.0±0.3
2014	9.6±0.4	2.73±0.05	2.13±0.04

Table 4.4: Comparison of the differential fluxes at 200 GeV for 1ES 1011+496 observed in 2007 [Albert et al. 2007a], 2008 [Ahnen et al. 2016b], between 2011 and 2012 [Ahnen et al. 2016a] and in 2014 with MAGIC. The differntial fluxes have been calculated from the log parabola fit to the observed spectrum of 2014 data and simple power law fits to the observed spectra of 2007, 2008, and 2011-2012. Note that, all the intrisic spectral indices are calculated from the simple power law fits to the EBL corrected spectra for all the mentioned years.

Combined MAGIC and *Fermi*-LAT spectrum

In order to study the SED of 1ES 1011+496 in GeV-TeV energy range, contemporaneous data with *Fermi*-LAT in HE γ rays to the MAGIC VHE γ-ray observations have been collected. For our analysis, we have used publically available LAT Pass 8[a] data from 24^{th} January to 8^{th} March 2014 in the energy range 0.1-500 GeV. The data were selected from the region of interest (ROI) of 10° and analyzed with the *Fermi Science Tools*[b] package v10r0p5. We used the 'Source' event class with instrument response function of P8R2_SOURCE_V6 along with *gll_iem_v06* Galactic diffuse emission model and the *iso_P8R2_SOURCE_V6_v06* model to account for the isotropic diffuse γ-ray background. Model files were created automatically with the script make3FGLxml.py from the third *Fermi*-LAT point source catalog 3FGL [Acero et al. 2015]. The spectral shape of 1ES 1011+496 in the GeV regime is a power law in 3FGL of the form:

$$\frac{dN}{dE} = f_0 \left(\frac{E}{E_0} \right)^{-\Gamma} \tag{4.5}$$

where f_0 is the flux normalization factor, E_0 is the normalization energy, and Γ is the spectral index. The fluxes were estimated from the unbinned likelihood fit to the data of the model, containing all the sources from the 3FGL [Acero et al. 2015] within a distance smaller than 1.5 times the ROI. The spectra of the fitted sources were assumed to be of a power law shape, with the best-fit spectral indices taken from 3FGL. For the power law fit, all parameters were left free for the data in the entire energy range of 0.1 to 500 GeV. Also, all other sources within a radius of 10°

[a] http://fermi.gsfc.nasa.gov/cgi-bin/ssc/LAT/LATDataQuery.cgi

[b] `http://fermi.gsfc.nasa.gov/ssc/data/analysis/scitools/likelihood_tutorial.html`

along with the Galactic diffuse emission were left free for the fit. However, all sources between 10°−15° were fixed to their catalog values.

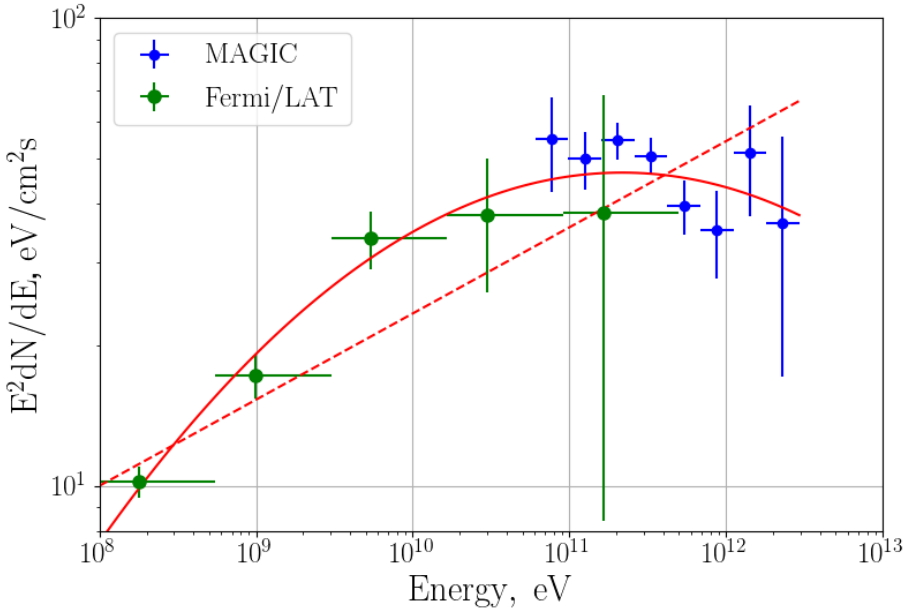

Figure 4.10: Combined MAGIC (EBL corrected) and quasi-simultaneous *Fermi*-LAT SED in the energy starting from 100 MeV until ∼3 TeV. The EBL correction was applied to the observed MAGIC SED using Franceschini 2008 model [Franceschini et al. 2008]. The solid red line corresponds to log parabola fit and the dashed red line corresponds to power law fit. Note that, MAGIC SED points which are below the energy threshold of 50 GeV (as effect of telescope systematics is not well known) or with uncertainty higher than 2σ level were not included in this plot.

Figure 4.10 shows the combined MAGIC and *Fermi*-LAT spectral energy distribution in the energy starting from 100 MeV until ∼3 TeV. Note that, MAGIC SED points which are below the energy threshold of 50 GeV (as it could be result of statistical fluctuation) and with uncertainty higher than 2σ level were not included in this plot. The spectrum was fitted with power law as given in equation 4.5 and also with a log parabola as given below:

$$\frac{dN}{dE} = f_0 \left(\frac{E}{E_0}\right)^{-(\Gamma+\beta log(E/E_0))} \tag{4.6}$$

where f_0 is the flux normalization factor, E_0 is the normalization energy, Γ and β are spectral index and curvature index respectively. In figure 4.10, the solid red line

corresponds to a log parabola fit, and the dashed red line corresponds to a power law fit. The parameters from the combined fit for power law and log parabola functions are given in table 4.5, which shows that log parabola fits the spectrum better than the power law. Thanks to increased sensitivity due to MAGIC upgrade and *Fermi*-LAT Pass 8 data, it was possible to achieve precise measurements of 1ES 1011+496 at high flare state, and also to obtain a gapless combined MAGIC and *Fermi*-LAT spectrum.

Spectral Parameters	Log Parabola	Power Law
f_0 (eV cm^{-2} s^{-1})	. 45.85 ± 3.85	35.68 ± 2.38
E_0 (GeV)	100	100
Γ	-1.95 ± 0.03	-1.81 ± 0.01
β	(-3.08 ± 0.75) × 10^{-2}	...
χ^2/dof	6.9/13	22.0/14
Probability	0.91	0.78

Table 4.5: Spectral fit parameters of 1ES 1011+496 for the combined MAGIC and quasi-simultaneous *Fermi*-LAT spectrum.

SED modeling

Figure 4.11 shows the MWL SED of 1ES 1011+496, which is constructed using the high flaring state VHE data taken with MAGIC during February-March 2014, and the quasi-simultaneous HE data with *Fermi*-LAT (see section 4.4.4), and UVOT and X-ray data with Swift. Both UVOT and X-ray data with Swift were corrected for Galactic extinction and the contribution from the host galaxy and taken from the already published data from [Sinha et al. 2017]. The VHE γ-ray data was corrected for the EBL using the [Franceschini et al. 2008] model. The SED is modeled under the scope of the simple leptonic scenario, which helps to understand the nature of the electron distribution responsible for the emission through synchrotron and SSC processes. Both the energy bumps of the SED, i.e., low and high, are well constrained by these quasi-simultaneous MWL data. The goodness of the model is judged by eye. Therefore, the curve represents only one working set of SED parameters, rather of being a real fit to the data.

As discussed in section 2.6.3, a one-zone SSC model from [Tramacere et al. 2011, Tramacere et al. 2009, Massaro et al. 2006] was applied to reproduce the broadband SED, assuming a spherical emission region with radius R, filled with tangled magnetic field strength B. A primary spectrum of a relativistic electron population is approximated by a broken power law energy distribution specified with the γmin, γmax, and the break at γb, Lorentz factors; the slopes before (n1) and after (n2)

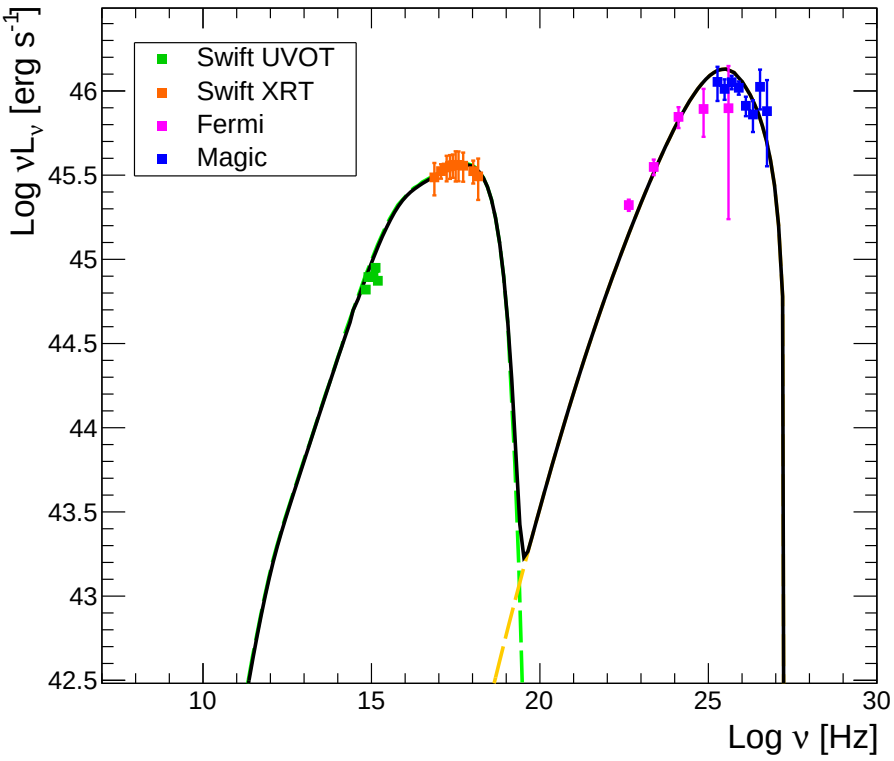

Figure 4.11: The broadband spectral energy distribution of 1ES 1011+496 constructed using the high flaring state VHE data taken with MAGIC during February-March 2014, and the quasi-simultaneous HE data with *Fermi*-LAT and UVOT and X-ray data with Swift. The solid black line represents the fit with a one-zone SSC model. The VHE γ-ray data was corrected for the EBL using the [Franceschini et al. 2008] model.

the break; and the electron density parameter K. Relativistic effects are taken into account by the Doppler factor δ. Therefore, the electron spectrum is given as:

$$N(\gamma)d\gamma = \begin{cases} K\gamma^{-n1}d\gamma & \gamma_{min} < \gamma < \gamma_b \\ K\gamma_b^{n_2-n_1}\gamma^{-n_2}d\gamma & \gamma_b < \gamma < \gamma_{max} \end{cases} \tag{4.7}$$

The modeling was performed using an online AGN SED tool[c]

For the SED presented here, the maximum luminosity for the synchrotron bump is $\nu L\nu_{Sync} = 3.64 \times 10^{45}$ erg s^{-1}, which peaks at $\nu_{Sync} = 6.09 \times 10^{17}$ Hz (2.5 keV), whereas, the maximum luminosity for the inverse Compton bump is $\nu L\nu_{SSC} = 1.35 \times 10^{46}$ erg s^{-1}, which peaks at $\nu_{SSC} = 3.17 \times 10^{25}$ Hz (131.1 GeV). Therefore, the SED

[c] `http://www.isdc.unige.ch/sedtool/PROD/html_js/SED_Web_tool/Doc/test_doc/index.html`

shows slight indication of an inverse Compton dominance. The physical parameters for the 2014 data and comparison with those derived from the previous observations are listed in table 4.6.

Year	γ_{min} [10^3]	γ_{break} [10^4]	γ_{max} [10^5]	n1	n2	B [G]	K 10^3 [cm^{-3}]	R 10^{16} [cm]	δ
2007	3.0	5.0	200.0	2.0	5.0	0.15	20	1.0	20.0
2008	7.0	3.4	8.0	1.9	3.3(3.5)	0.048	0.7(0.8)	3.25	26.0
2011-2012[a]	10.0	4.0	7.0	2.0	3.7	0.19	10.0	1.0	20.0
2011-2012[b]	10.0	3.3	4.0	2.0	3.8	0.19	13.4	0.9	20.0
2014	1.0	4.0	10.0	1.76	2.75	0.05	0.62	2.0	10.0

Table 4.6: Fitted one zone SSC model parameters for 1ES 1011+496 high flaring state data during February-March 2014. The corresponding broadband SED is shown in figure 4.11 by solid black line. For comparison, model parameters from previous observations performed in 2007 [Albert et al. 2007a], 2008[Ahnen et al. 2016b], 2011-2012[a] (X-ray spectrum from March 27, 2012) and 2011-2012 (X-ray spectrum from March 31, 2012) [Aleksić et al. 2015a] are also shown.

Once the variability timescales, frequencies, and fluxes at the two SED peaks are measured, the parameters of the one-zone SSC model can be uniquely fixed [Tavecchio et al. 1998]. In case of our VHE data with MAGIC, a night-wise variability was observed, and then considering a Doppler $\delta = 10$ (value typically found in such sources [Tavecchio et al. 2010], a radius of the emitting region was constrained to 2×10^{16} cm. The other parameters derived by reproducing the SED are also similar to those typically inferred for HBLs, in particularly the low magnetic field strength, leading to deviations from equipartition [Tavecchio et al. 2010, Dermer et al. 1993]. The ratio of the energy density of the electrons and the magnetic field, i.e., U_B/U_e corresponds to 0.003, indicating that the magnetic field is far below equipartition. This result is also re-confirming the general framework of the one-zone SSC model for TeV emitting blazars, that HBLs largely show a dominance of the particle energy density over the magnetic energy density. The comparison with previous models of the source SED indicates a good agreement for most of the parameters, except the Doppler factor. For 2007, 2011-2012 low state data, the values of the inferred magnetic field are higher than the 2014 data. The γmin and γmax Lorentz factors show relatively large variations among the models, but these parameters usually are not well constrained by the available data. The parameters from the 2008 modeling are in good agreement with the model presented here with 2014 data.

Summary

Here I have reported the observations of the extraordinary flare from 1ES 1011+496 during 6^{th} February to 7^{th} March 2014. The observations pertaining to this study were performed with MAGIC, and total 12.8 hrs of data were collected. The source was detected brightly with a significance of $63\,\sigma$. The flux observed during the flare was historically high from X-rays to TeV data. Compared to previous MAGIC observations, the peak flux was 14 and 17 times the mean integral flux from the observations performed in 2007 and 2008 respectively, and ∼29 times the mean integral flux from the observations performed during 2011-2012 MWL campaign. Also, compared to these previous low emission state MAGIC observations, the spectral index from the observed spectrum was found to be harder.

During the entire flare, only flux variations were seen, but no significant spectral variability was observed. This was the first time such an extraordinary flare was observed with the spectrum spanning from 48 GeV to 3.6 TeV, which allowed the better overlapping between MAGIC and *Fermi*-LAT spectrum. The parameters from the combined fit for MAGIC and *Fermi*-LAT show that a log parabola function fits the spectrum better than a power law. Thanks to increased sensitivity due to MAGIC upgrade and *Fermi*-LAT Pass 8 data, it was possible to achieve precise measurements of 1ES 1011+496 at high flare state, and also to obtain a gapless combined MAGIC and *Fermi*-LAT spectrum in the energy range of 100 MeV to ∼3 TeV. Also, this was the first time that the spectral shape of VHE spectrum with MAGIC showed intrinsic curvature and hence needed a complicated function for the fitting, whereas for all previous observations a simple power law was used for fitting the spectra. Interestingly, once the EBL was corrected spectrum could be fitted with just a simple power law, which indicates that we measured the EBL imprint clearly for the first time. This allowed us to further study the effect of EBL absorption on the spectra in detail. These results of the EBL study will be discussed in chapter 7.

I also presented the broadband SED of the 1ES 1011+496, which is constructed using a one-zone SSC model for the high flaring state VHE data taken with MAGIC during March-June 2014, and the quasi-simultaneous HE data with *Fermi*-LAT, and UVOT- X-ray data with Swift. The SED presented here shows a slight indication of the dominance of the inverse Compton with the peak at ∼131 GeV. The ratio of the energy density of the electrons and the magnetic field, indicating that the magnetic field is far below equipartition. This result is re-confirming the general framework of the one-zone SSC model, that HBLs largely show a dominance of the particle energy density over the magnetic energy density at TeV energies. In general, the model parameters from 2014 data are in good agreement with those adopted from 2007, 2008, and 2011-2012.

5. Monitoring of the distant HBL PKS 1424+240

Motivation

PKS 1424+240 is another extragalactic high-peaked BL Lac with redshift z>0.6035. It has been studied intensively with MAGIC at VHE γ rays since 2006. However, the VHE γ-ray emission was not discovered until 2009. At this high redshift, the VHE intrinsic γ-ray emission is significantly affected by EBL (see chapter 7). Therefore, with a strong signal and the right energy coverage, it is possible to measure the EBL imprint. This chapter aims to present the analysis and results from MAGIC monitoring of PKS 1424+240 observations performed during March to June 2014. These data show strong detection of the source. The flux and spectrum from these observations were found to be on a similar level as the previous MAGIC observations performed from 2009 to 2011. In the following sections, first I will discuss the status of the previous observations, then details about the observations and analysis with MAGIC. In the results section, first I will discuss the details of the signal detection plots (section 5.4.1), then light curve (section 5.4.2), energy spectrum (section 5.4.3 and 5.4.4), and multiwavelength spectral modeling (section 5.4.5). The high redshift and strong detection in these data make PKS 1424+240 an excellent case to study the effect of EBL on the AGN spectra. The EBL related results will be discussed later in chapter 7.

Status of the previous observations

PKS 1424+240 is an AGN classified as high-frequency peaked BL Lac (HBL) (see section 2.3), with RA: $14^{\mathrm{h}}\,27^{\mathrm{m}}\,00^{\mathrm{s}}$ and DEC:$+23^{\circ}\,47^{'}\,40^{''}$. In extragalactic γ-ray astronomy, redshift determination of BL Lac objects is challenging due to featureless non-thermal spectra. So, like many other BL Lac objects, the redshift of PKS 1424+240 is still uncertain. Despite several optical observation campaigns, no absorption or emission lines were detected in the optical spectra. Previous measurements resulted in lower limits on redshift of $z > 0.67$ [Sbarufatti et al. 2005] and upper limit of $z = 1.1$ [Rau et al. 2012]. Recently in 2013, a firm lower limit of $z \geq 0.6035$ was determined by [Furniss et al. 2013]. In this thesis, now onwards, I will use this lower limit as the redshift of this source for further analysis.

PKS 1424+240 was first discovered in the 1970s as a radio source by [Fanti et al. 1974], and later in 1988, it was identified as a blazar by Impey & Tapia [Impey & Tapia 1988]. During 2006-2007, the source was observed by MAGIC-I, which resulted in the upper limits on flux for E>120 GeV [Aleksić et al. 2011]. In 2009, the source was observed with *Fermi*-LAT from its bright source list, which resulted in the first detection at HE γ rays. The spectrum observed was rather hard with a spectral index of 1.85±0.07 [Abdo et al. 2009]. In spring 2009, it was observed with VERITAS [Acciari et al. 2010] and finally entered in the VHE source catalog (TeVcat[a]). The 2009 VERITAS observations were triggered by *Fermi*-LAT, which proves the key role of the *Fermi* satellite in hunting high energy sources.

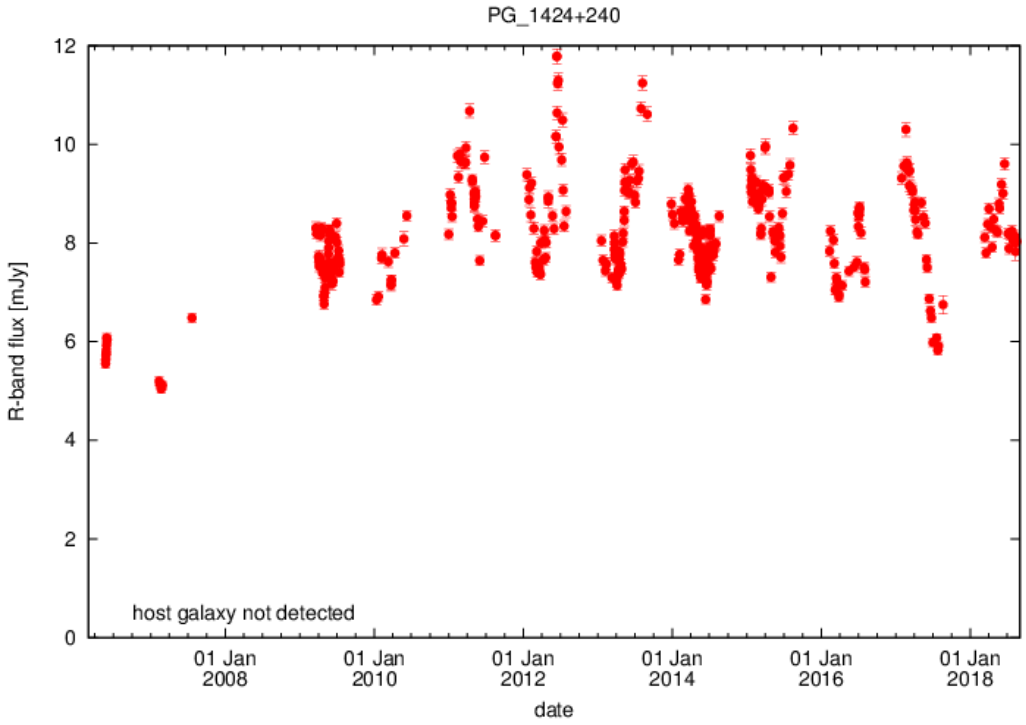

Figure 5.1: Long term optical light curve of PKS 1424+240 measured in R-band from the Tuorla Observatory Blazar Monitoring Program from 2006 to 2018. [Image credit: `http://users.utu.fi/kani/1m/PG_1424+240_jy.html`].

PKS 1424+240 is being monitored regularly with KVA and Turola observatory under the Blazar monitoring program in optical wavelengths at R-band (see figure 5.1) since 2006 to the present day. In April-June 2009, MAGIC observations in the mono mode were triggered by the optical outburst in R-band reported by Turola observatory, suggesting the source was in flaring state. As shown in figure 5.2, the

[a] `http://tevcat.uchicago.edu/`

observed spectrum was well fitted using a simple power law in the fit range of 150-400 GeV with normalization factor $f_0 = (1.3 \pm 0.6_{stat} \pm 0.4_{sys}) \times 10^{-10}$ TeV^{-1} cm^{-2} s^{-1}, a soft spectral index $\Gamma = 5.0 \pm 1.7_{stat} \pm 0.7_{sys}$ and normalization energy of 200 GeV. The mean integral flux for E>150 GeV was observed to be $(1.66 \pm 0.50) \times 10^{-11}$ photons cm^{-2} s^{-1}. Although the observation period was the same, due to the different time coverage, the observed differential fluxes with MAGIC and VERITAS were different; MAGIC flux was higher. Also, contrary to VERITAS observations, a hint of flux variability was observed in MAGIC 2009 observations on monthly scales.

The follow-up observations were performed during March-June 2010 with MAGIC in stereo mode. As shown in figure 5.2, the observed spectrum was well fitted using a simple power law in the fit range of 100-300 GeV with normalization factor $f_0 = (0.5 \pm 0.2_{stat} \pm 0.1_{sys}) \times 10^{-10}$ TeV^{-1} cm^{-2} s^{-1}, spectral index of $\Gamma = 3.5 \pm 1.2_{stat} \pm 0.5_{sys}$, which was harder compared to 2009 observations and normalization energy of 200 GeV. The mean integral flux for E>150 GeV was observed to be $(0.53 \pm 0.25) \times 10^{-11}$ photons cm^{-2} s^{-1}, which was lower than the 2009 observations. No significant flux variability was observed in MAGIC 2010 observations on daily or monthly scales.

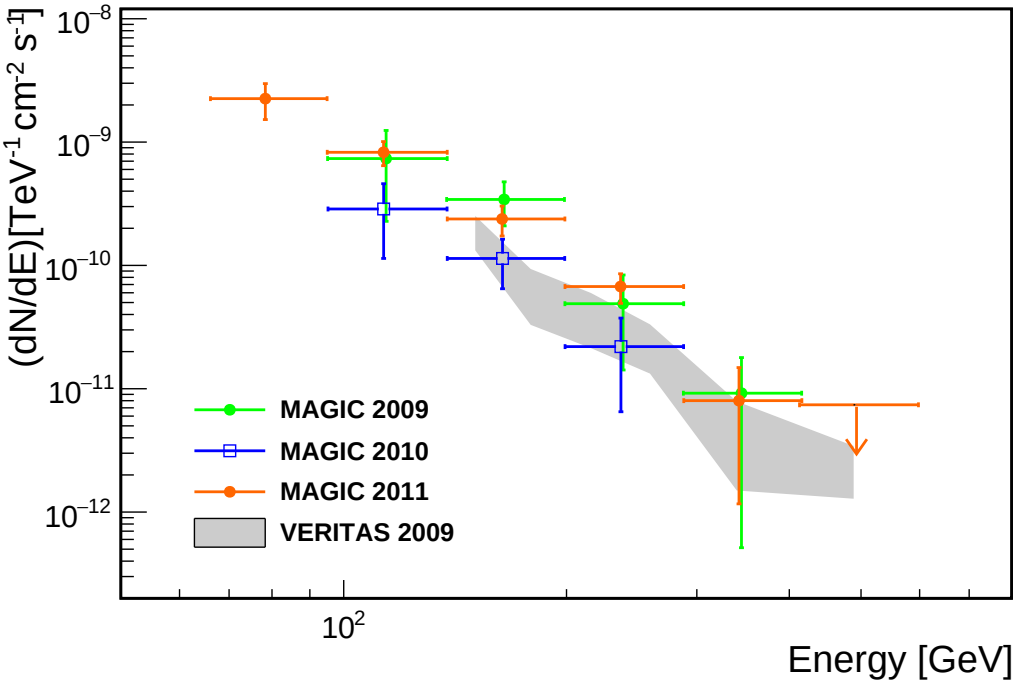

Figure 5.2: Comparison of PKS 1424+240 differential spectra for 2009-2011 archival data. The orange downward arrow represents the upper limit of the 95% confidence level for 2011 data. Image credit [Aleksić et al. 2014].

Monitoring of the source with MAGIC in stereo mode continued during April-May 2011. As shown in figure 5.2, the observed spectrum was well fitted using a simple power law in the fit range of 100-400 GeV with normalization factor $f_0 = (1.0 \pm 0.3_{stat} \pm 0.2_{sys}) \times 10^{-10}$ TeV^{-1} cm^{-2} s^{-1}, spectral index of $\Gamma = 3.9 \pm 0.7_{stat} \pm 0.2_{sys}$, which was also harder compared to 2009 observations, and on a similar level compared to 2010 observations and normalization energy of 200 GeV. The mean integral flux for E>150 GeV was observed to be $(1.0 \pm 0.23) \times 10^{-11}$ photons cm^{-2} s^{-1}, which was also lower than the 2009 observations, but on a similar level compared to 2010 observations. No significant flux variability was observed in MAGIC 2011 observations on daily or monthly scales.

Observations & Analysis

The monitoring observations of PKS 1424+240 with MAGIC started again in 2014 after a gap of three years. The observations were performed under the EBL key science program for 39 nights, during 24th March to 6th June 2014, in the zenith range of 5°−46°. As discussed in section 3.6.2.1, due to strong moonlight, NSB fluctuations in the data increases, which results in higher energy threshold for the detection. Therefore, no data were taken during the strong moon condition. Due to bad weather, the data taken on 11^{th} and 19^{th} April, 1^{st} May and 4^{th} June were discarded. The data were taken in the wobble-mode, where the pointing direction alternates between four sky positions at 0.4° away from the source (see section 3.5.2). To decrease the systematic uncertainties in the background estimation, four wobble positions were used. After applying the quality cuts, total 27.58 hrs of good quality data, in the zenith range of 5°−46°, were used for the further analysis. As discussed in section 3.6.1, data were analyzed with the standard MAGIC analysis using the routines in the MAGIC software package for stereoscopic analysis, MARS [Aleksić et al. 2016b].

Results

θ^2 plot and Skymaps

On applying low energy (LE) cuts (E<100 GeV, Hadronness < 0.28, size of events passing the image cleaning and stereoscopic reconstruction of >60 photo-electrons for each telescope) and the zenith angle range of 5°-46°, left us with a total selected data of 27.58 hrs which resulted in 1898.6 excess events above the background events.

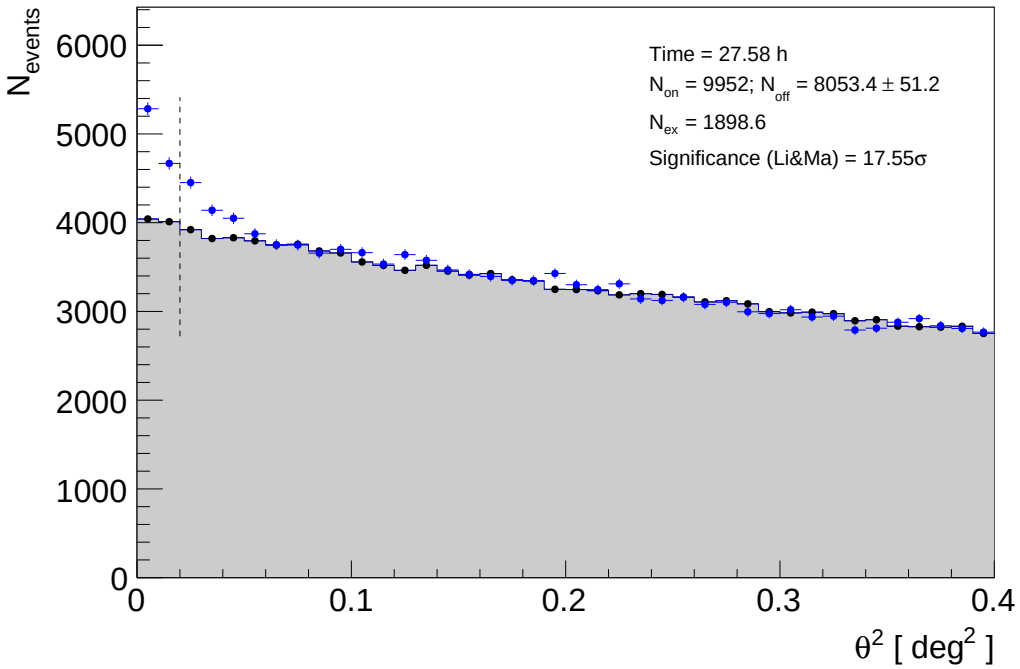

Figure 5.3: θ^2 distributions of the PKS 1424+240 signal and background estimation from 27.58 hrs of MAGIC stereo observations taken from 24^{th} March to 6^{th} June 2014. The signal region is defined between zero and the vertical dashed line at 0.026 degrees^2.

Figure 5.3 shows the distribution of the squared angular distance θ^2 between the reconstructed event direction and the nominal position of PKS 1424+240. The residual background events were estimated using three simultaneous OFF regions (OFF data is taken from the counter source position) with the same γ-ray acceptance as the ON-source region. The source was detected with a very strong detection with a significance of 17.55σ. However, no clear signal was detected in the individual night data, except for two nights; 2014-03-27 and 2014-04-05, where the source was detected with significance above 5 σ (see table 5.1). The summary of the observation dates, effective observation time and the individual significances is given in the table 5.1. The significance was calculated according to Li & Ma equation 3.15

[Li & Ma 1983] (see section 3.6.1.8 for details).

Fig. 5.4 shows the spatial distribution of the source significance above 100 GeV in the sky coordinates. To check the consistency of the reconstructed source position with the catalog position, a 2D Gaussian function was used to fit the excess of the skymap. The position obtained from this 2D Gaussian fit with RA: $14^h\ 27^m\ 8(3)^s$ and DEC: $+23°\ 48'\ 21(62)''$ is consistent with a point-like source located at the catalog position of PKS 1424+240 with a slight deviation observed in RA: 0.03(1)° and DEC: 0.01(1)°. The grey star in figure 5.4 indicates the reconstructed source position. The color scale on the right indicates the relative flux values (the ratio between the exposure map and the background map, i.e., $N_{ex}/N_{bg(<0.1deg)}$) of the source. Figure 5.5 shows the test statistics (TS) distribution of the source significance above 100 GeV, resulted in maximum TS value of >18. The color scale indicates the test statistic value defined as the significance from the Li & Ma equation 3.15 [Li & Ma 1983].

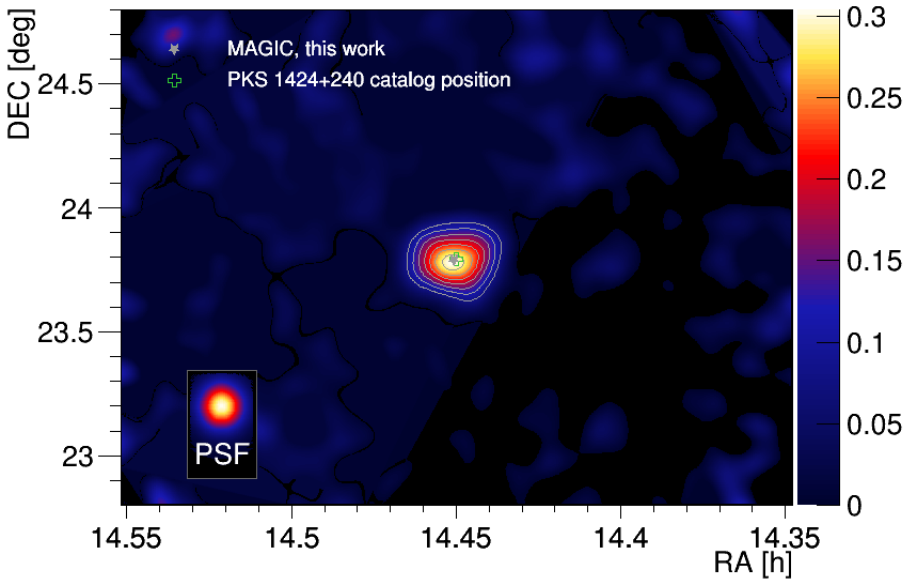

Figure 5.4: Flux map of PKS 1424+240 sky region above 100 GeV from 27.58 hrs of MAGIC stereo observations (24^{th} March to 6^{th} June 2014). The grey star indicates the reconstructed source position. The color scale represents the relative flux values in $N_{ex}/N_{bg(<0.1deg)}$. In the lower left is the point-spread function of 0.071° used for this analysis.

Light Curve

The integral fluxes (E >150 GeV) for the observed period of 24^{th} March to 6^{th} June 2014 are shown in the night-wise γ-ray light curve in Figure 5.6. Summary of the

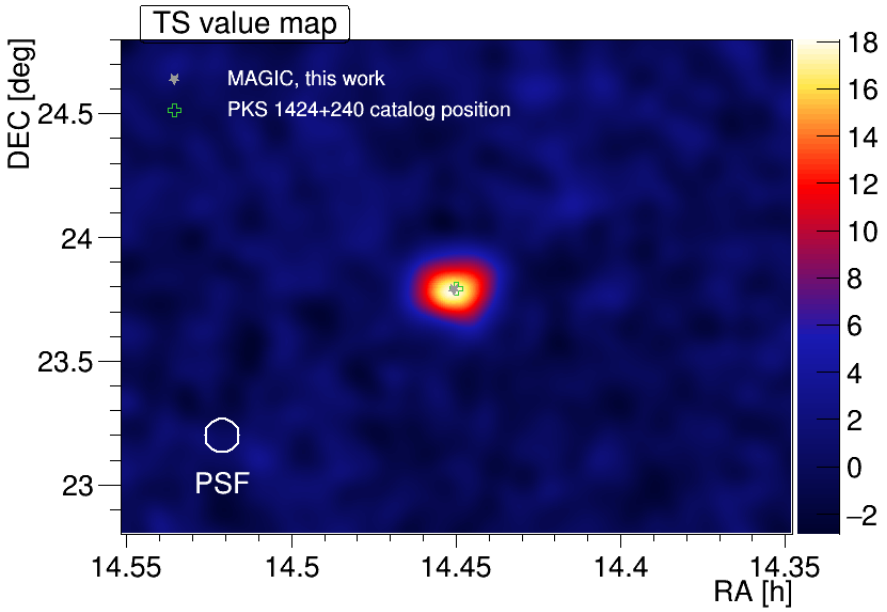

Figure 5.5: Significance map of PKS 1424+240 sky region above 100 GeV from 27.58 hrs of MAGIC stereo observations (24^{th} March to 6^{th} June 2014). The color scale represents the test statistics value distribution. In the lower left is the point-spread function of 0.071° used for this analysis.

observation dates, effective observation time and integral fluxes with a threshold of E>100 GeV for PKS 1424+240 2014 data is given in Table 5.1.

The mean integral flux measured was $(8.5 \pm 1.2) \times 10^{-12}$ cm^{-2}s^{-1} with a constant fit probability of 14% and $\chi^2/NDF = 42/33$. Even though the observation times of the individual nights were rather short as given in table 5.1, the significances of the integral fluxes derived on a nightly basis are above 3σ for 24^{th} March to 24^{th} April and above 2σ for most of the nights from 25^{th} April to 6^{th} June. During the whole observations, no significant night-wise, and intra-night flux variability was observed.

For comparison, mean integral fluxes from the previous observations are given in Table 5.2 and are also shown in Figure 5.6. During this monitoring, except for 2009 observations [Aleksić et al. 2014], the mean integral flux from 2014 observations is found to be on a similar level within the errors to the 2010 and 2011 observations [Aleksić et al. 2014].

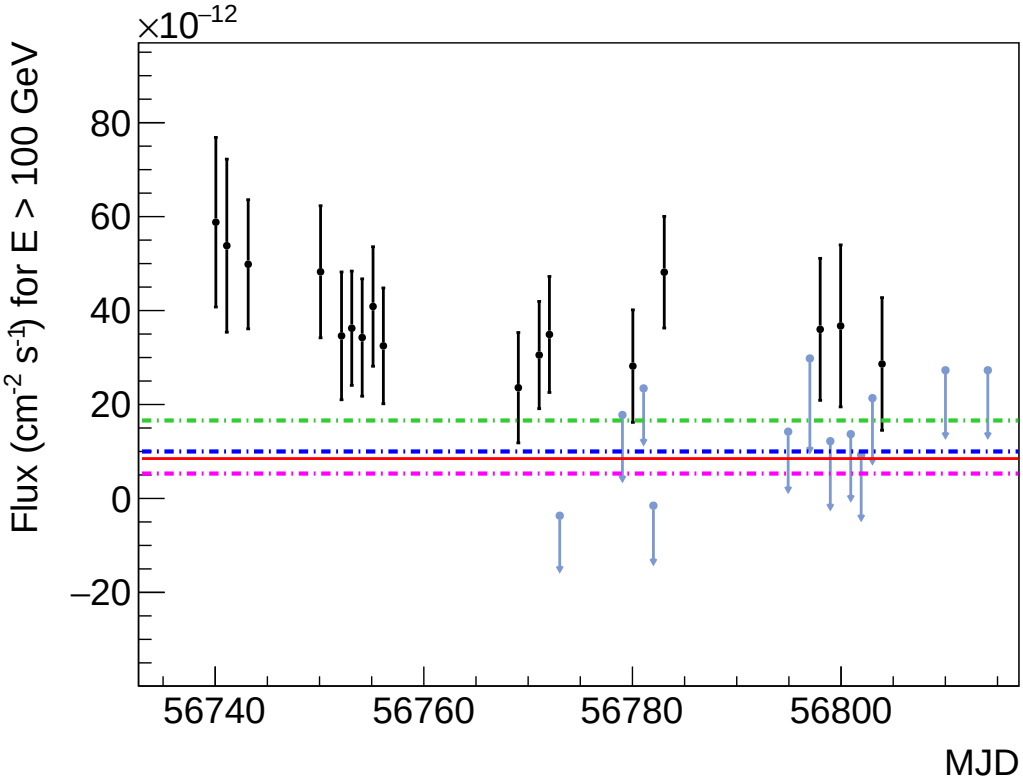

Figure 5.6: The night-wise light curve for PKS 1424+240. The integral fluxes with the threshold of E > 100 GeV are shown for the observed period of 24^{th} March to 6^{th} June 2014. The solid red line shows the mean integral flux from 2014 observation. For comparison, the mean integral fluxes from 2009 (green dot-dashed line), 2010 (magenta dot-dashed line) and 2011 (blue dot-dashed line) [Aleksić et al. 2014] are also shown. The 95% upper limits are shown in grey.

Differential energy spectrum

The unfolded observed (blue filled squares) and de-absorbed (magenta filled squares) differential energy spectra of the entire data of 27.58 hrs from 24^{th} March to 6^{th} June 2014 is shown in Figure 5.7. The unfolding was performed using the Tikhonov algorithm [Albert et al. 2007, Tikhonov & Arsenin 1977].
The observed spectrum is fitted with a simple power law of form:

$$\frac{dF}{dE} = f_0 \left(\frac{E}{E_0}\right)^{-\alpha} \tag{5.1}$$

where, normalization factor $f_0 = (6.89 \pm 0.95) \times 10^{-11}$ cm^{-2}s^{-1}TeV^{-1}, normalization energy $E_0 = 200$ GeV and the spectral index $\alpha = -3.67 \pm 0.14$. The fit resulted in $\chi^2/NDF = 5.72/4$ and probability of 22%.

Date	MJD	Effective time [hrs]	Significance [σ]	$F_{(E>100\,GeV)}$ [10^{-11} cm^{-2} s^{-1}]	U.L. [10^{-11} cm^{-2} s^{-1}]
2014-03-24	56740	0.49	3.02	5.88 ± 1.80	...
2014-03-25	56741	0.49	3.33	5.38 ± 1.84	...
2014-03-27	56743	0.97	5.62	4.98 ± 1.37	...
2014-04-03	56750	0.74	3.76	4.82 ± 1.40	...
2014-04-05	56752	0.86	6.37	3.46 ± 1.36	...
2014-04-06	56753	0.96	3.96	3.62 ± 1.21	...
2014-04-07	56754	0.97	4.28	3.42 ± 1.24	...
2014-04-08	56755	0.98	4.74	4.08 ± 1.27	...
2014-04-09	56756	0.93	4.60	3.24 ± 1.23	...
2014-04-22	56769	1.10	4.44	2.35 ± 1.17	...
2014-04-24	56771	1.07	3.36	3.05 ± 1.14	...
2014-04-25	56772	0.95	2.70	3.49 ± 1.23	...
2014-04-26	56773	0.98	1.63	-0.37 ± 1.17	2.41
2014-04-27	56774	0.98	2.43	3.20 ± 1.21	...
2014-04-29	56776	0.98	2.46	2.76 ± 1.19	...
2014-04-30	56777	0.93	3.53	2.54 ± 1.21	...
2014-05-01	56777	0.65	2.49	2.57 ± 1.19	...
2014-05-02	56779	0.98	2.94	1.77 ± 1.39	6.52
2014-05-03	56780	0.98	2.63	2.81 ± 1.19	...
2014-05-04	56781	0.97	3.61	2.34 ± 1.17	7.16
2014-05-05	56781	0.91	4.06	-0.15 ± 1.23	2.85
2014-05-06	56783	0.98	3.66	4.81 ± 1.18	...
2014-05-18	56794	0.76	0.23	1.42 ± 1.27	5.56
2014-05-19	56795	0.64	2.59	3.21 ± 1.54	...
2014-05-20	56796	0.65	3.56	2.98 ± 1.98	1.01
2014-05-21	56797	0.65	4.09	3.60 ± 1.51	...
2014-05-22	56798	0.65	1.58	1.21 ± 1.43	5.60
2014-05-23	56799	0.48	2.56	3.67 ± 1.72	...
2014-05-24	56800	0.65	0.69	1.36 ± 1.40	...
2014-05-25	56801	0.65	3.30	9.25 ± 1.37	4.92
2014-05-26	56802	0.65	2.26	2.13 ± 1.38	7.18
2014-05-27	56803	0.65	2.68	2.86 ± 1.41	...
2014-06-02	56809	0.65	1.45	2.72 ± 1.42	8.45
2014-06-06	56814	0.65	0.68	2.29 ± 1.57	7.89
All		27.58	17.55		

Table 5.1: Summary of the observation dates, effective observation time, significance of the VHE γ-ray signal and integral fluxes with threshold of E>100 GeV for PKS 1424+240 2014 data. The upper limits (U.L.) are calculated with 95% confidence level.

The de-absorbed spectrum was achieved after correcting the effect of EBL using Franceschini 2008 model (see chapter 7 for more details), and it was fitted with a simple power law function (magenta line). The fit results in χ^2/NDF=2.44/4 and probability of 65% with normalization factor $f_0 = (2.2 \pm 0.3) \times 10^{-10}$ cm^{-2}s^{-1}TeV^{-1}, normalization energy $E_0 = 200$ GeV and the spectral index $\alpha = -2.70 \pm 0.18$. All errors quoted here are only statistical. As the differential spectrum is rather soft, the significance drops dramatically above 200 GeV leading to larger uncertainties regarding the flux calculation.

For comparison, the differential spectra from MAGIC mono observation in 2009 (green filled circles) and stereo observations in 2010 and 2011 [Aleksić et al. 2014] (red and black filled triangle) are also shown in figure 5.7. The comparison of spectral parameters is given in the Table 5.2. The spectral index of the MAGIC 2014 spectrum is harder than the MAGIC 2009 mono observations; however, it is compatible within errors with MAGIC 2010 and 2011 spectra. The differential flux of 2014 observations is on a similar level within statistical errors to all previously mentioned observations, which indicates a rather constant VHE γ-ray emission. Thanks to the increased sensitivity of MAGIC after the upgrade, for the first time, the lower energy span of the observed spectrum for this source allowed the possibility of better overlapping of VHE spectrum with *Fermi*-LAT HE spectrum. However, even if statistically the spectral point is present at 40 GeV, it will not be used for further analysis in the following section, as the effect of the telescope systematics is not well known below the current MAGIC energy threshold of 50 GeV.

Year	$f_{(E=200\,\mathrm{GeV})}$ (10^{-10} cm^{-2} s$^{-1}TeV^{-1}$)	Γ_{obs}	$F_{>150\,\mathrm{GeV}}$ (10^{-12} ph cm^{-2} s^{-1})
2009	1.3±0.6	5.0±1.7	16.6±5.0
2010	0.5±0.2	3.5±1.2	5.3±2.5
2011	1.0±0.3	3.9±0.7	10.0±3.0
2014	0.69±0.09	3.67±0.14	8.5±1.2

Table 5.2: Comparison of the differential fluxes at 200 GeV and integral fluxes for $E > 150$ GeV for 1ES PKS 1424+240 observed in 2009, 2010, 2011 [Aleksić et al. 2014] and in 2014 with MAGIC. The differential and integral fluxes have been calculated from the simple power law fits to the observed spectra of 2009, 2010, 2011, and 2014 data.

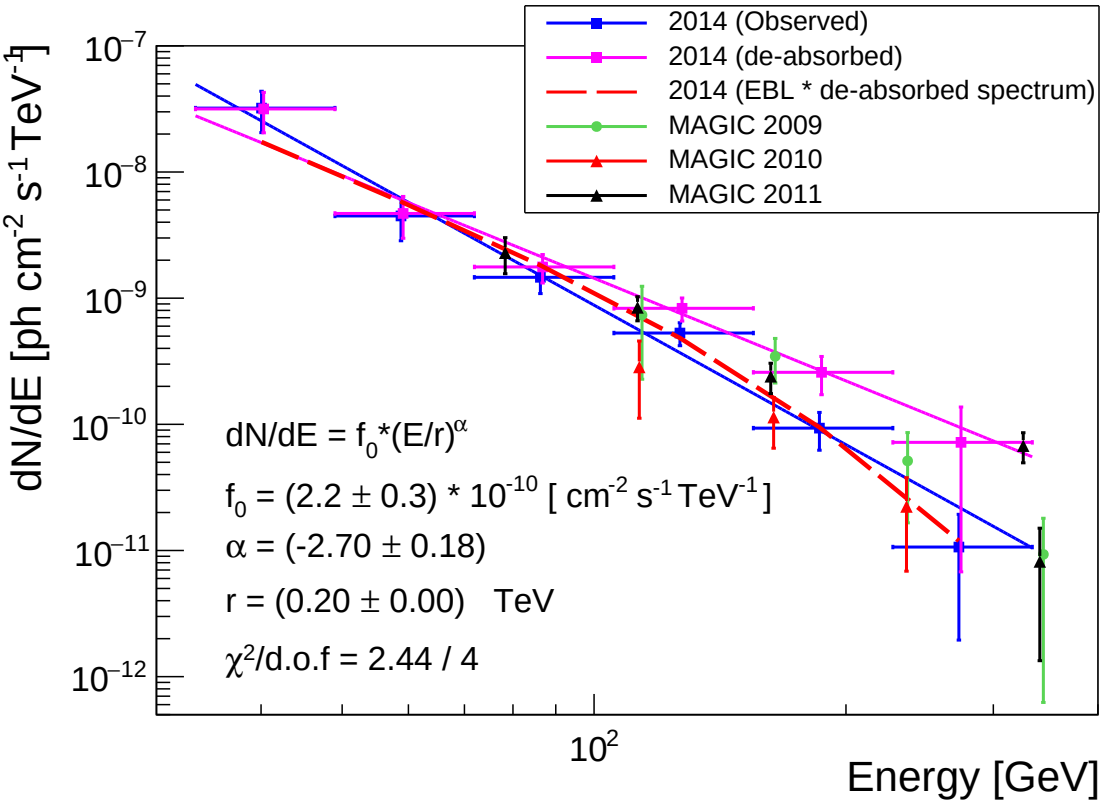

Figure 5.7: Unfolded differential spectrum (blue filled squares) of PKS 1424+240 MAGIC monitoring observations from 24^{th} March to 6^{th} June 2014. The EBL correction was applied to the observed differential spectrum using Franceschini 2008 model [Franceschini et al. 2008] (magenta filled squares). The observed differential spectrum and the EBL corrected spectrum were fitted with a simple power law function (blue and magenta line). The dashed red line shows the effect of EBL absorption on the observed spectrum. The parameters from the de-absorbed spectrum are given in the left corner. For comparison, we also show differential spectra from MAGIC observation prior to 2014 flare [Aleksić et al. 2014]

Combined MAGIC and *Fermi*-LAT spectrum

In order to study the SED of PKS 1424+240 in GeV-TeV energy range, contemporaneous data with *Fermi*-LAT in HE γ rays to the MAGIC VHE γ-ray observations have been collected. For our analysis, we have used publically available LAT Pass 8[b] data from March to June 2014 in the energy range 0.1-500 GeV. The data were selected from the region of interest (ROI) of 10° and analyzed with the

[b]http://fermi.gsfc.nasa.gov/cgi-bin/ssc/LAT/LATDataQuery.cgi

Fermi Science Tools[c] package v10r0p5. We used the 'Source' event class with instrument response function of P8R2_SOURCE_V6 along with *gll_iem_v06* Galactic diffuse emission model and the *iso_P8R2_SOURCE_V6_v06* model to account for the isotropic diffuse γ-ray background. Model files were created automatically with the script make3FGLxml.py from the third *Fermi*-LAT point source catalog 3FGL [Acero et al. 2015]. The spectral shape of PKS 1424+240 in the GeV regime is a power law in 3FGL of the form:

$$\frac{dN}{dE} = f_0 \left(\frac{E}{E_0} \right)^{-\Gamma} \tag{5.2}$$

where f_0 is the flux normalization factor, E_0 is the normalization energy, and Γ is the spectral index. The fluxes were estimated from the unbinned likelihood fit to the data of the model, containing all the sources from the 3FGL [Acero et al. 2015] within a distance smaller than 1.5 times the ROI. The spectra of the fitted sources were assumed to be of a power law shape, with the best-fit spectral indices taken from 3FGL. For the power law fit, all parameters were left free for the data in the entire energy range of 0.1 to 500 GeV. Also, all other sources within a radius of 10° along with the Galactic diffuse emission were left free for the fit. However, all sources between 10°−15° were fixed to their catalog values.

Figure 5.8 shows the combined MAGIC and *Fermi*-LAT spectral energy distribution in the energy starting from 100 MeV until 300 GeV. The spectrum was fitted with power law as given in equation 5.2 and also with a log parabola as given below:

$$\frac{dN}{dE} = f_0 \left(\frac{E}{E_0} \right)^{-(\Gamma + \beta log(E/E_0))} \tag{5.3}$$

where f_0 is the flux normalization factor, E_0 is the normalization energy, Γ and β are spectral index and curvature index respectively. In figure 5.8, the solid red line corresponds to a log parabola fit, and the dashed red line corresponds to a power law fit. The parameters from the combined fit for power law and log parabola functions are given in table 5.3. Thanks to increased sensitivity due to MAGIC upgrade and *Fermi*-LAT Pass 8 data, it was possible to achieve precise measurements of PKS 1424+240 at low emission state, and also to obtain a gapless combined MAGIC and *Fermi*-LAT spectrum without any break.

[c] http://fermi.gsfc.nasa.gov/ssc/data/analysis/scitools/likelihood_tutorial.html

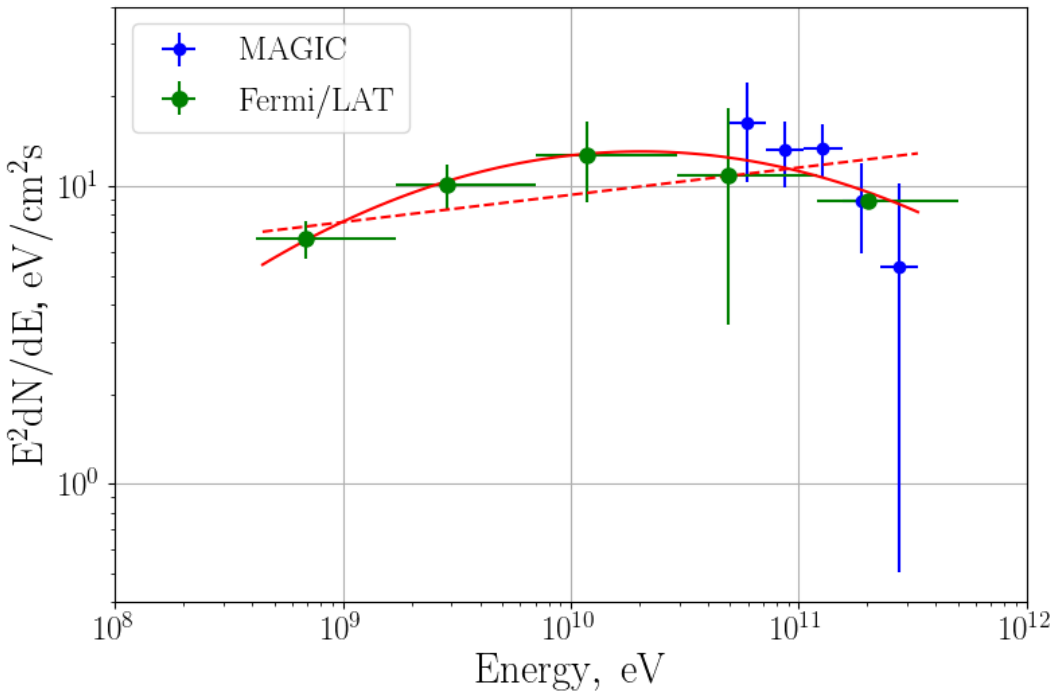

Figure 5.8: Combined MAGIC (EBL corrected) and quasi-simultaneous *Fermi*-LAT SED in the energy starting from 100 MeV until ∼300 GeV. The EBL correction was applied to the observed SED using Franceschini 2008 model [Franceschini et al. 2008]. The solid red line corresponds to log parabola fit and the dashed red line corresponds to power law fit. Note that, MAGIC SED points which are below the energy threshold of 50 GeV (as effect of telescope systematics is not well known) are not included in this plot.

Spectral Parameters	Log Parabola	Power Law
f_0 (eV cm^{-2} s^{-1})	11.23 ± 2.61	11.53 ± 2.27
E_0 (GeV)	100	100
Γ	-2.19 ± 0.16	-1.90 ± 0.04
β	(-5.98 ± 3.11) × 10^{-2}	...
χ^2/dof	1.4/7	5.1/8
Probability	0.98	0.75

Table 5.3: Spectral fit parameters of PKS 1424+240 for the combined MAGIC and quasi-simultaneous *Fermi*-LAT spectrum.

SED modeling

Figure 5.9 shows the broadband SED of PKS 1424+240, which is constructed using the low state VHE data taken with MAGIC during March-June 2014, and the quasi-simultaneous HE data with *Fermi*-LAT (see section 4.4.4), and UVOT and X-ray data with Swift. Both UVOT and X-ray data with Swift were corrected for Galactic extinction and the contribution from the host galaxy and provided by our MAGIC collaborator Mireia Nievas Rosillo. The VHE γ-ray data was corrected for the EBL using the [Franceschini et al. 2008] model. The SED is modeled under the scope of the simple leptonic scenario, which helps to understand the nature of the electron distribution responsible for the emission through synchrotron and SSC processes. Both the energy bumps of the SED, i.e., low and high, are well constrained by these quasi-simultaneous MWL data. The goodness of the model is judged by eye. Therefore, the curve represents only one working set of SED parameters, rather of being a real fit for the data.

The SED of PKS 1424+240 shows a wide synchrotron bump peaking around the optical regime. Here the peak of synchrotron bump looks narrower possibly due to the enormously reproduced X-ray luminosity. The location of the second peak is more uncertain but appears to be located at very high energies. This makes the separation between synchrotron and inverse Compton peak large. This feature is difficult to model with a traditional one zone SSC. With the typical one-zone SSC model it was not possible to fit the optical-UV part together with the VHE without applying a much higher Doppler factor ($\delta > 40$) than that observed in the parsec-scale jet by the VLBA in radio. Therefore, for PKS 1424+240 SED two zone SSC modeling was performed using the FSRQ model presented in [Tavecchio et al. 2011], with small modifications, such as contributions from disk, broad-line region, and external seed photons are assumed to be small and thus neglected, as PKS 1424+240 is a BL Lac object. The two emission regions are separated as; the inner region is assumed to be smaller and closer to the central black hole, or that it is a spine, the outer region is assumed to be the larger region, or that is a sheath. Both regions are described by the same parameters as the one-zone model, assuming an electron population distributed as a broken power law in each region as with the γmin, γmax and the break at γb, Lorentz factors; the slopes before (n1) and after (n2) the break; and the electron density parameter K:

$$N(\gamma)d\gamma = \begin{cases} K\gamma^{-n1}d\gamma & \gamma_{min} < \gamma < \gamma_b \\ K\gamma_b^{n_2-n_1}\gamma^{-n_2}d\gamma & \gamma_b < \gamma < \gamma_{max} \end{cases} \tag{5.4}$$

The modeling was performed similarly to 1ES 1011+496 using an online AGN SED tool[d]

The two-zone model results in an acceptable fit to the data. For the SED

[d] http://www.isdc.unige.ch/sedtool/PROD/html_js/SED_Web_tool/Doc/test_doc/index.html

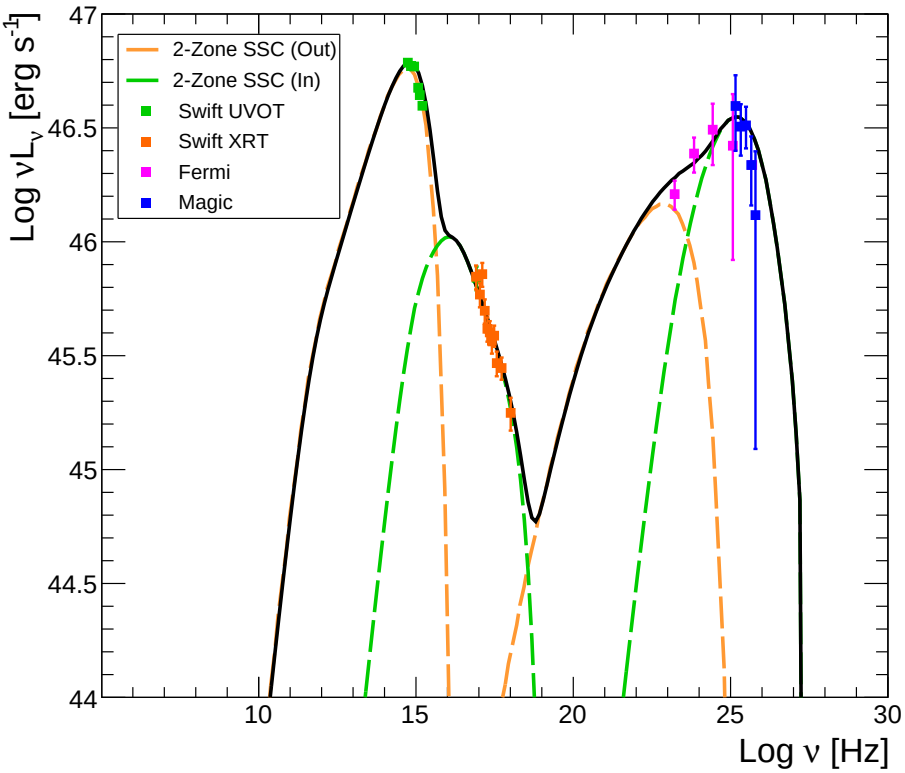

Figure 5.9: The broadband spectral energy distribution of PKS 1424+240 constructed using the low state VHE data taken with MAGIC during March-June 2014, and the quasi-simultaneous HE data with *Fermi*-LAT and UVOT and X-ray data with Swift. The VHE γ-ray data was corrected for the EBL using the [Franceschini et al. 2008] model. The solid black line represents the total fit with a two-zone SSC model, the orange long dashed line represents the emission from the outer region, and the green long dashed line represents the emission from the inner region.

presented here, the maximum luminosity for the synchrotron bump is $\nu L\nu_{Sync} = 5.69 \times 10^{46}$ erg s^{-1}, which peaks at $\nu_{Sync} = 4.98 \times 10^{14}$ Hz (2.1 eV), whereas, the maximum luminosity for the inverse Compton bump is $\nu L\nu_{SSC} = 3.55 \times 10^{46}$ erg s^{-1}, which peaks at $\nu_{SSC} = 1.77 \times 10^{25}$ Hz (73.2 GeV). Therefore, the SED shows no clear indication of an inverse Compton dominance.

Once the variability timescales, frequencies, and fluxes at the two SED peaks are measured, the parameters of the one-zone SSC model can be uniquely fixed [Tavecchio et al. 1998]. In the case of our VHE data with MAGIC in 2014, no clear significant variability was observed. Therefore, model parameters derived here are not uniquely fixed. As PKS 1424+240 had a low state during March-June 2014 similar to 2009, a starting parameter for the inner region we have used the Doppler

Year	γ_{min} [10^3]	γ_{break} [10^4]	γ_{max} [10^5]	n1	n2	B [G]	K 10^3 [cm^{-3}]	R 10^{16} [cm]	δ
2009-2011									
2 zones (in)	8.0	3.9	7.0	2.0	3.1	0.033	3.1×10^3	4.8	30.0
2 zones (out)	0.6	3.0	0.5	2.0	3.0	0.033	23.0	190.0	9.0
2014									
2 zones (in)	9.0	4.2	5.0	2.2	3.8	0.028	84.3×10^3	1.15	30.0
2 zones (out)	0.35	3.0	0.23	2.05	4.8	0.028	74.8	53.0	13.0

Table 5.4: Fitted two zone SSC model parameters for PKS 1424+240 low state data during March-June 2014. The corresponding broadband SED is shown in figure 5.9 by solid black line. For comparison, model parameters from previous observations performed in 2009-2011 [Aleksić et al. 2014] are also shown.

factor δ and R as $\sim$30 and 1×10^{16} cm respectively. The other parameters were derived by reproducing the SED. The physical parameters for the 2014 data and comparison with those derived from the previous observations are listed in table 5.4. The comparison with previous models of the source SED indicates a good agreement for most of the parameters, except for the values of K are higher, and values of R are lower in case of 2014 data.

The measured powers from the reproduced SED indicate a strange behavior of the magnetic field. For very different values of emission radius R, we obtain the same values of magnetic field B, which implies a very large magnetic energy zone. The behavior of the bulk Lorentz factor Γ suggests some deceleration of the flow [Georganopoulos & Kazanas 2003]. This behavior, however, is not sufficient to explain the values of the model. A possible explanation could be that the primary jet injection changes the parameters with time. Alternatively, the two regions are probably not located at different distances along the jet, they are rather cospatial and form a spine-layer structure [Ghisellini et al. 2005]. In case of a spine-layer form, it is possible to have a uniform magnetic field in the inner and outer, i.e., in the fast and slow region of the jet.

Summary

Here I have reported the monitoring observations of PKS 1424+240 during 24^{th} March to 6^{th} June 2014. The observations pertaining to this study were performed with MAGIC, and total 27.58 hrs of data were collected. The source was detected brightly with a significance of $17.55\,\sigma$. Compared to previous MAGIC observations, the mean integral flux from 2014 data is lower than 2009 MAGIC observation per-

formed in mono mode, however, on a similar level within errors with 2010 and 2011 stereo observations. The differential flux was compatible within errors with all previous MAGIC observations, which indicates a constant VHE γ-ray emission. The spectral index from observed spectrum was found to be harder than 2009 observations, however, compatible with 2010 and 2011 observations. During the entire monitoring performed in 2014, no significant night-wise and intra-night flux variability were observed. This was the first time that the observed spectrum is found to be spanning from as low as 40 GeV, which would allow the better overlapping between MAGIC and *Fermi*-LAT spectrum. However, even if statistically the spectral point is present at 40 GeV, it was not used in the MAGIC-*Fermi*-LAT combined spectrum, as the effect of the telescope systematics is not well known below the current MAGIC energy threshold of 50 GeV. The parameters from the combined fit with a power law and a log parabola function show statistical compatibility. Thanks to increased sensitivity due to MAGIC upgrade and *Fermi*-LAT Pass 8 data, it was possible to achieve precise measurements of PKS 1424+240 at low emission state, and also to obtain a gapless combined MAGIC and *Fermi*-LAT spectrum. The high redshift of 0.6 and signal excess past 100 GeV allowed us to further study the effect of EBL absorption on the spectra in detail. These results of the EBL study will be discussed in chapter 7. However, future work on this source includes gathering MWL data at radio, optical and X-ray wavelength for the SED modeling to study the low emission state process of the source.

I also presented the broadband SED of the PKS 1424+240, which is constructed using a two-zone SSC model for the low state VHE data taken with MAGIC during March-June 2014, and the quasi-simultaneous HE data with *Fermi*-LAT, and UVOT-X-ray data with Swift. With the typical one-zone SSC model it was not possible to fit the optical-UV part together with the VHE without applying a much higher Doppler factor ($\delta > 40$) than that observed in the parsec-scale jet by the VLBA in radio. However, two zone SSC model fits the data more properly. According to this model, the majority of the optical-UV emission originates in a larger emission region called as the outer region, and the X-ray to γ-ray emission originates mainly in a smaller emission region called an inner region, which also has a smaller contribution from the larger region in the *Fermi*-LAT energy band. To not overproduce the synchrotron emission in the optical-UV region, this model requires high values of γmin in the inner region than the outer region. As the SED studies here were done with the quasi-simultaneous data, we emphasize the need for strictly simultaneous multiwavelength observations to further investigate the emission regions in more details for this source.

6. Monitoring of the Radio galaxy M87 during a low emission state from 2012 to 2015 with MAGIC

Motivation

M87 is one of the closest extragalactic VHE objects and the first and brightest radio galaxy detected in the TeV regime. In 2005, the first time VHE γ-ray emission was detected, which displayed strong flux variability in 2008 and 2010 on short timescales as a day. For more than 10 years, along with the radio to X-ray, it has been monitored in the TeV band. MAGIC continued to monitor M87, but no major flares were detected since 2010. During my thesis, I studied the data taken from the MAGIC observations of M87 between 2012 to 2015. This chapter aims at locating the VHE emission region, studying the source properties and the emission mechanisms in the quiescent VHE γ-ray state, probing different emission scenarios to model the observed broadband spectral energy distribution. In the case of M87, most of the spectral modeling was done to interpret high or flaring states, whereas detailed characterization of the source's lower emission levels is still lacking. Thus in order to understand the flare, it is essential to study the low emission or quiescent state as its origin of emission could be different from the flare. From 2012-2015, we have collected $\sim$156 hours of data with MAGIC. It resulted in a significant detection of the source in each year, and these are one of the most sensitive measurements of M87 done so far in the low emission state. We have also combined this VHE monitoring data with HE γ rays to radio data from *Fermi*-LAT, *Chandra*, HST, EVN, and VLBA together with optical polarimetry data from the Liverpool Telescope. This work will be published in the Astronomy & Astrophysics Journal, of which I will be one of the corresponding authors [Ahnen et al. 2019].

The chapter is structured as follows: first I will discuss the basic information about M87, the observations, and analysis performed with MAGIC and with other instruments are presented in sections 6.3 and 6.5. In results, source detection plots, skymaps, the long-term light curves, discussion on emission region site and spectral energy distributions of the source in section 6.4. Combined results from MAGIC and *Fermi*-LAT are presented in section 6.4.5. The multi-wavelength light curve and the SED modeling is discussed in sections 6.5.1 and 6.5.2, and conclusions are listed in section 6.6.

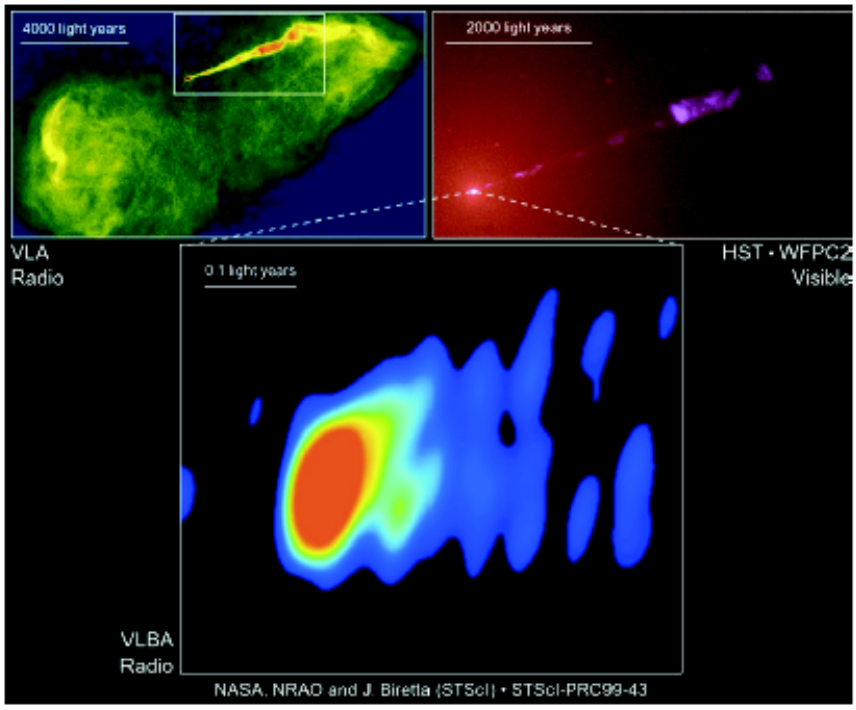

Figure 6.1: Images of the radio galaxy M87 at the center of the Virgo galaxy cluster in different wavelengths and at different spatial scales. The Very Large Array radio image side shows the kpc-scale jet inflating radio lobes (top left). The Hubble Space Telescope optical image shows the structure of the kpc-scale jet (top right). The Very Long Baseline Array image shows the sub-pc scale jet very close to the black hole (bottom center). [Credit: X-ray: NASA/CXC/MIT/H.Marshall et al., Radio: F.Zhou, F.Owen (NRAO), J.Biretta (STScI), Optical: NASA/STScI/UMBC/E.Perlman et al.]

Introduction

Messier 87, commonly known as M87, is a giant elliptical radio galaxy of Fanaroff-Riley-I-type (FR I, [Fanaroff & Riley 1974]) in the Virgo Cluster. It was first observed by Heber Doust Curtis in 1918, using the Lick Crossly Reflector and he categorized it as 'exceedingly bright galaxy with a sharp nucleus' [Curtis 1918]. FR-I sources have their high luminosity or brightness regions of radio emission close to the hosting central galaxy than their further regions. Therefore, as the distance from the central galaxy host increases, the luminosity of FR I sources decreases. Towards the extremities of the outer lobes, the sources become fainter, and here the spectra become steepest, which indicates that the radiating particles have aged the most. In 80% of the FR I galaxies jets are detected, which can begin as one-sided close to the core, but beyond a few kiloparsecs, it becomes two-sided and continuous.

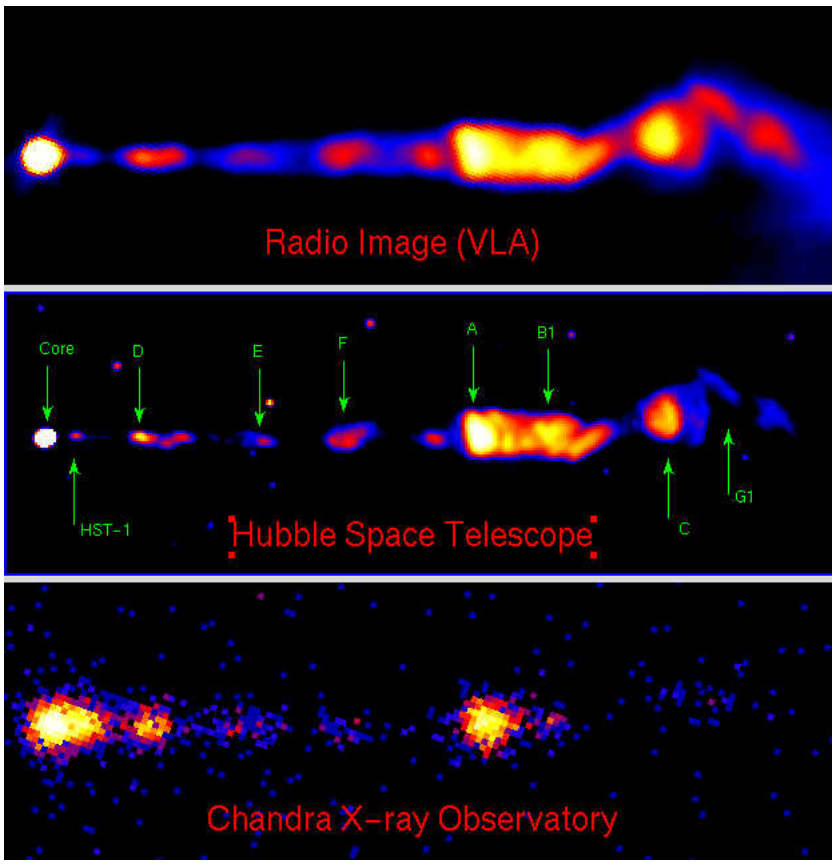

Figure 6.2: Image of the radio galaxy M87 jet at different wavelength. Top panel shows the Very Large Array (VLA) radio image, the middle panel shows the Hubble Space Telescope (HST) optical image which shows the structure of the kpc-scale jet, and bottom panel shows the *Chandra* X-ray image. [Credit: X-ray: NASA/CXC/MIT/H.Marshall et al., Radio: F.Zhou, F.Owen (NRAO), J.Biretta (STScI), Optical: NASA/STScI/UMBC/E.Perlman et al.]

M87 is one of the closest known extragalactic VHE object located at a distance of (16.7±0.2) Mpc [Mei et al. 2007] and powered by a super-massive black hole of (3.2± 0.9) $\times$ $10^9 M_\odot$ [Macchetto et al. 1997]. It is the first radio galaxy to be detected in the TeV regime and is well studied from radio to X-ray energies. Its jet is misaligned with respect to our line of sight with an angle between 5-25° [Biretta et al. 1999, Acciari et al. 2009]. It was the first jet ever observed [Curtis 1918], originating from the core, extends to 20" ([Marshall et al. 2002]; equivalent to a 2 kpc projected linear distance). There are also jets of emission extending to the extremities, which produces large radio lobes (see figure 6.1, top left). Note that, the western lobe (to the left) shown in VLA image takes a sudden turn to the south (bottom), which suggest that it is driving into a denser and unseen intracluster medium.

The proximity of M87 makes it one of the best system for the multi-wavelength study of the relativistic jets at high resolution (figure 6.1). The jet is spatially

resolved in X-ray (*Chandra*), optical and radio (VLA/VLBA) observations. As shown in figure 6.2 and table 6.1, M87 jet contains various features seen in radio, optical and X-ray referred as 'knots'. The feature closest to the nucleus is the knot 'HST-1', which is 0.86" (70 pc, projected) away. Further away, several knots are ranging from 3" to 20" (240 to 1600 pc, projected) from the nucleus with knot D and A being the most luminous in X-ray among these knots [cheung et al. 2007].

Table 6.1: Features in M87 jet [Owen et al. 2000]

Knot	$\theta^{*}_{projected}$ (arcsec)	$D^{+}_{projected}$ (kpc)
A ...	210	18
B ...	203	17
C ...	68	5.8
D ...	115	9.8
E ...	157	13
F ...	177	15
G ...	255	30
H ...	334	28

* $\theta_{projected}$: the angular projected distance of the feature from the core.
+ $D_{projected}$: the linear projected distance of the feature from the core.

The exact location of the VHE γ-ray emitting region in M87 has remained puzzling. At X-rays, *Chandra* provides the angular resolution to separate the nucleus and HST-1 and to describe in details the complex structure of the jet [Perlman et al. 2003]. At radio, VLBA observations also particularly provide key analysis of the area close to the core and the HST-1 knot [cheung et al. 2007]. However, it is not possible to resolve the $20''$ jet at γ-ray energies, as the angular resolution of γ-ray observatories is of the order of $\sim 0.1^{\circ} = 6'$. However, usually, the variability observed for a γ-ray emitting source can be used to constrain the size of the emission region by requiring that the variability time scale (t_{var}) is longer than the light travel time through the emission region due to causality. Thus a simple requirement can be derived for the variability timescale of the form $(\delta \cdot R)/c < t_{var}$, where δ is the bulk Doppler boosting in the direction of the observer, R is the radius of the emitting region, and c is the speed of light. A possible Doppler boosting of the emitting region relaxes constraints on its size, which is typically in the order of 10-50 in case of blazars, whereas for radio galaxies, due to the angle between the line of sight and the jet, they are thought to be an order of magnitude smaller. This is consistent with the radio to optical observations of superluminal motions of knots in the inner jets of radio galaxies.

The measured short timescale (down to minutes) variability at TeV from previous observations by MAGIC, H.E.S.S, and VERITAS [Abramowski et al. 2012] imply a

very compact source. Therefore, the outer lobes are excluded as possible sites for VHE emission. Only regions that are close to the core or innermost knot HST-1 are possible sites for the emission. However, this information alone is not enough to reveal the location of the emission region. The correlation between the multi-wavelength data and the VHE emission, in which the source is spatially resolved, provides a unique opportunity to locate the VHE process occurring in AGNs. It is strongly suggested that for a consistent description of the flares emission at different energy bands such as radio, X-ray, and γ-ray must be correlated, even if the cooling scales of relativistic particles are different at different energies. Therefore, Target of Opportunities (ToO) campaigns in X-ray, optical and radio are in place to be activated in case a TeV flare is observed during the monitoring.

In 2003, search for TeV γ rays from M 87 succeeded first by the HEGRA collaboration reporting a strong hint of VHE γ-ray emission from the source [Aharonian 2003]. The hint encouraged other IACTs to intensify their observations of M 87. In 2005, the H.E.S.S collaboration firmly established M87 as an emitter above 730 GeV and revealed flux variability on timescales of two days, suggesting the emission region of the γ rays being very compact, with a dimension similar to the Schwarzschild radius of the central black hole [Aharonian 2006b]. In 2007 campaign, the VERITAS also detected VHE γ-radiation from M87 above 250 GeV [Acciari et al. 2008], and monitored the source during the following years [Acciari et al. 2010a]. The differential energy spectrum of M87 at VHE γ rays can be well fit by a simple power law $\mathrm{d}N/\mathrm{d}E \propto E^{-\Gamma}$. The photon index of $\Gamma \approx 2.3$ is not found to be changing significantly during the flares detected so far [Abramowski et al. 2012]. At HE γ rays, M87 is routinely detected by the *Fermi*-LAT satellite above 100 MeV [Abdo et al. 2009a]. The differential energy spectrum obtained from these results shows energy flux is consistent with being constant and can also be well described by a power law with an index of 2.04 ± 0.07 [Acero et al. 2015], which is only slightly harder than the one found in VHE.

Since the beginning of observations in 2004, the MAGIC collaboration considered M 87 as one of the prime targets, and the observation strategy was focused on TeV monitoring of M 87 in trying to catch the flaring activity. The first reported detection of γ-ray emission from M87 by the MAGIC happened in 2005, and results of those observations together with 2006 and 2007 data were reported in [Aleksić et al. 2012b]. During the 2008 flare, MAGIC detected the source as well, observing a flux variability on timescales as short as a day [Acciari et al. 2008].

For more than 10 years, besides radio, optical, and X-ray bands, M87 has been monitored in the TeV band by MAGIC, VERITAS, and H.E.S.S. [Acciari et al. 2009, Beilicke et al. 2012, Abramowski et al. 2012]. Figure 6.3 shows the multi-wavelength light curves from 2001 to 2010. According to the available VHE γ-ray data, there were in total three periods of high activity: 2005, 2008 and 2010 (shown in grey vertical bands in Figure 6.3). During these high TeV emission activities, rapid flares with short timescale variability were detected. For 2005 VHE flare (only observed by H.E.S.S.), there was an argument that the multiyear peak in X-rays of HST-1 is

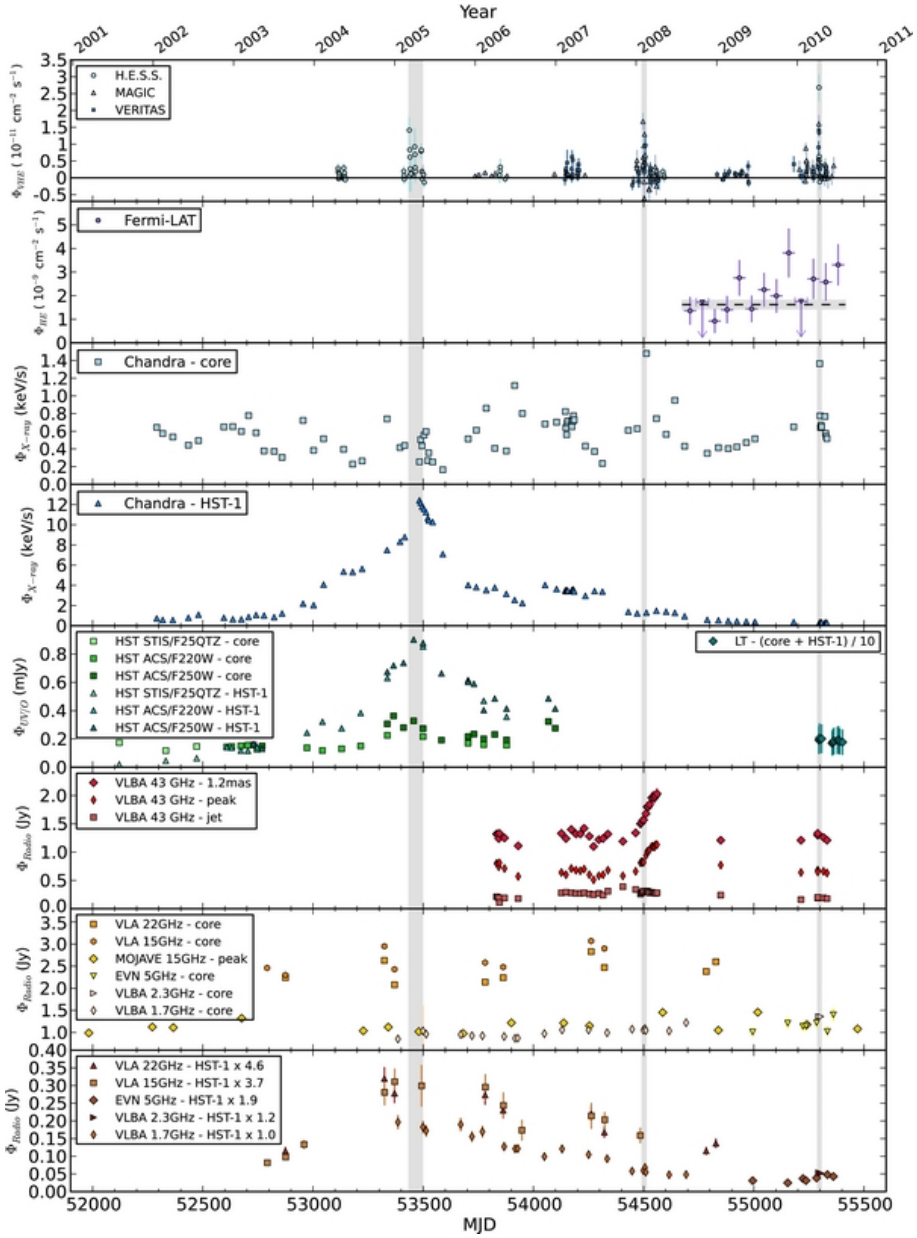

Figure 6.3: Multi-wavelength light curve of M 87 from 2001 to 2011. The VHE γ-ray flux (top panel) is calculated above an energy threshold of 350 GeV. Separate fluxes for the core and HST-1 are shown in cases where the instrument resolution is sufficient to separate the two components. Gray vertical bands mark the times of increased VHE activity in 2005, 2008, and 2010 [Abramowski et al. 2012].

related with the few days peak in TeV (see figure 6.3). It is generally not accepted that there were a clear correlation [Abramowski et al. 2012] between the high state

of VHE data and *Chandra* X-ray HST-1 data. Whereas, 2008 VHE flare shows a correlation between TeV and X-ray-radio data of M87 core. However, third VHE flare activity in 2010 happened when both core and HST-1 showed low state activity in X-ray and Radio. Note that since the monitoring in VHE γ rays is not very dense ($\sim 40 hrs/year$) and as the source is visible from La Palma only from December to July during the year due to the sun constraints, it must be assumed that several other flaring episodes might have taken place in the last years and remained undetected.

Therefore, MAGIC continued to monitor M87, but no major flares were detected since 2010. During my thesis, I studied the data taken from the MAGIC observations of M87 between 2012 to 2015. These observations allowed me to study the source in quiescent flux state. In the case of M87, most of the spectral modeling was done to interpret high or flaring states, whereas detailed characterization of the source's lower emission levels is still lacking. Thus in order to understand the flare, it is essential to study the low emission or quiescent state, as its origin of emission could be different from the flaring state. From 2012-2015, we have collected ∼156 hours of data with MAGIC, resulting in a significant detection of the source in the quiescent state in each year. Due to increased sensitivity of MAGIC telescopes, after the camera and readout upgrade [Aleksić et al. 2016a], M87 2012-2015 observations described here are one of the most sensitive measurements done so far in the low emission state. The data quality is sufficient to constrain some models and study broadband spectral energy distribution of M87 from radio to VHE, using MAGIC and broadband data available. In the following sections, first I will describe the observations, data analysis and results with MAGIC data. Then the observations, data analysis for the several multi-wavelength instruments involved are presented. Then the Then results are discussed, consisting the long-term light curves and the SED modeling.

Observations & analysis

M87 observations were performed from December to July (visibility from La Palma) every year from 2012-2015 at zenith angles ranging from $15° - 50°$ during the dark time and under Moonlight conditions. The data were taken in the so-called wobble-mode [Fomin et al. 1994] alternating the pointing direction between four sky positions at a 0.4° offset from the source. To evaluate the residual background of the observation, three control regions with the same γ-ray acceptance as the ON region were used to estimate the residual background recorded together with the signal.

Data were analyzed using the moon adapted MAGIC analysis as discussed in section 3.6.2, using the routines in the MAGIC software package for stereoscopic analysis, MARS [Aleksić et al. 2016b]. The recorded shower images were calibrated, cleaned and parametrized according to [Hillas 1985] for each telescope individually. Since the Moonlight increases the background signal in each pixel, data were processed by applying a higher image cleaning level of 8-4 phe for core-boundary pixels than the standard one of 6-3.5 phe for core-boundary pixels to the data (see sec-

tion 3.6.2.1). Hense, cleaning levels were optimized based on two criterion: 1) the percentage of pedestal events surviving the cleaning should be less than 10% (artificially triggered events which include electronic noise and night sky background (NSB), without any showers), and 2) number of spurious islands events, which are the isolated groups of pixels also known as islands that survive the image cleaning of real data. Monte Carlo simulations were tuned to the Moonlight conditions by increasing the fluctuations of the pedestal baseline to mimic the effect of a higher NSB level (see section 3.6.2.2). After applying the quality cuts, a total of 156.51 hours (Table 6.2) of effective observation time of good data were used for further analysis.

Results

θ^2 plot and Skymaps

MAGIC detected M87 in every yearly campaign from 2012 to 2015. θ^2 plots for 2012 to 2015 data are shown in figures 6.4 and 6.5. θ^2 is the squared angular distance between the source position and the reconstructed arrival direction of each event (see section 3.6.1.8 for details). The cuts for the full range were applied to get the θ^2 plots are: E<250 GeV, Hadronness < 0.16, size of events passing the image cleaning and stereoscopic reconstruction of >300 photo-electrons for each telescope. The significance was calculated according to the Li & Ma equation (see equation 3.15) [Li & Ma 1983].

In 2012, as the MAGIC telescopes were going through upgrade [Aleksić et al. 2016a], there were many changes in the hardware. This resulted in four different sets of Monte Carlos, which makes the analysis complicated and time intensive. The data collected in January-February and December 2012 were discarded due to bad weather and mono mode of the observation due to unavailability of Monte Carlo simulations. Hence we finally selected data taken in stereo mode between March-June 2012. During the whole observation period of 2012, the source was observed with an offset of 0.24° in the Declination due to a mistake in the observation schedule. Therefore, in each analysis step this offset needed to be corrected carefully. After data quality cuts, total 38.75 hours of data were selected. The applied cuts and zenith angle of observations resulted in 5.36σ detection with an excess 95 γ rays above the background level (see figure 6.4a). The average integral flux above 300 GeV was $(1.15 \pm 0.35) \times 10^{-12}$ cm^{-2} s^{-1}.

Between January-June 2013, after data quality cuts, total 34.82 hours of data in the stereo mode were selected. The applied cuts and zenith angle of observations resulted in 8.75σ detection with an excess 171.6 γ rays above the background level (see figure 6.4b). The average integral flux above 300 GeV was $(1.87 \pm 0.30) \times 10^{-12}$ cm^{-2} s^{-1}.

Between December 2013 - June 2014, after data quality cuts, total 49.88 hours of data in the stereo mode were selected. The applied cuts and zenith angle of observations resulted in 7.29σ detection with an excess 167.8 γ rays above the background level (see figure 6.5a). The average integral flux above 300 GeV was $(1.48 \pm 0.22) \times 10^{-12}$ cm^{-2} s^{-1}.

Between December 2014 - May 2015, after data quality cuts, total 32.72 hours of data in the stereo mode were selected. The applied cuts and zenith angle of observations resulted in 5.96σ detection with an excess 116.8 γ rays above the background level (see figure 6.5b). The average integral flux above 300 GeV was $(1.25 \pm 0.33) \times 10^{-12}$ cm^{-2} s^{-1}.

Table 6.2 lists the effective observation time and significance of the VHE γ-ray signal and integral fluxes observed from M87 above 300 GeV between 2012 and 2015. The significance was calculated according to Li & Ma equation [Li & Ma 1983] (see

section 3.6.1.8 for details). In 2005 to 2007 MAGIC mono observations, 5σ was achieved in altogether 3 years of data ($\sim$128 hrs) taken with low zenith angles below 30° with some exceptions up to 45° in dark conditions [Aleksić et al. 2012b]. Whereas, from 2012 to 2015, due to increased sensitivity of MAGIC after the upgrade, M87 was detected with significance $>5\sigma$ in each year.

Year	T_{eff} [h]	Significance [σ]	$F_{>300\,\text{GeV}}$ [$\times 10^{-12}$ cm^{-2} s^{-1}]
2012	38.75	5.4	1.15 ± 0.35
2013	34.82	8.7	1.87 ± 0.30
2014	49.88	7.2	1.48 ± 0.22
2015	32.72	5.9	1.25 ± 0.33

Table 6.2: Effective observation time, significance and mean integral flux of the VHE γ-ray signal observed from M87 above 300 GeV from 2012 to 2015. The Mean integral flux was obtained from a constant fit to the monthly binned light curves (Figure 6.8).

Figure 6.6 shows the spatial distribution of the source significance above 100 GeV in the sky coordinates. To check the consistency of the reconstructed source position with the catalog position, a 2D Gaussian function was used to fit the excess of the skymap. The position obtained from this 2D Gaussian fit with RA: $12^{\text{h}}\,30^{\text{m}}\,49.5(9)^{\text{s}}$ and DEC: $+12^{\circ}\,23^{\text{m}}\,38(14)^{\text{s}}$ is consistent with a point-like source located at the catalog position of M87 with a slight deviation observed in RA: 0.009(3)° and DEC: 0.003(4)°. The grey star in figure6.6 indicates the reconstructed source position. The color scale on the right indicates the relative flux values (the ratio between the exposure map and the background map, i.e., $N_{ex}/N_{bg(<0.1deg)}$) of the source. Figure 6.7 shows the test statistics (TS) distribution of the source significance above 100 GeV, resulted in maximum TS value of >18. The color scale indicates the test statistic value defined as the significance from Li & Ma equation (see equation 3.15) [Li & Ma 1983]. The comparison with previous localization of γ rays from M87 is given in section 6.4.3.

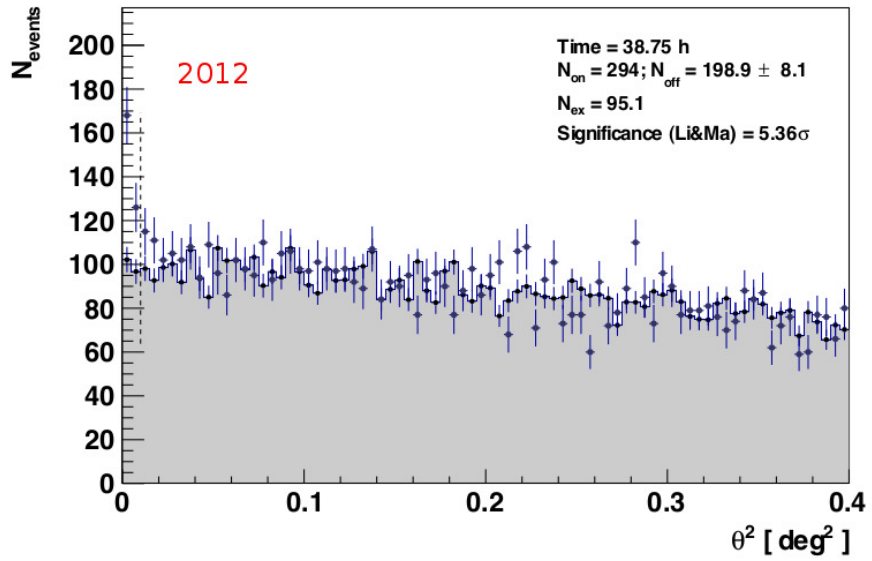

(a)

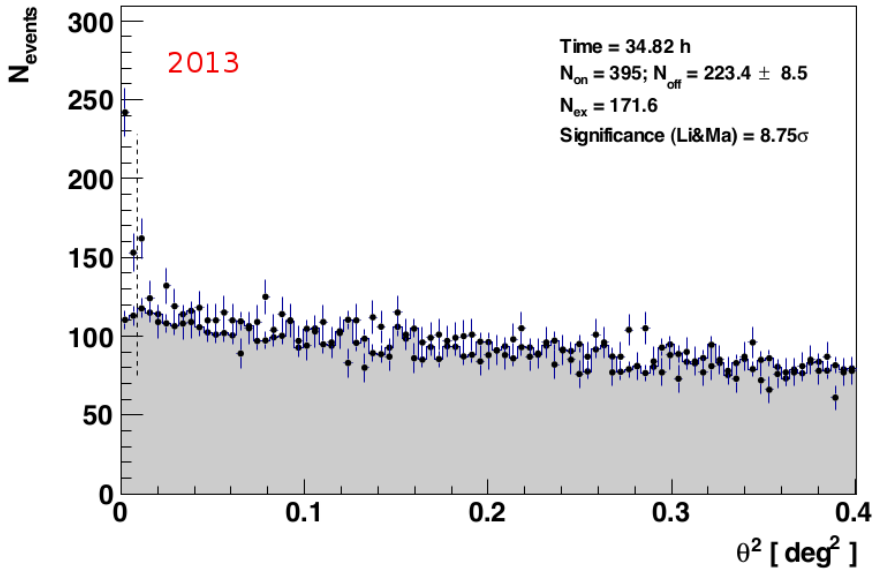

(b)

Figure 6.4: θ^2 distributions of the M87 signal and background estimation from MAGIC stereo observations taken in 2012 ($\sim$38.75 hours data) resulted in 5.4σ significance and in 2013 ($\sim$34.82 hours data) resulted in 8.7σ significance. The signal region is defined between zero and the vertical dashed line at 0.026 degrees^2.

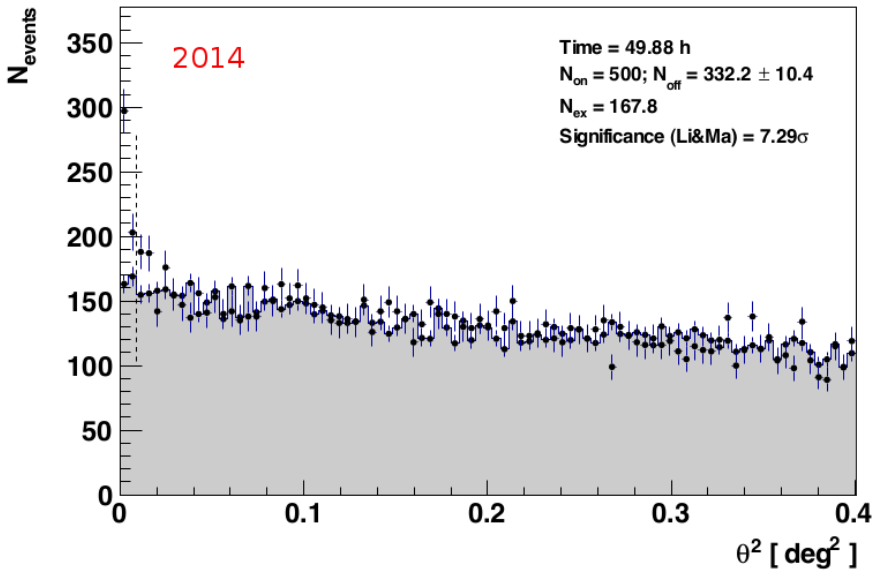

(a)

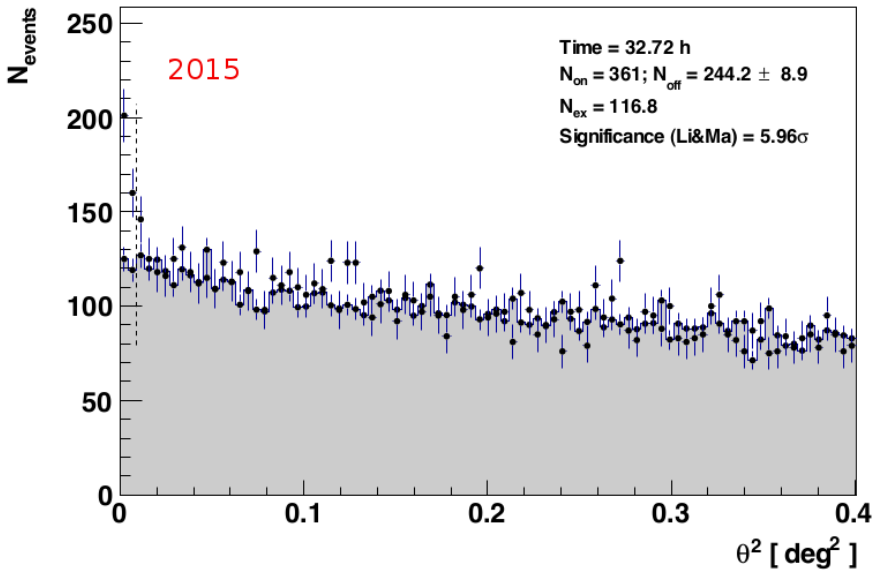

(b)

Figure 6.5: θ^2 distributions of the M87 signal and background estimation from MAGIC stereo observations taken in 2014 ($\sim$49.88 hours data) resulted in 7.2σ significance and in 2015 ($\sim$32.72 hours data) resulted in 5.9σ significance. The signal region is defined between zero and the vertical dashed line at 0.026 degrees^2.

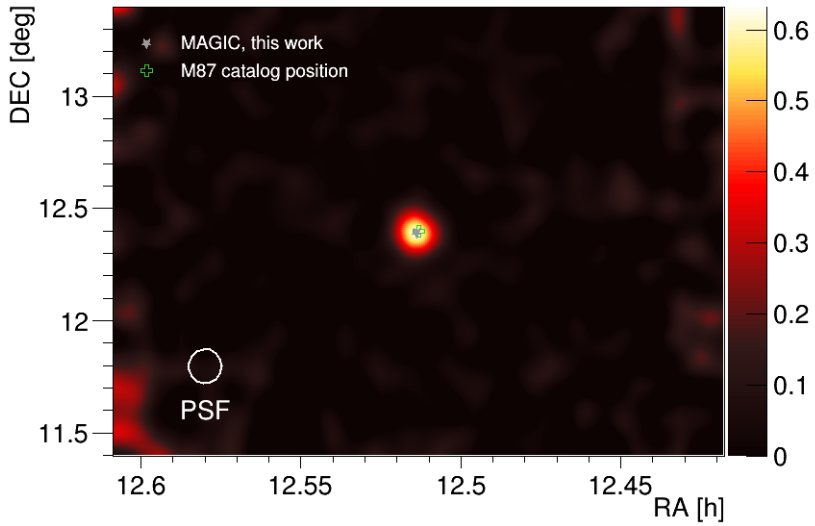

Figure 6.6: Flux map of M87 sky region above 250 GeV from ∼156 hours of MAGIC stereo observations taken in 2012-2015. The grey star indicates the reconstructed source position. The color scale represents the relative flux values in $N_{ex}/N_{bg(<0.1deg)}$. In the lower left is the point-spread function of 0.054° used for this analysis.

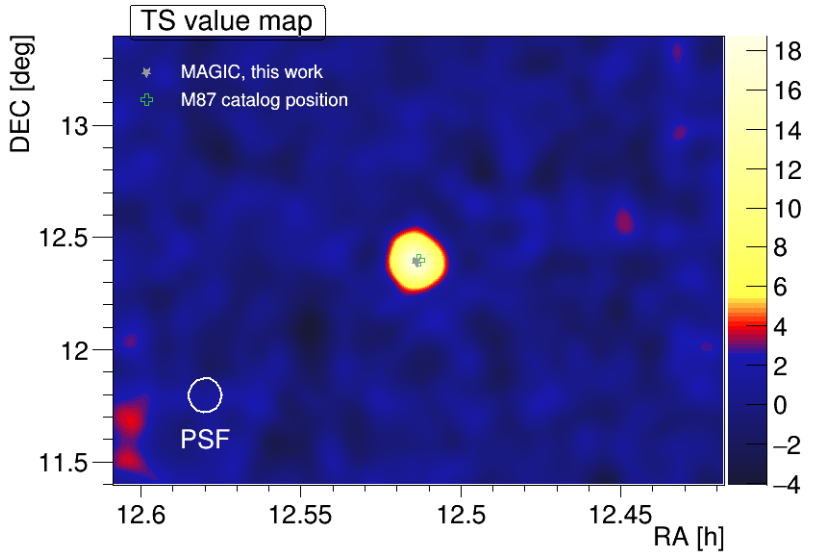

Figure 6.7: Significance map of M87 sky region above 250 GeV from ∼156 hours of MAGIC stereo observations taken in 2012-2015. The color scale represents the test statistics value distribution. In the lower left is the point-spread function of 0.054° used for this analysis.

Light Curve

The daily and monthly-binned light curves above 300 GeV are as shown in Figure 6.8 and the mean integral flux of each year, which was obtained by a constant fit to the monthly-binned light curves, is reported in Table 6.2. Variability on different time scales was investigated. No significant variability observed on monthly and yearly scales. A hint of variability on a 3σ level on daily scale has been observed in 2013 (the probability for a fit with a constant is 0.3%), while for the other years the light curves were found to be compatible with a constant flux (the probability for a fit with a constant is $> 38\%$). For 2013 data, by assuming an additional systematic uncertainty of 11% on the measured flux [Aleksić et al. 2016b], we obtain a probability for the fit with constant of 0.9%, which still shows a hint of variability on a daily scale.

Year	$F_{E>300\,\mathrm{GeV}}$ $[\times 10^{-12}$ cm^{-2} s$^{-1}]$
2012	1.15 ± 0.35
2013	1.87 ± 0.30
2014	1.48 ± 0.22
2015	1.25 ± 0.33

Table 6.3: Mean integral flux above 300 GeV observed with MAGIC between 2012 and 2015 obtained from a constant fit to the monthly binned light curves (Figure 6.8).

Year	$F_{400\,\mathrm{GeV}<E<1\,\mathrm{TeV}}$ [cm^{-2} s^{-1}]
HESS 2004	$(0.51 \pm 0.18) \times 10^{-9}$
HESS 2005	$(1.97 \pm 0.31) \times 10^{-9}$
MAGIC 2005 − 2007	$(0.90 \pm 0.19) \times 10^{-9}$
VERITAS 2007	$(1.30 \pm 0.26) \times 10^{-9}$
MAGIC 2008	$(5.09 \pm 0.72) \times 10^{-9}$
MAGIC 2012 − 2015	$(0.73 \pm 0.05) \times 10^{-9}$

Table 6.4: Comparison of the integral fluxes above 400 GeV observed in 2004-2005 with HESS [Aharonian 2006b], 2005-2007 with MAGIC [Aleksić et al. 2012], in 2007 with VERITAS [Acciari et al. 2008], in 2008 with MAGIC [Albert et al. 2008d] and in 2012-2015 with MAGIC. The integral fluxes have been extrapolated from a simple power law fits to the observed spectra.

For each data set, we estimate an integral flux F(E>400 GeV) using the energy spectra and the integral fluxes information on the previous data from the literature (see [Aharonian 2006b, Albert et al. 2008d, Aleksić et al. 2012]), shown in

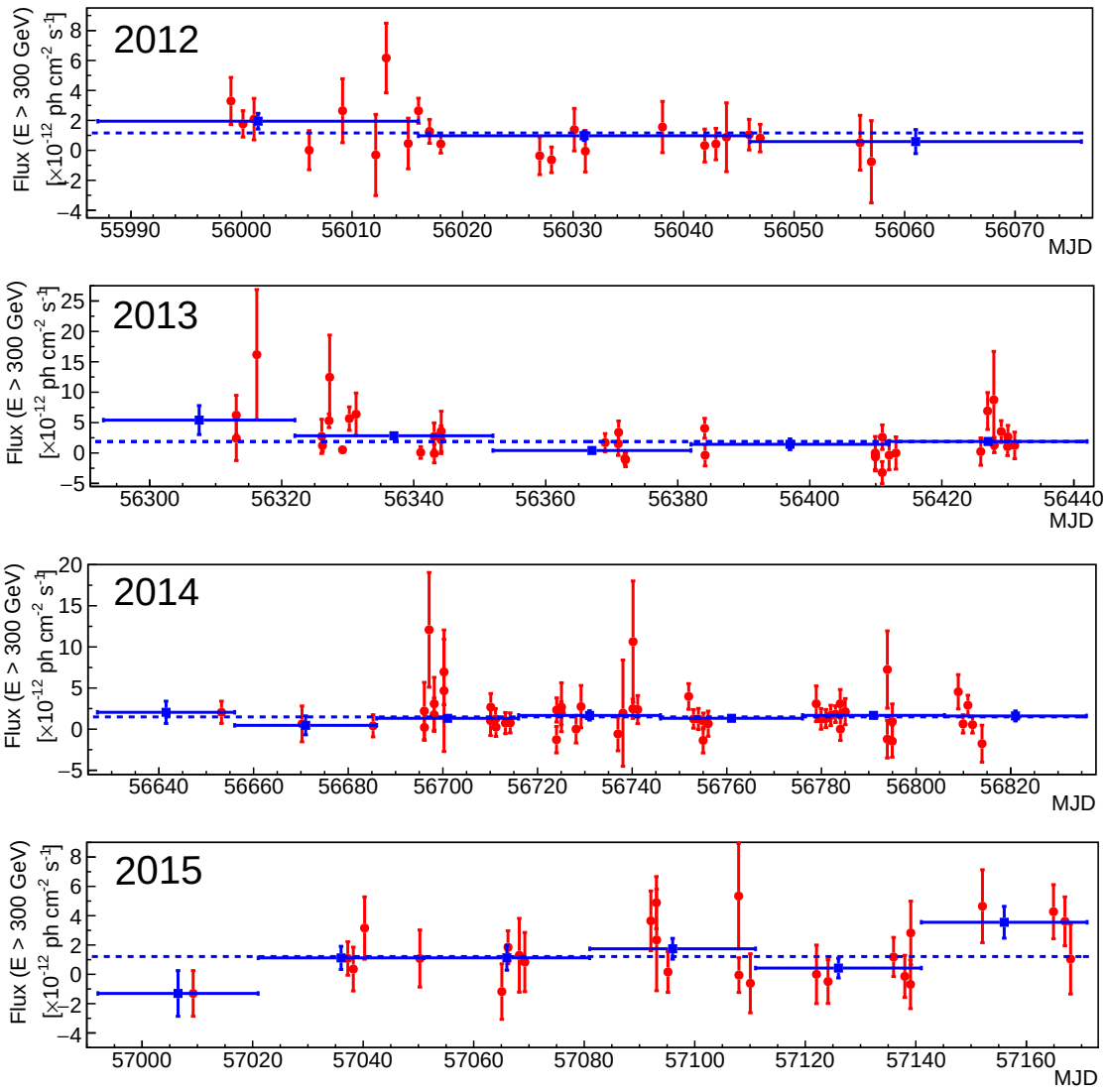

Figure 6.8: Daily and monthly binned light curves shown in red and blue respectively from 2012 to 2015 (top to bottom). The mean flux from a fit with a constant to the monthly-binned light curves is indicated by a blue dotted line, which is also reported in Table 6.2.

(Table 6.4). To have common energy range to calculate the integral flux in all these spectra, E>400 GeV was chosen, as H.E.S.S. spectra start from 400 GeV. In order to compare the new data set between 2012 and 2015 with the older M87 observations, we calculate an integral flux by extrapolating the integral flux ($E > 400$ GeV) for MAGIC, HESS and VERITAS observations (Table 6.4). Figure 6.10 shows the simple power law fits of the observed spectra for the observations mentioned above. The integral flux level above 400 GeV between 2012 and 2015 is compatible with

the flux observed with HESS in 2004 [Aharonian 2006b] and with MAGIC in 2005-2007 [Aleksić et al. 2012].

Morphology

In figure 6.9 we show VLA radio image at 327 MHz of M87 [Owen et al. 2000] together with the positions fitted to the VHE signal observed by MAGIC from 2012 to 2015 (red cross), H.E.S.S. from 2004 to 2005 (orange cross) [Aharonian 2006b] and by VERITAS in 2007 (green cross) [Acciari et al. 2008]. The red circle indicates the upper limit at 99.9% confidence level of an extended VHE γ-ray signal observed by MAGIC which is of the size of 0.042°, corresponding to 11.5 kpc.

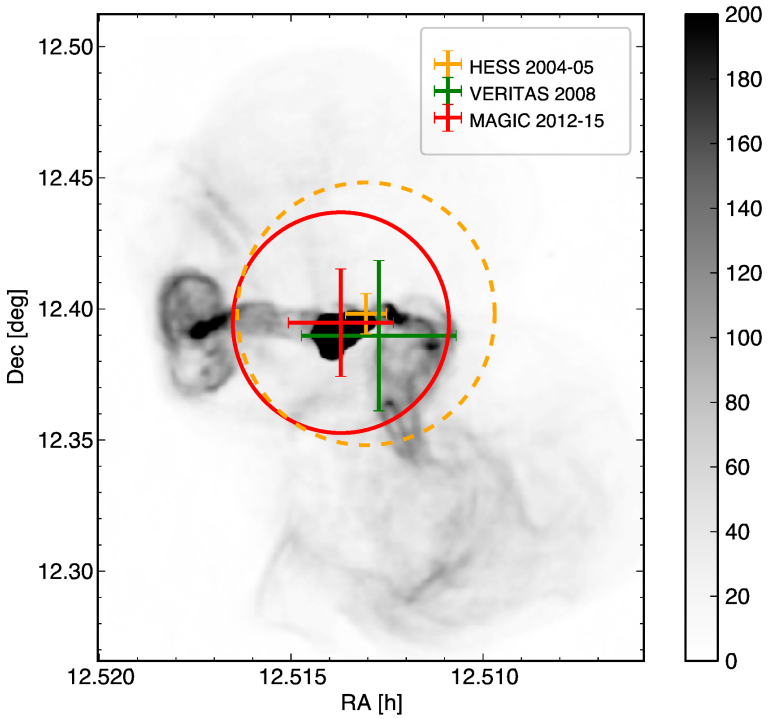

Figure 6.9: VLA radio image at 327 MHz of M87 [Owen et al. 2000]. We show the positions fitted to the VHE signal observed by MAGIC from 2012 to 2015 (blue cross), H.E.S.S. from 2004 to 2005 (red cross) [Aharonian 2006b] and by VERITAS in 2007 (green cross) [Acciari et al. 2008]. The blue circle indicates the 99.9% confidence level of a extended γ-ray signal.

As discussed in section 6.4.2, no significant variability was detected for 2012-2015 M87 data, however, hint for variability on 3σ level on a day timescale was observed in 2013 data. Further, considering this hint of observed variability on time scale of $\Delta t \sim 1$ day requires a very compact emission region because of the light-crossing time (R/c) of the black hole located at the center of M87. The characteristic size R can calculated as:

$$R \leq c \times \Delta t \times \delta \approx 5 \times 10^5 \delta \approx 5 \times \delta R_s \tag{6.1}$$

where δ is the relativistic Doppler factor, and $R_s \approx 10^{15}$ cm is the Schwarzschild radius of the M87 supermassive black hole [Aharonian 2006b]. From the fitted position of 2012 -2015 data (as shown in figure 6.9) it is clear that the outer lobes are excluded as possible sites for VHE emission. Only regions that are close to the core or HST-1 are possible sites for this emission.

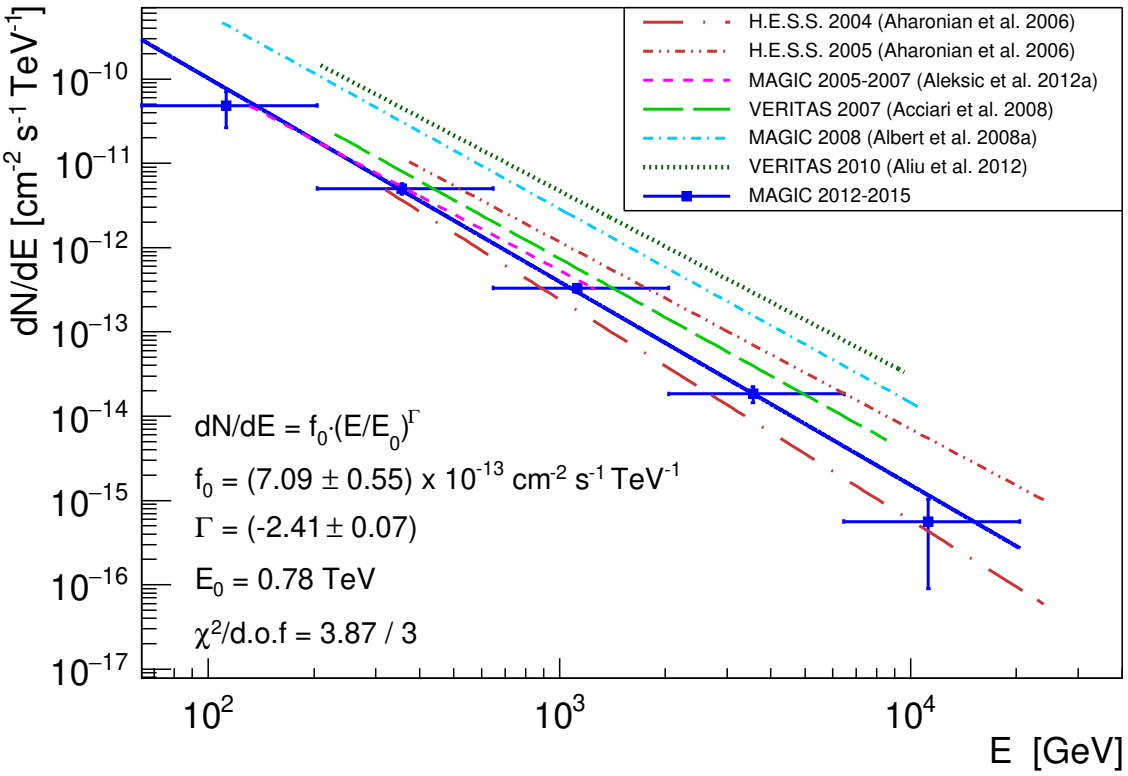

Figure 6.10: Averaged differential spectrum (blue points) from 2012 to 2015 MAGIC observations to which we fit a simple power law (blue line). For comparison we show the simple power law fits describing the averaged differential spectrum for low emission state observed in 2004 with HESS [Aharonian 2006b] (red long dashed-dotted line) and 2005-2007 with MAGIC [Aleksić et al. 2012] (blue dashed line), and for flaring state observed in 2005 with HESS [Aharonian 2006b] (red short dashed-dotted line), in 2007 with VERITAS [Acciari et al. 2008] (green long dashed line) and in 2008 with MAGIC [Albert et al. 2008d] (blue short dashed-dotted line). We compare the differential flux at 784 GeV adopting the parameters of the individual fits.

Year	Γ	$f_{E=784\,\mathrm{GeV}}$ [$\mathrm{cm^{-2}\ s^{-1}\ TeV^{-1}}$]
HESS 2004	-2.62 ± 0.75	$(0.45 \pm 0.14) \times 10^{-12}$
HESS 2005	-2.22 ± 0.15	$(2.00 \pm 0.28) \times 10^{-12}$
MAGIC 2005 – 2007	-2.21 ± 0.21	$(0.92 \pm 0.24) \times 10^{-12}$
VERITAS 2007	-2.31 ± 0.17	$(1.29 \pm 0.30) \times 10^{-12}$
MAGIC 2008	-2.30 ± 0.11	$(5.05 \pm 0.66) \times 10^{-12}$
MAGIC 2012 – 2015	-2.49 ± 0.07	$(0.70 \pm 0.05) \times 10^{-12}$

Table 6.5: Comparison of the spectral index obtained from the simple power law fit to the VHE γ-ray spectrum of M87 data observed in 2004-2005 with HESS [Aharonian 2006b], 2005-2007 with MAGIC [Aleksić et al. 2012], in 2008 with MAGIC [Albert et al. 2008d] and VERITAS 2007 [Acciari et al. 2008], and in 2012-2015 with MAGIC. We compare the differential flux at 784 GeV adopting the parameters of the individual fits.

The differential energy spectrum of the entire data set of ∼156 hours between 2012 and 2015 is shown in Figure 6.10. It is well described by a power law of the form $\mathrm{dN/dE} = \mathrm{f_0 \times (E/E_0)^{\Gamma}}$, with flux normalization constant $\mathrm{f_0} = (7.09 \pm 0.55)$ 10^{-13} $\mathrm{cm^{-2}\ s^{-1}\ TeV^{-1}}$, the decorrelation energy $E_0 = 780\,\mathrm{GeV}$ and a spectral index $\Gamma = (-2.41 \pm 0.07)$. The errors quoted here are only statistical. The power law fit results in $\chi^2/\mathrm{dof} = 3.87/3$. The observed spectrum is not affected significantly by the evolving extragalactic background light (EBL) due to the proximity of M87 [Neronov & Aharonian 2007]. The comparison of the spectral indices and differential fluxes is shown in Table 6.5. The spectral index of the MAGIC 2012-2015 spectrum is compatible with MAGIC 2005-2007 and HESS 2004 low emission state and also with the flaring state of HESS 2005, MAGIC and VERITAS 2008. The level of the differential flux between 2012 and 2015 is on a similar level as in low emission state of MAGIC 2005-2007 and HESS 2004 data, whereas it is lower than all previously mentioned flaring states.

Fermi-LAT data

In order to study the SED of M87 in GeV-TeV energy range, contemporaneous data with *Fermi*-LAT in HE γ rays to the MAGIC VHE γ-ray observations have been collected. For our analysis, we have used publically available LAT Pass 8[a] data from March 2012 to May 2015 in the energy range 0.1-300 GeV. The photons were selected from the circle with the size roughly double of that of the *Fermi*-LAT PSF[b] at the lowest considered energy e.g. 19° at 100 MeV, 8° at 300 MeV, and for the energies >300 MeV where the PSF size is small, a fixed selection radius of 5° was applied. The fluxes were estimated from the unbinned likelihood fit to the data of the model, containing all the sources from the four-year LAT point source catalog (3FGL, [Acero et al. 2015]) within a distance smaller than 1.5 times the photon selection radius. The spectra of the fitted sources were assumed to be of a power law shape, with the best-fit spectral indices taken from 3FGL. To simplify the convergence of the fit, the spectral indices were frozen at the values suggested in 3FGL and only their normalizations were allowed to vary. The fitted model also contained the *gll_iem_v06* Galactic diffuse emission model and the *iso_P8R2_SOURCE_V6_v06* model to account for the isotropic diffuse γ-ray background.

Combined *Fermi* and MAGIC spectrum

Figure 6.11 shows the combined MAGIC and *Fermi* spectral energy distribution over five orders of magnitude in energy starting from 200 MeV until 10 TeV. For comparison, the historical spectra from *Fermi*-LAT 2008-2009 [Abdo et al. 2009a] and the MAGIC 2005-2007 [Aleksić et al. 2012b] observations are also shown.

The combined spectrum was fitted with power law and log parabola. The equations for these are given below:

Power law:

$$\frac{dN}{dE} = f_0 \left(\frac{E}{E_0}\right)^{\Gamma} \tag{6.2}$$

Log parabola:

$$\frac{dN}{dE} = f_0 \left(\frac{E}{E_0}\right)^{(\Gamma+\beta log(E/E_0)} \tag{6.3}$$

where f_0 is the flux normalization factor, E_0 is the normalization energy, Γ and β are spectral index and curvature index, respectively. These parameters are given in table 6.6.

In figure 6.11, the solid red line corresponds to log parabola fit, and the dashed red line corresponds to power law fit. From the table 6.6, it is clear that both fits are statistically compatible. Thanks to increased sensitivity due to MAGIC upgrade and

[a] http://fermi.gsfc.nasa.gov/cgi-bin/ssc/LAT/LATDataQuery.cgi
[b] http://www.slac.stanford.edu/exp/glast/groups/canda/lat_Performance.htm

Fermi Pass 8 data, these are the most precise measurements of M87 at low emission state. It is the first time to obtain a gapless combined MAGIC and *Fermi* spectrum with no break or change in spectral slope. The 2012-2015 combined MAGIC *Fermi* spectra is compatible with combined *Fermi*-LAT 2008-2009 and MAGIC 2005-2007 spectrum [Aleksić et al. 2012b].

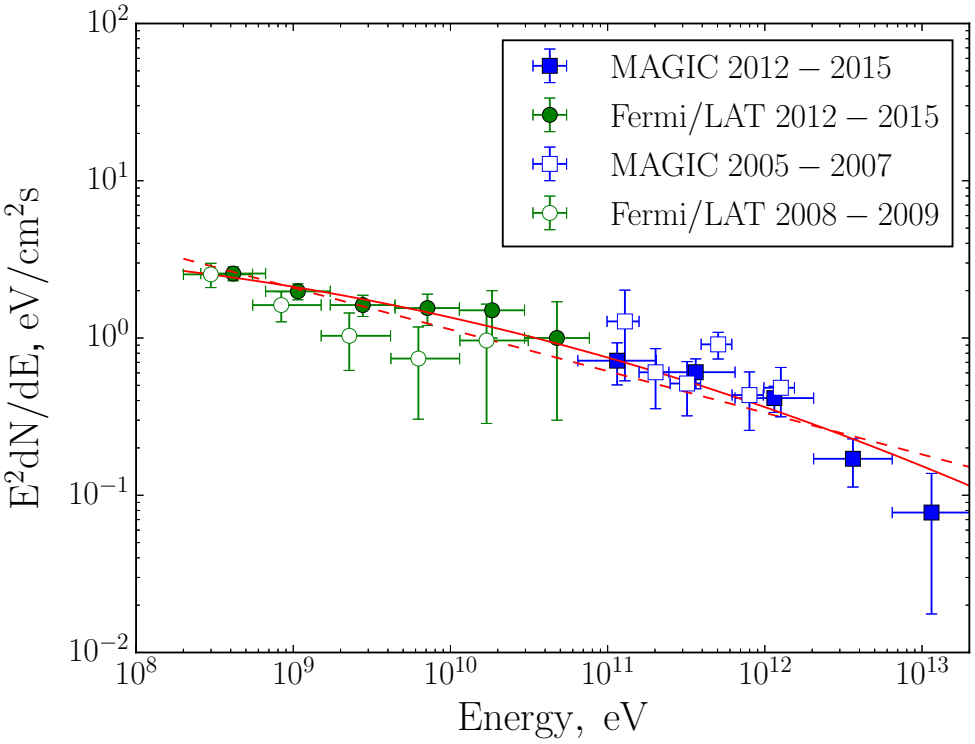

Figure 6.11: Combined MAGIC (blue filled squares) and quasi-simultaneous *Fermi*-LAT (green filled squares) spectral energy distribution over five orders of magnitude in energy starting from 200 MeV until 10 TeV. The solid red line corresponds to log parabola fit and the dashed red line corresponds to power law fit. Both fits are statistically compatible with the absence of a spectral break. For comparison, historical data from the *Fermi*-LAT 2008-2009 [Abdo et al. 2009a] and the MAGIC 2005-2007 [Aleksić et al. 2012b] observations are also shown.

Fermi-LAT Light Curve

The M87 light curve was constructed for E > 300 MeV with 30 days time bins (see figure 6.12). All the events in the 8° of ROI centered at M87 position were selected. A separate likelihood analysis was performed on each time bin. All point sources from 3FGL [Acero et al. 2015] that lied within 12° from M87, were included in the model over each time interval. From those bins where a detection significance exceeds 3σ (TS≥10), fluxes were calculated, otherwise 90% confidence upper limits

Spectral Parameters	Log Parabola	Power Law
$f_0(eVcm^{-2}s^{-1})$	0.75 ± 0.12	0.61 ± 0.05
E_0 (GeV)	100	100
Γ	-2.28 ± 0.02	-2.26 ± 0.01
β	-0.013 ± 0.009	...
χ^2/dof	3.7/8	5.7/9
Probability	0.88	0.77

Table 6.6: Spectral fit parameters of M87 for the combined MAGIC and quasi-simultaneous *Fermi*-LAT spectrum.

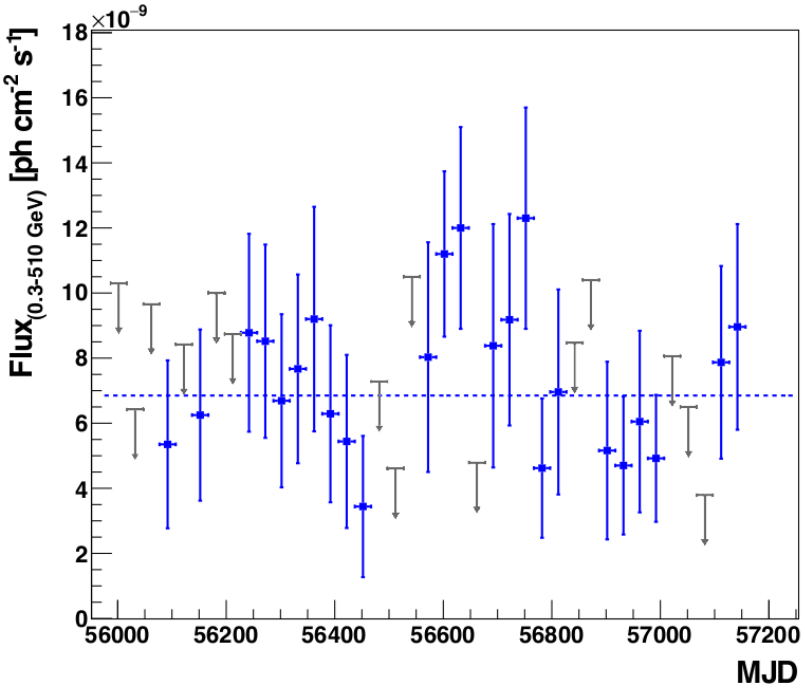

Figure 6.12: M87 light curve with *Fermi*-LAT for E > 300 MeV with 30 days time bins obtained with the fitted fixed photon index of Γ = -2.0. The average flux of (6.85 ± 0.56) 10^{-9} ph cm^{-2} s^{-1}) is indicated with the dotted red line. Data points with TS < 10 (i.e., 3σ) are shown as 90% confidence upper limits.

were calculated. For all the sources within the ROI, the fitting was done by fixing the photon index of each source to the best fit value from the 3FGL catalog and leaving the normalization parameter free. The resulting weighted average flux for the light curve has a value of (6.85 ± 0.56) 10^{-9} ph cm^{-2} s^{-1}. The fit result in a χ^2/ndf of 17.63/23 with a fit probability of 0.78, which shows that there is no hint of variability within the statistical errors.

Multiwavelength campaign

As discussed in the previous section, the joint spectrum between MAGIC and the *Fermi*-LAT, for the first time shows an amazing match with a power law over 5 decades in energy from 200 MeV to ∼10 TeV. In order to further study the source in a complete multiwavelength picture from radio to VHE, a campaign has been coordinated including additional optical polarimetry data to study the SED in detail. Radio data were taken with EVN at 1.7 and 5 GHz were provided by K. Hada, and with VLBA were provided by R. C. Walker. J. Madrid provided the optical data taken with HST, and H. Jermak provided the optical polarimetry data with Liverpool telescope. F. Massaro provided X-ray data with Chandra. As these multi-wavelength observations were organized separately, this campaign contains data only quasi-simultaneous to 2012-2015 MAGIC observations.

Multi-wavelength light curve

The MWL light curve of M87 between 2012 and 2015 is shown in figure 6.13. The VHE and HE data by MAGIC and *Fermi*-LAT are shown in blue and magenta circles respectively. For *Chandra* X-ray data, observations are corrected for the Galactic absorption and extinction following [Cardelli et al. 1989] for the core and HST-1 (green circle and crosses). Optical data taken with HST for the core and HST-1 is shown orange circle and crosses. Optical polarimetry data taken with V+R filter are by the Liverpool telescope with RINGO2 (2012) and RINGO3 (2014-2015) and radio data are provided by the EVN (core: black filled/blank points; HST-1: blue filled/blank points) and VLBA (1.2 mas: black star; peak: red star; down jet: blue star), respectively. Downward gray arrows indicate upper limits of 95% confidence level.

The light curves are daily binned except VHE and HE γ rays, where a monthly and 30-day binning are applied.

In the period of 2012 to 2015, covered from radio to VHE by these various instruments, the multi-wavelength picture remains stable, and no enhanced activity was detected compared to the flares detected so far. Both the core and the innermost knot in the jet HST-1, are found in the low emission state. This is in contrast to 2005, 2008 and 2010 VHE γ-ray fares, which happened after an increase either for the X-ray flux of HST-1 over several years or the radio flux of the core (see figure 6.3) [Abramowski et al. 2012]. Table 6.7 shows the constant flux probability and χ^2/dof from HE to radio data. Except for EVN 1.7 GHz core and 5 GHz HST-1 data, no clear variability was found at lower frequencies neither for the core nor for the jet, and also for the data from HE and VHE. The optical polarimetry data suggest a long-term rotation from $\sim 0^\circ$ to $\sim 400^\circ$, while the polarization remained in general at a rather low level of few percents expect some higher polarization of up to $\sim 25\%$ around the beginning of the MAGIC observation periods in 2012.

Waveband	Constant flux probability	χ^2/d.o.f.
HE	0.77	17.63/23
X-rays (core)	7.5×10^{-15}	72.29/4
X-rays (HST-1)	6.5×10^{-10}	48.87/4
UV (core)	0.11	7.64/4
UV (HST-1)	1.4×10^{-6}	32.63/4
Radio		
VLBA* (1.2 mas)	0.67	2.37/4
VLBA* (Peak)	0.44	3.73/4
VLBA* (Down jet)	0.88	1.22/4
EVN$^\bullet$ (Core)	0.40	5.15/5
EVN$^\circledcirc$ (Core)	1.1×10^{-8}	39.95/3
EVN$^\bullet$ (HST-1)	1.5×10^{-13}	69.27/5
EVN$^\circledcirc$ (HST-1)	0.12	5.85/5

Table 6.7: Probability for a fit of a constant to the flux observed in the individual wavebands (see Fig. 6.13).
Notes: $\star$: VLBA data at 43 GHz, $\bullet$: EVN data at 5 GHz, and $\circledcirc$: EVN data at 1.7 GHz

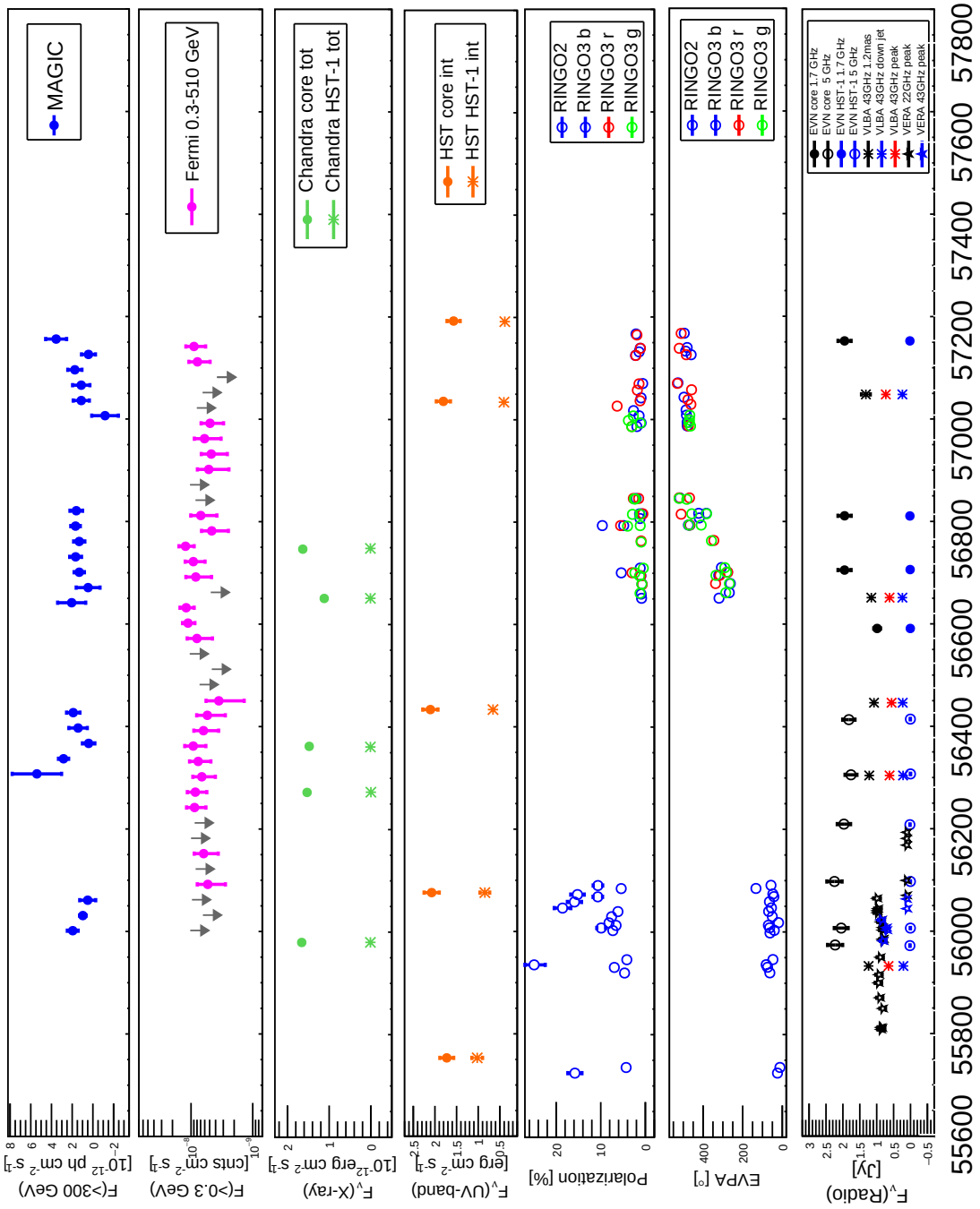

Figure 6.13: Multi-wavelength light curve for M87.

SED modelling

Figure 6.14 shows the MWL SED of M87, which is constructed using the low emission state VHE data taken with MAGIC from 2012 to 2015, and the quasi-simultaneous HE data with *Fermi*-LAT (section 6.4.5), X-ray data with Chandra, Optical and UV data with HST, and radio data with EVN and VLBA (see section 6.5). The modeling was performed incorporated with our collaborators K. Asano, F. Spanier, and S. Richter. The SED has modeled under the scope of two different scenarios: the leptonic as well as the photo-hadronic scenario. Leptonic scenario helps to understand the nature of the electron distribution responsible for the emission through synchrotron and SSC processes. Photo-hadronic scenario helps to understand the nature of the highly relativistic primary protons inside the jet and their synchrotron radiation and also the emerging photo-hadronic cascades [Mannheim 1993, Böttcher 2009]. Both the energy bumps of the SED, i.e., low and high, are well constrained by these quasi-simultaneous MWL data.

Previously, to model 2005 to 2007 low-state data SED, [Aleksić et al. 2010] applied a structured-jet model from [Tavecchio & Ghisellini 2008] & [Ghisellini et al. 2005] assuming a jet with a fast spine and a slower layer and thus two zones to explain the TeV flares. It proposed by [Lenain et al. 2008] that this flaring emission would occur while the jet is collimating, and [Georganopoulos et al. 2005] while it is decelerating. However, an alternative scenario to explain these VHE flares was proposed by [Giannios et al. 2010], which is based on misaligned mini-jets driven by magnetic reconnection moving within the jet with relativistic velocities relative to it. [Istomin & Sol 2009] proposed a two-step acceleration model to TeV energies involving initial particle acceleration within the accretion disk and then further centrifugal acceleration in the rotating magnetosphere. [Levison & Rieger 2011] discuss the variable TeV emission possibly to be produced in a starved magnetospheric region.

- **Leptonic model:**
  First, we apply the leptonic model to account for the broadband spectrum of M87 with the numerical code in [Asano et al. 2014] (see [Asano & Hayashida 2015] & [Asano & Hayashida 2018] also). The code calculates the temporal evolutions of the electron, and photon energy distributions in the plasma rest frame along the jet (radius R from the central engine), which is similar to the `BLAZAR` code in [Moderski et al. 2003] (for application examples see, [Kataoka et al. 2008, Hayashida et al. 2012]). Here, we assume a steady conical outflow, in which the temporal evolution along the jet is equivalent to the radial evolution. The conically expanding jet naturally leads to adiabatic cooling of electrons, which is a similar effect to the electron escape in one-zone steady models. In this 1-D code, we do not need a parameter for the electron escape. The magnetic field decreases as $B = B_0(R/R_0)^{-1}$. The macroscopic model parameters are the Lorentz factor Γ, the initial radius R_0, the initial magnetic field B_0, the electron luminosity L_j (including the counter-jet), the jet opening angle θ_j, and

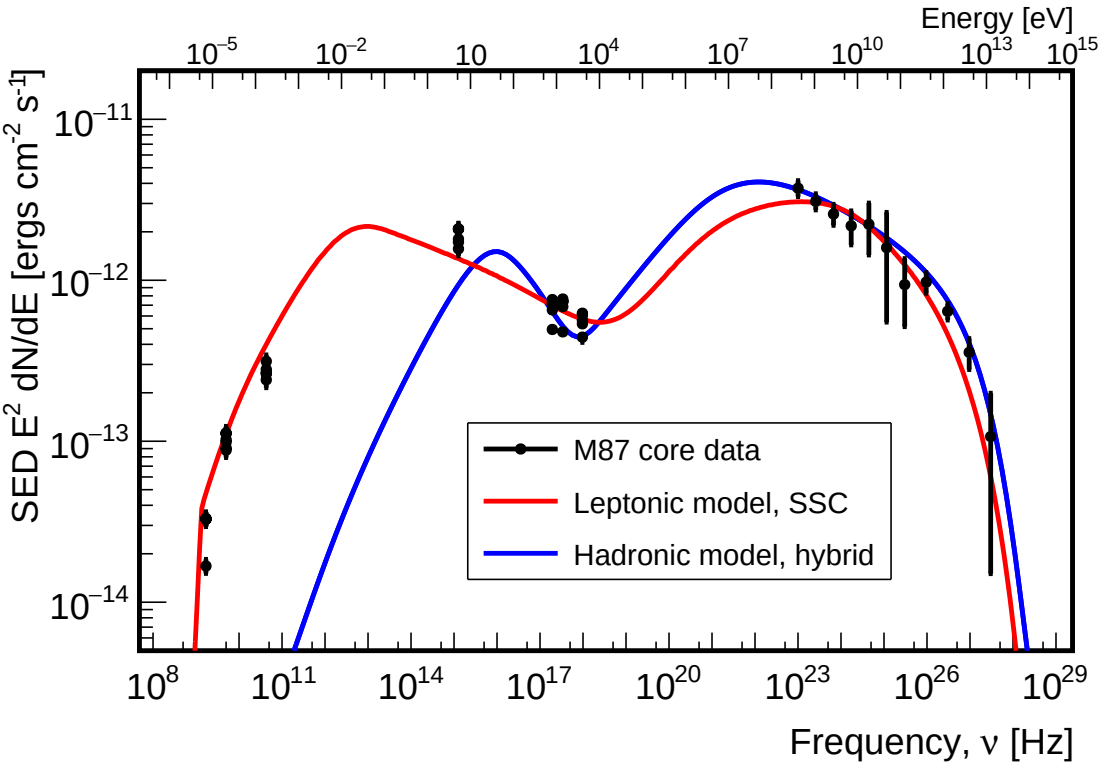

Figure 6.14: Averaged SED of the radio core of M87 compiled from quasi-simultaneous 2012–2015 MWL observations. We combine VHE γ-ray observations by MAGIC, HE γ-ray data from *Fermi*-LAT; *Chandra* data, optical data in the UV band from *HST*, radio data at 1.7 GHz and 5 GHz provided by the EVN and at 43 GHz (symbol) by VLBA. The models represent two possible scenarios: in the leptonic scenario the high energy part is dominated by the SSC emission, whereas in the hybrid scenario the high energy part is dominated by the synchrotron radiation of the relativistic protons.

the viewing angle θ_v. Here, we adopt $\Gamma = 3$, $\theta_j = 1/\Gamma = 19°$ and $\theta_v = 15°$. We inject electrons during the dynamical timescale $R_0/(c\Gamma)$ in the plasma rest frame. In this timescale, the injection rate into a given volume $V \propto R^2$ is constant. The evolutions of the electron energy distribution and photon emission are calculated as far as $R = 30R_0$, taking into account synchrotron, inverse Compton scattering with the Klein–Nishina effect, $\gamma\gamma-$absorption, secondary pair injection, synchrotron self-absorption, and adiabatic cooling. The model parameters for the electron injection spectrum are the electron Lorentz factors for minimum γ_{min}, break γ_{br}, and maximum γ_{max}, and power law indices p_1 and p_2 for below and above γ_{br}, respectively. The parameter values are summarized in Table 6.8.

Table 6.8: Parameters used for the M87 SED fiting with leptonic model in Fig. 6.14

sim	Γ	R_0 $[10^{17}\,\mathrm{cm}]$	B_0 [mG]	L_j $[10^{44}\,\mathrm{erg\,s^{-1}}]$	θ_j [°]	θ_v [°]	γ_min	γ_br $[10^4]$	γ_max $[10^7]$	p_1	p_2
	3	4.0	3.1	2.5	19	15	500	1.4	3.0	1.9	3.2

The MAGIC observation reveals that the GeV–TeV emission consist of a single component. As Figure 6.14 shows, the SSC component for the leptonic model reproduces the GeV–TeV spectrum. The synchrotron emission also explains the component from radio to X-ray with a break at ~ 0.03 eV. The required electron luminosity is comparable to the total jet power estimated from the large-scale radio structure [Owen et al. 2000]. However, the relatively high SSC flux requires a very low magnetization: the energy density ratio of the magnetic field to the non-thermal electrons is 5.2×10^{-5} at $R = 2R_0$, which is much smaller than the typical value in other blazars such as 10^{-1}–10^{-2} [Asano & Hayashida 2018]. [Asada & Nakamura 2012] claimed that the radio image of the M87 jet is consistent with a parabolic streamline, which supports the magnetically driven jet [Komissarov et al. 2009]. Later, [Ammons et al. 2014] showed that the gradual acceleration through a distance of 10^6 times the Schwarzschild radius also supports the magnetically driven jet model. In addition, [Kino et al. 2015] pointed out that the radio data at 230 GHz obtained by the event horizon telescope implies the magnetically dominated jet. Those results seem inconsistent with the very low magnetization at ~ 200 times the Schwarzschild radius indicated by the broadband spectrum. Other than the large-scale component constrained by radio observations, a very low-magnetized emission region is required to explain the γ-ray spectrum by the leptonic model. The physical picture of the M87 jet remains unrevealed yet, which provides great motivation for future observational and theoretical study for this object and blazars.

- **Photo-Hadronic model:**
  Here, as no clear variability in the TeV regime is detected, the model constraints are not as strict. However, we attempt to model the particle acceleration and the γ-ray emission consistently. Our model assumes that the acceleration and emission zones (where the emission zone is directly connected to the acceleration zone, representing the downstream region of a shock front) are at a distance of some $60 - 200Rs$, where R is the Schwarzschild radius of the central black hole. We also assume that in the simultaneous multiwavelength data, the relevant parts connected to the TeV γ-ray emission zone are the GeV data from *Fermi*-LAT and the X-ray data detected for the core region by Chandra. The radio data from VLBA and EVN originate from a larger region since the assumed densities in the modeled radiation zone will prevent effective radiative trans-

port due to synchrotron self-absorption. The optical data from HST detected from the core of M 87 presumably originates much closer to the black hole and where the jet is launched, as suggested by General Relativistic Radiation Magnetohydrodynamics [Ryan et al. 2015]. We are, therefore, modeling the X-ray, GeV and TeV data, while the radio to optical data are considered to be upper limits to our models.

The applied model was designed as a hybrid model and can cover the range from purely leptonic scenarios to the full photo-hadronic reaction chain. The fully time-dependent implementation is based on the geometry of [Weidinger & Spanier 2010]. The acceleration mechanism and the implementation of all leptonic processes were adopted from [Richter & Spanier 2016], and the photo-hadronic framework was implemented following [Hümmer et al. 2010]. The acceleration of particles is closely modeled to the Fermi-I acceleration. Assuming that the particle distribution is quickly reaching isotropy in the downstream region of the shock, the model follows the evolution of the injected, monoenergetic particle distribution towards a power law. The shape of the particle distribution and the relevant timescales follow consistently from the input shock parameters.

Table 6.9: Summary of the parameters used for the M87 SED modeling.

parameter	description
R_{rad}	the size of the radiation zone
R_{acc}	the size of the acceleration zone
$\gamma_{inj}^{species}$	the injection energy protons,electrons
$Q_{inj}^{species}$	number of injected particles protons,electrons
B	magnetic field strength
η	particle diffusion coefficient
V_S	shock speed
r	shock compression ratio
$\mathcal{D}$	Doppler factor

Best fit models (given the uncertainty on the assumption, no proper fitting on the parameters was done, just fit by eye) together with the available contemporaneous data can be seen in Fig. 6.14. In the leptonic model, the GeV-TeV emission is dominated by the inverse Compton emission, while radio to X-ray emission is synchrotron emission from the same electron population. In the hybrid model, the radio to X-ray parts also originates from synchrotron emission of electrons. Due to the higher magnetic field and the assumption of protons being injected into the acceleration zone, the higher energies are dominated by synchrotron emission of protons in this case.

The most important parameters of the model are summarized in table 6.9 and the parameters used for the presented fits are shown in table 6.10.

Table 6.10: Parameters used for the M87 SED fitting with leptonic and photo-hadronic models curves in Fig. 6.14

sim	R_{acc} $[10^{12}\,\mathrm{cm}]$	R_{rad} $[10^{15}\,\mathrm{cm}]$	N_{inj}^{pro} $[10^{42}\,\mathrm{s}^{-1}]$	γ_{inj}^{pro}	N_{inj}^{el} $[10^{40}\,\mathrm{s}^{-1}]$	γ_{inj}^{el} $[10^3]$	B [G]	r	η	$\mathcal{D}$
leptonic	1	4.2	–	–	2940	2	0.15	3.65	10	2.0
hadronic	35	30	8.77	10	2	10	3	3.50	1	5.3

The stock speed was set to $V_S = 0.1\,\mathrm{c}$ and Fermi-II acceleration neglected in both scenarios. The spatial diffusion parameter is mass dependent and can be calculated as $\eta_{pro} = \eta_{el} \cdot m_p/m_e$. The escape time from each region is calculated as $t_{esc} = \eta R/c$ and the acceleration timescale follows, depending on the spectral index, from $t_{acc} \gtrsim t_{esc} = \eta R_{acc}/c$ (for details see [Protheroe & Clay 2004]). We note that Chandra data $(10^{17} - 10^{18})\,\mathrm{Hz}$ are in the sensitive area of the transition between the two bumps in the SED. In the leptonic model, we did not succeed to match the Chandra photon index properly, that seems to be softer than in the model. The reason for that is a rather flat SSC spectrum in the Inverse Compton (IC) regime up to 10 TeV without an apparent cutoff in the data. This requires high maximum energies for the electron population, leaving the IC in the Klein-Nishina regime and resulting in a different, softer photon index in the IC regime. The high *Fermi* flux, in comparison to the Chandra flux, adds to the difficulties and requires a high particle density. The resulting Doppler factor is low, as one might expect so close to the black hole.

Summary

We had 4 years of data between 2012 and 2015 (∼40 hrs per year) to monitor M 87. The source was detected significantly in every yearly campaign, and no flare was detected. Due to increased sensitivity of MAGIC telescopes, after the camera and readout upgrade [Aleksić et al. 2016a], M87 2012-2015 observations described here are one of the most sensitive measurements done so far in the low emission state. In 2012, 2014 and 2015 data, no clear variability was observed on daily and monthly timescales. A hint for variability ($\sim 3\,\sigma$ level) was found in 2013 data on a daily timescale. This hint of the variability remains at a similar significance level even if variable systematic uncertainties of the MAGIC measurements are taken into account. The VHE γ-ray flux level above 300 GeV between 2012 and 2015 is the lowest observed since 2005. The combined spectral energy distribution between MAGIC and the *Fermi*-LAT, for the first time shows an amazing match with a power law over 5 decades in energy from 200 MeV to ∼10 TeV. We further found that the fitted position of M87 from 2012 -2015 data and a hint of variability on a day timescale, the outer lobes are excluded as possible sites for the VHE emission. Only regions that are close to the core or HST-1 are possible sites for this emission, which indicates the

TeV γ rays seem to come from the same or nearby site as during the flares. Due to the limitation of angular resolution of current generation IACTs, the exact location of the VHE γ-ray emitting region in M87 is puzzling. However, soon, with the help of multiwavelength studies performed along with high sensitivity instrument such as CTA, it might be possible to pinpoint the exact location of VHE γ-ray emission region in M87.

In the period of 2012 to 2015, covered from radio to VHE by these various instruments, the multi-wavelength picture remains stable, and no enhanced activity was detected compared to the flares detected so far. Both the core and the HST-1, are found in the low emission state. Except for EVN 1.7 GHz core and 5 GHz HST-1 data, no clear variability was found at lower frequencies neither for the core nor for the jet, and also for the data from HE and VHE. The optical polarimetry data suggest a long-term rotation from $\sim 0°$ to $\sim 400°$, while the polarization remained in general at a rather low level of few percents expect some higher polarization of up to $\sim 25\%$ around the beginning of the MAGIC observation periods in 2012.

I also presented the broadband SED of the M87, which is constructed using two different models: 1) a homogeneous leptonic model and 2) for the first time a hybrid photo-hadronic model, for the low emission state VHE data taken with MAGIC 2012-2015, and the quasi-simultaneous HE γ rays to radio data from *Fermi*-LAT, *Chandra*, HST, EVN, and VLBA. A homogeneous leptonic model can describe the five orders in magnitude flat photon spectrum in HE and VHE γ rays (*Fermi*-LAT and MAGIC), but it must be pushed to extreme limits and still has possible troubles in reproducing the X-ray data. In the hybrid scenario, it is easier to fit the available data. However, the number of parameters are higher than in the leptonic case, and the two components (synchrotron from electrons and synchrotron from protons) are independent of each other, as their densities are unrelated. On the other hand, the hybrid model has a precise prediction on the flux of π_0 decay at ~ 10 PeV, which can be probed by instruments like HAWC after long exposure. The SED modeling presented here has been done with the quasi-simultaneous data. However, to further investigate the emission regions in more details for this source strictly simultaneous multiwavelength observations are needed.

7. Extragalactic Background Light

Motivation

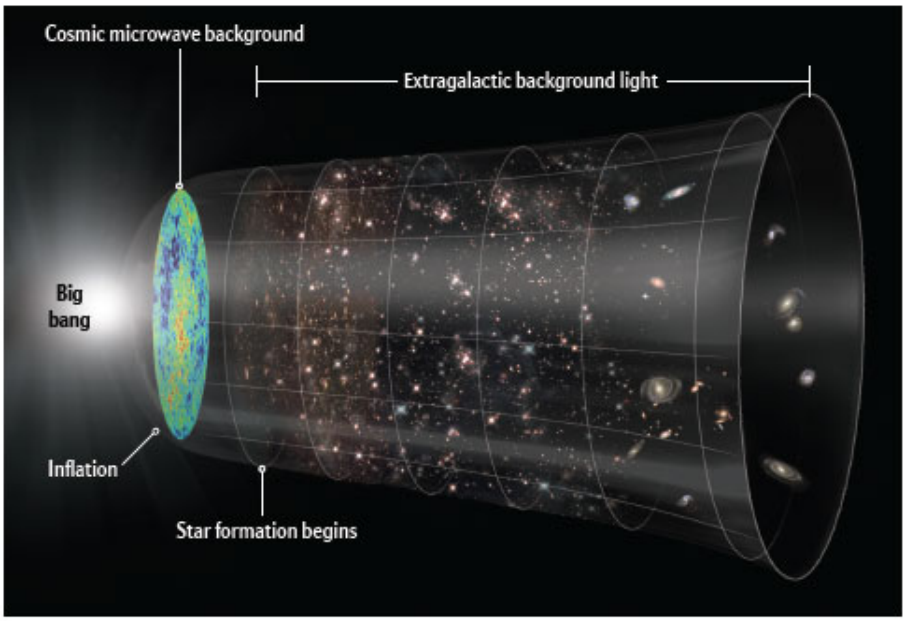

Figure 7.1: Extragalactic background radiation illustration from big bang to present day. Image creadi:
`http://www.nature.com/scientificamerican/journal/v312/n6/images/scientificamerican0615-38-I5.jpg`

The extragalactic background light (EBL) is the diffuse and isotropic radiation field accumulated in the ultraviolet to far-infrared wavelengths through the star and galaxy formation history of the Universe (see figure 7.1). EBL is one of the fundamental observational quantity in cosmology and thus plays a key role to understand the VHE extragalactic sky and its luminosity. It is redshifted at the observer's point depending on the redshift of the emitting epoch. When VHE γ rays from distant sources, such as AGNs, interact with the EBL photons, they get absorbed via electron-positron pair production. This interaction attenuates the γ-ray flux from these extragalactic sources, which affects the observed energy spectra and leaves a

unique imprint of EBL. The attenuation is strongly energy and redshift dependent. Only because of this strong dependency we can constrain the EBL density well. Therefore, in this study, we have used exceptionally high flare data of HBL 1ES 1011+496 (z=0.212) and monitoring data of another HBL PKS 1424+240 (z=0.6) to measure the EBL density. As an outcome of this work, we have successfully tested the EBL hypothesis and achieved significant results from 1ES 1011+496. These results are already published in [Ahnen et al. 2016] for which I am one of the corresponding authors. In the following sections, first I will describe the basic concepts of EBL along with the EBL measurements, then the method used for constraining the EBL is explained. In results, details of EBL analysis carried out for 1ES 1011+496 and PKS 1424+240 are given.

Introduction

Extragalactic background light (EBL) is the diffused radiation and one of the fundamental observation quantities in cosmology. It consists of the sum of the starlight emitted by galaxies and also the re-radiation of stellar light at longer wavelengths due to dust. Therefore it gives a great deal of information about the baryons and nucleosynthesis across the cosmic time. The intensity and spectral shape of EBL hold key information about the formation and evolution of the galaxies throughout the history of the universe [Dwek & Krennrich 2013].

To highlight the importance of the EBL, figure 7.2 shows the extragalactic background radiation spectrum from radio to high energy γ rays. Among different backgrounds, the cosmic microwave background (CMB), which is the remains of blackbody radiation at 2.7 K from the Big Bang, contains the highest amount of electromagnetic energy. In figure 7.2, the background light from UV to far infrared (FIR) wavelengths is called as EBL (shown in a blue ellipse). The EBL produces the second-most energetic diffused background, after the CMB, thus being essential for understanding the full energy balance of the Universe. The radiation covers the wavelength range from ultraviolet to infrared (IR) regions of the electromagnetic spectrum ($\sim$0.1 to 1000 μm). Thus, studies of the EBL spectrum can serve as important tracers of the formation of the first stars, which may have formed before galaxy formation began.

In Fig. 7.3, closer view to the UV-IR backgrounds is shown, i.e., the SED of the three major components are shown: CMB, cosmic infrared background (CIB) and cosmic optical background (COB), and in the boxes, their approximate integrated brightness nW m^{-2} sr^{-1} is shown. From the plot it is very clear that the CMB dominates others by a factor of $\sim$20 and accounts for about 960 nW m^{-2} sr^{-1} and, whereas, the CIB and COB each account for 23 and 24 nW m^{-2} sr^{-1}, respectively. The CIB and COB are collectively referred to as EBL and thus represent about 5% of the brightness of the CMB. Half of the energy comes in the form of starlight (COB) and half as dust-reprocessed starlight (CIB). The maximum of the power distribution

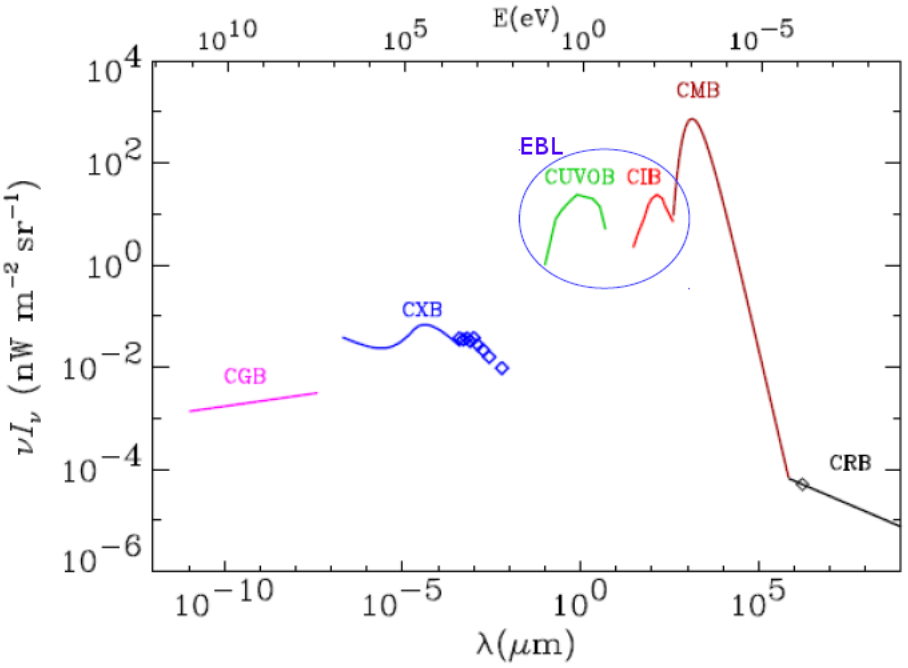

Figure 7.2: Spectrum of the cosmic background radiations. The cosmic radio background (CRB) is represented by a $\nu I\nu \propto \nu^{0.3}$ spectrum, which is normalized to value at 170 cm [Bridle 1967]. The cosmic microwave background (CMB) is a blackbody spectrum at 2.725 K. The backgrounds from UV-optical (CUVOB) and infrared (CIB) form the EBL, its closer view is shown in figure 7.3. The X-ray background (CXB) data are from [Wu et al. 2001], and the curves are analytical descriptions reviewed by [Fabian & Barcons 1992]. The γ-ray background (CGB) is represented by the power law given by [Sreekumar et al. 1998]. Image adapted from [Hauser & Dwek 2001].

is at $\sim$1.3 μm for the COB and $\sim$150 μm for the CIB. Other contributions from the extragalactic VHE sources such as AGNs and quasars are expected to produce $\sim$5-20% of the total EBL density in mid-IR [Dole & Lagache 2006].

Attenuation of γ rays

On the way to Earth, the VHE γ rays from extragalactic sources such as AGNs pass through the radiation field of EBL and interact with the EBL photons, which results in production of electron-positron pairs (figure 7.4) (provided $E_{\gamma\ VHE} E_{\gamma\ EBL} > (m_e c^2)^2$):

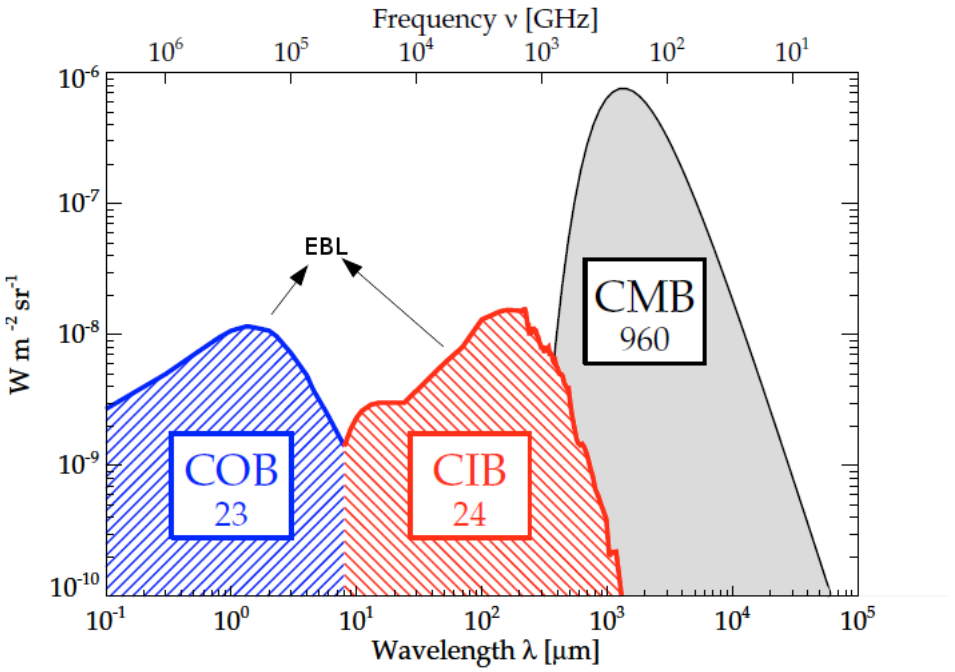

Figure 7.3: Schematic SED of the major backgrounds in the Universe by intensity i.e. cosmic microwave background (CMB), cosmic infrared background (CIB) and cosmic optical background (COB) and in the boxes their approximate brightness in nW m^{-2} sr^{-1} are shown. Image credit: [Dole & Lagache 2006].

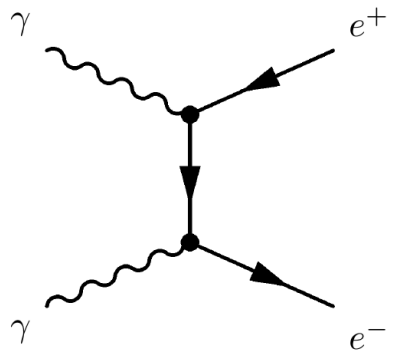

Figure 7.4: Schematic of $\gamma - \gamma$ interaction with pair production reaction (Image credit: `https://i.stack.imgur.com/hmbiG.png`)

$$\gamma_{VHE} + \gamma_{EBL} \rightarrow e^+ + e^- \tag{7.1}$$

This interaction attenuates the γ-ray flux from these extragalactic sources and

affects the observed energy spectra. The attenuation is strongly energy and redshift dependent. Only because of this strong dependency we can constrain the EBL well.

This e^+e^- pair production has a threshold ϵ_{th} as given below, whereas the opposite reaction does not have any threshold.

$$\epsilon_{th}(E_\gamma, \mu) = \frac{2(m_e c^2)^2}{E_\gamma(1-\mu)} \tag{7.2}$$

$$\implies E_\gamma = \frac{2(m_e c^2)^2}{\epsilon_{th}(E_\gamma, \mu)(1-\mu)} \tag{7.3}$$

As discussed in [Dwek & Krennrich 2005, Dwek & Krennrich 2008], the Thomposn's cross section for the $\gamma-\gamma$ interaction between a γ-ray photon and a background photon is given as:

$$\sigma_{\gamma\gamma}(E_\gamma, \epsilon, \mu) = \frac{3\sigma_T}{16}(1-\beta^2)\left[2\beta(\beta^2-2) + (3-\beta^4)\ \ln\left(\frac{(1+\beta)}{(1-\beta)}\right)\right] \tag{7.4}$$

Here, σ_T is the Thompson's cross-section, E_γ (from a source with redshift of z) and ϵ (energy of background photon) are the energies of one of the photons at the moment they interact, $\mu = \cos\theta$, and θ is the angle between two interacting photons as shown in Figure 7.4.

$$\beta = \sqrt{\left(1 - \frac{\epsilon_{th}}{\epsilon}\right)} \tag{7.5}$$

In figure 7.5, the Thompson's cross section for $\gamma - \gamma$ interaction and it's dependence on the factor β is shown. With $\sigma_T = 6.65 \times 10^{-25}$ cm^2 and $\beta = 0.70$, this $\gamma-\gamma$ cross section with an isotropic distribution of background photons has a peak value of 1.70×10^{-25} cm^2, which corresponds to:

$$E_\gamma \epsilon \approx 4(m_e c^2)^2 \approx 1\text{MeV}^2 \tag{7.6}$$

$$\implies E_\gamma(\text{TeV}) = 0.86\lambda_\epsilon(\mu m) \tag{7.7}$$

Here, λ_ϵ is the background photon wavelength. $E_\gamma TeV$ is the energy of VHE γ rays in the units of TeV. As discussed in [Dwek & Krennrich 2005], the optical depth traveled by a photon, which observed at energy E_γ and emitted by a source at redshift of z is given by,

$$\tau_\gamma(E_\gamma, z) = \int_0^z \left(\frac{dl}{dz'}\right) dz' \int_{-1}^{+1} d\mu \frac{1-\mu}{2} \int_{\epsilon'_{th}}^{\infty} d\epsilon' n_\epsilon(\epsilon', z') \sigma_{\gamma\gamma}(E'_\gamma, \epsilon', \mu) \tag{7.8}$$

where $n_\epsilon(\epsilon, z) \equiv dn(\epsilon, z)/d\epsilon$ is the specific comoving number density of background photons of energy ε and redshift z in cm^3 eV^{-1}, $(1+z)^3$ is the conversion

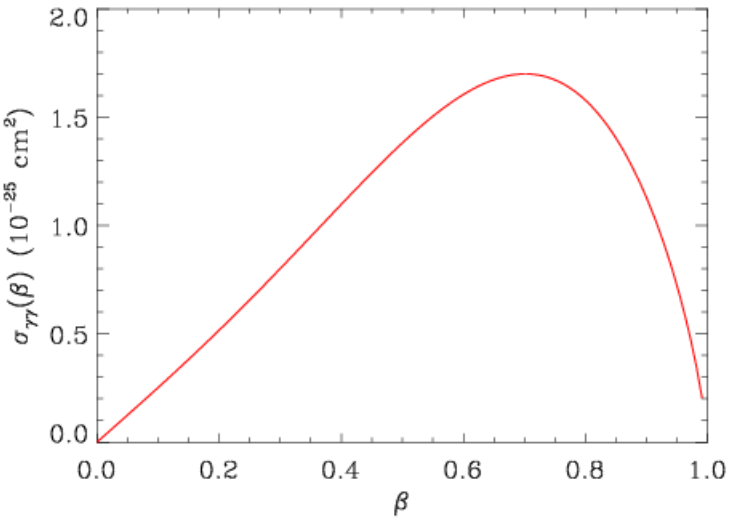

Figure 7.5: Thompson's cross section for $\gamma - \gamma$ interaction and it's dependence on β 7.5 [Dwek & Krennrich 2013].

factor of proper number density. Here $(1 + z)$ factor takes into account that the observed γ-ray photons had a higher energy at the redshift of the γ-γ interaction.The threshold energy for pair productions is given as:

$$\epsilon'_{th} = \frac{2(m_e c^{2)^2}}{E_\gamma(1-\mu)(1+z)} \tag{7.9}$$

Here $(1 + z)$ factor takes into account that the observed γ-ray photons had a higher energy at the redshift of the γ-γ interaction. Then the factors β' and dl/dz are given as:

$$\beta' = \left(1 - \frac{\epsilon'_{th}}{\epsilon}\right)^{0.5} \tag{7.10}$$

$$\frac{dl}{dz} = c \mid \frac{dt}{dz} \mid \tag{7.11}$$

Here, c is the speed of light, and l is the proper distance. The wavelength range of EBL photons responsible for absorption of VHE γ rays is quite large, as the background light from IR to UV interacts with photons of few GeV to tens of TeV. The threshold of γ rays of E = 20 TeV is at $\lambda \approx 100 \mu m$. Note that the influence of the CMB (2.7K) can be ignored for energies up to ≈30TeV (see equation 7.6 and 7.7). Due to its high density, the CMB absorbs the TeV photons while towards shorter wavelength the background photons interact with VHE γ rays of

lower energies where the cross section of photon-photon interaction is maximum. Then, the relation between the EBL wavelength at the peak of the cross section for the photon-photon interactions and the γ-ray of energy from the source, measured in the observed frame, is given by,

$$\lambda_{EBL}(\mu\mathrm{m}) = 1.187 \times \mathrm{E}_{\gamma}(\mathrm{TeV}) \times (1 + \mathrm{z})^2 \tag{7.12}$$

here z is the redshift of the source, E_γ is the γ-ray energy from the source, and λ_{EBL} is the EBL wavelength of the cross-section.

Status of EBL measurements

The intensity and shape of the EBL hold key information about the epochs of star formation and the evolution of galaxies in cosmic time. The SED of EBL is expected to have double-humped shape, first hump by the direct starlight from galaxies in optical and near-IR (NIR) and mid-IR (MIR) wavelengths known as COB part, and second hump by the light reprocessed by the dust in MIR and far-IR (FIR) wavelengths known as CIB part [Costamante 2013] (see figures 7.3 and 7.6). In the following sub-sections, I describe in brief the direct and indirect EBL measurements and the limits.

Direct measurements

Direct measurements of the EBL poses considerable technical and astronomical challenges. Technical challenges include absolute calibration of the instruments and understanding and elimination of all measurements uncertainties. Astronomical challenges include the removal of strong foreground emission from interplanetary dust particles, also known as the zodiacal light (ZL) and from stellar and interstellar emission components in the Milky Way [Dwek & Krennrich 2013]. Observationally all the scattered and diffracted light from the local sources such as Sun, Earth, and Moon also must be eliminated. So it means, the observations should be conducted with cryogenically cooled, carefully designed spaceborne instruments, i.e., satellites.

The solid lower limits for the COB part of the EBL level were achieved by adding up light emitted by resolved galaxies. [Madau & Pozzetti 2000] performed these deep galaxy counts in different wavebands by selecting 50×50 arcsec^2 portion of the sky using HST data. These measurements are considered as lower limits, however, even in deep surveys, the merging of the integrated galaxy light does not guarantee the measurement of the total EBL intensity, as the low surface brightness regions of galaxies may be missed in standard aperture photometry [Bernstein et al. 2002, Levenson & Write 2008].

The studies based on the COBE data show substantial evidence for direct detection of the CIB measurements [Boggess et al. 1992]. The Diffuse Infrared Background Experiment (DIRBE) onboard COBE was designed primarily to search for

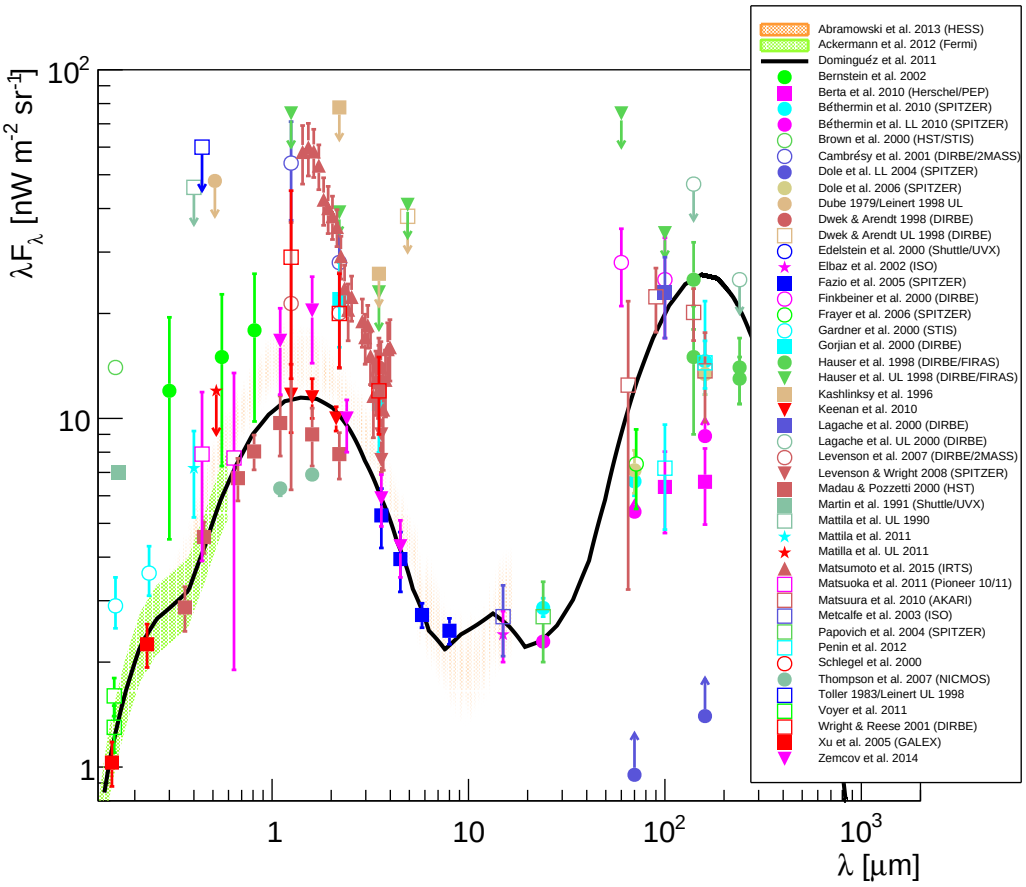

Figure 7.6: Extragalactic background light intensity versus wavelength at $z = 0$. The solid black line shows the EBL template model by [Domínguez et al. 2011] at $z = 0$. The contours from Fermi [Ackermann et al. 2012a] and HESS data [Abramowski et al. 2013] are shown in orange and green shaded area, along with many other direct and large anisotropy measurements, upper limits and galaxy counts data. The direct measurements included here are by [Dwek & Arendt 1998], [Hauser et al. 1998], [Finkbeiner et al. 2000], [Lagache et al. 2000], [Gorjian et al. 2008], [Bött et al. 2010], [Write et al. 2001], [Bernstein et al. 2002], [Matsumoto et al. 2005], [Matsuoka et al. 2011], and [Matsumoto et al. 2015]. Also galaxy-count data is included, from [Brown et al. 2000], [Gardner et al. 2000], [Madau & Pozzetti 2000], [Elbaz et al. 2002], [Metcalfe et al. 2003], [Dole et al. 2004], [Papovich et al. 2004], [Fazio 2005], [Xu et al. 2005], [Frayer et al. 2006], [Levenson et al. 2007], [Thompson et al. 2007], [Levenson & Write 2008], [Béthermin et al. 2010], [Berta et al. 2010], [Keenan et al. 2010] and [Voyer et al. 2011]. The upper limits shown are from [Dube et al. 1979], [Martin & Rouleau 1991], [Mattila et al. 1991], [Kashlinsky et al. 1996] and [Edelstein et al. 2000]. Also shown are large-scale anisotropy measurements from [Penin et al. 2012] and [Zemcov & Smidt 2014].

the CIB from 1.25 to 240 m. [Hauser et al. 1998] searched the CIB using DIRBE data for 10 DIRBE wavelength bands[a]. The final photometric reduction of these data resulted in conservative upper limits at all wavelengths based on the darkest measured sky brightness at each wavelength [Hauser et al. 1998, Hauser & Dwek 2001].

[Dole & Lagache 2006] also done direct measurements of CIB using data from the Spitzer Observatory. They performed direct measurements of CIB in mid-IR (MIR) region with using stacking analysis technique, in which images of detected sources at one wavelength were stacked together to improve signal over background fluctuations. The integrated light obtained by this method is thus closer to the EBL intensity than that obtained by integration down to the confusion limit.

In addition, in near-IR (NIR) region, between 1.5 and 4 μm, direct measurements were performed with IRTS satellite [Matsumoto et al. 2005]. These measurements lead to a controversial discussion about its origin due to a significant excess of EBL, which is too bright to be accounted for by the integrated light of missed faint galaxies [Costamante 2013]. If this claimed excess of the EBL is real, it raises the issue of possible contribution from other sources, especially from Population III stars with ∼zero metallicity during the intense star formation at $z \sim 10$. All these measurements are shown in figure 7.6.

Indirect measurements

As discussed before, direct measurements of the EBL are challenging due to foregrounds of the zodiacal light and gives strict lower limits on the EBL. The indirect measurements of extragalactic sources of VHE γ rays were performed in the energy range of 30 GeV to 30 TeV. As the sketch is shown in figure 7.7, VHE photons coming from cosmological distances are attenuated by electron-positron pair production when interacting with EBL photons [Gould & Schréder 1967].

The attenuation caused by EBL is redshift and energy dependent and results in the unique imprint on the observed VHE spectra. However, the EBL density is model dependent, as the intrinsic spectra are not known accurately. The unknown AGN intrinsic spectrum then the problem in the EBL constraints because we have the ambiguity in the EBL effect vs. intrinsic feature.

The curve shown in figure 7.6 is from [Domínguez et al. 2011] EBL model. The attenuation due to EBL modifies the observed VHE spectra, therefore assuming properties of the EBL-corrected or intrinsic spectra, constraints can be set on the EBL. The upper limits on the EBL can be derived when the redshift of the source is known and also the maximum slope of the EBL-corrected spectra (see [Aharonian et al. 2006, Mazin & Raue 2007] for more details). Thus the understanding of the EBL is also fundamental for extragalactic VHE astronomy. The main advantages of studying EBL via indirect measurements include:

[a]DIRBE wavelength bands: 1.25, 2.2, 3.5, 4.9, 12, 25, 60, 100, 140, and 240 μm [Hauser et al. 1998]

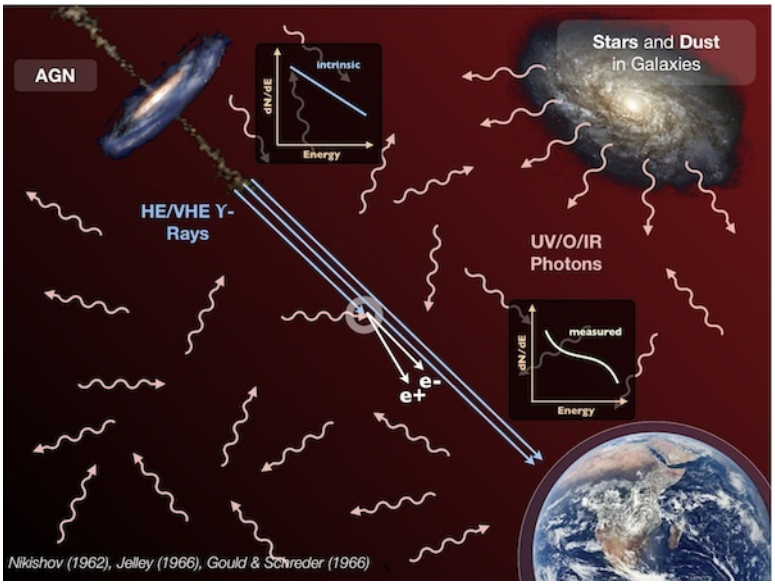

Figure 7.7: Very high energy γ rays get attenuated by interactions with the EBL. (Image credit: Martin Raue)

- If the EBL and redshift of the source are known, then the intrinsic properties of the source can be studied ([Abdo et al. 2011]).
- If the intrinsic properties of the source and EBL effect are known, then redshift of the source can be determined ([Prandini et al. 2010, Yang & Wang 2010]).
- If redshift of the source is known and intrinsic properties of the source are assumed, then limits on the EBL can be set (see [Aharonian et al. 2006] and [Mazin & Raue 2007] for more details).

Status of the previous HE-VHE EBL measurements:

Recently, the *fermi*-LAT data were extrapolated to set constraints on the VHE intrinsic spectra from distant sources [Ackermann et al. 2012a]. Along with *fermi*-LAT observations, upper limits on the EBL density were derived from IACT observations of the same sources (see [Georganopoulos et al. 2010, Orr et al. 2011], and [Meyer et al. 2012]). In 2012, using a likelihood ratio test on *Fermi*-LAT data taken from a number of extragalactic sources, the *Fermi* collaboration employed a technique actually to measure the EBL density [Ackermann et al. 2012a]. Spectral energy distributions from 150 BL Lacs in the redshift range 0.03 - 1.6 were modeled as log parabola in the optically thin regime ($E < 25\,GeV$). Then these SEDs were extrapolated to higher energies and they compared with the observed photon fluxes. To determine the best-fit scaling factor, a likelihood ratio test was used for the optical depth $\tau(E, z)$ according to a given EBL model, hence providing a measurement of the EBL density relative to the model prediction. Various EBL models

were tested using this technique, e.g., [Stecker et al. 2006, Finke et al. 2010], including the most widely and recently used by IACTs by [Franceschini et al. 2008, Domínguez et al. 2011]. The measurements obtained consisted of the UV component of the EBL of 3 ± 1 nW m^{-2} sr^{-1} at $z \approx 1$, which is the average redshift of the most constraining bin i.e. $0.5 < z < 1.6$. For other two redshift bins, i.e. $Z < 0.2$ and $0.2 < z < 0.5$ results were less constraining with test statistics < 25.

The H.E.S.S. collaboration used a similar likelihood ratio test as *Fermi*-LAT to measure the EBL taking advantage of their observations of distant sources at VHE. As mentioned before, the EBL absorption is expected to leave a unique imprint on the observed VHE spectra observable by IACTs between $\sim$ 100 GeV and $\sim$5-10 TeV. This feature is clearly visible in the flux vs. energy representation in logarithmic scale as an inflection point. Using simple functions having up to four free parameters, the H.E.S.S collaboration modeled the intrinsic spectra for several AGNs. Their source sample consisted of 17 observations of different flux states of seven BL Lacs: Mrk421, 1ES 0347-121, 1ES 0229+200, 1ES 1101-232, PKS 2005-489, PKS 2155-304, H 2356-309, with their redshifts range between 0.031 and 0.188. Then they applied a flux suppression factor $\exp(-\alpha \times \tau(E, z))$ to the observed spectra, where τ is the optical depth according to a given EBL model, and α is a scaling factor. A scan over α was performed to achieve the best fit to the observed VHE spectra [Abramowski et al. 2013]. The no-EBL hypothesis, i.e. $\alpha = 0$, was excluded at the 8.8σ level, and the EBL flux density was constrained in the wavelength range between 0.30 μm and 17 μm (optical to NIR) with a peak value of $15 \pm 2_{stat} \pm 3_{sys}$ nW m^{-2} sr^{-1} at 1.4 μm (orange shaded area in figure 7.6). In figure 7.8, as it can be seen from the TS values, these EBL measurements by H.E.S.S. are dominated by the observation of PKS 2155-304, at redshift z = 0.116.

Status of the EBL models

Various models have been proposed to describe the spectral luminosity distribution of the EBL as a function of redshift, i.e., the evolution of EBL. The models are divided into four categories as forward evolution, backward evolution, cosmic chemical, and semi-analytical models. Most of these models were originally proposed to probe galaxy evolution in deep photometric surveys to predict the galaxy number count. These models vary from each other in their degree of complexity, physical realism, and ability to account for observations or to make predictions. Brief details of the models are given below. See reviews by [Hauser & Dwek 2001, Dwek & Krennrich 2013] and the references therein for more details.

- **Forward evolution models**
  The starting point for the forward evolution (FE) models is the cosmic star formation rate (CSFR) and its dependence on the redshift using semi-analytical models (SAMs) of galaxy formation. Examples of FE models are [Finke et al. 2010].
- **Backward evolution models**

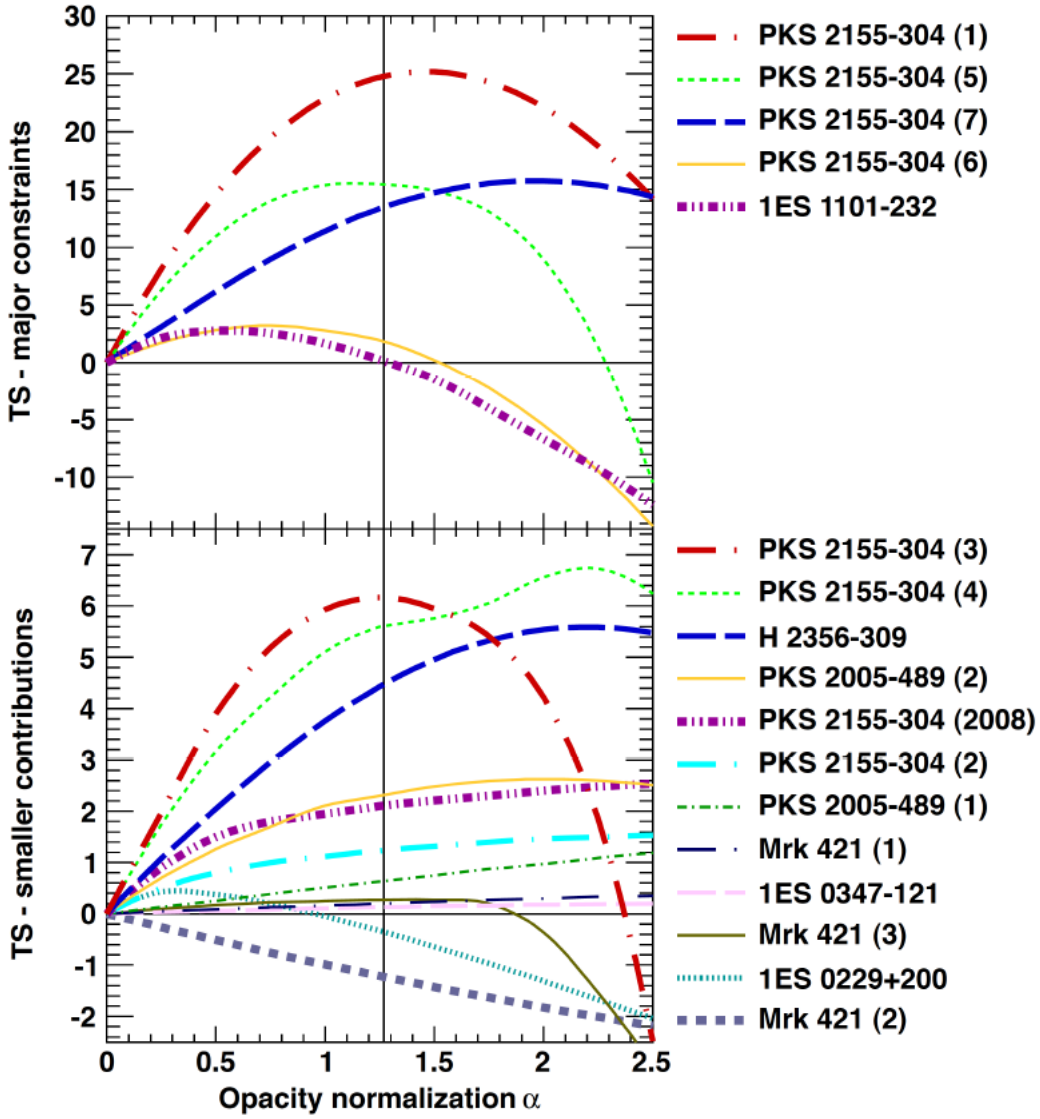

Figure 7.8: Test Statistics as a function of the EBL opacity normalization for the best fit intrinsic models for each spectrum in the sample of H.E.S.S.. The top panel shows the most constraining data sets, while the bottom panel shows the less constraining contributions. The vertical line indicates the best fit value from all contributions. Image credit [Abramowski et al. 2013].

Backward evolution models (BE), also referred to as no-evolution models, assume that neither the SED nor the comoving number density of galaxies evolve with time. Thus, extrapolation is done to the spectral characteristics of the

galaxies with present redshift to the higher redshifts (i.e., backward in time). Recent examples of these models are by [Stecker et al. 2006], [Franceschini et al. 2008] and [Domínguez et al. 2011].

- **Cosmic chemical evolution models**
  Cosmic chemical evolution (CCE) models treat the universe as a closed system, within which all galaxies in a large comoving volume element are represented by their basic ingredients, such as, stars, interstellar gas, metallicity, and radiation.
- **Semi-analytical models**
  Semi-analytical (SA) models use the cosmological parameters derived from the 5-year Wilkinson Microwave Anisotropy Probe (WMAP5) observations as the initial conditions to follow the formation and evolution of galaxies in a cold dark matter Lambda-dominated (ΛCDM) universe. Here, the model prediction is compared to a basic set of observational constraints, such as the cosmic star formation rate, the observed characteristics of galaxies, and their integrated cosmological properties as their number counts and luminosity function in different wavebands and redshifts, and the EBL generated by them. [Gilmore et al. 2011] gives an example of the SA model.

EBL constraints

As we have seen in section 7.3, the interaction of γ rays from extragalactic sources such as blazars with EBL photons causes attenuation in the observed spectrum of the source. The relation between the observed and intrinsic spectrum of the blazar is formed as:

$$\left(\frac{dN}{dE}\right)_{int} = \left(\frac{dN}{dE}\right)_{obs} \times e^{\tau(E,z)} \tag{7.13}$$

Where, $(dN/dE)_{obs}$ is the observed spectrum, $(dN/dE)_{int}$ is the intrinsic spectrum and $\tau(E,z)$ is the EBL induced energy and distance-dependent optical depth optical depth of VHE γ rays. Using the measured observed spectrum of a source and assuming some limits on the intrinsic spectrum of the source, it is possible to constrain the optical depth τ and, thus, to constrain the EBL density. From the general consideration about source's physics, the functional form of the intrinsic spectrum is assumed.

According to an accepted model, the VHE γ-ray emission in blazars is produced by VHE electrons or protons, which are accelerated to VHE energies by the shock acceleration. The alignment of the jet in blazar towards the observer and the high bulk motion Lorentz factor in the jet enhances chances to detect VHE γ-ray emission. In general, for blazars, the SEDs are commonly described with leptonic emissions such as synchrotron self-Compton (SSC) models where the ultra-relativistic electrons and their target photons are closely linked via synchrotron radiation. The detailed

SED fitting of blazar spectra requires extensive MWL monitoring including data from radio, optical, X-ray, and γ rays.

Electrons accelerating at ultra-relativistic energies result in a power law spectrum $dN/dE \propto E^{-\Gamma}$ with spectral index about $\Gamma_e \sim 2$. However, the steeper spectral index than Γ_e is resulting from the difference in the cooling process, as high energy electrons cool faster than low energy electrons. In the diffusive shock acceleration models of blazar jets, the energy spectrum produced by these high energy electrons strongly constrains the hardness of the resulting γ-ray spectra, limiting the hardest power law index value obtained to 1.5, as $\Gamma = \frac{\Gamma_e+1}{2} = 1.5$ [Malkov & Drury 2001]. Under most circumstances, for electrons, the emitted γ-ray energy spectrum through inverse Compton scattering is expected to be steeper than 1.5. Therefore, by assuming $\Gamma = 1.5$ to be the hardest possible intrinsic spectrum, stringent EBL limits were derived [Aharonian et al. 2003a, Aharonian et al. 2006, Albert et al. 2008e]. However, no harder spectra with $\Gamma < 1.5$ have been observed at lower energies, where no EBL absorption can take place. So more realistically, the flux and spectrum at VHE should always be lower and steeper than at HE ($\Gamma_{VHE} \geq \Gamma_{LAT}$) [Ackermann et al. 2012a]. If intrinsic effects such as the electron spectrum inside the jet which is responsible for producing photon spectrum or the scattering process takes place in the Klein-Nishina regime, the spectral index will be harder, i.e., resulting spectrum will be steeper, or the spectrum is expected to have a possible cut-off in electron distribution [Ramolia et al. 2017]. Due to this too high EBL density may result in a de-absorbed spectrum, which violates this limit of $\Gamma < 1.5$. Therefore this method allows to set upper limits to the EBL density (e.g., [Aharonian et al. 2006, Mazin & Raue 2007]).

Therefore, based in what is expected from the SSC models from previous *Fermi* and IACT observations of BL Lacs in HE and VHE regime, the intrinsic differential energy spectrum from a blazar can be modeled with a smooth and concave function. The simplest approximation to a spectrum is a power law (PWL). For precise and sufficiently long observations with wide energy range, a power law might provide a poor fit. So, the next-order polynomial, in a log-log energy scale, is the log-parabola function (LP) or if the blazar spectrum has a cut-off at VHE, then it can be modeled with an exponential cut-off.

Additionally, the following constraints were applied to the modeling:

- the shape of the spectrum cannot be convex, i.e., spectrum's hardness cannot increase with energy (as the available emission models do not support this, and also it has not been observed in optically thin HE region with *Fermi*-LAT data).
- based on SSC models (and observations with *Fermi*-LAT) the HE-VHE region shows concave function for blazar spectra. Therefore, for VHE spectra, the spectral index cannot be harder than the source's spectral index in HE region with *Fermi*-LAT data.

Here are the functions used for the modeling of the intrinsic spectrum:

power law (PWL):

$$\frac{dN}{dE} = f_0 \left(\frac{E}{E_0}\right)^{-\Gamma} \tag{7.14}$$

Log Parabola (LP):

$$\frac{dN}{dE} = f_0 \left(\frac{E}{E_0}\right)^{(-a-blog(E/E_0))} \tag{7.15}$$

power law with Exponential Cutoff (EPWL):

$$\frac{dN}{dE} = f_0 \left(\frac{E}{E_0}\right)^{-\Gamma} \exp\left(-\frac{E}{E_{cut}}\right) \tag{7.16}$$

In this section, a method from [Abramowski et al. 2013] is explained to perform the EBL measurements for the maximum likelihood ratio test to compare the no-EBL hypothesis with the best-fit EBL hypothesis. Therefore the intrinsic spectrum was calculated by slighly modifying the equation 7.13 as:

$$\left(\frac{dN}{dE}\right)_{int} = \left(\frac{dN}{dE}\right)_{obs} \times e^{(\alpha \times \tau(E,z))} \tag{7.17}$$

Here $e^{-\alpha\tau(E,z)}$ is the EBL absorption, in which the optical depth $\tau(E,z)$ depends on the γ-ray energy E and redshift z and it is predicted by the EBL models such as [Franceschini et al. 2008] or [Domínguez et al. 2011] and the optical depth is scaled by the normalization factor α which represents the EBL level.

To search for the EBL imprint on the observed spectrum, a scan over optical normalization factor α was computed, varying the value from 0 to 2.5. For each value of α, the intrinsic spectrum was modified according to the scaling of optical depth, i.e., $\alpha \times \tau(E,z)$, as shown in the equation 7.17. Therefore, for each α, using the measured observed spectrum $(dN/dE)_{obs}$, we reconstruct the intrinsic spectrum for every assumed EBL model $(\tau(E,z))$ and a given α. The optical depth was obtained from the EBL model [Domínguez et al. 2011]. Then the intrinsic spectrum was fitted with PWL, LP, and EPWL functions separately. Then for each function at each α, the χ^2, χ^2-probability and residuals (the ratio between observed and fitted points) were calculated from a fit of a function to the reconstructed spectrum.

The EBL absorption at VHE is expected to leave an imprint in the observed spectra, coming from a distinctive feature (an inflection point in the log flux-log E representation) between ∼100 GeV and ∼5-10 TeV, a region observable by IACTs. This feature is due to a peak in the optical region of the EBL flux density, which is powered mainly by starlight. The energy dependence of the EBL absorption deviates from small concavity and redshift dependent inflection points in the observed spectra comprise the key imprint that is reconstructed in this study [Raue & Mazin 2010, Abramowski et al. 2013]. Figure 7.9 shows the γ-ray attenuation provided by [Domínguez et al. 2011], [Franceschini et al. 2008] and [Gilmore et al. 2012] EBL

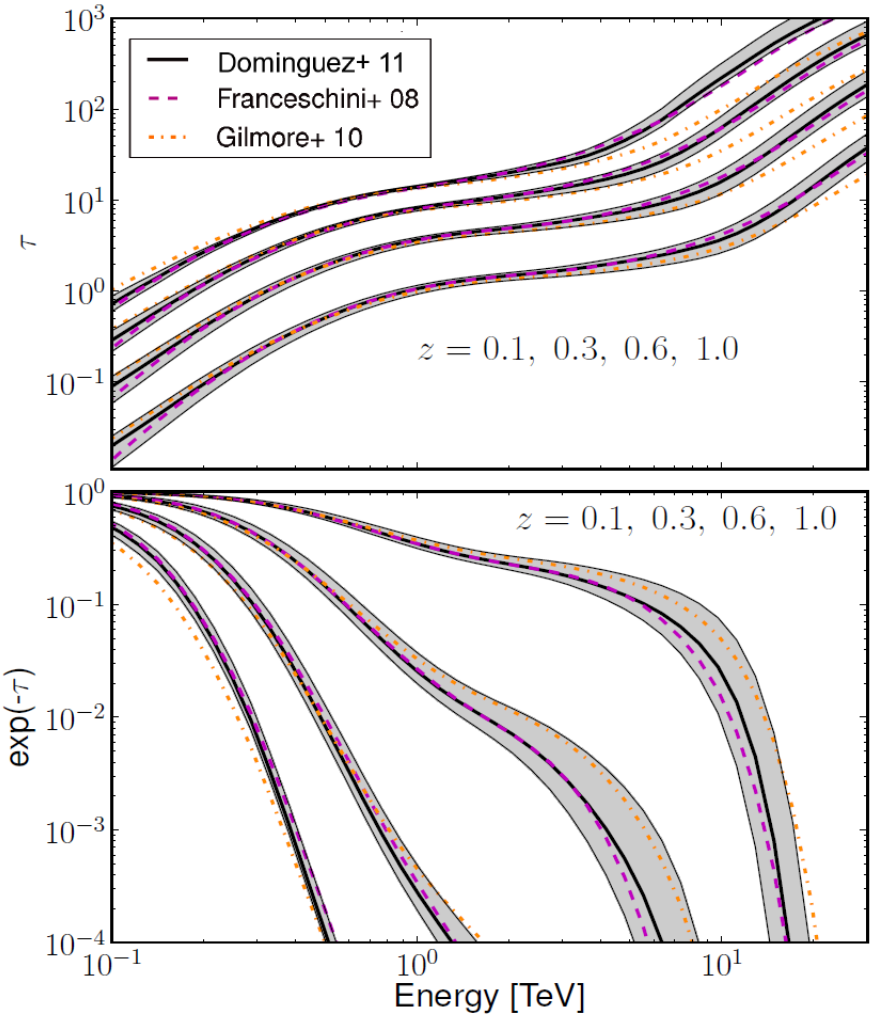

Figure 7.9: The γ-ray attenuation provided by [Domínguez et al. 2011, Franceschini et al. 2008] and [Gilmore et al. 2012] EBL models. Upper panel shows the variations of the optical depth and the lower panel shows the flux attenuation predicted by these EBL models at redshifts of z= 0.1, 0.3, 0.6, 1.0. The EBL uncertainties for [Domínguez et al. 2011] propagated to the optical depth and flux attenuation are shown with a shadow region. Image Cradit: [Domínguez et al. 2011].

models. Upper panel shows the variations of the optical depth and the lower panel shows the flux attenuation predicted by these EBL models at redshifts of z= 0.1, 0.3, 0.6, 1.0. The EBL uncertainties for [Domínguez et al. 2011] propagated to the optical depth and flux attenuation are shown with a shadow region. From the figure, it can be seen clearly that as the redshift of the source increases, the absorption

feature magnitude or (inflection points) also increases and appears at lower energies. The region seen at a low redshift between 1 to 10 TeV is a product of the mid-IR valley in the EBL spectrum. Therefore, to measure the EBL imprint, it is necessary to correct this EBL effect which caused the inflection points. To measure the EBL signature amplitude on MAGIC spectra, the best fit maximum likelihood L was converted into an equivalent $\chi^2 = -2logL_\alpha$ allowing the goodness of the fit with the conventional χ^2 probability as a function of α [Abramowski et al. 2013].

The maximum likelihood ratio test is then performed over null hypothesis i.e. no EBL (α=0) with the best fit EBL hypothesis ($\alpha = \alpha_0$). Then the test statistic (TS) is calculated as using the Wilks theorem as:

$$TS = 2log\left(\frac{L(\alpha = \alpha_0)}{L(\alpha = 0)}\right) \tag{7.18}$$

Here, two hypotheses differ by just one free parameter, i.e., α, therefore the TS will asymptotically follow a χ^2 distribution with one degree of freedom. As discussed in [Abramowski et al. 2013], the intrinsic model was selected on the basis of the highest χ^2 probability anywhere in the scanned range of α. A similar approach is followed in our studies along with some extra considerations such as reasons for spectral curvature in the observed spectrum. If the curvature is present in the observed spectrum then, choosing a PWL as the preferred model for the intrinsic spectrum is rather problematic since it would not allow any intrinsic spectral curvature. It means all curvature in the observed spectrum will be attributed to the EBL absorption. After considering all this, once the function for the intrinsic spectrum modeling is selected, the EBL opacity scaling will be indicated by the maximum in the likelihood profile at α_0. Then, the EBL density is calculated using the relation between the EBL wavelength at the peak of the cross section for the photon-photon interactions and the γ-ray of energy from the source, measured in the observed frame as given in equation 7.12.

Results

1ES 1011+496

As seen in chapter 4, during February-March 2014, the exceptionally high flare of 1ES 1011+496 was observed with MAGIC. The data from these observations provided good quality spectra spanning from ∼0.06 to 2.5 TeV. The energy span of the observed spectrum is well within the optically thick region where the EBL induced unique feature is seen [Ahnen et al. 2016]. Due to the redshift of z=0.212 and the energy span of the spectra, these data motivated us to perform the EBL measurements. The observed SED of 1ES 1011+496 for the 17 nights of observations between February 6^{th} and March 7^{th} 2014 is shown in figure 7.10.

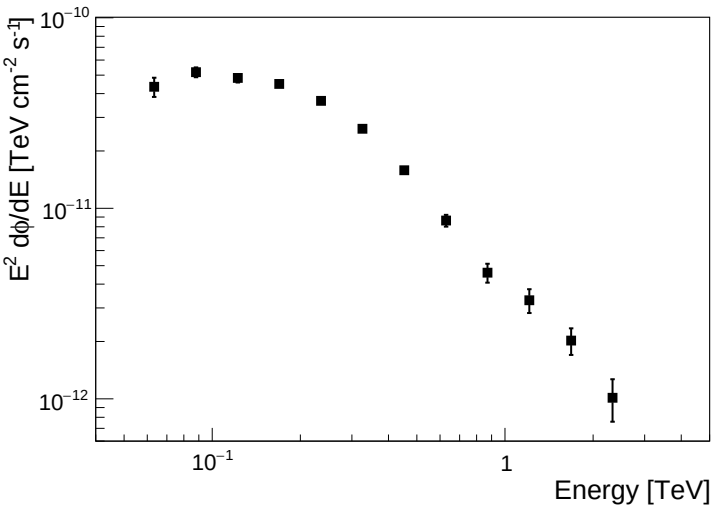

Figure 7.10: Observed SED of 1ES 1011+496 for the 17 nights of observations between February 6^{th} and March 7^{th} 2014.

To measure the EBL imprint from 1ES 1011+496 spectrum, we followed the procedure described in the previous section 7.6. Since during the flare high flux variability was observed (see section 4.4.2), it was important to check if the spectral shape was changing in individual night data. To check the stability of the spectral shape, a constant was fitted to the spectral index distribution from individual night data as shown in figure 7.11, where each spectral index was calculated from a power law fit to the de-absorbed spectrum of individual night data assuming the EBL with alpha = 1.1.

It resulted in χ^2/NDF=18.34/15 and χ^2-probability=24.5%, which confirmed the stability of the spectral shape. Therefore, to improve the statistics, the average spectrum from all the nights data was used for the maximum likelihood analysis method to derive the EBL level. A varying spectral shape could cause difficulty

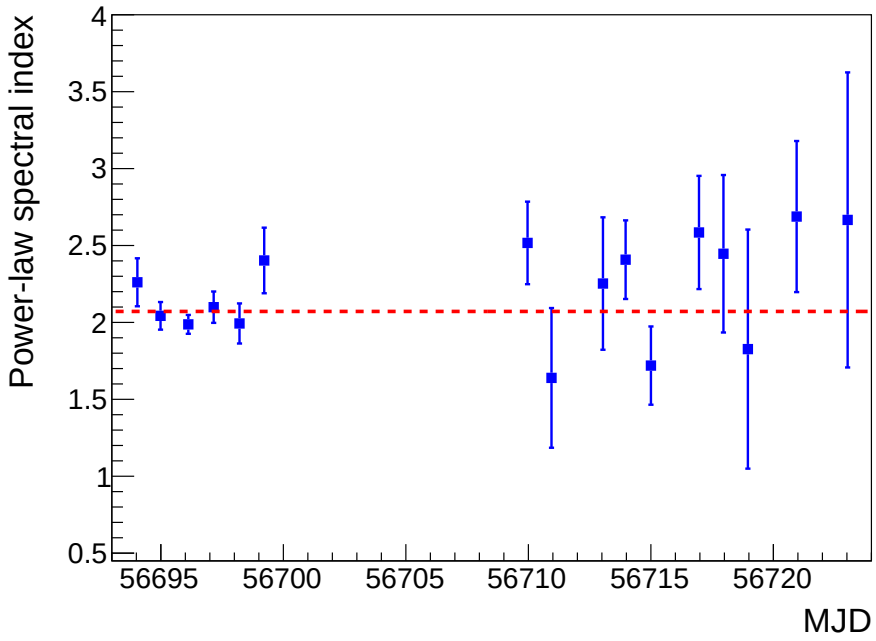

Figure 7.11: Spectral index distributions for the de-absorbed spectrum of 1ES 1011+496 (blue filled squares). Each spectral index from individual night data was calculated by fitting the constant to a power law fit to the de-absorbed spectrum (red dotted line).

in determining the expected EBL induced feature. Thus, the stability of spectral shape is one of the essential qualities in this analysis. Therefore, even though during the exceptional flare, flux level was changing during individual nights, the overall spectral shape did not change.

The intrinsic spectrum was obtained by applying the EBL absorption to the observed spectrum of 1ES 1011+496 as shown in equation 7.17. Then scan over α was computed from 0 to 2.5. Since the observed spectrum was clearly showing some curvature, for modeling the intrinsic spectrum at each α, along with PWL (equation 7.14), we also used LP (equation 7.15) and EPWL (equation 7.16). For LP we used the first constraint on the spectral shape as discussed in the section 7.6 i.e., the spectral shape cannot be convex. It means the spectrum's hardness cannot increase with energy and the curvature in LP will have only positive values. The convex spectral shape, i.e., curvature in energy flux is upward rather than downward is not expected in emission models, nor has it been observed in any BL Lac in the optically thin regime. This also means that any absorption corrected γ-ray spectrum showing an exponential rise cannot represent a physical source spectrum, and might have its origin in an over-correction for EBL absorption [Dwek & Krennrich 2013]. The positive curvature was achieved by using the squared value of "b" in LP equation 7.15. Then from the fitting of the intrinsic spectrum with PWL, LP, and EPWL,

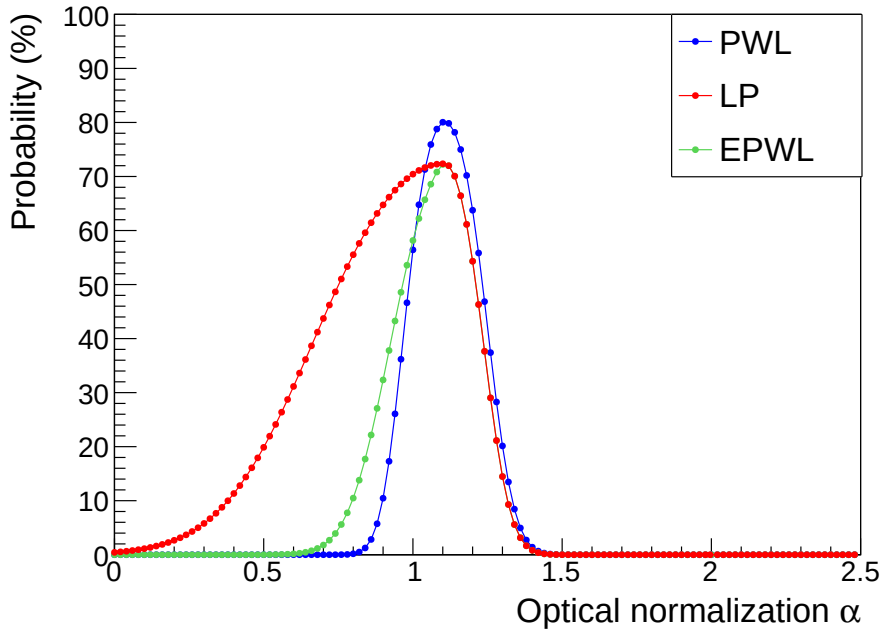

Figure 7.12: χ^2 probability distributions for the average spectrum of the Feb-March flare of 1ES 1011+496 for the three models tested. PWL in blue (dashed line), LP in red (solid line), EPWL in green (solid line).

χ^2 and χ^2-probability were calculated. These profiles are shown in figures 7.12 and 7.13. The null hypothesis or no EBL case is at α=0, whereas the model gives highest χ^2-probability and lowest χ^2 at α=1.1, thus called as the best α value. From figure 7.13, it is clearly seen that after reaching the minimum, χ^2 values are the same for all the functions, as LP and EPW converge to PWL. This happens because of the applied concavity restriction on the curvature, without which for higher α values after the best α value, all the curve function will become more and more convex.

Then the maximum likelihood and TS was calculated from the equation 7.18. TS values for all three functions are shown in figure 7.14. The vertical lines show the maximum TS and the uncertainty corresponding to $1\,\sigma$. From figure 7.14, for the PWL the maximum TS of 335.65 is at best fit $\alpha = 1.1^{+0.07}_{-0.07}$ and for LP the maximum TS of 17.78 is at best fit $\alpha = 1.1^{+0.07}_{-0.23}$. The errors quoted here on α are only statistical.

By following the approach in [Abramowski et al. 2013] would direct us to choose the PWL as the model for the intrinsic spectrum. However, choosing a PWL as the preferred model is rather problematic since it would not allow any intrinsic spectral curvature. It means all curvature in the observed spectrum will be attributed to the EBL absorption. If this procedure is applied to a large number of spectra, as in [Biteau & Williams 2015], individual $<2\sigma$ hints of intrinsic (concave) curvature might be overlooked and accumulate to produce a bias in the EBL estimation

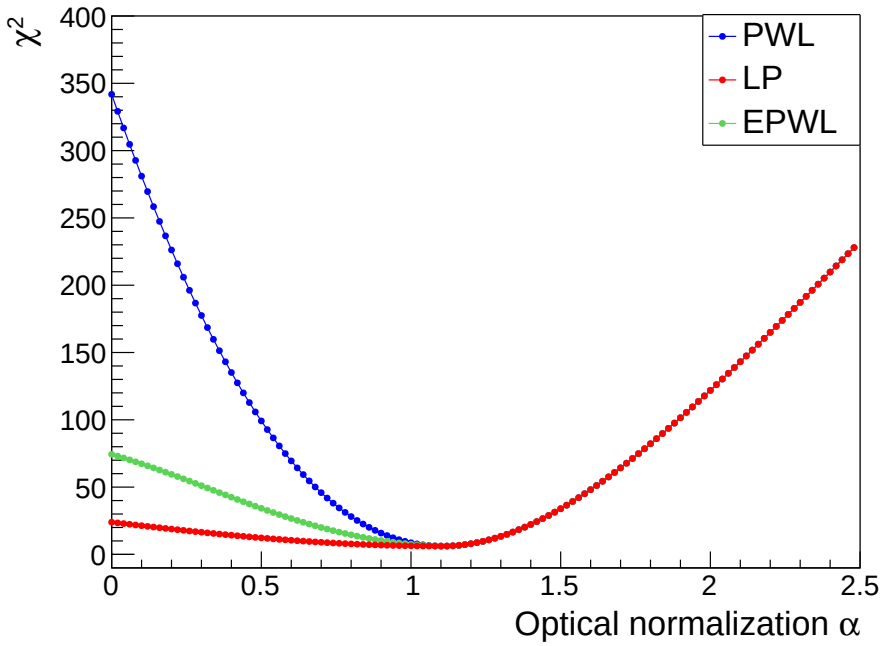

Figure 7.13: Fit χ^2 distributions for the average spectrum of the Feb-March flare of 1ES 1011+496 for the three models tested. PWL in blue (dashed line), LP in red (solid line), EPWL in green (solid line). Notice how all curves converge after reaching the minimum.

[Ahnen et al. 2016]. Here, with PWL the likelihood ratio test to prefer the best fit α over null hypothesis is $\sim 18\,\sigma$, whereas with LP it is $\sim 4.2\,\sigma$. We prefer to adopt a more conservative approach by choosing the next-best function, the LP. Note that, at the best-fit α, all the tested functions become simple power laws; therefore, the fit probabilities depend on the number of free parameters at the peak. Table 7.1 summarizes the values of χ^2-probability at α=0 and at best fit α=1.1 and TS at best fit α for each function.

Function	χ^2-Probability at α=0	χ^2-Probability at α=1.1	Test statistics (TS) at α=1.1
PWL	2.16×10^{-65}	0.80	335.65
LP	4.4×10^{-3}	0.72	17.78
EPWL	2.09×10^{-10}	0.72	68.20

Table 7.1: χ^2 probabilities for the null hypothesis at $\alpha = 0$ and at best fit $\alpha = 1.1$ and maximum TS at best fit α for 1ES 1011+496 February-March 2014 flare data

Figure 7.15 shows the residuals calculated from the ratio between observed data and the corresponding fit values from the intrinsic spectrum function LP at α=0

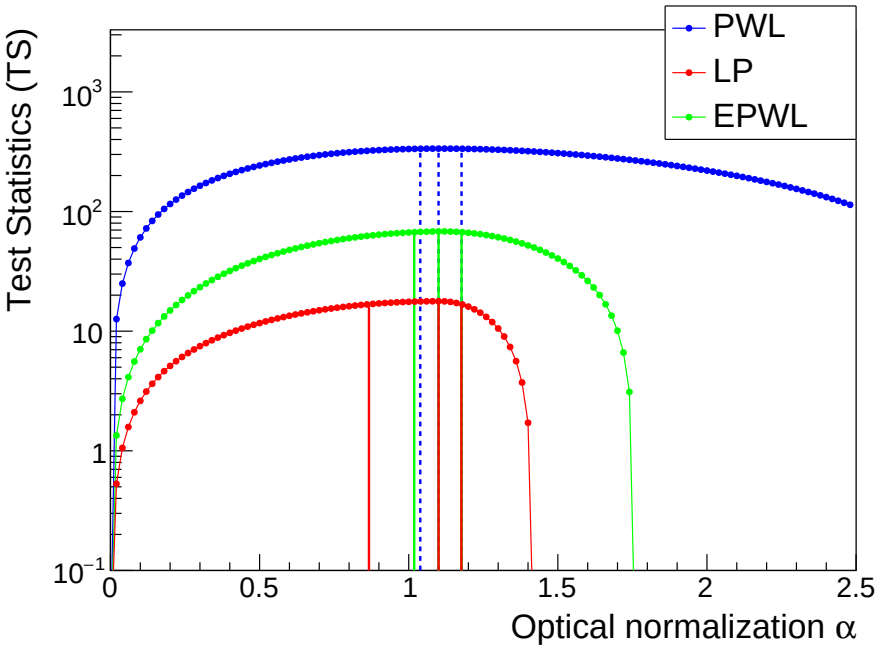

Figure 7.14: Test statistics distribution for the data sample for the February-March 2014 flare of 1ES 1011+496. The vertical lines mark the maximum and the uncertainty corresponding to $1\,\sigma$.

(left plot) and at the best value of α=1.1 (right plot). From the residuals, it is clear that the difference between these two plots start to show after 0.2 TeV, which is the region where EBL induced feature (inflection points) can be seen. The EBL constraint based on the test statistics value is calculated from the difference generated due to this feature. From the plots we can see, for α=0 the feature from 0.2 to 1 TeV and pile-up at higher energies got corrected at α=1.1. In both plots the red line indicates residuals=0.

Systematic uncertainties:
As discussed in MAGIC performance paper [Aleksić et al. 2016b], MAGIC telescopes have a systematic uncertainty of 15% in the absolute energy scale, for which the primary cause is the uncertain knowledge of the atmospheric transmission. The other factors which affect the systematics are background subtractions, pointing accuracy, night to night systematic uncertainty due to weather conditions and possible technical problems and also systematic uncertainties in flux normalization and slope.

To evaluate how this uncertainty influences our EBL constraint, a similar procedure was used as presented in [Aleksić et al. 2016b]. The calibration constants used to convert the pixel-wise digitized signals into photoelectrons were multiplied by a scaling factor (the same for both telescopes) spanning the range -15% to +15% in steps of 5% [Ahnen et al. 2016]. For each of the scaling factors, spectra were

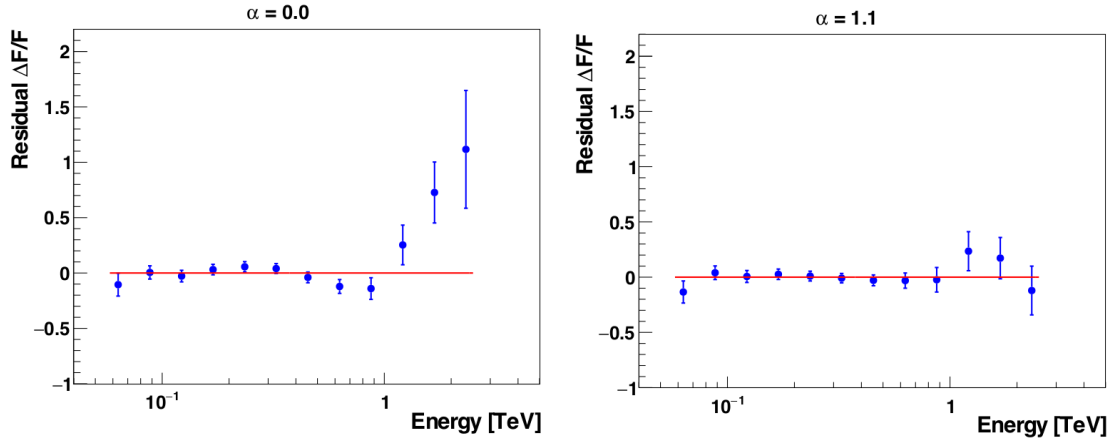

Figure 7.15: Ratio between the observed data and the corresponding fit values from the intrinsic spectrum function, $\alpha = 0$ (left plot) and $\alpha = 1.1$ (right plot), which corresponds to the maximum χ^2-probability and minimum χ^2 value. In both plots, the line that corresponds to a ratio = 0 is shown.

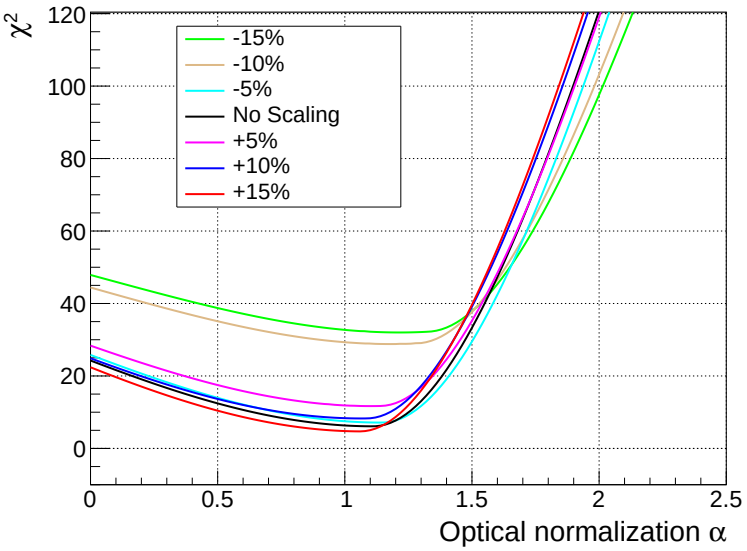

Figure 7.16: χ^2 profiles for the average spectrum of the February-March flare of 1ES 1011+496 for scaling factors of -15% to +15% applied to the data. The profile corresponding to a signal with scaling of +15% (shown in red line) has the minimum χ^2 value.

processed using the standard MARS routine 'flute' for this observation period. For all scaled flute output spectra, χ^2 profiles for α between 0 and 2.5 were computed. As shown in Figure 7.16, the lowest χ^2 was found from the +15% scaling profile. Therefore, from the 1σ uncertainty ranges in α obtained for the different shifts in the light scale, we determine the largest departures from our best-fit value α_0, arriving to the final result $\alpha_0 = 1.1^{+0.17}_{-0.28}$ $(stat + sys)$ using the 15% profile. The statistic and systematic errors were then added in quadrature as:

$$\text{Error}_{stat+sys} = \sqrt{(\text{Error}_{stat})^2 + (\text{Error}_{sys})^2} \tag{7.19}$$

Thus including systematic errors, for PWL the maximum TS is at $\alpha = 1.1^{+0.17}_{-0.17}$ $(stat+sys)$ and for LP the maximum TS is at $\alpha = 1.1^{+0.17}_{-0.28}$ $(stat+sys)$. To check the compatibility of our results, the same procedure was applied using the EBL model template [Franceschini et al. 2008]. It resulted for the PWL the maximum TS of 338.96 is at best fit $\alpha = 1.2^{+0.18}_{-0.19}$ and for LP the maximum TS of 19.43 is at best fit $\alpha = 1.2^{+0.18}_{-0.27}$. The errors quoted here on α are statistical and systematics.

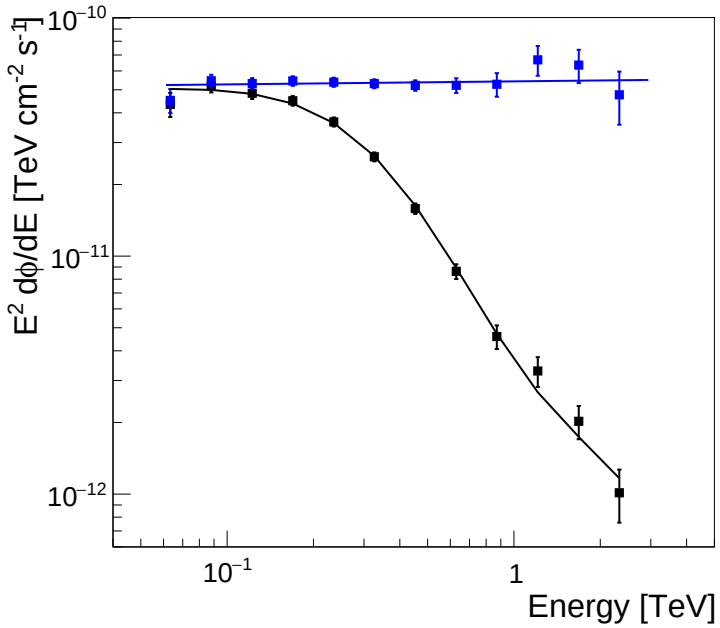

Figure 7.17: SED of 1ES 1011+496 for the 17 nights of observations between February 6^{th} and March 7^{th} 2014. The black and blue filled squares show the observed and EBL corrected de-absorbed spectrum respectively. The solid blue line shows a power law fit to the de-absorbed spectrum. The absorption was applied from the EBL model [Domínguez et al. 2011] for z=0.212. The solid black line shows the effect of EBL absorption on the observed spectrum.

In figure 7.17, the observed and de-absorbed SEDs of 1ES 1011+496 for the 17

nights of observations between February 6^{th} and March 7^{th} 2014 are shown. The observed spectrum is shown in black filled squares, and the EBL corrected de-absorbed spectrum is shown in blue filled squares. The solid blue line shows a power law fit to the de-absorbed spectrum derived using the EBL model [Domínguez et al. 2011] and best fit $\alpha = 1.1$. The solid black line is the convolution of the best fit to the intrinsic spectrum and the EBL with $\alpha = 1.1$.

Measurement of the EBL intensity

The EBL density was calculated using the relation between the γ-ray energy and the EBL wavelength of the cross-section as given in equation 7.12. The energy range used here for our calculations was between 0.06 and 2.5 TeV. However, the constraining of the EBL, following the method from [Abramowski et al. 2013], is based on the fact that, after de-absorbing the EBL effect, the feature between ∼100 GeV and ∼5-10 TeV is suppressed. In figure 7.15, the comparison is shown between the two cases where the residuals were computed for the null EBL hypothesis $\alpha = 0$ and for the case of the best fit EBL scaling $\alpha = 1.1$. The variations start to show after 200 GeV, a region where the EBL introduces a feature, i.e., an inflection point that cannot be fitted by the log parabola. This is the feature which prompts the TS value on which the EBL constraint is based. Therefore, we calculate the EBL wavelength range for which our conclusion is valid from the VHE range between 0.2 and 2.5 TeV.

As the interaction between the EBL photons and the γ-ray can happen in any point between the source and the Earth, so, the energy range has to take into account the redshift dependency in the equation 7.12. The range is between $[(1 + z)^2 E_{min}, E_{max}]$, resembles a wavelength range of the EBL where the interaction with the γ-ray can take place along the entire path between the source and the Earth. In figure 7.18, the contours from the stat+syst uncertainty of the EBL flux density are shown, which were derived by scaling up the EBL template model by [Domínguez et al. 2011] at redshift z = 0 (solid black line). The wavelength coverage is in the cosmic optical background (COB) part of the EBL in the wavelength range of 0.23 to 2.96 μm where we found the peak flux density $\lambda F_\lambda = 12.61^{+2.40}_{-2.63}$ nW m^{-2} sr^{-1} (stat+sys) at 1.4 μm, which ranks among the strongest EBL density constraints obtained from VHE data of a single source. For comparison, the contours from *Fermi* [Ackermann et al. 2012a] and HESS data [Abramowski et al. 2013] are shown in the orange and green shaded area, along with many other direct and large anisotropy measurements, upper limits and galaxy counts data. Our results overlap the similar COB region and are in good agreement with the EBL flux density measured by [Abramowski et al. 2013] over almost two decades of wavelengths with a peak amplitude at 1.4 μm of $\lambda F_\lambda = (15 \pm 2 \pm 3)$ nW m^{-2} sr^{-1} (stat+sys). Note that, for the H.E.S.S. data analyses, the EBL density was derived by scaling up the EBL template model by [Franceschini et al. 2008] at redshift z = 0. Hence the little difference can be seen in the values of λF_λ compared to our values of EBL density.

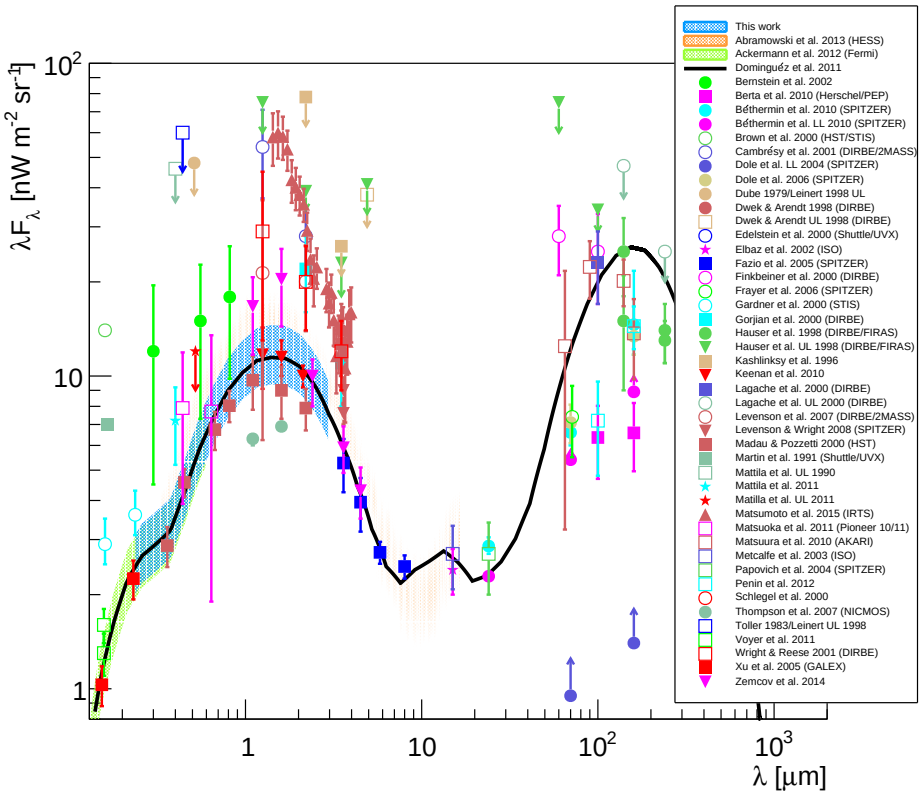

Figure 7.18: Extragalactic background light intensity versus wavelength at $z = 0$. The contours of the EBL density shown in blue shaded area span for the wavelength (0.24 to 4.14 μm) in which our constraints derived from MAGIC data are valid. The errors on the EBL density include statistical as well as systematic uncertainties. The solid black line shows the EBL template model by [Domínguez et al. 2011] at redshift z=0. For comparison, the contours from *Fermi* [Ackermann et al. 2012a] and HESS data [Abramowski et al. 2013] are shown in orange and green shaded area, along with many other direct and large anisotropy measurements, upper limits and galaxy counts data. The direct measurements included here are by [Dwek & Arendt 1998], [Hauser et al. 1998], [Finkbeiner et al. 2000], [Lagache et al. 2000], [Gorjian et al. 2008], [Bött et al. 2010], [Write et al. 2001], [Bernstein et al. 2002], [Matsumoto et al. 2005], [Matsuoka et al. 2011], and [Matsumoto et al. 2015]. Also galaxy-count data is included, from [Brown et al. 2000], [Gardner et al. 2000], [Madau & Pozzetti 2000], [Elbaz et al. 2002], [Metcalfe et al. 2003], [Dole et al. 2004], [Papovich et al. 2004], [Fazio 2005], [Xu et al. 2005], [Frayer et al. 2006], [Levenson et al. 2007], [Thompson et al. 2007], [Levenson & Write 2008], [Béthermin et al. 2010], [Berta et al. 2010], [Keenan et al. 2010] and [Voyer et al. 2011]. The upper limits shown are from [Dube et al. 1979], [Martin & Rouleau 1991], [Mattila et al. 1991], [Kashlinsky et al. 1996] and [Edelstein et al. 2000]. Also shown are large-scale anisotropy measurements from [Penin et al. 2012] and [Zemcov & Smidt 2014].

Thus including systematic errors, for PWL the maximum TS is at $\alpha = 1.1^{+0.17}_{-0.17}$ (stat+sys) and for LP the maximum TS is at $\alpha = 1.1^{+0.17}_{-0.28}$ ($stat + sys$). To check the compatibility of our results, the same procedure was applied using the EBL model template [Franceschini et al. 2008]. It resulted for the PWL the maximum TS of 338.96 is at best fit $\alpha = 1.2^{+0.18}_{-0.19}$ and for LP the maximum TS of 19.43 is at best fit $\alpha = 1.2^{+0.18}_{-0.27}$. The errors quoted here on α are statistical and systematics.

PKS 1424+240

As seen in chapter 5, PKS 1424+240 is an extragalactic HBL with a redshift of z=0.6. At this redshift, the VHE intrinsic γ-ray emission is significantly affected by EBL. Therefore, the source has been studied under the EBL key science project. The observations pertaining to this study were performed during March to June 2014, in which the source was strongly detected and resulted in good quality spectra in the energy range of $\sim$50 to 200 GeV. At this redshift the energy span is well within the optically thick region were the EBL induced unique feature is seen, thus motivated us to perform the EBL measurements. The observed SED of PKS 1424+240 for the observations between March to June 2014 is shown in figure 7.19.

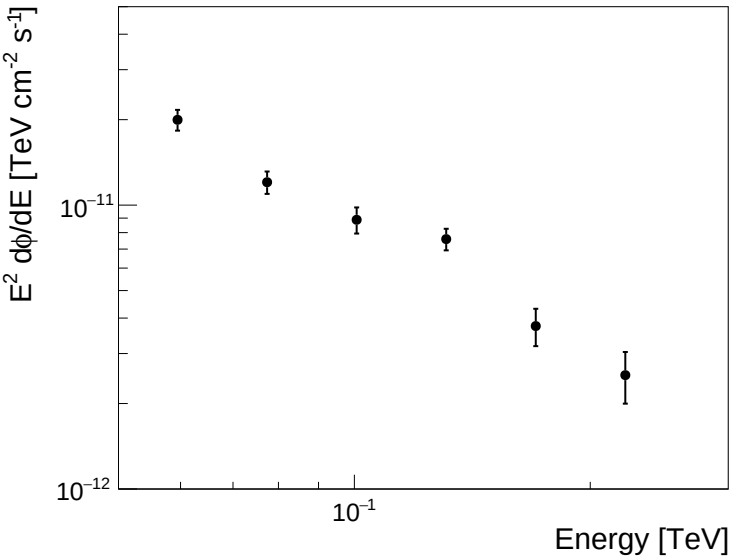

Figure 7.19: SED of PKS 1424+240 for the observations between March and June 2014.

To measure the EBL imprint from PKS 1424+240 spectrum, we followed the same procedure described in the previous sections 7.6 and 7.7.1. Since the source was in low emission state, it was not possible to detect it in night-wise data. In addition to that no significant flux variability has been observed; therefore the spectral shape is assumed to be constant. To improve the statistics, the average spectrum from all the nights data was used for the maximum likelihood analysis method.

The intrinsic spectrum was obtained by applying the EBL absorption to the observed spectrum of PKS 1424+240 as shown in equation 7.17. Then scan over α was computed from 0 to 2.5. For modeling the intrinsic spectrum at each α, along with PWL (equation 7.14), we also used LP (equation 7.15) and EPWL (equation 7.16). Similar to 1ES 1011+496 we have applied a constraint on the curvature, i.e., the spectral shape cannot be convex. The positive curvature was achieved by using

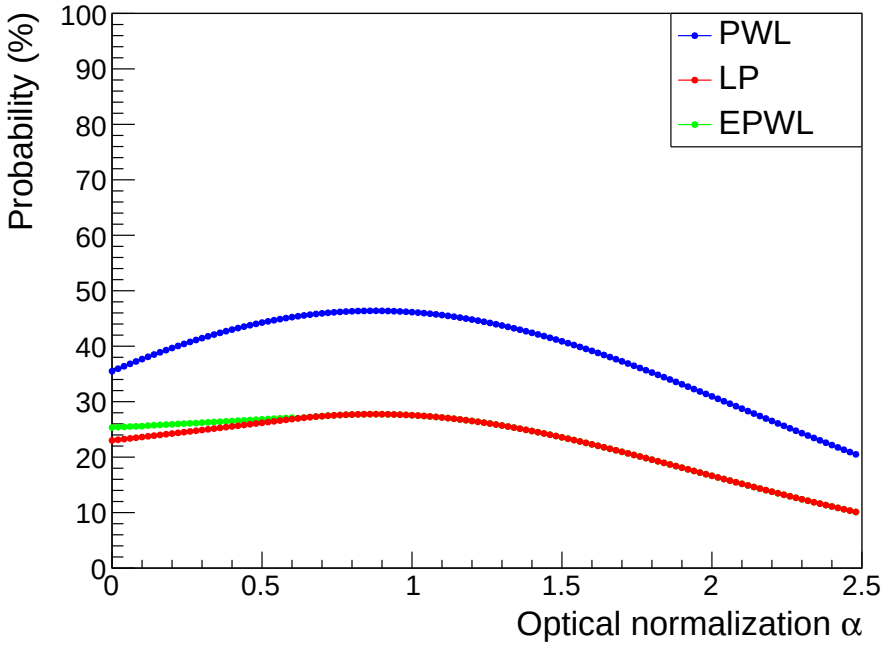

Figure 7.20: χ^2 probability distributions for the average spectrum of the March-May 2014 data of PKS 1424+240 for the three models tested. PWL in blue (solid line), LP in red (solid line), EPWL in green (solid line).

the squared value of "b" in LP equation 7.15. Then from the fitting of the intrinsic spectrum with PWL, LP, and EPWL, χ^2 and χ^2-probability were calculated. These profiles are shown in figure 7.20 and 7.21. The null hypothesis or no EBL case is at α=0, whereas the model gives highest χ^2-probability and lowest χ^2 at α=0.88, thus called as the best α value. From figure 7.21, it is clearly seen that after reaching the minimum, χ^2 values are the same for all the functions, as LP and EPWL converge to PWL. This happens because of the applied concavity restriction on the curvature.

Then the maximum likelihood and TS was calculated from equation 7.18. TS values for all three functions are shown in figure 7.22. The vertical line shows the maximum TS. In figure 7.22, for the PWL the maximum TS of 0.68 is at best fit $\alpha = 0.88^{+1.11}_{-1.88}$ and for LP the maximum TS of 0.37 is at best fit $\alpha = 0.88^{+1.11}_{-1.88}$. The errors quoted here on α are only statistical. As the quoted errors on α are large, it was not possible to show the 1σ uncertainties in the α range of 0 to 2.5. Table 7.2 summarizes the values of χ^2-probability at α=0 and at best fit α=0.88 and TS at best fit α for each function.

From the TS values, it is clear that the constraints on the EBL cannot be derived significantly. It suggests that the spectrum of the source is affected by the combined effects of intrinsic spectral softening as well as the effect of EBL absorption. It is quite complicated to resolve the EBL effect from intrinsic spectral softening, as it requires a clear understanding of the physical processes that are responsible for causing the

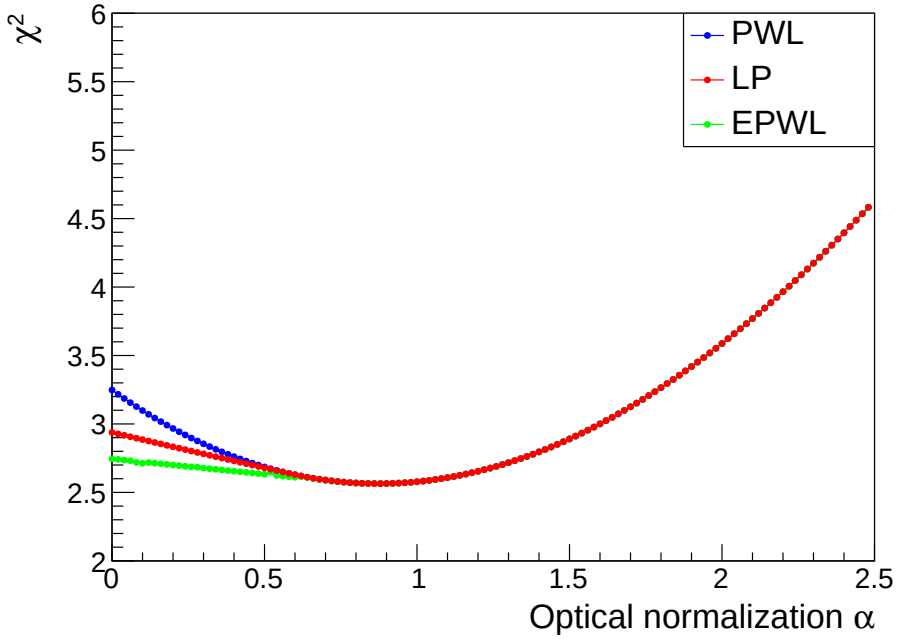

Figure 7.21: χ^2 distributions for the average spectrum of the March-May of PKS 1424+240 for the three models tested. PWL in blue (solid line), LP in red (solid line), EPWL in green (solid line). Notice how all curves converge after reaching the minimum.

Function	χ^2-Probability at α=0	χ^2-Probability at α=0.88	Test statistics (TS) at α=0.88
PWL	0.35	0.46	0.68
LP	0.23	0.27	0.37
EPWL	0.25	0.27	0.18

Table 7.2: χ^2 probabilities for the null hypothesis at $\alpha = 0$ and at best fit $\alpha = 0.88$ and maximum TS at best fit α for PKS 1424+240 March-May 2014 data.

intrinsic softening of the sources spectrum. To solve this problem, multiwavelength data from radio to TeV is required. Therefore we calculated the upper limits on the EBL constraint, as it is not possible to distinguish intrinsic features from EBL-caused ones is a bit weak. Therefore, assuming that all curvature is due to the EBL one can derive a conservative EBL upper limit, i.e., EBL can be lower but cannot be higher (shown in figure 7.23). The upper limits were derived by applying the second constraint as discussed in the section 7.6 i.e., the spectral index of the VHE spectrum cannot be harder than the HE spectrum with *Fermi*-LAT data. It means once the spectral index of the de-absorbed spectrum will reach to the power law spectral index of -1.77 (taken from 2^{nd} *Fermi*-LAT catalog [2FGL] [Nolan et al. 2012]), then it is

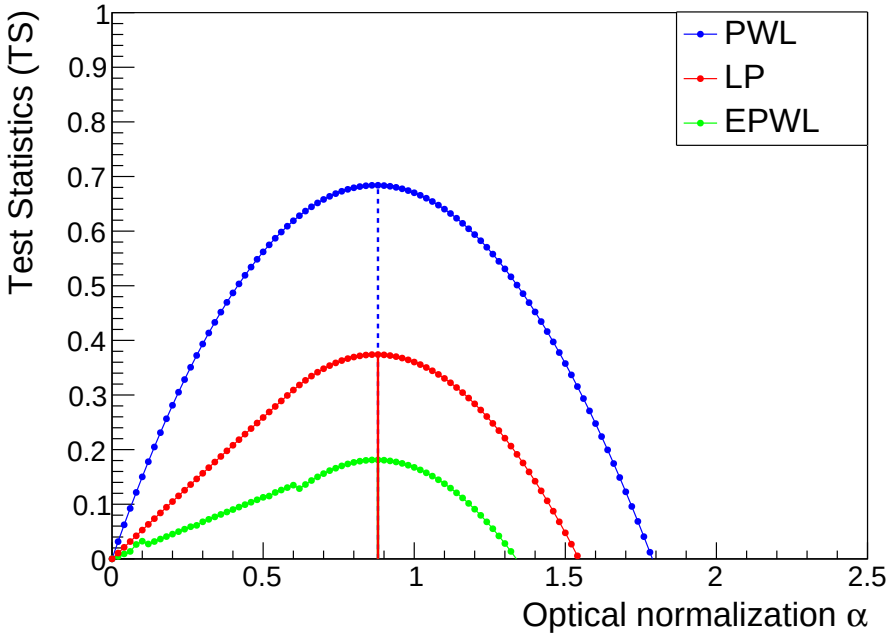

Figure 7.22: Test statistics distribution for the data sample for the March-May 2014 of PKS 1424+240. The vertical lines mark the maximum and the uncertainty corresponding to 1 σ.

fixed to -1.77. With this approach for PWL we got the maximum TS of 52.01 at best fit $\alpha = 1.74^{+0.26}_{-0.24}$ using the EBL model [Domínguez et al. 2011]. The errors quoted on α includes only statistical uncertainties.

In figure 7.24, the observed and de-absorbed SEDs of PKS 1424+240 for the observations between March and June 2014 are shown. The observed spectrum is shown in black filled squares, and the EBL corrected de-absorbed spectrum is shown in blue filled squares. The solid blue line shows a power law fit to the de-absorbed spectrum derived using the EBL model [Domínguez et al. 2011] and best fit $\alpha = 0.88$. The solid black line is the convolution of the best fit to the intrinsic spectrum and the EBL with $\alpha = 0.88$.

Combined TS

As a concluding step, we calculated the combined TS from the 1ES 1011+496 flare data (figure 7.14) and PKS 1424+240 monitoring data (figure 7.22). To combine the TS values, as mentioned before in the sections 7.7.1 and 7.7.2, [Domínguez et al. 2011] EBL model was used. Combined TS values for all three functions are shown in figure 7.25. The vertical line shows the maximum TS and the corresponding 1σ uncertainty. In figure 7.25, for the PWL the maximum TS of 336.29 is at best fit $\alpha = 1.1^{+0.07}_{-0.06}$ and for LP the maximum TS of 18.11 is at best fit $\alpha = 1.1^{+0.07}_{-0.23}$. The errors quoted

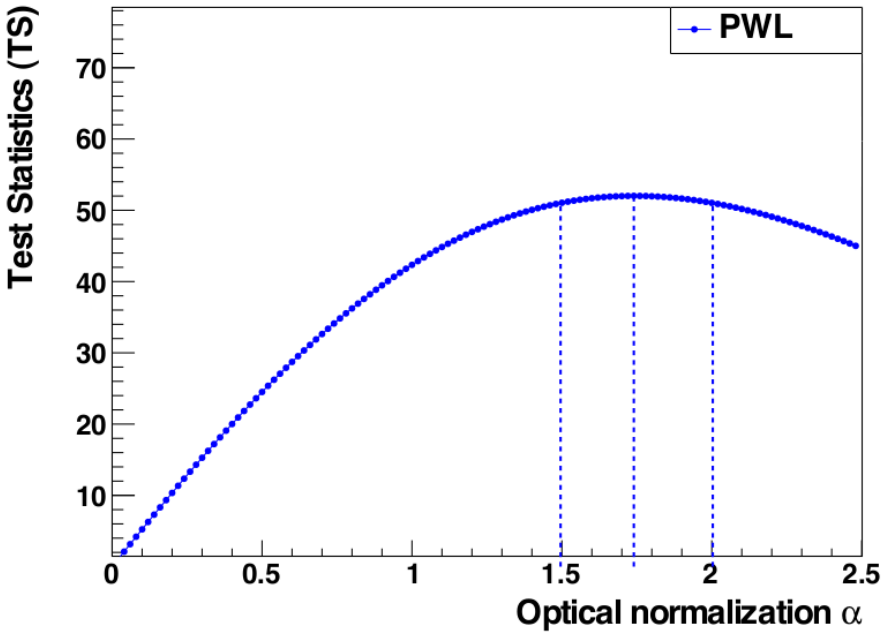

Figure 7.23: Upper limit on the EBL constraint with PKS 1424+240 data using the test statistics distribution for power law function. The vertical lines mark the maximum and the uncertainty corresponding to 1 σ.

here on α are only statistical.

Table 7.3 summarizes the values of maximum TS at best fit α for each function. As mentioned before, due to the possible spectral softening of the PKS 1424+240 spectrum, it is clear that the constraints on the EBL cannot be derived significantly. The 1ES 1011+496 flare data clearly dominate the combined TS values. Therefore, the inclusion of PKS 1424+240 data did not improve the overall result significantly. Here, with PWL the likelihood ratio test to prefer the best fit α over null hypothesis is $\sim$18.3 σ, whereas with LP it is $\sim$4.25 σ. As discussed before in case of 1ES 1011+496, choosing a PWL as the preferred model is rather problematic since it would not allow any intrinsic spectral curvature. It means all curvature in the observed spectrum will be attributed to the EBL absorption. If this procedure is applied to a large number of spectra, as in [Biteau & Williams 2015], individual $<2\sigma$ hints of intrinsic (concave) curvature might be overlooked and accumulate to produce a bias in the EBL estimation [Ahnen et al. 2016]. Therefore, we prefer to adopt a more conservative approach by choosing the next-best function, the LP, which also is used to calculate the final EBL density.

Then the EBL density was calculated using the relation between the γ-ray energy and the EBL wavelength of the cross-section as given in equation 7.12. Details about the EBL density are given in the previous section 7.7.1.1. The peak EBL density was calculated from equation 7.12 $\lambda F_\lambda = 12.61^{+2.41}_{-2.64}$ nW m^{-2} sr^{-1} at 1.4 μm, in the

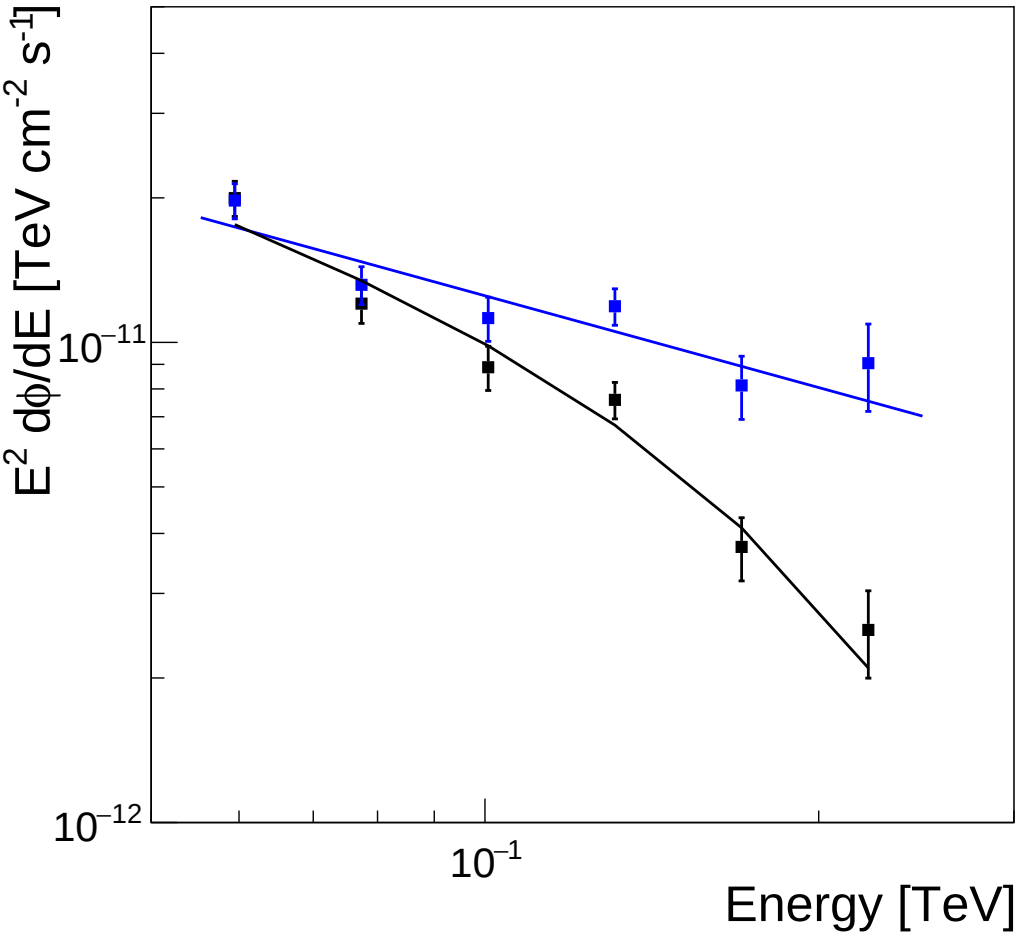

Figure 7.24: SED of PKS 1424+240 for the observations between March and June 2014. The black and blue filled squares show the observed and EBL corrected de-absorbed spectrum respectively. The solid blue line shows a power law fit to the de-absorbed spectrum. The EBL absorption was applied from [Domínguez et al. 2011] for z=0.6. The solid black line shows the effect of EBL absorption on the observed spectrum.

wavelength range of 0.23 to 2.96 μm, which covers the COB part of the EBL. The errors on the EBL density include only statistical uncertainties.

Summary

In this study, we present a model-dependent approach of constraining the EBL in the optical to far-infrared, i.e., COB part of EBL for the first time for MAGIC observations. In this method, we used VHE γ-ray spectra obtained with MAGIC

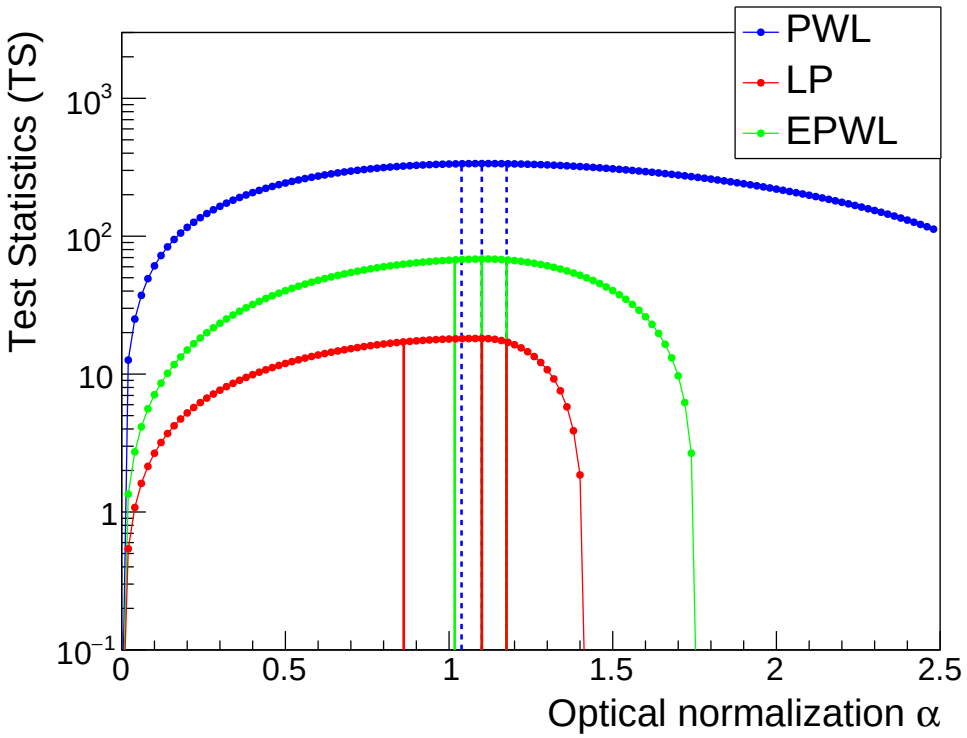

Figure 7.25: Combined test statistics distribution for the data sample for the February-March 2014 flare data of 1ES 1011+496 and March-May 2014 of PKS 1424+240. The vertical lines mark the maximum and the uncertainty corresponding to 1 σ.

Function	α	Test statistics (TS)
PWL	1.1	336.29
LP	1.1	18.11
EPWL	1.1	68.34

Table 7.3: α and maximum TS from the combined TS values of 1ES 1011+496 and PKS 1424+240 data. The errors on α includes only statistical uncertainties.

from extraordinary flare data of HBL 1ES 1011+496 (z=0.212) and monitoring data of HBL PKS 1424+240 (z=0.6). The energy span of the observed spectrum of both sources is well within the optically thick region where the EBL induced unique feature is seen [Abramowski et al. 2013]. Due to the redshift of the source and the energy span of the spectra, these data enabled us to perform the EBL measurements. During the flare of 1ES 1011+496, high flux variability has been observed in night-

wise data; however, the spectral shape of these individual night spectra was stable. This allowed us to use the average spectrum from all the data to carry out further EBL measurements. In the case of PKS 1424+240, we used the average spectrum from all the data assuming the spectral shape was stable as the source was in the low emission state. For both spectra, the curvature and wide energy span observed, which makes these observations ideal for constraining the EBL.

For EBL measurements, different functions were used for modeling the EBL absorbed or the intrinsic spectrum. Spectra from both sources are examined with the same algorithm. For the intrinsic spectrum, we used the conservative approach from the theory of the VHE γ-ray emission from TeV blazars. The spectral shape was restricted to have a concave shape, and spectral hardness limited to the spectral index from the *Fermi*-LAT data. After applying these two constraints, residuals were calculated from the intrinsic spectral fitting. The EBL imprint can be seen in the fit residuals for the best fit achieved under no-EBL hypothesis. Following this procedure, the best-fit EBL density for 1ES 1011+496 at $\lambda F_\lambda = 12.61^{+2.40}_{-2.63}$ nW m^{-2} sr^{-1} at 1.4 μm for the EBL level $\alpha = 1.1^{+0.17}_{-0.28}$, in the wavelength range of 0.23 to 2.96 μm, which covers the COB part of the EBL. Here, the errors include statistical as well as systematic uncertainties. Thus the EBL level from these data is compatible with the EBL level predicted by the [Domínguez et al. 2011] model and no significant excess have been found. This is the first significant EBL resolving measurement carried out using MAGIC data. The constraints on EBL density positions the first and strongest obtained from a single source VHE data. For PKS 1424+240 data, no significant constraints were derived due to possible intrinsic spectrum softening. Therefore the upper limit was calculated from these data. Then combined test statistics were calculated from both the sources. It is highly dominated by 1ES 1011+496 test statistic value and therefore, results in EBL density of $\lambda F_\lambda = 12.61^{+2.41}_{-2.64}$ nW m^{-2} sr^{-1} at 1.4 μm, in the wavelength range of 0.23 to 2.96 μm for the EBL level $\alpha = 1.1^{+0.07}_{-0.23}$, which is very similar to 1ES 1011+496 case. Here, errors include only statistical uncertainty. Our results overlap the similar COB region and are in good agreement with the EBL flux density measured by [Abramowski et al. 2013] over almost two decades of wavelengths with a peak amplitude at 1.4 μm of $\lambda F_\lambda = (15 \pm 2 \pm 3)$ nW m^{-2} sr^{-1} (stat+sys). Note that, for the H.E.S.S. data analyses, the EBL density was derived by scaling up the EBL template model by [Franceschini et al. 2008] at redshift z = 0. Hence the little difference can be seen in the values of λF_λ compared to our values of EBL density.

To check the compatibility of our results, the opacity normalization α was also calculated using the EBL model template [Franceschini et al. 2008]. It resulted for the PWL the maximum TS of 338.96 is at best fit $\alpha = 1.2^{+0.18}_{-0.19}$ and for LP the maximum TS of 19.43 is at best fit $\alpha = 1.2^{+0.18}_{-0.27}$. The errors quoted here on α include statistics and systematics. The opacity normalization value found by [Abramowski et al. 2013] is $\alpha_0 = 1.27(-0.15, +0.18)_{stat} \pm 0.25_{sys}$ using [Franceschini et al. 2008] as the EBL model template, which is in a good agreement with our measurements. They discarded the null EBL hypothesis with a significance of 8.8σ with this value of α. Even

though the H.E.S.S. measurement has a higher significance than our measurement, it should be noted that our measurement was performed using data from only one source. Also, we have used a more conservative approach using LP as the function to allow more possibilities in the curvature, whereas they have used PWL as the function. In addition to this, the data set used by the H.E.S.S. measurement is statistically dominated by the data from PKS 2155-304, which is at redshift z = 0.116, while the redshift of 1ES 1011+496 is z = 0.212. Thus, 1ES 1011+496 is farther away than any of the sources used by H.E.S.S..

The measurements of the EBL imprint presented here are the first one to resolving the EBL significantly using MAGIC from individual sources on the observed spectra. This unfolds the possibility to measure the EBL intensity in specific directions in the sky and also to search for possible angular distribution of the EBL. Now the same method is being implemented for many other MAGIC sources to measure the evolution of EBL at different redshift. At present, for most of these observations of relatively high redshift sources by MAGIC (or current IACTs) are performed during flaring states. However, with high sensitivity instrument such as CTA, it should be easier to produce good quality spectra to study EBL effects from sources with relatively high redshift, even if the source is not in a flaring state.

8. Conclusion and Outlook

In this Ph.D. thesis, I have contributed to a scientific research activity carried out as a member of the MAGIC collaboration in the field of VHE γ-ray astrophysics. In this work, the detailed study of the VHE γ-ray emission of the two TeV blazars 1ES 1011+496 (z=0.212) and PKS 1424+240 (z=0.6), and the radio galaxy M87 located at a distance of 16 Mpc, were carried out. The observations pertaining to this study were performed with the upgraded stereoscopic system of the MAGIC telescopes.

For the first time, an exceptionally high VHE γ-ray flaring state of 1ES 1011+496 was observed with MAGIC in February-March 2014, and the energy spectrum has been measured from 48 GeV to 3.6 TeV. During the entire flare, only flux variations were seen on the night-wise timescale; however, no significant spectral variability was observed. This was the first time that the spectral shape of the VHE spectrum with MAGIC showed intrinsic curvature and hence needed a complicated function for the fitting. Interestingly, once the EBL was corrected, the spectrum could be fitted with just a simple power law, which indicates that we measured the EBL imprint clearly for the first time. The broadband SED of 1ES 1011+496 is constructed using the 2014 MAGIC and the quasi-simultaneous HE, optical and X-ray data, supports a one-zone SSC model for a leptonic scenario of the γ-ray emission. Within this scenario, a slight indication of the dominance of the inverse Compton with a peak at $\sim$131 GeV is found. The ratio of the energy density to the magnetic field indicates that the magnetic field is far below equipartition. This result re-confirms the general framework of the one-zone SSC models at TeV energies.

In contrast, the monitoring observations of PKS 1424+240 during March-June 2014 with MAGIC reveals a low VHE γ-ray emission state. No significant night-wise or intra-night flux variability were observed during the entire monitoring. This was the first time that the observed spectrum is found to be spanning from 40 to 274 GeV, which allowed a better overlapping between the MAGIC and *Fermi*-LAT spectrums. However, even if statistically the spectral point is present at 40 GeV, it was not used in the MAGIC-*Fermi*-LAT combined spectrum, as effects of the telescope systematics are not well known below the current MAGIC energy threshold of 50 GeV. The broadband SED of PKS 1424+240 is constructed using the 2014 MAGIC and the quasi-simultaneous HE, optical and X-ray data, for which a one-zone SSC model does not fit. However, broadband SED can be fitted with a two-zone SSC model for a leptonic scenario of the γ-ray emission. For the two-zone SSC model, the majority of the optical-UV emission originates in a larger emission region called the outer region, and the X-ray to γ-ray emission originates mainly in a smaller emission region closer to the black hole called an inner region, which also has a smaller contribution from

the larger region in the *Fermi*-LAT energy band.

The monitoring of the radio galaxy M87 between 2012 and 2015 unveiled a low VHE γ-ray emission state. The source was detected significantly in every yearly campaign; however, no flare was detected. Due to increased sensitivity of the MAGIC telescopes after the upgrade, M87 2012-2015 observations described here are ones of the most sensitive measurements done so far in the low emission state, as this was a long multi-year campaign with a lot of data taken ($\sim$156 hrs). In 2012, 2014 and 2015 data, no clear variability was observed on daily and monthly time scales. A hint for variability on a $\sim 3\,\sigma$ level was found in 2013 data on a daily timescale. The VHE γ-ray flux level observed from these data above 300 GeV is the lowest observed since 2005. The combined SED between MAGIC and the *Fermi*-LAT, shows for the first time an amazing match with a power law over 5 decades in energy from 200 MeV to $\sim$10 TeV. Further, I also investigated the possible VHE γ-ray emission site for M87. From the fitted spatial location of the M87 excess in TeV γ rays from 2012-2015 data and a hint of variability on a daily timescale, the outer lobes are excluded as possible sites for the VHE emission. Only regions that are close to the core or HST-1 are possible sites for this emission, which indicates the TeV γ rays seem to come from the same or nearby site as during the flares. Due to the limitation of angular resolution of current generation IACTs, the exact location of the VHE γ-ray emitting region in M87 is puzzling. However, soon, with the help of multiwavelength studies performed along with high sensitivity instruments such as CTA, it might be possible to uncover the emission properties, as well pinpoint the exact location of VHE γ-ray emission region in M87. The broadband SED of M87 is constructed using the 2012-2015 MAGIC and the quasi-simultaneous radio to HE data, using a one-zone SSC and for the first time a photo-hadronic model, to explore a leptonic as well as a hybrid lepto-hadronic scenario of the γ-ray emission. Within the leptonic scenario, the model can describe the five orders in magnitude flat photon spectrum in HE and VHE γ rays, but it must be pushed to extreme limits and still has possible troubles in reproducing the X-ray data. In the hybrid scenario, it is easier to fit the available data. However, the number of free model parameters is higher than in the leptonic case, and the two components such as synchrotron from electrons and synchrotron from protons, are independent of each other, as their densities are unrelated.

The available measurements of VHE γ-ray spectra from the high flaring state of 1ES 1011+496 and low emission state of PKS 1424+240 were used to constrain the density of the EBL. In this study, a model-dependent approach was used to constrain the EBL in the optical to far-infrared, i.e., COB part of EBL, for the first time for MAGIC observations. Due to the redshift of these sources and the energy span of the spectra, these data enabled us to perform the EBL measurements. For 1ES 1011+496 data, the best-fit EBL density is found at $\lambda F_\lambda = 12.61^{+2.40}_{-2.63}$ nW m^{-2} sr^{-1} at 1.4 μm for the EBL level $\alpha = 1.1^{+0.17}_{-0.28}$, in the wavelength range of 0.23 to 2.96 μm, which covers the COB part of the EBL. The normalization factor α represents the EBL level, which is a scaling factor for the optical depth. Here, α is calculated using the [Domínguez et al. 2011] EBL model. The errors quoted on λF_λ and α

include statistical as well as systematic uncertainties. Thus, the EBL level from these data is compatible with the EBL level predicted by the [Domínguez et al. 2011] model, and no significant excess has been found. This is the first significant EBL resolving measurement carried out using MAGIC data. The constraints on EBL density positions the first and strongest obtained from single source VHE data. For PKS 1424+240 data, no significant constraints were derived due to possible intrinsic spectrum softening. Therefore, an upper limit on the EBL density was calculated from these data. The combined test statistics is highly dominated by 1ES 1011+496 test statistic value and therefore, results in EBL density of $\lambda F_\lambda = 12.61^{+2.41}_{-2.64}$ nW m^{-2} sr^{-1} at 1.4 μm, in the wavelength range of 0.23 to 2.96 μm for the EBL level $\alpha = 1.1^{+0.07}_{-0.23}$, which is very similar to the 1ES 1011+496 case. Here, errors include only statistical uncertainty. They overlap the similar COB region and are in good agreement with the EBL flux density measured by [Abramowski et al. 2013] with a peak amplitude at 1.4 μm of $\lambda F_\lambda = (15 \pm 2 \pm 3)$ nW m^{-2} sr^{-1} (stat+sys) over almost two decades of wavelengths. This unfolds the possibility to measure the EBL intensity in specific directions in the sky and also to search for possible angular distribution of the EBL.

The method of constraining EBL presented in this thesis is being implemented for many other MAGIC sources to measure the evolution of EBL at different redshift. Therefore, using more accurate measurements of the available GeV-TeV blazars, EBL constraints can even be further improved. One of the important goals of future observations is to detect new extragalactic VHE γ-ray sources to explore the redshift range of these sources to study the evolving EBL. At present, most of these observations of relatively high redshift sources by MAGIC (or current IACTs) are performed during flaring states. However, with high sensitivity instruments such as CTA, it should be easier to produce good quality spectra to study EBL effects from sources with relatively high redshift, even if the source is not flaring. Once the energy spectra of extragalactic sources are corrected for the effects of the EBL, we gain insights into the intrinsic processes inside the plasma jets.

The future observations of extragalactic VHE γ-ray sources will significantly benefit from the currently planned CTA. CTA aims to increase the flux sensitivity by a factor of 10, lower the energy threshold to $\sim$20 GeV, and increase the accessible energy range up to $\sim$300 TeV. It promises a new era of observations by this higher sensitivity and significantly improved angular and energy resolution compared to current generation IACTs. Therefore, it will also increase the possibility to discover many more VHE sources by order of magnitude, which will undoubtedly benefit not only AGN and EBL studies but could also serve as excellent sites to test the laws of fundamental physics, e.g., Lorentz Invariance and new physics beyond the standard model. Projects like CTA promises a further dynamical development of VHE γ-ray astrophysics to extensively improve our current understanding of the extreme universe.

Bibliography

[Abdo et al. 2009] Abdo, A. A., Ackermann, M., Ajello, M., et al., *Fermi Observations of TeV-Selected Active Galactic Nuclei*, *ApJ*, 2009, **707**, 1310-1333

[Abdo et al. 2009a] Abdo, A. A., Ackermann, M., Ajello, M., et al. *Fermi/Large Area Telescope Bright Gamma-Ray Source List*, *ApJS*, 2008, **183**, 46, arXiv:0902.1340

[Abdo et al. 2010] Abdo, A. A., Ackermann, M., Ajello, M., et al., *Fermi Large Area Telescope First Source Catalog*, *ApJS*, 2010, **188**, 405-436

[Abdo et al. 2010a] Abdo, A. A., Ackermann, M., Ajello, M., et al., *The Spectral Energy Distribution of Fermi Bright Blazars*, *ApJ*, 2010, **716**, 30

[Abdo et al. 2010b] Abdo, A. A., Ackermann, M., Ajello, M., et al., *Fermi Large Area Telescope Constraints on the Gamma-ray Opacity of the Universe*, *ApJ*, 2010, **723**, 1082

[Abdo et al. 2011] Abdo, A. A., Ackermann, M., Ajello, M., et al., *Erratum: "Multiwavelength Observations of the Flaring Gamma-ray Blazar 3C 66A in 2008 October*, *ApJ*, 2011, **726**, 43

[Abraham et al. 2010] Abraham, J., Abreu, P., Aglietta, M., et al., *Measurement of the energy spectrum of cosmic rays above 10^{18} eV using the Pierre Auger Observatory*, *Physics Letters B*, 2010, **685**, 239-246.

[Abramowski et al. 2012] Abramowski, A., Acero, F., Aharonian, F., et al., *The 2010 very high energy gamma-ray flare & 10 years of multi-wavelength observations of M 87*, *ApJ*, 2012, **746**, 151

[Abramowski et al. 2013] Abramowski, A., Acero, F., Aharonian, F., et al., *Measurement of the extragalactic background light imprint on the spectra of the brightest blazars observed with H.E.S.S.*, *A&A*, 2013, **550**, A4.

[Acciari et al. 2008] Acciari, V. A., Beilicke, M., Blaylock, G., et al., *Observation of gamma-ray emission from the galaxy M87 above 250 GeV with VERITAS*, *ApJ*, **679** (2008), 397, arXiv:0802.1951

[Acciari et al. 2009] Acciari, V., Aliu, E., Arlen, T., et al., *Radio Imaging of the Very-High-Energy Gamma-Ray Emission Region in the Central Engine of a Radio Galaxy*, *Science*, 2009, **325**, 444, arXiv:0908.0511

[Acciari et al. 2010] Acciari, V. A., Aliu, E., Arlen, T., et al., *Discovery of Very High Energy Gamma Rays from PKS 1424+240 and Multiwavelength Constraints on Its Redshift*, *ApJ*, 2010, **708**, L100

[Acciari et al. 2010a] Acciari, V. A., Aliu, E., Arlen, T., et al., *VERITAS 2008 - 2009 monitoring of the variable gamma-ray source M87*, *ApJ*, **716** (2010), 819, arXiv:1005.0367

[Acero et al. 2015] Acero, F., Ackermann, M., Ajello, M., and *Fermi*-LAT Collaboration, *Fermi Large Area Telescope Third Source Catalog*, *ApJS*, 2015, **218**, 23

[Ackermann et al. 2010] Ackermann, M., Ajello, M., Allafort A., et al., *Fermi Observations of GRB 090510: A Short-Hard Gamma-ray Burst with an Additional, Hard Power-law Component from 10 keV to GeV Energies*, *ApJ*, 2010, **716**, 1178-1190

[Ackermann et al. 2012] Ackermann, M., Ajello, M., Allafort, A., et al., *Search for Gamma-ray Emission from X-Ray-selected Seyfert Galaxies with Fermi-LAT*, *ApJ*, 2012, **747**, 104

[Ackermann et al. 2012a] Ackermann, M., Ajello, M., Allafort, A., et al., *The Imprint of the Extragalactic Background Light in the Gamma-Ray Spectra of Blazars*, *Science*, 2012, **338**, 1190.

[Ackermann et al. 2015] Ackermann, M., Ajello, M., Atwood, W. B., et al., *The Third Catalog of Active Galactic Nuclei Detected by the Fermi Large Area Telescope*, *ApJ*, 2015, **810**, 14

[Aharonian 2000] Aharonian, F., *TeV gamma rays from BL Lac objects due to synchrotron radiation of extremely high energy protons*, *New Astronomer*, 2000, **5**, 377-395

[Aharonian 2003] Aharonian, F. *Is the giant radio galaxy M 87 a TeV gamma-ray emitter?*, *A&A*, 2003, **403**, L1, arXiv:0302155

[Aharonian et al. 2003a] Aharonian, F., Akhperjanian, A., Beilicke, M., et al., *Observations of H1426+428 with HEGRA, Observations in 2002 and reanalysis of 1999 & 2000 data*, *A&A*, 2003, **403**, 523-528

[Aharonian et al. 2004] Aharonian, F., Akhperjanian, A., Beilicke, M., et al., *Observations of 54 Active Galactic Nuclei with the HEGRA system of Cherenkov telescopes*, *A&A*, 2004, **421**, 529-537

[Aharonian 2004] Aharonian, F., *Very high cosmic gamma radiation: a crucial window on the extreme universe*, *World Scientific Publishing Co. Pte. Ltd.*, 2004

[Aharonian et al. 2006] Aharonian, F., Akhperjanian, A. G., Bazer-Bachi, A. R., et al., *A low level of extragalactic background light as revealed by γ-rays from blazars*, *Nature*, 2006, **440**, 1018.

[Aharonian et al. 2006a] Aharonian, F., Akhperjanian, A. G., Bazer-Bachi, A. R., et al., *Observations of the Crab nebula with HESS*, *A&A*, 2006, **457**, 899

[Aharonian 2006b] Aharonian, F., Akhperjanian, A. G., Bazer-Bachi, A. R., et al., *Fast Variability of Tera-Electron Volt γ Rays from the Radio Galaxy M87*, *Science*, 2006, **314**, 1424, arXiv:0612016

[Aharonian et al. 2007] Aharonian, F., Akhperjanian, A. G., Bazer-Bachi, A. R., et al., *An Exceptional Very High Energy Gamma-Ray Flare of PKS 2155-304*, *ApJL*, 2007, **664**, L74

[Aharonian et al. 2007a] Aharonian, F., Akhperjanian, A. G., Bazer-Bachi, A. R., et al., *Discovery of a point-like very-high-energy -ray source in Monoceros*, *A&A*, 2007, **469**, L1-L4

[Aharonian et al. 2008] Aharonian, F., Buckley, J., Kifune, T., et al., *High energy astrophysics with ground-based gamma ray detectors*, *Reports on Progress in Physics*, 2008, **71**, 9, 096901.

[Ahnen et al. 2016] Ahnen, M., Ansoldi, S., Antonelli, L., et al., *MAGIC observations of the February 2014 flare of 1ES 1011+496 and ensuing constraint of the EBL density*, *A&A*, 2016, **590**, A24

[Ahnen et al. 2016a] Ahnen, M., Ansoldi, S., Antonelli, L., et al., *Insights into the emission of the blazar 1ES 1011+496 through unprecedented broadband observations during 2011 and 2012*, *A&A*, 2016, **591**, A10

[Ahnen et al. 2016b] Ahnen, M., Ansoldi, S., Antonelli, L., et al., *Multiwavelength observations of the blazar 1ES 1011+496 in Spring 2008*, *MNRAS*, 2016, **459 (3)**, 2286-2298

[Ahnen et al. 2016c] Ahnen, M., Ansoldi, S., Antonelli, L., et al., *Long-term multiwavelength variability and correlation study of Markarian 421 from 2007 to 2009*, *A&A*, 2016, **593**, A91

[Ahnen et al. 2017] Ahnen, M., Ansoldi, S., Antonelli, L., et al., *Performance of the MAGIC telescopes under moonlight*, *astro-ph.IM*, 2017, `arXiv:1704.00906`

[Ahnen et al. 2019] Ahnen, M., Ansoldi, S., Antonelli, L., et al., *Monitoring of the Radio galaxy M 87 during a low emission state from 2012 to 2015 with MAGIC*, *In A&A Preperation*, 2019

[Albert et al. 2007] Albert, J. and Aliu, E. and Anderhub, H., et al., *Unfolding of differential energy spectra in the MAGIC experiment*, *NIMPRA*, 2007, **583**, 494-506

[Albert et al. 2007a] Albert, J. and Aliu, E., Anderhub, H., et al., *Discovery of Very High Energy γ-Rays from 1ES 1011+496 at z = 0.212*, *ApJ*, 2007, **667**, L21

[Albert et al. 2007b] Albert, J. and Aliu, E., Anderhub, H., et al., *Variable Very High Energy γ-Ray Emission from Markarian 501* , *ApJ*, 2007, **669**, 862-883.

[Albert et al. 2007c] Albert, J. and Aliu, E., Anderhub, H., et al., *Discovery of Very High Energy γ-Rays from 1ES 1011+496 at z = 0.212*, *ApJ*, 2007, **667**, L21

[Albert et al. 2007d] Albert, J. and Aliu, E., Anderhub, H., et al., *Very High Energy Gamma-Ray Radiation from the Stellar Mass Black Hole Binary Cygnus X-1*, *ApJ*, 2007, 665, L51

[Albert et al. 2007e] Albert, J., Aliu, E., Anderhub, H., et al., *Unfolding of differential energy spectra in the MAGIC experiment*, *NIM*, 2007, 583, 494

[Albert et al. 2008] Albert, J., Aliu, E., Anderhub, H., et al., *Implementation of the Random Forest method for the Imaging Atmospheric Cherenkov Telescope MAGIC*, *NIMPRA*, 2008, **588**, 424

[Albert et al. 2008a] Albert, J., Aliu, E., Anderhub, H., et al., *VHE γ-Ray Observation of the Crab Nebula and its Pulsar with the MAGIC Telescope*, *ApJ*, 2008, **674**, 1037

[Albert et al. 2008b] Albert, J., Aliu, E., Anderhub, H., et al., *FADC signal reconstruction for the MAGIC telescope*, *NIMPRA*, 2008, **594**, 407-419

[Albert et al. 2008c] Albert, J., Aliu, E., Anderhub, H., et al., *Systematic Search for VHE Gamma-Ray Emission from X-Ray-bright High-Frequency BL Lac Objects*, *ApJ*, 2008, **681**, 944-953

[Albert et al. 2008d] Albert, J., Aliu, E., Anderhub, H., et al., *Very High Energy Gamma-Ray Observations of a Strong Flaring Activity in M87 in 2008 February*, *ApJ*, 2008, **685**, L23, `arXiv:0806.0988`

[Albert et al. 2008e] Albert, J., Aliu, E., Anderhub, H., et al., *Very-High-Energy gamma rays from a Distant Quasar: How Transparent Is the Universe?*, *Science*, 2008, **320**, 1752

[Albert et al. 2009] Albert, J., Aliu, E., Anderhub, H., et al., *Periodic Very High Energy -Ray Emission from LS I +61° 303 Observed with the MAGIC Telescope*, *ApJ*, 2009, 693, 303

[Aleksić et al. 2010] Aleksić, J., Antonelli, L. A., Antoranz, P., et al., *Search for an extended VHE gamma-ray emission from Mrk 421 and Mrk 501 with the MAGIC Telescope*, *A&A*, 2010, **524**, A77, `arXiv:1004.1093`

[Aleksić et al. 2011] Aleksić, J., Antonelli, L. A., Antoranz, P., et al., *Gamma-ray Excess from a Stacked Sample of High- and Intermediate-frequency Peaked Blazars Observed with the MAGIC Telescope*, *ApJ*, 2011, **729**, 115

[Aleksić et al. 2011a] Aleksić, J., Antonelli, L. A., Antoranz, P., et al., *Searches for Dark Matter annihilation signatures in the Segue 1 satellite galaxy with the MAGIC-I telescope*, *Journal of Cosmology and Astroparticle Physics*, 2011, **06**, 035

[Aleksić et al. 2012] Aleksić, J., Antonelli, L. A., Antoranz, P., et al., *Performance of the MAGIC stereo system obtained with Crab Nebula data*, *ApJ*, 2012, **35**, 435-448

[Aleksić et al. 2012b] Aleksić, J., Antonelli, L. A., Antoranz, P., et al., *MAGIC observations of the giant radio galaxy M87 in a low-emission state between 2005 and 2007* , *A&A*, 2012, **544**, A96, `arXiv:1207.2147`

[Aleksić et al. 2014] Aleksić J., Ansoldi S., Antonelli L., et al., *MAGIC long-term study of the distant TeV blazar PKS 1424+240 in a multiwavelength context*, *A&A*, 2014, **567**, A135

[Aleksić et al. 2015] Aleksić, J., Antonelli, L. A., Antoranz, P., et al., *Measurement of the Crab Nebula spectrum over three decades in energy with the MAGIC telescopes*, *JHEA*, 2015, **5-6**, 30-38

[Aleksić et al. 2015a] Aleksić, J., Antonelli, L. A., Antoranz, P., et al., *Unprecedent insights in the blazar 1ES 1011+496 via MAGIC observations in 2011 and 2012 in combination with simultaneous MWL observations and polarimetry data*, *In preparation*, 2015.

[Aleksić et al. 2016a] Aleksić, J. and Ansoldi, S., Antonelli, L. A. et al., *The major upgrade of the MAGIC telescopes, Part I: The hardware improvements and the commissioning of the system*, *APh*, 2016, **72**, 61-75

[Aleksić et al. 2016b] Aleksić, J., Antonelli, L. A., Antoranz, P., et al., *The major upgrade of the MAGIC telescopes, Part II: The achieved physics performance using the Crab Nebula observations*, *APh*, 2016, **72**, 76-94

[Aliu et al. 2008] Aliu, E., Anderhub, H., Antonelli, L. A., et al., *Observation of Pulsed γ-Rays Above 25 GeV from the Crab Pulsar with MAGIC*, *Science*, 2008, **322**, 1221

[Aliu et al. 2009] Aliu, E., Anderhub, H., Antonelli, L. A., et al., *Improving the performance of the single-dish Cherenkov telescope MAGIC through the use of signal timing*, *APh*, 2009, **30**, 293-305

[Ammons et al. 2014] Ammons, S., Wong, K., Zabludoff, A., et al., *Mapping Compound Cosmic Telescopes Containing Multiple Projected Cluster-scale Halos*, *ApJ*, 2014, **781**, 18

[Antonucci 1993] Antonucci, R., *Unified models for active galactic nuclei and quasars*, *Annual Rev. Astron. Astrophys.*, 1993, **31**, 473-521

[Armada 2005] Armada A., *Characterization and some application of the anode current monitoring system of the magic telescope*, Master's thesis, Universitat Autónoma de Barcelona, 2005

[Asada & Nakamura 2012] Asada, K., & Nakamura, M., *The Structure of the M87 Jet: A Transition from Parabolic to Conical Streamlines*, *ApJL*, 2012, **745**, L28

[Asano et al. 2014] Asano, K., Takahara, F., Kusunose, M., et al., *Time-dependent Models for Blazar Emission with the Second-order Fermi Acceleration*, *ApJ*, 2014, **64**, 12

[Asano & Hayashida 2015] Asano, K., & Hayashida, M., *The Most Intensive Gamma-Ray Flare of Quasar 3C 279 with the Second-order Fermi Acceleration*, *ApJL*, 2015, **808**, L18

[Asano & Hayashida 2018] Asano, K., & Hayashida, M., *Blazar Spectra with Hard-sphere-like Acceleration of Electrons*, *ApJ*, 2018, **861**, 31

[Arnold et al. 2012] Arnold, D., Steele, I., Bates, S., et al., *RINGO3: a multi-color fast response polarimeter*, *Ground-based and Airborne Instrumentation for Astronomy IV. Proceedings of the SPIE*, 2012, **8446**, 8

[Atwood et al. 2009] Atwood, W., B., Abdo, A. A., Ackermann, M., et al., *The Large Area Telescope on the Fermi Gamma-Ray Space Telescope Mission*, *ApJ*, 2009, 697, 1071

[Bauleo & Martino 2009] Bauleo, P.M. and Martino, J.R., *The dawn of the particle astronomy era in ultra-high-energy cosmic rays*, *Nature*, 2009, **458**, 7240, 847-851

[Bastieri et al. 2005] Bastieri, D., Bigongiari, C., Bisesi, E., et al., *Using the photons from the Crab Nebula seen by GLAST to calibrate MAGIC and the imaging air Cherenkov telescopes*, *APh*, 2005, **29**, 572-576

[Beckmann & Shrader 2012] Beckmann, V. and Shrader, C.R., *Active Galactic Nuclei*, *Wiley-VCH Verlag GmbH*, 2012

[Beckmann & Shrader 2013] Beckmann, V. and Shrader, C., *The AGN phenomenon: open issues*, *PoS*, 2013, `arXiv:1302.1397`

[Begelman et al. 2008] Begelman, M. C., Fabian, A. C., & Rees, M. J., *Implications of very rapid TeV variability in blazars*, *MNRAS*, 2008, **384**, L19

[Beilicke et al. 2012] Beilicke, M. for the VERITAS Collaboration, *AIP Conference Proceedings*, 2012, **1505**, 586

[Beringer et al. 2012] Beringer, J., Arguin, J., F., Barnett, R., M., et al., *Review of particle physics*, *Physical Review D*, 2012, **86(1)**

[Bernstein et al. 2002] Bernstein, R., Freedman, W., & Madore, F., *The First Detections of the Extragalactic Background Light at 3000, 5500, and 8000 . I. Results*, *ApJ*, 2002, *571*, 56

[Berta et al. 2010] Berta, S., Magnelli, B., Lutz, D., et al., *Dissecting the cosmic infra-red background with Herschel/PEP* , *AAP*, 2010, **518**, L30

[Bertero 1989] Bertero, M., *Linear inverse and ill-posed problems. Advances in Electronics and Electron Physics*, *astro-ph*, 1989, **75**, 1-120

[Béthermin et al. 2010] Béthermin, M., Dole, H., Beelen, A., et al., *Spitzer deep and wide legacy mid- and far-infrared number counts and lower limits of cosmic infrared background*, *AAP*, 2010, **512**, A78

[Biretta et al. 1999] Biretta, J., A., Sparks, W., B., & Macchetto, F., *Hubble Space Telescope Observations of Superluminal Motion in the M87 Jet*, *ApJ*, 1999, **520**, 621-626

[Biteau & Williams 2015] Biteau, J., & Williams, D., A., *The Extragalactic Background Light, the Hubble Constant, and Anomalies: Conclusions from 20 Years of TeV Gamma-Ray Observations*, *ApJ*, 2015, **812**, 60

[Blandford & Znajek 1977] Blandford, R., D., & Znajek, R., L., *Electromagnetic extraction of energy from Kerr black holes*, *MNRAS*, 1977, **179**, 433-456

[Blandford & Königl 1979] Blandford, R., D., & Königl, A., *Relativistic jets as compact radio sources*, *ApJ*, 1979, **232**, 34-48

[Blandford & Levinson 1995] Blandford, R., D., & Levinson, A., *Pair cascades in extragalactic jets. 1: Gamma rays*, *ApJ*, 1995, **441**, 79-95

[Błażejowski et al. 2000] Błażejowski, M., Sikora, M., Moderski, R., et al., *Comptonization of Infrared Radiation from Hot Dust by Relativistic Jets in Quasars*, *ApJ*, 2000, **545**, 107

[Błażejowski et al. 2005] Błażejowski, M., Blaylock, G., Bond, I., H., et al., *A Multiwavelength View of the TeV Blazar Markarian 421: Correlated Variability, Flaring, and Spectral Evolution*, *ApJ*, 2005, **630**, 130-141

[Bloom & Marscher 1996] Bloom, S. D. & Marscher, A. P., *An Analysis of the Synchrotron Self-Compton Model for the Multi-Wave Band Spectra of Blazars*, *ApJ*, 1996, **461**, 657

[Biland et al. 2008] Biland, A., Garczarczyk, M., Anderhub, H., et al., *The Active Mirror Control of the MAGIC Telescopes*, *ICRC*, 2008, **3**, 1353-1356

[Blümer et al. 2009] Blümer, J., Engel R. & Hörandel J, *Cosmic rays from the knee to the highest energies*, *Progress in Particle and Nuclear Physics*, 2009, **63**, 293-338

[Boggess et al. 1992] Boggess, N., Mather, J., Weiss, R., et al., *The COBE mission - Its design and performance two years after launch*, *ApJ*, 1992, **397**, 420-429

[Böttcher et al. 2010] Böttcher, M., Hivick, B., Dashti, J., et al., *Optical Spectral Variability of the Very High Energy Gamma-ray Blazar 1ES 1011+496*, *ApJ*, 2010, **725**, 2344-2348

[Böttcher 2009] Böttcher, M., Reimer, A., & Marscher, A., *Implications of the very High Energy Gamma-Ray Detection of the Quasar 3C279*, *ApJ*, 2009, **703**, 1168

[Böttcher 2012] Böttcher, M. *Modeling the Spectral Energy Distributions and Variability of Blazars*, *astro-ph*, 2012, `arXiv:1205.0539`

[Böttcher et al. 2013] Böttcher, M., Reimer, A., Sweeney, K., et al., *Leptonic and Hadronic Modeling of Fermi-Detected Blazars*, *ApJ*, 2013, **768**, 1

[Breiman 2001] Breiman L., *Random forests*, *Machine learning*, 2001, **45(1)**, 5-32.

[Bridle 1967] Bridle, A. H., *The spectrum of the radio background between 13 and 404 MHz*, *MNRAS*, 1967, **136**, 219-240

[Bringmann & Weniger 2012] Bringmann, T. & Weniger, C., *Gamma ray signals from dark matter: Concepts, status, and prospects Physics of the Dark Universe*, *Physics of the Dark Universe*, 2012, **1**, 194-217

[Brown et al. 2000] Brown, T., M., Kimble, R., A., Ferguson, H., C., et al., *Measurements of the Diffuse Ultraviolet Background and the Terrestrial Airglow with the Space Telescope Imaging Spectrograph*, *AJ*, 2000, **120**, 1153

[Brun & Rademakers 1997] Brun, R., & Rademakers, F., *ROOT-An object oriented data analysis framework*, *NIMPRA: Accelerators, Spectrometers, Detectors and Associated Equipment* , 1997, **389(1-2)**, 81-86.

[Bött et al. 2010] Cambrésy, L., Reach, W., T., Beichman, C., A., et al., *The Cosmic Infrared Background at 1.25 and 2.2 Microns Using DIRBE and 2MASS: A Contribution Not Due to Galaxies?* , *ApJ*, 2001, **555**, 563

[Cardelli et al. 1989] Cardelli, J., Clayton, G., & Mathis, J., *The Relationship between Infrared, Optical, and Ultraviolet Extinction*, *ApJ*, 1989, **345**, 245

[Chang et al. 2008] Chang, J., Adams, J., H., Ahn., H., S., et al., *An excess of cosmic ray electrons at energies of 300-800 GeV*, *Nature*, 2008, **456**, 362-365

[cheung et al. 2007] Cheung C., Harris D., & Stawarz L., *Superluminal Radio Features in the M87 Jet and the Site of Flaring TeV Gamma-Ray Emission*, *ApJ*, 2007. **663**, 65-68

[Chowdhury et al. 2011] Chowdhury D., Vempati S.K. & Jog C.J., *Results from PAMELA, ATIC and FERMI: Pulsars or dark matter?*, *Pramana*, 2011, **76(1)**, 1-22, `arXiv:0909.1182`

[Clarke & Neumayer 2002] Clarke, D. & Neumayer, D., *Experiments with a novel CCD stellar polarimeter*, *A&A*, 2002, **383**, 360

[Colin et al. 2009] Colin, P., Borla Tridon, D., Carmona, E., et al., *Performance of the MAGIC telescopes in stereoscopic mode*, *astro-ph*, 2009, `arXiv:0907.0960`

[Cooray et al. 2010] Cooray, A., Bock, J., J., Keatin, B., et al., *First Star Signature in Infrared Background Anisotropies*, *ApJ*, 2004, **606**, 611

[Cortina et al. 2010] Cortina, J., Goebel, F., Schweizer, T. et al, *Technical Performance of the MAGIC Telescopes*, *astro-ph*, 2009, `arXiv:0907.1211`

[Costamante 2013] Costamante, L., *Gamma-rays from Blazars and the Extragalactic Background Light*, *International Journal of Modern Physics D*, 2013, **22**, 1330025

[CTA Consortium 2010] CTA Consortium, *Design Concepts for the Cherenkov Telescope Array*, *astro-ph*, 2010, `arXiv:1008.3703`

[CTA Consortium, 2018] CTA Consortium, *Science with the Cherenkov Telescope Array*, *astro-ph*, 2018, `arXiv:1709.07997`

[Curtis 1918] Curtis, H., *Descriptions of 762 Nebulae and Clusters Photographed with the Crossley Reflector*, *Publications of the Lick Observatory (University of California Press)*, 1918, **13**, 31

[Dermer et al. 1992] Dermer, C., D., Schlickeiser, R., & Mastichiadis, A., *High-energy gamma radiation from extragalactic radio sources*, *A&A*, 1992, **256**, L27-L30

[Dermer & Schlickeiser 1993] Dermer, C. D. & Schlickeiser, R., *Model for the High-Energy Emission from Blazars*, *ApJ*, 1993, **416**, 458

[Dermer et al. 1993] Dermer, C., Dahai, L., Finke, J., et al., *Near-Equipartition jets with log-parabola electron energy distribution and the blazar spectral-index diagrams*, *ApJ*, 2015, **809**, 2

[Dermer et al. 1997] Dermer, C. D., Sturner, Steven, J., & Schlickeiser, R., *Nonthermal Compton and Synchrotron Processes in the Jets of Active Galactic Nuclei*, *ApJSS*, 1997, **109**, 103-137

[Doeleman et al. 2012] Doeleman, S., Fish, V., Schenck, D. et al., *VizieR Online Data Catalog: 1.3mm VLBI detections of M87*, *VizieR Online Data Catalog*, 2012, **0210**, 338

[Doeleman et al. 2015] Doeleman, S., Fish, V. L., Schenck, D., et al., *Jet-Launching Structure Resolved Near the Supermassive Black Hole in M87*, *Science*, 2012, **338**, 355

[Dole et al. 2004] Dole, H., Rieke, G., H., Lagache, G., et al., *Confusion of Extragalactic Sources in the Mid- and Far-Infrared: Spitzer and Beyond*, *ApJS*, 2004, **154**, 93

[Dole & Lagache 2006] Dole, H. & Lagache, G., *The cosmic infrared background resolved by Spitzer. Contributions of mid-infrared galaxies to the far-infrared background*, *A&A*, 2006, **451**, 417

[Domínguez et al. 2011] Domínguez, A., Primack, J., R., Rosario, D., J., et al., *Extragalactic background light inferred from AEGIS galaxy-SED-type fractions*, *MNRAS*, 2011, **410**, 2556.

[Domínguez et al. 2013] Domínguez, A., Finke, J., D., Prada, F., et al., *Detection of the Cosmic γ-Ray Horizon from Multiwavelength Observations of Blazars*, *ApJ*, 2013, **770**, 77

[Donath et al. 2017] Donath, A., Francois B., Ryan C. et al., *The H.E.S.S. galactic plane survey*, *AIP Conference Proceedings*, 2017, **1792**, 1

[Donato et al. 2001] Donato, D., Ghisellini, G., Tagliaferri, G., et al., *Hard X-ray properties of blazars*, *A&A*, 2001, **375**, 739-751.

[Dube et al. 1979] Dube, R., R., Wickes, W., C., & Wilkinson, D., T., *Upper limit on the extragalactic background light*, *ApJ*, 1979, **232**, 333

[Dwek & Arendt 1998] Dwek, E., & Arendt, R., G., *A Tentative Detection of the Cosmic Infrared Background at 3.5 μm from COBE/DIRBE Observations*, *ApJL*, 1998, **508**, L9

[Dwek & Krennrich 2005] Dwek, E., & Krennrich., F., *Simultaneous Constraints on the Spectrum of the Extragalactic Background Light and the Intrinsic TeV Spectra of Markarian 421, Markarian 501, and H1426+428.*, *ApJ*, 2005, **618**, 657

[Dwek & Krennrich 2008] Dwek, E. & Krennrich., F., *The Extragalactic Background Light and the Gamma-ray Opacity of the Universe*, 2008, `arXiv:1209.4661`

[Dwek & Krennrich 2013] Dwek, E. & Krennrich., F., *The extragalactic background light and the gamma-ray opacity of the universe*, *APh*, 2013, **43**, 112-133

[Edelstein et al. 2000] Edelstein, J., Bowyer, S., & Lampton, M., *Reanalysis of Voyager Ultraviolet Spectrometer Limits to the Extreme-Ultraviolet and Far-Ultraviolet Diffuse Astronomical Flux*, *ApJ*, 2000, **539**, 187-190

[Eichmann et al. 2012] Eichmann, B., Schlickeiser, R., & Rhode, W. *Differences of leptonic and hadronic radiation production in flaring blazars*, *ApJ*, 2012, **749**, 155

[Elbaz et al. 2002] Elbaz, D., Flores, H., Chanial, P., et al., *ISOCAM mid-infrared detection of HR 10: A distant clone of Arp 220 at z = 1.44*, *AAP*, 2002, **381**, L1

[Elvis et al. 1992] Elvis, M., Plummer, D., Schachter, J., et al., *The Einstein Slew Survey*, *ApJS*, 1992 **80**, 257-303

[Fabian & Barcons 1992] Fabian, A., C., & Barcons, X., *The origin of the X-ray background*, *ARA&A*, 1992, **30**, 429-456

[Fanti et al. 1974] Fanti, R., Fanti, C., Fanti, R., et al., *The B2 catalogue of radio sources - fourth part*, *A&ASS*, 1974, **18**, 147

[Fanaroff & Riley 1974] Fanaroff, B., & Riley, J., *The morphology of extragalactic radio sources of high and low luminosity MNRAS*, 1974, **167**, 31P

[Fazio et al. 2004] Fazio, G., G., Ashby, M., L., N., Barmby, P., et al., *Number Counts at 3 μm λ 10 μm from the Spitzer Space Telescope*, *ApJS*, 2004, **154**, 39.

[Fazio 2005] Fazio, G. G., *Recent Results from the Spitzer Space Telescope: A New View of the Infrared Universe*, *Neutrinos and Explosive Events in the Universe*, 2005, 47

[Fegan et al. 2005] Fegan, S., J., Badran, H., M., Bond, I., H., et al., *A Survey of Unidentified EGRET Sources at Very High Energies*, *ApJ*, 2005, **624**, 638-655

[Fermi 1949] Fermi, E., *On the origin of the cosmic radiation*, *Phys. Rev.*, 1949, **75**, 1169

[Fernandez et al. 2010] Fernandez, E., R., Komatsu, E., Iliev, I., T., et al., *The Cosmic Near-Infrared Background. II. Fluctuations*, *ApJ*, 2010, **710**, 1089.

[Fichtel et al. 1994] Fichtel, C., E., Bertsch, D., L., Chiang, J., et al., *The first energetic gamma-ray experiment telescope (EGRET) source catalog*, *ApJS*, 1994, **94**, 551-581

[Finkbeiner et al. 2000] Finkbeiner, D., P., Davis, M., & Schlegel, D., J., *Detection of a Far-Infrared Excess with DIRBE at 60 and 100 Microns*, *ApJ*, 2000, **544**, 81

[Finke et al. 2010] Finke, J., D., Razzaque, S. & Dermer, C., D., *Modeling the Extragalactic Background Light from Stars and Dust*, *ApJ*, 2010, **712**, 238

[Fomin et al. 1994] Fomin, V., P., Stepanian, A., A., Lamb, R., C., et al., *New methods of atmospheric Cherenkov imaging for gamma-ray astronomy. I. The false source method*, *APh*, 1994, **2**, 137

[Fossati et al. 1998] Fossati, G., Maraschi, L., Celotti, A., et al., *A unifying view of the spectral energy distributions of blazars*, *MNRAS*, 1998, **299**, 433

[Franceschini et al. 2008] Franceschini, A., Rodighiero, G., & Vaccari, M., *Extragalactic optical-infrared background radiation, its time evolution and the cosmic photon-photon opacity*, *A&A*, 2008, 837.

[Frank et al. 1992] Frank, J., King, A., & Raine, D., J., *Accretion Power in Astrophysics*, *Cambridge University Press, Cambridge*, 1992

[Frayer et al. 2006] Frayer, D., T., Huynh, M., T., Chary, R., et al., *Spitzer 70 Micron Source Counts in GOODS-North*, *ApJL*, 2006, **647**, L9

[Fraschetti 2008] Fraschetti, F., *On the acceleration of Ultra-High-Energy Cosmic Rays*, *Phil.Trans.Roy.Soc.Lond.*, 2008, **A366**, 4417-4428

[Fruck 2015] Fruck C., *The Galactic Center resolved with MAGIC and a new technique for Atmospheric Calibration*, Ph.D. thesis, Technische Universitt München, 2015.

[Furniss et al. 2013] Furniss, A., Williams, D., A., Danforth, C. et al., *The Firm Redshift Lower Limit of the Most Distant TeV-detected Blazar PKS 1424+240*, *ApJL*, 2013, **768**, 31

[García et al. 2014] García, J., Dazzi, F., Häfner, D., et al., *Status of the new Sum-Trigger system for the MAGIC telescopesThe major atmospheric gamma-ray imaging cherenkov telescope.*, *Proceedings of 33th ICRC*, 2014, `arXiv:1404.4219`

[Garczarczyk 2011] Garczarczyk, M., *The major atmospheric gamma-ray imaging cherenkov telescope.*, *NIMPRA: Accelerators, Spectrometers, Detectors and Associated Equipment*, 2011, **639**, 1, 33-36

[Gardner et al. 2000] Gardner, J., P., Brown, T., M., & Ferguson, H., C., *Ultraviolet Galaxy Counts from Space Telescope Imaging Spectrograph Observations of the Hubble Deep Fields*, *ApJL*, 2000, **542**, L79

[Garrington & Conway 1991] Garrington, S., T., & Conway, R., G., *The interpretation of asymmetric depolarization in extragalactic radio sources*, *MNRAS*, 1991, **250**, 198-208

[Gaug et al. 2005] Gaug, M., Bartko, H., Cortina, J. et al., *Calibration of the MAGIC Telescope*, *International Cosmic Ray Conference*, 2005, **5**, 375

[Georganopoulos & Kazanas 2003] Georganopoulos, M. & Kazanas, D., *Decelerating Flows in TeV Blazars: A Resolution to the BL Lacertae-FR I Unification Problem*, *ApJ*, 2003, **594**, L27-L30

[Georganopoulos et al. 2005] Georganopoulos, M., Perlman, E., S., & Kazanas, D., *Is the Core of M87 the Source of Its TeV Emission? Implications for Unified Schemes*, *ApJL*, 2005, **634**, L33

[Georganopoulos et al. 2010] Georganopoulos, M., Finke, J., D., & Reyes, L. C., *A Method for Setting Upper Limits to the Extragalactic Background Light with Fermi-lat and TeV Observations of Blazars*, *ApJ*, 2010, **714**, L157

[Ghisellini & Madau 1996] Ghisellini, G., & Madau, P., *On the origin of the gamma-ray emission in blazars*, *MNRAS*, 1996, **280, 67-76**

[Ghisellini 2000] Ghisellini, G., *Special Relativity at Action in the Universe*, *In B. Casciaro, D. Fortunato, M. Francaviglia and A. Masiello, editors, 'Recent Developments in General Relativity'*, 2000, **page 5**

[Ghisellini et al. 2005] Ghisellini, G., Tavecchio, F., & Chiaberge, M., *Structured jets in TeV BL Lac objects and radiogalaxies. Implications for the observed properties*, *A&A*, 2005, *432*, 401-410

[Ghisellini & Tavecchio 2008] Ghisellini, G., & Tavecchio, F., *The blazar sequence: a new perspective*, *MNRAS*, 2008, 386, L28

[Ghisellini et al. 2017] Ghisellini, G., Righi, C., Costamante, L., et al., *The Fermi blazar sequence*, *MNRAS*, 2017, **469**, 255

[Giannios et al. 2009] Giannios, D., Uzdensky, D., A., & Begelman, M., C., *Fast TeV variability in blazars: jets in a jet* , *MNRAS*, 2009, **395**, L29

[Giannios et al. 2010] Giannios, D., Uzdensky, D., A., & Begelman, M., C., *Fast TeV variability from misaligned minijets in the jet of M87*, *MNRAS*, 2009, **402**, 1649

[Gilmore et al. 2009] Gilmore, R., Madau, P., Primack, J., et al., *GeV gamma-ray attenuation and the high-redshift UV background*, *MNRAS*, 2009, **399**, 4

[Gilmore et al. 2011] Gilmore, R., Somerville, R., S., Primack, J., R., et al., *Semi-analytic modeling of the EBL and consequences for extragalactic gamma-ray spectra*, 2011, `arXiv:1104.0671`

[Gilmore et al. 2012] Gilmore, R., Somerville, R., S., Primack, J., R., et al., *Semi-analytic modeling of the EBL and consequences for extragalactic gamma-ray spectra*, 2012, *MNRAS*, 2012, **422**, 3189

[Giovannini et al. 2011] Giovannini, G., Casadio, C., Giroletti, M., et al., *The jet in M87 from e-EVN observations*, *Proceedings of the IAU Symposium*, 2011, **275**, 150-154

[Giroletti at al. 2012] Giroletti, M., Hada, K., Giovannini, G., et al., *The kinematic of HST-1 in the jet of M 87*, *A&A*, 2012, **538**, L10

[González 2015] González A., *Measurement of the gamma-ray opacity of the Universe with the MAGIC telescopes*, Ph.D. Thesis, UAB, 2015.

[Gorjian et al. 2008] Gorjian, V., Wright, E., L., & Chary, R., R., *Tentative Detection of the Cosmic Infrared Background at 2.2 and 3.5 Microns Using Ground-based and Space-based Observations*, *ApJ*, 2000, **536**, 550

[Gould & Schréder 1967] Gould, R., J., & Schréder, G., P., *Opacity of the Universe to High-Energy Photons*, *Physical Review*, 1967, **155**, 1408

[Graff et al. 2008] Graff, P., Georganopoulos, M., Perlman, E., at al., *A Multizone Model for Simulating the High-Energy Variability of TeV Blazars*, *ApJ*, 2008, **689**, 68-78

[Greisen 1966] Greisen, K., *End to the cosmic-ray spectrum?*, *Physical Review Letters*, 1966, **16**, 748

[Haarsma et al. 2000] Haarsma, D., B., Partridge, R., B., Windhorst, R., et al., *Faint Radio Sources and Star Formation History*, *ApJ*, 2000, **544**, 641-658

[Hada et al. 2014] Hada, K., Giroletti, M., Kino, M., et al., *A Strong Radio Brightening at the Jet Base of M 87 during the Elevated Very High Energy Gamma-Ray State in 2012*, *ApJ*, 2014, **788**, 165

[Hada et al. 2015] Hada, K., Giroletti, M., Giovannini, G., et al., *Continuing EVN monitoring of HST-1 in the jet of M87*, *Proceedings of 12th European VLBI Network Symposium and Users Meeting*, 2015, `arXiv:1504.01808`

[Haefner 2011] Haefner D., *New improved Sum-Trigger system for the MAGIC telescopes*, 2011, `arXiv:1111.1299`

[Haefner et al. 2012] Haefner, D., Schweizer, T., Shayduk, M., et al., *A Tunable Delay Line for Fast Analog Pulses as Key Element of a New Sum-Trigger for Cherenkov Telescopes*, *Nuclear Science, IEEE Transactions on*, 2012, **59(2)**, 289-293

[Harris et al. 2003] Harris, D., Biretta, J., Junor, W., et al., *Flaring X-Ray Emission from HST-1, a Knot in the M87 Jet*, *ApJ*, 2003, **586**, L41

[Harris 2009] Harris, w. E. *The Globular Cluster System in M87: A Wide-Field Study with CFHT/Megacam*, *ApJ*, 2009, **703**, 939, `arXiv:0908.1120`

[Harris et al. 2011] Harris, D., Massaro, F., Cheung, C., et al., *An Experiment to Locate the Site of TeV Flaring in M87*, *ApJ*, 2011, **743**, 177

[Hassan et al. 2017] Hassan, T., Arrabito, L., Bernlöhr, K., et al., *Monte Carlo performance studies for the site selection of the Cherenkov Telescope Array*, *APh*, 2017, **93**, 76-85

[Hauser et al. 1998] Hauser, M., G., Arendt, R., G., Kelsall, T., et al., *The COBE Diffuse Infrared Background Experiment Search for the Cosmic Infrared Background. I. Limits and Detections*, *ApJ*, 1998, **508**, 25

[Hauser & Dwek 2001] Hauser, M., G., & Dwek, E., *The Cosmic Infrared Background: Measurements and Implications*, *ARA&A*, 2001, **39**, 249.

[Hayashida et al. 2012] Hayashida, M., Madejski, G., Nalewajko, K., et al., *The Structure and Emission Model of the Relativistic Jet in the Quasar 3C 279 Inferred from Radio to High-energy γ-Ray Observations in 2008-2010*, *ApJ*, 2012, **754**, 114

[Heck et al. 1998] Heck, D., Knapp, J., Capdevielle, J., et al., *CORSIKA: a Monte Carlo code to simulate extensive air showers*, *FZKA*, 1998, **6019**

[Heitler 1954] Heitler, W., *The quantum theory of radiation, third edition*, *Clarendon Press, Oxford*, 1954

[Hernandez 2014] Hernandez, S. 2014, STIS Instrument Handbook, Version 13.0, (Baltimore: STScI)

[Hillas 1984] Hillas A.M., *The Origin of Ultra-High-Energy Cosmic Rays*, *ARA&A*, 1984, **22**, 425-444

[Hillas 1985] Hillas A.M., *Cerenkov light images of EAS produced by primary gamma*, *ICRC proceeding*, 1985, **3**, 445-448

[Holder 2007] Holder, J., *VERITAS: Status and Performance*, In M. M. Massai, N. Omodei, & G. Spandre, editor, *Science with the New Generation of High Energy Gamma-Ray Experiments*, 2007, pages 69

[Holder 2017] Holder, J., The VERITAS and MAGIC Collaborations, *TeV gamma-ray emission from PSR J2032+4127/ MT91 213*, *The Astronomer's Telegram*, 2014, **10810**

[Hümmer et al. 2010] Hümmer, S., Rüger, M., Spanier, F., et al., *Simplified Models for Photohadronic Interactions in Cosmic Accelerators*, *ApJ*, 2010, **721**, 630

[Impey & Tapia 1988] Impey, C. & Tapia, S., *New blazars discovered by polarimetry*, *ApJ*, 1988, **333**, 666-672

[Istomin & Sol 2009] Istomin, Ya. N. & Sol, H. *Acceleration of particles in the vicinity of a massive black hole*, *Ap&SS*, 2009, **321**, 57

[Jakobsson et al. 2006] Jakobsson, P., Levan, A., Fynbo, J., P., U., et al., *A mean redshift of 2.8 for Swift gamma-ray bursts*, *A&A*, 2006, **447(3)**, 897-903

[Jelley & Porter 1963] Jelley, J. V. & Porter, N. A., *Čerenkov Radiation from the Night Sky, and its Application to γ-Ray Astronomy*, *QJRAS*, 1963, **4**, 275

[Jermak et al. 2016] Jermak, H., Steele, I. A., Lindfors, E., et al., *The RINGO2 and DIPOL optical polarization catalogue of blazars*, *MNRAS*, 2016, **462**, 4267-4299

[Jorstad et al. 2001] Jorstad, S., Marscher, A., Mattox, J., et al., *New blazars discovered by polarimetry*, *ApJ*, 2001, **556**, 738-748

[Kalberla et al. 2005] Kalberla, P., Burton, W., & Hartmann, D., *The Leiden/Argentine/Bonn (LAB) Survey of Galactic HI. Final data release of the combined LDS and IAR surveys with improved stray-radiation corrections*, *A&A*, 2005, **440**, 775

[Kashlinsky et al. 1996] Kashlinsky, A., Mather, J., C., Odenwald, S., et al., *Clustering of the Diffuse Infrared Light from the COBE DIRBE Maps. I. C(0) and Limits on the Near-Infrared Background*, *ApJ*, 1996, **470**, 681

[Kataoka et al. 2008] Kataoka, J., Madejski, G., Sikora, M., et al, *Multiwavelength Observations of the Powerful Gamma-Ray Quasar PKS 1510-089: Clues on the Jet Composition*, *ApJ*, 2008, **672**, 787-799

[Keenan et al. 2010] Keenan, R., C., Barger, A., J., Cowie, L., L., et al., *The Resolved Near-infrared Extragalactic Background*, *ApJ*, 2010, **723**, 40

[Kelsall et al. 1998] Kelsall, T., Weiland, J., Franz, B., et al., *The COBE Diffuse Infrared Background Experiment Search for the Cosmic Infrared Background. II. Model of the Interplanetary Dust Cloud*, *ApJ*, 1998, **508**, 44-73

[Kellermann 2011] Kellermann H., *Präzise Vermessung der fokussierten Reflektivität der MAGIC-Teleskopspiegel und Charakterisierung des hierfür verwendeten diffusen Reflektors*, Diploma thesis, Munich University for Applied Sciences, 2011

[Kellermann et al. 1989] Kellermann, K. I., Sramek, R., Schmidt, M., et al., *VLA Observations of Objects in the Palomar Bright Quasar Survey*, *ApJ*, 1989. **98**, 1195

[Kellermann et al. 2004] Kellermann, K., Lister, M., Homan, D., et al., *Sub-Milliarcsecond Imaging of Quasars and Active Galactic Nuclei. III. Kinematics of Parsec-scale Radio Jets*, *ApJ*, 2004. **609**, 539-563

[Kennicutt 1998] Kennicutt, Robert C., Jr., *Star Formation in Galaxies Along the Hubble Sequence*, *Annual Review of Astronomy and Astrophysics*, 1998, **36**, 189-232

[Kino et al. 2002] Kino, M., Takahara, F., & Kusunose, M., *Energetics of TeV Blazars and Physical Constraints on Their Emission Regions*, *ApJ*, 2002, **564**, 97-107

[Kino et al. 2015] Kino, M., Takahara, F., Hada, K., et al., *Magnetization Degree at the Jet Base of M87 Derived from the Event Horizon Telescope Data: Testing the Magnetically Driven Jet Paradigm*, *ApJ*, 2015, **803**, 12

[Kirk et al. 1998] Kirk, J. G., Rieger, F. H., & Mastichiadis, A., *Particle acceleration and synchrotron emission in blazar jets*, *A&A*, 1998, **333**, 452

[Kneiske et al. 2002] Kneiske, T., M., Mannheim, K., & Hartmann, D., H., *Implications of cosmological gamma-ray absorption. I. Evolution of the metagalactic radiation field*, emphAAP, 2002, **386**, 1

[Knoetig et al. 2013] Knoetig, M., Biland, A., Bretz., T., et al. (FACT Collaboration), *FACT - Long-term stability and observations during strong Moon light*, *ICRC proceedings*, 2013, `arXiv1307.6116`

[Kohnle et al. 1996] Kohnle A., Aharonian, F., Akhperjanian, A., et al., *Stereoscopic imaging of air showers with the first two HEGRA Cherenkov telescopes*, *APh*, 1996, **5**, 119.

[Komissarov et al. 2009] Komissarov, S., Vlahakis, N., Königl, A., et al., *Magnetic acceleration of ultrarelativistic jets in gamma-ray burst*, *MNRAS*, 2009, **394**, 1182-1212

[Krause 2012] Krause, J., *Resolved gamma ray emission of the supernova remnant W51C and HESS J1857+026 obtained with the MAGIC telescopes*, Ph.D. thesis, Ludwig-Maximilians-Universität, München, 2012

[Krolik 1999] Krolik, J., *Active galactic nuclei: from the central black hole to the galactic environment*, *Princeton University Press*, 1999

[Kudo et al. 2004] Kubo, H., Asahara, A., Bicknell, G., V., et al., *Status of the CANGAROO-III project*, *New A Rev.*, 2004, **48**, 323-329.

[Lagache et al. 2000] Lagache, G., Haffner, L., M., Reynolds, R., J., et al., emphEvidence for dust emission in the Warm Ionised Medium sing WHAM data, *AAP*, 2000, **354**, 247

[Laing et al. 1988] Laing, R.A., *The sidedness of jets and depolarization in powerful extragalactic radio sources*, *Nature*, 1988, **331**, 149-151

[Lenain et al. 2008] Lenain, J., P., Boisson, C., Sol, H., et al., *A synchrotron self-Compton scenario for the very high energy γ-ray emission of the radiogalaxy M 87. Unifying the TeV emission of blazars and other AGNs?*, *A&A*, 2008, **478**, 111

[Levenson et al. 2007] Levenson, L., R., Wright, E., L., & Johnson, B., D., *DIRBE Minus 2MASS: Confirming the CIB in 40 New Regions at 2.2 and 3.5 μm* , *ApJ*, 2007, **666**, 34

[Levenson & Write 2008] Levenson, L., R., & Wright, E., L., *Probing the 3.6 μm CIRB with Spitzer in Three DIRBE Dark Spots*, *ApJ*, 2008, **683**, 585

[Levison & Rieger 2011] Levinson, A., & Rieger, F., *Variable TeV emission as a manifestation of jet formation in M87?*, *ApJ*, 2011, **730**, 123

[Li & Ma 1983] Li, T., & Ma, Y., *Analysis methods for results in gamma-ray astronomy*, *ApJ*, 1983, **317**, 272

[Lin et al. 1996] Lin, Y., C., Bertsch, D., L., Dingus, B., L., et al., *EGRET observations of BL Lacertae objects with redshifts below 0.2*, *A&AS*, 1996, **120**, C499

[Longair 1992] Longair, M., S., *High energy astrophysics. Vol.1: Particles, photons and their detection*, *Cambridge University Press*, 1992

[Longair 1994] Longair, M., S., *High energy astrophysics. Volume 2. Stars, the Galaxy, and the interstellar medium*, *Cambridge University Press*, 1994

[Longair 2011] Longair M.S., *High energy astrophysics. Third edition*, *Cambridge University Press*, 2011

[Lombardi 2011] Lombardi, S., *Advanced stereoscopic gamma-ray shower analysis with the MAGIC telescopes*, *Proceedings of the 32nd ICRC, Beijing*, 2011, **3**, 262, `arXiv:1109.6195`

[Lorenz 2004] Lorenz, E., *Status of the 17 m ϕ MAGIC telescope*, 2^{nd} VERITAS Symposium on the Astrophysics of Extragalactic Sources, *New Astronomy Reviews*, 2004, **48 (5-6)**, 339-344.

[Lyden-Bell & Rees 1971] Lynden-Bell, D. & Rees, M.J., *On quasars, dust and the galactic centre*, *MNRAS*, 2013, **152**, 461

[Machalski & Condon 1983] Machalski, J. & Condon, J.J., *A complete sample of intermediate strength radio sources selected from the GB/GB2 1400-MHz surveys. IV. VLA Observations and Optical Identifications of a Set of Sources with 0.20 $\leq S \leq$ 0.55 Jy. AJ*, 1993, **88**, 1591-1615.

[Macchetto et al. 1997] Macchetto, F., Marconi, A., & Axon, D., *The supermassive black hole of M87 and the kinematics of its associated gaseous disk*, *ApJ*, 1997, **489**, 579,

[Macri et al. 1999] Macri, L., Huchra, J., P., Stetson, P., B., et al., *The Extragalactic Distance Scale Key Project. XVIII. The Discovery of Cepheids and a New Distance to NGC 4535 Using the Hubble Space Telescope*, *ApJ*, 1999, **521**, 155

[Madau & Pozzetti 2000] Madau, P., & Pozzetti, L., *Deep galaxy counts, extragalactic background light and the stellar baryon budget*, *MNRAS*, 2000, **312**, L9

[Madrid 2009] Madrid, J., *Hubble Space Telescope Observations of an Extraordinary Flare in the M87 Jet*, *AJ*, 2009, **137**, 3864

[MAGIC Collaboration et al. 2007] MAGIC Collaboration: Goebel, F., Bartko, H., Carmona, E., et al., *Upgrade of the MAGIC Telescope with a Multiplexed Fiber-Optic 2 GSamples/s FADC Data Acquisition system*, 2007, `arXiv:0709.2363`

[Malkov & Drury 2001] Malkov, M. & Drury, L., *Nonlinear theory of diffusive acceleration of particles by shock waves*, *Reports on Progress in Physics*, 2001, **64**, 429-481

[Mannheim & Biermann 1992] Mannheim, K. & Biermann, P. L., *Gamma-ray flaring of 3C 279 : a proton-initiated cascade in the jet ?*, *A&A*, 1992, **253**, L21-L24

[Mannheim 1993] Mannheim, K., *The proton blazar*, *A&A*, 1993, **269**, 67-69

[Mankuzhiyil et al. 2010] Mankuzhiyil, N., Persic, M., & Tavecchio, F., *High-frequency-peaked BL Lacertae Objects as Spectral Candles to Measure the Extragalactic Background Light in the Fermi and Air Cherenkov Telescopes Era*, *ApJL*, 2010, **715**, L16

[Marscher & Gear 1985] Marscher, A. P. & Gear, W. K., *Models for high-frequency radio outbursts in extragalactic sources, with application to the early 1983 millimeter-to-infrared flare of 3C 273*, *ApJ*, 1985, **298**, 114-127

[Marshall et al. 2002] Marshall, H., L., Miller, B., P., Davis, D., S., et al., *A High-Resolution X-Ray Image of the Jet in M87*, *The Astrophysical Journal*, 2002, **564** 683

[Marachi et al. 1992] Maraschi, L., Ghisellini, G. & Celotti, A., *A jet model for the gamma-ray emitting blazar 3C 279*, *ApJL*, 1992, **397**, L5-L9

[Martin & Rouleau 1991] Martin, P., G., & Rouleau, F., *Extreme Ultraviolet Opacity with Interstellar Dust*, *Extreme Ultraviolet Astronomy*, 1991, 341

[Mortlock et al. 2011] Mortlock, D., Warren, S., Patel, M., et al., *The discovery of a luminous redshift 7.1 quasar*, *Galaxy Formation*, 2011, 88

[Massaro et al. 2006] Massaro, E., Tramacere, A., Perri, M., et al., *Log-parabolic spectra and particle acceleration in blazars. III. SSC emission in the TeV band from Mkn501*, *A&A*, 2006, **448**, 861-871

[Massaro et al. 2009a] Massaro, F., Chiaberge, M., Grandi, P., et al., *Extended X-Ray Emission in Radio Galaxies: The Peculiar Case of 3C 305*, *ApJ*, 2009, **692L**, 123

[Massaro et al. 2009b] Massaro, F., Harris, D., Chiaberge M., et al., *The Jet of 3C 17 and the Use of Jet Curvature as a Diagnostic of the X-ray Emission Process*, *ApJ*, 2009, **696**, 980

[Massaro et al. 2010] Massaro, F., Harris, D., Tremblay, G., et al. *Chandra Observations of 3C Radio Sources with $z < 0.3$: Nuclei, Diffuse Emission, Jets, and Hotspots*, *ApJ*, 2010, **714**, 589

[Massaro et al. 2011] Massaro, F., Harris, D., & Cheung, C., *Large-scale Extragalactic Jets in the Chandra Era. I. Data Reduction and Analysis*, *ApJS*, 2011, **197**, 24

[Massaro et al. 2012] Massaro, F., Tremblay, G., Harris, D., et al., *Chandra Observations of 3C Radio Sources with $z < 0.3$. II. Completing the Snapshot Survey*, *ApJS*, 2012, **203**, 31

[Massaro et al. 2013] Massaro, F., Harris, D., Tremblay, G. et al., *A Chandra Snapshot Survey for 3C Radio Galaxies with Redshifts between 0.3 and 0.5*, *ApJS*, 2013, **206**, 7

[Massaro et al. 2015] Massaro, F., Harris, D., Liuzzo, E., et al., *The Chandra Survey of Extragalactic Sources in the 3CR Catalog: X-ray Emission from Nuclei, Jets, and Hotspots in the Chandra Archival Observations*, *ApJS*, 2015, **220**, 5

[Matsumoto et al. 2005] Matsumoto, T., Matsuura, S., Murakami, H., et al., *Infrared Telescope in Space Observations of the Near-Infrared Extragalactic Background Light*, *ApJ*, 2005, **626**, 31

[Matsumoto et al. 2015] Matsumoto, T., Kim, M., G., Pyo, J., et al., *Reanalysis of near-infrared extragalactic background light based on the IRTS observation*, *astro-ph*, 2015, `arXiv:1501.01359`

[Matsuoka et al. 2011] Matsuoka, Y., Ienaka, N., Kawara, K., et al., *Cosmic Optical Background: The View from Pioneer 10/11* , *ApJ*, 2011, **736**, 119

[Mattila et al. 1991] Mattila, K., Leinert, C., & Schnur, G., *The extragalactic background light : optical and near-infrared observations*, *The Early Observable Universe from Diffuse Backgrounds*, *Proceedings of the 26th Rencontres de Moriond, 11th Moriond Astrophysics Meetings*, 1991, 133

[Mattox et al. 2001] Mattox, J., R., Hartman, R., C., & Reimer, O., *A Quantitative Evaluation of Potential Radio Identifications for 3EG EGRET Sources*, *ApJSS*, 2001, **135**, 155

[Mazin & Raue 2007] Mazin, D. and Raue, M., *New limits on the density of the extragalactic background light in the optical to the far infrared from the spectra of all known TeV blazars*, *A&A*, 2007, **471**, 439

[Mazin et al. 2013] Mazin, D. and Tescaro, D. et al., *Upgrade of the MAGIC telescopes*, `arXiv:1410.5073`, 2013.

[Mei et al. 2007] Mei S., Blakeslee, J., P., Côté, P., et al., *The ACS Virgo Cluster Survey. XIII. SBF Distance Catalog and the Three-dimensional Structure of the Virgo Cluster*, *ApJ*, 2007, **655**, 144-162

[Meliani et al. 2010] Meliani, Z., Sauty, C., Tsinganos, K., et al., *Relativistic spine jets from Schwarzschild black holes: Application to AGN radio-loud sources*, *A&A*, 2010, **521**, 11

[Meyer et al. 2012] Meyer, M., Raue, M., Mazin, D. et al., *Limits on the extragalactic background light in the Fermi era*, *A&A*, 2012, **542**, A59.

[Metcalfe et al. 2003] Metcalfe, L., Kneib, J., P., McBreen, B., et al., *An ISOCAM survey through gravitationally lensing galaxy clusters. I. Source lists and source counts for A370, A2218, and A2390*, *AAP*, 2003, **407**, 791

[Mirzoyan 1997] Mirzoyan, R., *On the calibration accuracy of light sensors in atmospheric Cherenkov fluorescence and neutrino experiment*, *International Cosmic Ray Conference*, 1997, **7**, 265

[Mirzoyan 2014] Mirzoyan, R., MAGIC Collaboration, *Exceptionally high 100 GeV flux state of 1ES 1011+496*, *The Astronomer's Telegram*, 2014, **5887**, 1

[Mirzoyan 2019] Mirzoyan, R., MAGIC Collaboration, *First time detection of a GRB at sub-TeV energies; MAGIC detects the GRB 190114C*, *The Astronomer's Telegram*, 2019, **12390**

[Moderski et al. 2003] Moderski, R., Sikora, M., & Błażejowski, M., *Numerical simulations of radiation from blazar jets*, *A&A*, 2003, **406**, 855-865

[Mücke & Protheroe 2000] Mücke, A., & Protheroe, R.J., *Modeling the April 1997 flare of Mkn 501*, *In B.L. Dingus, M.H. Salamon and D.B. Kieda, editors, 'American Institute of Physics Conference Series'*, 2000, **515**, 149-153

[Mücke et al. 2003] Mücke, A., Protheroe, R., J., Engel, R., et al., *BL Lac objects in the synchrotron proton blazar model*, *APh*, 2003, **18**, 593-613

[Mushotzky 1982] Mushotzky, R., *The X-ray spectrum and time variability of narrow emission line galaxies ApJ*, 1982, **256**, 92

[Napier et al. 1993] Napier, P., Bagri, D., Clark, B., et al., *The Very Long Baseline Array*, *Proceedings of IEEE*, 1993, **82**, 658

[Nieppola et al. 2006] Nieppola, E., Tornikoski, M. & Valtaoja, E. *Spectral energy distributions of a large sample of BL Lacertae objects*, *A&A*, 2006, **445**, 441-450.

[Neronov & Aharonian 2007] Neronov, A., & Aharonian, F., *Production of TeV Gamma Radiation in the Vicinity of the Supermassive Black Hole in the Giant Radio Galaxy M87*, *ApJ*, 2007, **671**, 85

[Nolan et al. 2012] Nolan, P., Abdo, A., Ackermann, M., et al., *Fermi Large Area Telescope Second Source Catalog*, *ApJS*, 2012, **199**, 31

[Orr et al. 2011] Orr, M. R., Krennrich, F., & Dwek, E., *Strong New Constraints on the Extragalactic Background Light in the Near- to Mid-infrared*, *ApJ*, 2011, **733**, 77.

[Owen et al. 2000] Owen, F., N., Eilek, J., A., & Kassim, N., E., *M87 at 90 Centimeters: A Different Picture*, *ApJ*, 2000, **543**, 611

[Padovani 1999] Padovani, P., *High energy emission from AGN and unified schemes In F. Giovannelli and G. Mannocchi, editors, Vulcano Workshop 1998: Frontier Objects in Astrophysics and Particle Physics*, 1999, 159

[Padovani et al. 2017] Padovani, P., Alexander, D., Assef, R., et al., *Active galactic nuclei: whats in a name? Astron.Astrophys.Rev*, 2017, **25**, 1-2

[Palenzuela et al. 2011] Palenzuela, C., Bona, C., Lehner, L. et al., *Robustness of the Blandford-Znajek mechanism*, *Classical and Quantum Gravity*, 2011, **28**, 13

[Papovich et al. 2004] Papovich, C., Dole, H., Egami, E., et al., *The 24 Micron Source Counts in Deep Spitzer Space Telescope Surveys*, *ApJS*, *astro-ph/0406035*, 2004, **154**, 70

[Penin et al. 2012] Pénin, A., Lagache, G., Noriega-Crespo, A., et al., *An accurate measurement of the anisotropies and mean level of the cosmic infrared background at 100 μm and 160 μm*, *AAP*, 2012, **543**, A123

[Perkins 2009] Perkins, D., *Particle Astrophysics*, Second Edition, *Oxford Master Series In Physics*, 2009

[Perlman et al. 2003] Perlman, E., Harris, D., Biretta, J., et al., *Month-Timescale Optical Variability in the M87 Jet*, *ApJL*, 2003, 599, L65

[Perlman et al. 2011] Perlman, E., Adams, S., Cara, M., et al., *Optical Polarization and Spectral Variability in the M87 Jet*, *ApJ*, 2011, 743, 119

[Persic & Rephaeli 2011] Persic, M., & Rephaeli, Y., *High-energy emission from star-forming galaxies*, *astro-ph.HE*, 2011, `arXiv:1101.4404`

[Primack et al. 2005] Primack, J., R., Bullock, J., S., Somerville, R., S., et al., *Observational Gamma-ray Cosmology*, *2nd International Symposium on High Energy Gamma-Ray Astronomy*, 2005, **745**, 23-33

[Prandini et al. 2010] Prandini, E., Bonnoli, G., Maraschi, L., et al., *Constraining blazar distances with combined Fermi and TeV data: an empirical approach*, *MNRAS*, 2010, **405**, L76-L80

[Primack et al. 2011] Primack J. R., Domínguez, A., Gilmore, R., C., et al., *Extragalactic Background Light and Gamma-Ray Attenuation*, *American Institute of Physics Conference Series*, 2011, **1381**, `arXiv:1107.2566`

[Proffitt et al. 2003] Proffitt, C., Brown, T., Mobasher, B., et al., *Instrument Science Report, STIS 2003-01 (Baltimore, MD: STScI)*, 2003, `http://www.stsci.edu/hst/stis/documents/isrs/200301.pdf`

[Protheroe & Clay 2004] Protheroe, R., J., & Clay, R., W., *Ultra High Energy Cosmic Rays*, *Publications of the Astronomical Society of Australia*, 2004, **21**, 1, `arXiv:astro-ph/0311466`

[Rachen & Mészáros 1998] Rachen, J., P., & Mészáros, P., *Photohadronic neutrinos from transients in astrophysical sources*, *Phys. Rev.*, 1998, **58**, 12-15

[Ramolia et al. 2017] Romolia, C., Taylora, A., Aharoniana, F., *Cut-off Characterisation of Energy Spectra of Bright Fermi Sources: Current instrument limits and future possibilities*, *APh*, 2017, **88**, 38-45, `arXiV:1202.2867`

[Rau et al. 2012] Rau A., Schady P., Greiner J., and et al., *BL Lacertae objects beyond redshift 1.3 - UV-to-NIR photometry and photometric redshift for Fermi/LAT blazars*, *A&A*, 2012, **538**, A26

[Raue & Mazin 2010] Raue, M., & Mazin, D., *Potential of the next generation VHE instruments to probe the EBL (I): The low- and mid-VHE*, *APh*, 2010, **34**, 245

[Reinthal et al. 2012] Reinthal, R., Rügamer, S., Lindfors, E., J., et. al., *Multiwavelength Observations of the HBL 1ES 1011+496 in Spring 2008*, *Journal of Physics Conference Series*, 2012, **355**, 1

[Richter & Spanier 2016] Richter, R. & Spanier, F., *A numerical model of parsec scale SSC morphologies and their radio emission*, *ApJ*, 2016, **829**, 8, `arXiv:1606.02078`

[Ryan et al. 2015] Ryan, B., Dolence, J., & Gammi, C., *bhlight: General Relativistic Radiation Magnetohydrodynamics with Monte Carlo Transport*, *ApJ*, 2015, **807**, 20

[Salpeter 1964] Salpeter, E., E., *Accretion of interstellar matter by massive objects*, *ApJ*, 1964, **635**, 796-800

[Sanders et al. 1989] Sanders, D. B., Phinney, E. S., Neugebauer, G., et al., *Continuum Energy Distributions of Quasars: Shapes and Origins*, *ApJ*, 1989, **347**, 29

[Sbarufatti et al. 2005] Sbarufatti, B., Treves, A., & Falomo, R., *Imaging Redshifts of BL Lacertae Objects*, *ApJ*, 2005, **635**, 173-179

[Schmidt 2014] Schmidt F., *CORSIKA Shower Images*, 2014, `http://www.ast.leeds.ac.uk/fs/showerimages.html`

[Schmelling 1994] Schmelling, M., *The method of reduced cross-entropy. A general approach to unfold probability distributions*, *NIM*, 1994, **340**, 400

[Schultz 2013] Schultz, C., *Development of New Composite Mirrors for Imaging Cherenkov Telescopes and Observations of the Two Blazar Objects 1ES 0806+524 and 1ES 1011+496 with MAGIC*, Ph.D. Thesis, University, and INFN Padova, 2013.

[Seyfert 1943] Seyfert, C., K., *Nuclear emission in spiral nebulae*, *ApJ*, 1943, **97**, 28

[Shepherd et al. 1994] Shepherd, M., C., Pearson, T., J., & Taylor, G., B., *DIFMAP: an interactive program for synthesis imaging*, *Bulletin of the Astronomical Society*, 1994, **26**, 987

[Sitarek et al. 2013] Sitarek J., Gaug M., Mazin D., et al., *Analysis techniques and performance of the Domino Ring Sampler version 4 based readout for the MAGIC telescopes*, *NIMPRA*, 2013, **723**, 109-120.

[Sitarek et al. 2013a] Sitarek, J., Carmona, E., Colin, P., et al., *Physics performance of the upgraded MAGIC telescopes obtained with Crab Nebula data*, *Proceedings of 33rd ICRC*, 2013, `arXiv:1308.0141`

[Sinha et al. 2017] Sinha, A., Sahayanathan, S., Acharya, B. et al., *On the Spectral Curvature of VHE Blazar 1ES 1011+496: Effect of Spatial Particle Diffusion*, *ApJ*, 2017, **836**, 83

[Simpson 1983] Simpson, J., *Elemental and isotopic composition of the galactic cosmic rays*, *Annual Review of Nuclear and Particle Science*, 1983, **33(1)**, 323-382

[Sowards-Emmerd et al. 2005] Sowards-Emmerd, D., Romani, R., W., Michelson, P., F., et al., *A Northern Survey of Gamma-Ray Blazar Candidates*, *ApJ*, 2005, **626**, 95-103

[Sparke & Gallagher 2007] Sparke, L. & Gallagher, J. S. III, *Galaxies in the Universe: An Introduction*, Second edition, *Cambridge University Press*, 2007

[Sreekumar et al. 1998] Sreekumar, P., Bertsch, D., L., Dingus, B. L., et al, *EGRET Observations of the Extragalactic Gamma-Ray Emission*, *ApJ*, 1998, **494**, 523-534

[Stecker et al. 1996] Stecker, F. W. and de Jager, O. C., *Absorption of high energy gamma-rays by low energy intergalactic photons*, *Space Science Reviews*, 1996, **75**, 401.

[Stecker et al. 2006] Stecker, F., W., Malkan, M., A., & Scully, S., T., *Intergalactic Photon Spectra from the Far-IR to the UV Lyman Limit for 0<z<6 and the Optical Depth of the Universe to High-Energy Gamma Rays*, *ApJ*, 2006, **774**.

[Steele et al. 2004] Steele, I., Smith, R., Rees, P., et al., *The Liverpool Telescope: performance and first results* , *Ground-based Telescopes. Edited by Oschmann, Jacobus M., Jr. Proceedings of the SPIE*, 2004, **5489**, 679

[Su et al. 2013] Su, M. & Finkbeiner, D. P. *Evidence for Gamma-ray jets in the Milky Way*, *ApJ*, 2013. **753**, 61

[Tavani et al. 2009] Tavani, M., Barbiellini, G., Argan, A., et al., *The AGILE Mission*, *A&A*, 2009, **502**, 995-1013.

[Tavecchio et al. 1998] Tavecchio, F., Maraschi, L., & Ghisellini, G., *Constraints on the Physical Parameters of TeV Blazars*, *ApJ*, 1998, **509**, 608.

[Tavecchio & Ghisellini 2008] Tavecchio, F., & Ghisellini, G., *Spine-sheath layer radiative interplay in subparsec-scale jets and the TeV emission from M87*, *MNRAS*, 2008, **385**, L98

[Tavecchio et al. 2010] Tavecchio, F., Ghisellini, G., Ghirlanda, G., et al., *TeV BL Lac objects at the dawn of the Fermi era*, *MNRAS*, 2008, **401**, 1570-1586

[Tavecchio et al. 2011] Tavecchio, F., Becerra-Gonzalez, J., Ghisellini, G., et al., *On the origin of the γ-ray emission from the flaring blazar PKS 1222+216*, *A&A*, 2011, **534**, 8

[Thompson et al. 2007] Thompson, R., Eisenstein, D., Fan, X., et al., *Constraints on the Cosmic Near-Infrared Background Excess from NICMOS Deep Field Observations*, *ApJ*, 2007, **657**, 2

[Tescaro 2010] Tescaro, D., *TeV γ-ray observation of nearby Active Galactic Nuclei with the MAGIC telescope: exploring the high energy region of the multi-wavelength picture*, Ph.D. Thesis, UAB, 2010.

[Tescaro et al. 2012] Tescaro D., *The upgraded readout system of the MAGIC telescopes*, *Nuclear Science Symposium and Medical Imaging Conference (NSS/MIC)*, *IEEE*, 2012, 1901-1904

[Tikhonov & Arsenin 1977] Tikhonov, A.N. and Arsenin, V.A., *Solution of iII-posed Problems*, *Winston & Sons, Washington*, 1977

[Tramacere et al. 2009] Tramacere, A., Giommi, P., Perri, M., et al., *Swift observations of the very intense flaring activity of Mrk 421 during 2006. I. Phenomenological picture of electron acceleration and predictions for MeV/GeV emission*, *A&A*, 2009, **501**, 879-898

[Tramacere et al. 2011] Tramacere, A., Massaro, E., & Taylor, A. M., *Stochastic Acceleration and the Evolution of Spectral Distributions in Synchro-Self-Compton Sources: A Self-consistent Modeling of Blazars' Flares*, *ApJ*, 2011, **739**, 16

[Tridon et al. 2010] Tridon D.B. et al., *The MAGIC-II gamma-ray stereoscopic telescope system*, *NIMPRSA: Accelerators, Spectrometers, Detectors and Associated Equipment*, 2010, **623(1)**, 437-439

[Tridon et al. 2011] Tridon, D., B., Schweizer, T., Goebel, F., et al., *Measurement of the cosmic electron plus positron spectrum with the MAGIC telescopes*, *astro-ph*, 2011, `arXiv:1110.4008`

[Trimble 1973] Trimble, V., *The Distance to the Crab Nebula and NP 0532*, *PASP*, 1973, **85**, 579

[Ulrich et al. 2011] Ulrich, R., Engel, R. & Unger, M., *Hadronic multiparticle production at ultrahigh energies and extensive air showers*, *Phys. Rev. D*, 2011, **83**, 5, 054026.

[Urry & Padovani 1995] Urry, C.M. & Padovani, P., *Unified Schemes for Radio-Loud Active Galactic Nuclei*, *PASP*, 1995, **107**, 803

[Vasileiadia et al. 2005] Vasileiadis, G. and H.E.S.S. Collaboration, *The H.E.S.S experimental project*, *NIMPRA*, year, **553**, 268-273

[Voyer et al. 2011] Voyer, E., N., Gardner, J., P., Teplitz, H., I., et al., *Far-ultraviolet Number Counts of Field Galaxies*, *ApJ*, 2011, **736**, 80

[Walker et al. 2014] Walker, R., C., *VLBA Scientific Memo*, 2014, **37**, `http://library.nrao.edu/public/memos/vlba/sci/VLBAS_37.pdf`

[Wagner 2006] Wagner R., *Measurement of VHE gamma-ray emission from four blazars using the MAGIC telescope and a comparative blazar study*, Ph.D. thesis, Technische Universität München, 2006.

[Weekes et al. 1989] Weekes, T., C., Cawley, M., F., Fegan, D., J., et al., *Observation of TeV gamma rays from the Crab Nebula using the atmospheric Cerenkov imaging technique*, *ApJ*, 1989, **342**, 379-395.

[Weekes et al. 2002] Weekes, T., C., Badran, H., Biller, S., D., et al., *VERITAS: the Very Energetic Radiation Imaging Telescope Array System*, *APh*, 2002, **17**, 221

[Weidinger & Spanier 2010] Weidinger, M., & Spanier, F., *Modeling the emission from blazar jets: the case of PKS 2155-304*, *IJMPhysD*, 2010, **19**, 887

[Weidinger & Spanier 2010a] Weidinger, M., & Spanier, F., *Modelling the variability of 1ES1218+30.4*, *A&A*, **515**, 18

[Weidinger & Spanier 2015] Weidinger, M., & Spanier, F., *A self-consistent and time-dependent hybrid blazar emission model Properties and application*, *A&A*, 2015, **573**, A7

[Woosley et al. 2006] Woosley, S.E. and Bloom, J.S., *The Supernova Gamma-Ray Burst Connection*, *ARA&A*, 2006, **44**, 507-556

[Write et al. 2001] Wright, E., L., *DIRBE minus 2MASS: Confirming the Cosmic Infrared Background at 2.2 Microns*, *ApJ*, 2001, **553**, 538

[Wu et al. 2001] Wu, X., Hamilton, T., Helfand, D. J., et al., *The intensity and spectrum of the diffuse X-ray background*, *ApJ*, 1991, **379**, 564-575

[Xu et al. 2005] Xu, C., K., Donas, J., Arnouts, S., et al. *Number Counts of GALEX Sources in Far-Ultraviolet (1530 Å) and Near-Ultraviolet (2310 Å) Bands*, *ApJL*, 2005, **619**, L11

[Yang & Wang 2010] Yang, J. & Wang, J., *Redshifts of Distant Blazars Limited by Fermi and VHE -Ray Observations*, *Astronomical Society of Japan*, 2010, **62**, L23-L26

[Yao et al. 2006] Yao, W., Amsler, C., Asner, D., et al. *Some New Particles beyond the Standard Model*, *Review of Particle Physics. Journal of Physics*, 2006, **G**, 33:1

[Zanin et al. 2013] Zanin, R., Carmona, E., Sitarek, J., et al., *MARS, the MAGIC analysis, and reconstruction software*, *Proc of the 33rd ICRC, Rio de Janeiro*, 2013, **2**, 773

[Zel'dovich et al. 1964] Zel'dovich, Y., B., & Novikov, I., D., *The radiation of gravity waves by bodies moving in the field of a collapsing star*, *Sov. Phys. Dokl.*, 1964, **9**, 246

[Zatsepin & Kuzmin 1966] Zatsepin, G., T., & Kuzmin, V., A., *Upper limit on the spectrum of cosmic rays*, *JETP Letters*, 1966, **4**, 78

[Zemcov & Smidt 2014] Zemcov, M. & Smidt, J. et al., *On the origin of near-infrared extragalactic background light anisotropy*, *Science*, 2014, **346**, 732.

Acknowledgements

I would like to take this opportunity to show my gratitude to everyone who supported me during the Ph.D. time, as my thesis truly felt as exciting as a roller coaster ride. First, I would like to thank my day to day supervisor Daniel Mazin for giving me this opportunity to pursue my Ph.D. in this exciting field of γ-ray astronomy. I am thankful for his support, trust in me, valuable advice, fruitful discussions and patience with my work. I would also like to thank Prof. Masahiro Teshima for giving me the opportunity to join the MAGIC experiment and to do my Ph.D. thesis at the Max-Planck-Institute for physics in Munich. I would also like to thank him for his support, encouragement, and helpful discussions. I am grateful to Prof. Christian Kiesling for being my official supervisor at the Ludwig Maximilian University, Munich, and being very helpful and supportive throughout this thesis. I am especially thankful to him for organizing very helpful and insightful lectures on particle physics and cosmology. Many thanks also go to Razmik Mirzoyan, David Paneque and Thomas Schweizer, for their continuous support, valuable comments, and many fruitful discussions in their offices. Special thanks to Jürgen Besenrieder and David Fink for all their help in the lab. I also want to express my deepest gratitude for late Eckart Lorenz. I was fortunate to get a chance to work with him, as he was undoubtedly a great scientist and an encouraging personality. I would also like to thank for the opportunities to join the workshops, summer schools, and national and international conferences.

I would like to thank everyone in the MAGIC MPP group in Munich, for the very positive and friendly working atmosphere. I enjoyed all the physics and technical discussions with them very much and found them very constructive and motivating. I want to thank my MPP colleagues Jezabel R. García, Hanna Kellermann, Christian Fruck, Takeshi Toyama, and Uta Colin for being extremely helpful, kind, and being there for me in my happiness as well as in most difficult times. I also appreciated a lot working in this positive atmosphere with Ievgen Vovk, David Green, Pierre Colin, Julian Krause, Marcel Stryzs, Giovanni Ceribella, Martin Will, Lea Heckmann, Yusuke Suda, Julien-Christopher Beyer, Wojciech Idec, Koji Noda, Kazuma Ishio, Max Knöttig, Alexander Hahn, Juliane van Scherpenberg, Daniel Hoff, Yoshiki Ohtani, Stefan Keller, Giacomo DAmico, Moritz Huetten, Yating Chai, Corina Brunnlechner, Alfred Kriesel, Arthur Erhardt, Uwe Leupold, and many others. I would like to especially thank Sybille Rodriguez and Petra Lindemann for their encouragement, help, support and always being there for me when I needed the most. I would also like to thank Diana Werner for all her recent help and support.

I would like to thank all members of the MAGIC collaboration for the great

positive atmosphere. It always felt like being a part of one big family. Special thanks to Julian Sitarek for all his help regardless of the topic of science or technical support. I would also like to thank Marina Manganaro, Cornelia Arcaro, Biswajit Banerjee, Iva Šnidarić, Konstancja Satalecka, Daniela Hadasch, Ruben Lopez, Diago Tescaro, Gianluca Giavitto, and Pratik Majumdar. Many thanks to Ana Babic for helping me a lot with the technical problems and discussions during the datacheck shift.

I would also like to take this opportunity to thank Prof. S. Ananthkrishnan, Prof. V. K. Kulkarni and Prof. Maura McLaughlin, for being always so caring, motivating and keeping my spirits up in every difficult situation during my thesis time. Special thanks also goes to Prof. John Conway for his help and support.

I could not have done this thesis without the warm support of all my friends, with whom I had a wonderful time along the way. I am also delighted to have found many new friends outside MAGIC collaboration during my Ph.D. time. I want to thank Sovan Chakraborty and Aparna Mukherjee for all the delicious food, making all the fun time in Munich most memorable and have countless discussions not just on science topics but also on life, politics, and history as well. I would especially like to thank Frederic Jaron, whose friendship was invaluable help, and pleasure, and who stayed on my side by always motivating and supporting me. I want to thank all my dear friends; Guari Patil, Manpreet Kaur, Jayanth Chennamangalam, Yogesh Chandola, Shweta Kuvalekar, Yogesh Karandikar, Sagar Godambe, Bhushan Billade, Sumedh Mahashabde, Minal Dubewar, Sudeep Banthia, Sebastian Lange, Priyanka Chaturvedi, Mayank Narang, Santosh Jagade, Shweta Srivastava, and Ujjwal Kumar. Thank you for all the fun, craziness and being there for me in all the happy and challenging moments.

Last but not least, I am incredibly grateful to have a loving and caring family. I want to thank my brother in law Ravikant and my lovely nephew Dhruva, for their good wishes and especially supporting my stay during the writing phase of the thesis. I am forever thankful to my parents Suresh and Lata, and to my sister Mukta, for their unconditional love, support and belief in me, without it this work would not have been possible at all.